To the Graduate Council:

I am submitting herewith a dissertation written by Abraham Joseph Meganathan entitled "Adaptive Control of Axisymmetric Jets by Cavities". I have examined the final electronic copy of this dissertation for form and content and recommend that it be accepted in partial fulfillment of the requirements for the degree of Doctor of Philosophy, with a major in Mechanical Engineering.

Ahmad D. Vakili
Major Professor

We have read this dissertation
and recommend its acceptance:

Roy J. Schulz

Gary A. Flandro

Basil N. Antar

K.C. Reddy

Accepted for Council:

Anne Mayhew
Vice Chancellor and Dean of
Graduate Studies

(Original signatures are on file with official student records.)

ADAPTIVE CONTROL OF AXISYMMETRIC JETS BY CAVITIES

A dissertation
Presented for the
Doctor of Philosophy
Degree
The University of Tennessee, Knoxville

Abraham Joseph Meganathan

May 2005

ACKNOWLEDGEMENT

The author thankfully acknowledges the love, support and guidance of GOD and his family that has sustained him throughout the years of his life.

Sincere appreciation and thanks is expressed to the author's faculty advisor Dr. Ahmad Vakili for his continuous encouragement, valuable advice and support throughout the course of this study.

The author would like to thank his dissertation committee members Dr. Basil Antar, Dr. Gary Flandro, Dr. K.C. Reddy and Dr. Roy Schulz for their advice and constructive comments regarding this work.

Special thanks are expressed to the UTSI Gas Propulsion Lab support personnel Mr. Chris Armstrong, Mr. Jim Goodman, Mr. Gary Payne and last but not the least Mr. Keith Walker particularly for his help in making the phase locked measurements.

The author wishes to extend his thanks to friends and well-wishers who have encouraged, supported and prayed for him at various periods during the course of this study.

ABSTRACT

Actuators capable of producing large amplitude oscillations at desired frequencies are needed in many flow control applications. In this dissertation, turbulent jets were actuated using self-sustaining oscillations in axisymmetric cavities. Tested geometries include baseline turbulent jets passing through axisymmetric cavities, with and without peripheral walls. Cavity length to depth ratio (L_c/D_c) was varied from 1 to 5 and data were collected at several intermediate steps. Tests were performed with air over a Reynolds number, based on jet exit diameter, range of 40,000 to 225,000 in low to high subsonic jet flow conditions. Pressure signals, 2D velocity data obtained using Particle Image Velocimetry (PIV) and 2D axisymmetric Computational Fluid Dynamics (CFD) modeling were concurrently used to analyze and understand the problem.

Measurements on baseline turbulent jets showed that the near field coherent structures and their residence time are two important factors that could be manipulated to influence the initial growth rate of a jet. Frequency of oscillation of the pressure field within the cavity was primarily dependent on the length scale (length to depth ratio and the pipe diameter) of the cavity and the Mach number of the flow. Axisymmetric cavities with cavity length to depth ratio 1.5 – 2.0, preferably 1.75, placed immediately after the exit of the jet exhibited a resonant condition (between the axial shallow cavity mode and the radial acoustic mode of the pipe) with very high amplitude oscillations (in excess of 180 dB within the cavity) at moderate to high Reynolds number range of this study. Comparison with baseline jets based on centerline velocity decay and lateral jet spread rate showed that mixing characteristics had improved significantly. The potential core length (location of 90% jet exit velocity) for the best case was at 1D as compared to 5D for the baseline jet. Ensemble averages of different phases of an oscillation cycle (along the jet flow direction and in the cross-section) were used to recreate the oscillation cycle (flow visualization images, velocity and vorticity fields) and study the flow structures in the near field. Mode of oscillation (axial / helical) of the jet exiting the cavity was found to be dependent on the inlet and exit boundary conditions of the cavity. Cavities with sharp orifices at the inlet and exit boundaries had complex helical mode structures in the near field of the jet. When the exit boundary of the cavity had a short pipe instead of a sharp orifice, only axial mode vortex rings remained in the near field. However the jet entrainment was not as high, as in the case of sharp orifices.

Keywords: Turbulent Jet, Jet Actuator, Flow Control, Phase Locked Measurements, Particle Image Velocimetry (PIV)

TABLE OF CONTENTS

LIST OF TABLES

TABLE **PAGE**

LIST OF FIGURES

LIST OF SYMBOLS

Geometrical Parameters

D_c - Cavity diameter
D_e - Exit diameter
D_j - Jet diameter
D_p - Pipe diameter
L_c - Cavity length
r - Radius of the cavity pipe = $D_p/2$ in this study
T_d - Thickness of the downstream baffle
T_u - Thickness of the upstream baffle
θ_d - Angle of the bevel in downstream baffle
θ_u - Angle of the bevel in upstream baffle

PIV parameters

C(s) - Cross-correlation between interrogation spots of two sequential image frames I_1 and I_2
c_τ - Constant depends on the ability of the analysis procedure to determine the displacement between images
d_e - Optical image diameter of the seeding particle before being recorded
d_p - Seeding particle diameter
d_r - Resolution of a pixel in the recording device
d_s - Diffraction limited spot diameter
DSR - Dynamic spatial resolution
DVR - Dynamic velocity range
d_τ - Recorded image diameter of the seeding particle
$f^\#$ - Aperture value
I_1 - Image frame 1 in a cross-correlation sequence
I_2 - Image frame 2 in a cross-correlation sequence
L_x - Recording dimension in the object plane
M - Image magnification
N - Total number of image frames used for averaging
U(x,y) - Mean velocity in the 'x' direction
$U_p(x,y)$ - Mean velocity in the 'x' direction for a particular phase 'p'
u' - Fluctuating velocity in the 'x' direction
u_i - Velocity in the 'x' direction of the i^{th} image frame
$u_{i,p}$ - Velocity in the 'x' direction of the i^{th} image frame for phase 'p'
V(x,y) - Mean velocity in the 'y' direction

$V_p(x,y)$ - Mean velocity in the 'y' direction for a particular phase 'p'
v' - Fluctuating velocity in the 'y' direction
v_i - Velocity in the 'y' direction of the i^{th} image frame
$v_{i,p}$ - Velocity in the 'y' direction of the i^{th} image frame for phase 'p'
Δt - Time interval between image pairs in a cross-correlation sequence
Δx - Displacement between image pairs in a cross-correlation sequence
λ - Wavelength of the light used in PIV (532 nm for green)
σ_u - RMS error that defines minimum resolvable fluctuations
$\omega(x,y)$ - Mean vorticity at a point in the 2D plane
$\omega_p(x,y)$ - Mean vorticity at a point in the 2D plane for a particular phase 'p'
ω_i - Vorticity of the i^{th} image frame
$\omega_{i,p}$ - Vorticity of the i^{th} image frame for phase 'p'

Numerical Modeling Parameters

$\partial/\partial t$ - first derivative in time
$\partial/\partial x$ - first derivative in 'x' direction
$\partial/\partial y$ - first derivative in 'y' direction
$\partial/\partial z$ - first derivative in 'z' direction
C_s - constant based on the isotropy of the small scales assumption (0.05-0.2)
Δf - filter width
f - field variable
$\overline{f}$ - filtered value of the field variable
G - filter, a symmetric function with compact support
γ_t - sub-grid scale eddy viscosity
$\nabla\bullet$ - divergence of a function
$\overline{S}_{i,j}$ - local strain rate
$\tau_{i,j}$ - sub-grid scale stresses $= \overline{u_i u_j} - \overline{u_i}\,\overline{u_j}$

Flow Parameters

a - speed of sound
A - Constant
B - decay rate coefficient
β - jet spread angle
C - volumetric flow coefficient
δ^* - displacement thickness
f - frequency of the oscillation
f_{1-L} - side band peak to the left of the major peak in the pressure spectrum

$f_{1\text{-}R}$	-	side band peak to the right of the major peak in the pressure spectrum
f_i	-	frequency after i^{th} vortex merging
f_m	-	modulating frequency
f_o	-	frequency of oscillation (major peak in the pressure spectrum)
η	-	similarity parameter for the shape of the velocity profile
H	-	shape factor
$j'_{m,n}$	-	$(n+1)^{th}$ positive zero of the derivative of Bessel function
J_o	-	momentum flux through any arbitrary x = constant surface
K	-	convection velocity ratio
M	-	Mach number
n	-	mode of oscillation n=1,2,3…
θ	-	momentum thickness
Q	-	volumetric flow rate
q_z	-	axial modes
Re_D	-	Reynolds number based on jet diameter
SPL	-	Sound pressure level in dB
St	-	Strouhal number
U_c	-	convection velocity
U_{CL}	-	Velocity along centerline
ω_a	-	resonant frequency based on the azimuthal, radial and axial modes
x	-	location in the jet flow direction
λ_{DPW}	-	wavelength of the downstream propagating wave
X_i	-	location of the i^{th} vortex merging
x_o	-	distance of the virtual origin from jet exit
λ_{UPW}	-	wavelength of the upstream propagating wave
y	-	location in the radial direction of the jet
$y_{1/2}$	-	jet half-width (location of the 50% centerline velocity)

Chapter 01

INTRODUCTION

Flow control as an art has been pursued since pre-historic times and still is one of the most actively researched areas in modern day fluid mechanics. In the context of this study, flow control is defined, as the ability to manipulate a flow field and to achieve specific desired effects that greatly improve the efficiency of a fluid system. Experiments have shown that under certain conditions, with small levels of energy external or otherwise, selectively applied at strategic points in a flow, major changes in the large-scale structures of flow field may be accomplished [*Vakili & Chang 1991*].

From streamlined spears and fin-stabilized arrows, the intent of current researchers of flow control has evolved to delay or to advance transition, to suppress or to enhance turbulence and to prevent or to promote separation, resulting in drag reduction, lift enhancement, mass, momentum and heat transfer enhancement and flow-induced noise reduction. Flow control is still more of an art than science, because the objectives of flow control are often inter-related, leading to potential conflicts, necessitating intelligent design trade-offs.

1.1 Coherent Structures

Historically, study of turbulence has been approached from two different viewpoints [*Ho & Huerre 1984*]. The first viewpoint is the classical approach that turbulence is strictly a random process that can be described statistically. The second more widely accepted and current viewpoint is that the quasi-periodic, large-scale vortex structures are the main elements of turbulent flows. The fact that turbulent flows at certain regions are not completely random, but possess large-scale, spatially correlated motions was experimentally discovered in the middle part of last century [*Townsend 1952, Crow & Champagne 1971, Brown & Roshko 1974*]. Hussain [*Hussain 1980, 1983, 1986*] defines coherent structures as a connected turbulent fluid mass with instantaneously phase correlated vorticity over its spatial extent and thereby emphasized vorticity as a characteristic measure of coherent structures. Robinson [*Robinson 1991*] defines a coherent motion as a three-dimensional region of flow over which at least one fundamental flow variable exhibits significant correlation with itself or with another variable over a range of space and / or time that is significantly larger than the smallest local scales of the flow. Coherent structures have been studied extensively and have been shown to be an important factor in governing the macro-characteristics (transport properties) of turbulent flows, like mass, momentum and heat transfer properties [*Winnant & Browand 1974, Browand & Weidman 1976, Ho & Huang 1982*].

Coherent structures have been observed in all types of turbulent flows including free-shear flows [*Brown and Roshko 1971, 1974, Roshko 1976, Fiedler 1988,1998*] and wall-bounded flows [*Townsend 1961, 1970, Bakewell & Lumley 1967*] even though they are much easier to detect in the former. The existence of large-scale coherent motions in mixing layers, jets and wakes is a manifestation of the dynamic instability associated with the local inflectional mean-velocity profiles. So, free shear layers have pronounced organized motions and wavelike structures [*Fiedler 1988,1998*]. These structures have been observed even at high Reynolds numbers far from transitional. Figure 1.1 [*Brown & Roshko 1974*] shows the mixing of a fast moving stream of helium (top) and a slower stream of nitrogen (bottom) both moving from left to right. The Reynolds number is in the order of 10^6. Increasing the Reynolds number further, produces more small-scale structures without significantly altering the large eddies.

The major interest in coherent structures is due to the realization that they can be used for flow control. Liepmann [*Liepmann 1979*] was perhaps the first to suggest that the existence of deterministic eddies in turbulent flows could be exploited for control purposes via direct interference with these large structures. It is recognized that the large-scale structures are a manifestation of hydrodynamic instabilities. Also they are sensitive to initial and environmental conditions within certain energetic threshold and spectral ranges and are thus susceptible to control [*Liu 1989*].

1.2 Mixing

Efficient mixing of fluids is crucial in many engineering devices. Fuel efficiency and reduction of toxic emissions are governed by the degree of mixing between fuel and the oxidizer. Incomplete or non-uniform mixing leads to unburned reactants and production of pollutants. In the combustor of a jet engine, time and space are rare quantities. Fuel and air both at high velocities must mix within a very short length.

Mixing is a process involving a reduction of length scales [*Hak 2000*]. At very small scales, and high gradients, molecular diffusion dominates. The rate of transport by molecular diffusion depends on (1) the surface area, (2) the appropriate diffusion coefficient (e.g., viscosity coefficient when transporting momentum or vorticity), and (3) the gradient of the transported quantity. Given unlimited time and space, molecular diffusion alone can solely achieve any desired transport of mass, momentum or energy. Microscopic fluid motions are responsible for molecular diffusion. At scales much larger than molecular diffusion, mixing is enhanced by advection. Macroscopic fluid motions are responsible for advection. This is the mechanism by which distant fluid particles eventually come in contact with one another. This can be represented as the stretching and folding of material surfaces in three-dimensional flowfields. The enhanced stretching and folding process can result in greater surface areas and higher gradients available for molecular diffusion to complete the mixing process by eliminating any remaining discontinuities. These macroscopic motions can be either incoherent and unorganized small-scale structures (random turbulent fluctuations), or coherent and organized large-scale structures/eddies. Usually, the large-scale coherent structures are filled with incoherent motions of smaller scales. The large eddies control the dynamics of the flow and any type of flow control to enhance mixing should be directed towards processes that produce and sustain the large eddies for the required period of time

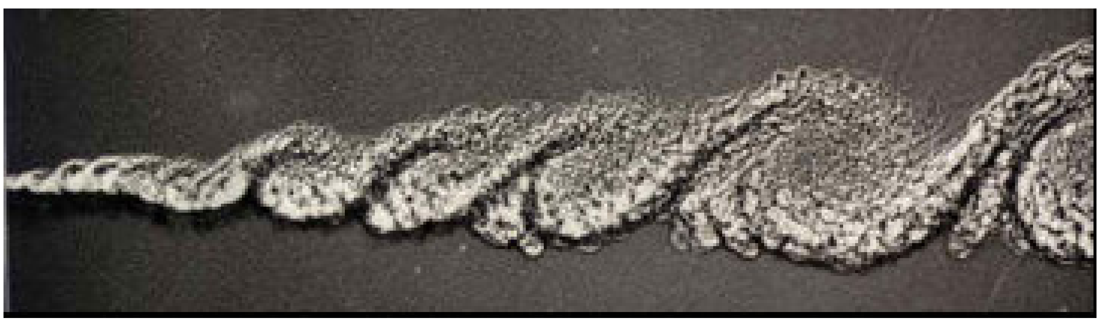

Figure 1.1. Shadowgraph of a mixing layer between two gaseous streams flowing from left to right. [*Brown and Roshko*, 1974]

The goal is to achieve an order one effect using an order ε perturbation. The control is best carried out in the initial stages of development because the growth of shear layers is rather sensitive to their initial conditions.

Several studies [*Wu et. al 1988, Vakili & Chang 1990, 1991, 1994, 1995, Johari et. al 1998, Vakili & Sauerwein 1999, Vakili & Miller 1999*] have shown that pulsed jets have increased penetration into a cross flow and increased entrainment as compared to steady jets. The primary reason for the increased penetration is the formation of vortex rings at each pulse. The increase in penetration has been observed to be higher for lower frequencies as compared to higher frequencies for a given injection velocity to free stream velocity ratio. The increase in flow penetration is affected by the interactions between adjacent vortex rings. At higher frequencies the spacing between adjacent vortex rings is reduced. As a result, adjacent vortex rings stretch and deform under their mutual induced flow fields, reducing their self-induced translation velocity. If the objective of the application is to increase blockage of the cross flow, one would desire the vortex rings to remain very closely spaced and to travel deep into the cross flow. However, as mentioned above, for the rings to travel farther into the flow, they must not be too close to each other. However, if the objective of the application is to mix two fluids as in the combustion chamber of an aircraft, it might be advantageous for the vortex rings to form, grow and collapse into turbulence within the shortest distance possible.

1.3 Motivation and State of the Art

The desire for this study has its origins in applications requiring high amplitude, high frequency and high bandwidth actuators. Examples of such applications include flow attachment over airfoils, underwater sound generation, deep-hole drilling and mixing of fluids as in aircraft combustion chambers, jet noise control, thrust vector control, metal deposition and gas dynamic lasers [*Gutmark et. al 1995*]. The basic fact behind these actuators is the highly organized vortical structures that make momentum or mass transfer possible more effectively. Different applications require different types of organization of the coherent structures for achieving the objective of the application.

1.3.1 Current Jet Excitation Techniques

Frequently, in many of these applications, a fluid is injected into the main flow. As the jet exits from the nozzle, a shear layer is formed. As previously mentioned, shear layers formed in the jets are inherently unstable and lend them to flow control methods especially in the subsonic regime where compressibility effects are not significant. Even in the supersonic regime, the jet's shear layer can be manipulated even though it is more stable and requires strong sources of excitation. Jet excitation techniques can be broadly grouped in two categories.

1. Passive control techniques
2. Active control techniques

Passive control techniques are realized by changing the geometry of the nozzle from which the jet exits. They do not require any supply of external energy to excite the flow. These devices make use of the kinetic energy of the jet. Therefore, total pressure losses could be expected. The design trade-off would be to evaluate the mixing enhancement as compared to the loss of energy from the main flow. According to Vakili [*Vakili 1990*], the basic principle for passive control is to accommodate the flow such that resonance occurs between the shear layer instabilities and a feedback generated by the boundaries through geometrical control of some characteristic length(s). This may be accomplished in practice by precise control of geometry, termed, "Tuned Boundaries". The feedback loop created under tuned condition ensures the self-sustaining interactions by proper phase relationship between the downstream and upstream for a given flow. A boundary may be tuned to fundamental frequencies, sub-harmonics or higher harmonics of shear layer instabilities.

Geometry modification, being simple and quite effective has been extensively studied and has resulted in the discovery of new phenomena like axis switching. Most commonly attempted passive excitation is to change the shape of the nozzle from which the jet exits. Examples of non-circular shape nozzles studied are: square jets [*Trentcoste et. al 1967*], rectangular jets [*Sfeir 1979*], triangular jets [*Sforza et. al 1966, Schadow & Gutmark 1988*], elliptic jets [*Gutmark & Ho 1982, 1987, Hussain 1983*], orifice jets [*Gutmark 1987*], lobbed nozzles [*Tillman & Presz 1993, Presz 1994, Hu et. al 1996, Power et. al 1994, Smith et. al 1997*], crown shaped nozzles [*Longmire 1991*], inclined nozzles [*Gutmark 1992*] and stepped nozzles [*Schadow et. al 1990*]. Some of these methods take advantage of a phenomenon called axis switching [*Koshigoe 1989*] which could help in the breakdown of the vortices thereby enhancing small-scale mixing. Another way of passive excitation is to introduce some element in the flow with the purpose of generating vortices. Some can take advantage of the self-sustaining flow instabilities produced by these elements. Examples include trip wires in plane shear layers, splitter plates, mechanical tabs [*Reeder & Samimy 1993, 1996, Zaman 1991*] of different shapes especially delta tabs [*Zaman 1994*], whistler nozzles [*Selerowicz 1991, Schreck 1993*], cylinders [*Umeda 1987*] and cavities [*Yu et.al 1994*] placed upstream or downstream of the exit.

Active control techniques are realized by supplying external energy at frequencies that match with the flow instability band of the jet and take advantage of the natural amplification of the flow. One can exert control over entrainment rates and even control the molecular mixing as a result of the dynamics of the large-scale structures. Proper selection of the excitation frequencies could either enhance or suppress the growth and entrainment characteristics of the shear layer. Examples include mechanical devices such as fluctuating flaps [*Binder & Didelle 1981*], spinning butterfly valves and vibrating ribbons, electromagnetic devices such as piezo-electric shims [*Kibens & Glezer 1992*], acoustical perturbations using loud speakers [*Borisov & Gynkina 1975, Tam 1978, Lepicovsky 1986*], hydrodynamic methods such as periodic suction or blowing [*Strykowski & Krothapalli 1993*], thermal techniques such as heating strips or electric discharge [*Martens et. al 1994*] and fluidic actuators based on synthetic jet technology [*Glezer & Amitay 2002*]. Excitation can be applied as a single frequency forcing or a multiple frequency excitations. It has been shown that with multiple mode excitations, especially a combination of axial and azimuthal modes can remarkably alter the structure and the vortex topology of the jets [*Reynolds* *et. al 2003*]. At proper combinations of these modes, the jet can be separated into two (bifurcated), three (trifurcated) or more jets which at higher numbers are called blooming jets. Despite these remarkable achievements, it remains to be seen whether these techniques, rather the apparatus required for these techniques to work, can withstand the harsh environment of combustors and reactors or produce high enough power to make significant contributions towards organizing the structures [*Hussain & Hussain 1983*].

Jet excitation techniques can also be classified on the basis of the source of the energy supplied to excite the flow. The three different groups are

1. Mechanical Excitation
2. Acoustic Excitation
3. Fluidic Excitation

Mechanical excitation involves the physical movement (vibration / rotation) of an element placed on the nozzle. The element might be a flap, a vane or a piezo electric material placed at regions of maximum sensitivity. These devices can produce very large amplitude oscillations. But, they might not be suitable for situations where very high frequency oscillations are required. Also the ability of electromechanical devices to perform under harsh conditions is still not very clear.

Acoustic excitation involves directing intense sound energy to the jet. This is one of the easiest ways to produce high amplitude oscillations in controlled environments as in labs. Very good frequency control can be achieved using acoustic excitations. Controlled excitations of multiple frequencies, which result in bifurcations and related phenomena, can be readily achieved through acoustic excitations. This method also suffers from the same problems related to its suitability in harsh environments and requirements of very high power when applied to practical applications.

Fluidic excitation takes advantage of certain geometrical features in the nozzle, which can produce self-sustaining oscillations. They can produce very large amplitude oscillations at certain combinations of geometrical and flow parameters. So they don't allow for a smooth control of frequencies. And they might also have much greater cycle-to-cycle variations than the other methods. But fluidic devices can be more robust in harsh environments and is the major reason for the continued interest in these devices.

1.4 Approach of the Current Study

Evolution of coherent structures are dependent on the initial and environmental conditions and hence different modes can be achieved with a better understanding of the effects of these conditions on the evolution of organized structures in shear flows.

In this study, pulsed flow is generated using the interaction of a passive enclosed geometry and the jet. Flows in cavity type geometry are susceptible to generate self-sustained oscillations [*Krishnamurthy 1955, Rossiter 1964, Rockwell & Naudascher 1978, 1979, Sarohia 1977*]. These types of configurations are usually called impingement type geometries because they contain an obstructed shear layer.

Figure 1.2 shows a list of configurations that are susceptible to develop self-sustained oscillations. A schematic of the self-sustaining oscillation mechanism is shown in Figure 1.3. Energy is introduced in the form of a constant momentum jet with turbulent boundary layer. Due to the inherent instability of the jet's shear layer, small perturbations grow to form vortex structures. These vortices are convected downstream where they interact with a solid boundary or other large scale eddies. As the vortices interact with the solid boundary, a fluctuating pressure field is created which travels upstream to create perturbations at the upstream edge. Thus a self-sustained oscillation is set up. When the instability caused by the cavity dimensions match with the shear layer instability generating mechanisms, it is possible to achieve very high amplification rates of the instability of the jet shear layer. Flow over external and internal cavities have been studied for a very long time with an emphasis on reducing the flow oscillations caused by them. Here we attempt to use the self-sustaining cavity oscillations to provide a source for organizing an axisymmetric jet's flow structure.

Experiments were conducted to study the effect of two different impingement geometries on axisymmetric jets.

Case 1. A radially unconfined cavity of infinite depth – (also called a 'hole-tone' device)

An axisymmetric jet interacts with an orifice plate while the space between the exit and the orifice plate is unconfined in the radial direction.

Case 2. A confined cavity placed at the jet-exit.

Effects of different cavity inlet and exit boundary conditions on these geometries were also studied.

There is a need for pulsing devices that would be able to tune to a wide range of frequencies and still have high amplitude fluctuations. Even though many devices have been designed and tested, there still is a lack of complete understanding of the various mechanisms that play a crucial role in the production, sustenance and modulation of the pulses of an injected fluid especially for high speed applications. The lack of the availability of high bandwidth and high amplitude actuators has been one of the major obstacles in active control of high-speed flows. This study is an effort to understand the basic physics necessary to design efficient fluidic devices for applications requiring rapid mixing of fluids as in aircraft combustion chambers, jet noise control, thrust vector control, metal deposition and gas dynamic lasers.

1.5 Objectives

Control of jet development for practical applications strongly depend on a thorough understanding of how coherent structures are formed, how they interact, how they breakdown into turbulence and how their dynamics affect the growth of the jet. The objectives of this study are

1. To provide an explanation, from a fluid mechanics point of view, of the process that takes place when a relatively steady axisymmetric jet is subjected to the presence of different passive impingement devices.

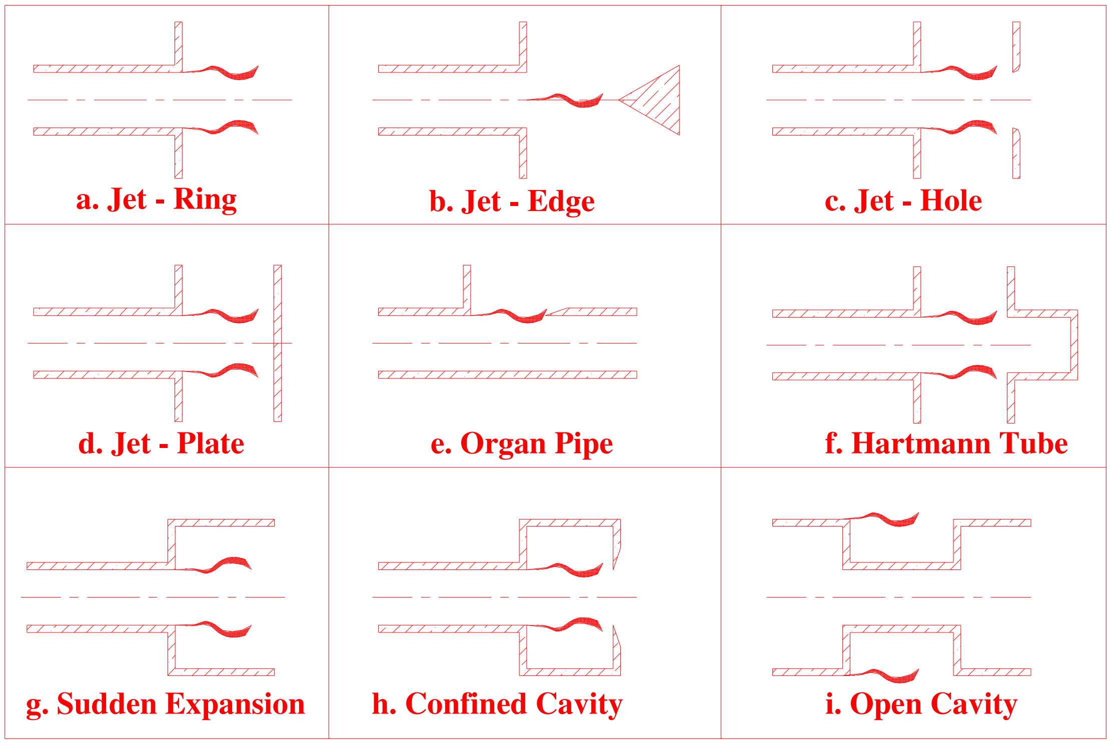

Figure 1.2. Examples of shear-layer and impingement geometries that produce self-sustained oscillations. [*Rockwell and Naudascher,* 1979 *and from other sources*]

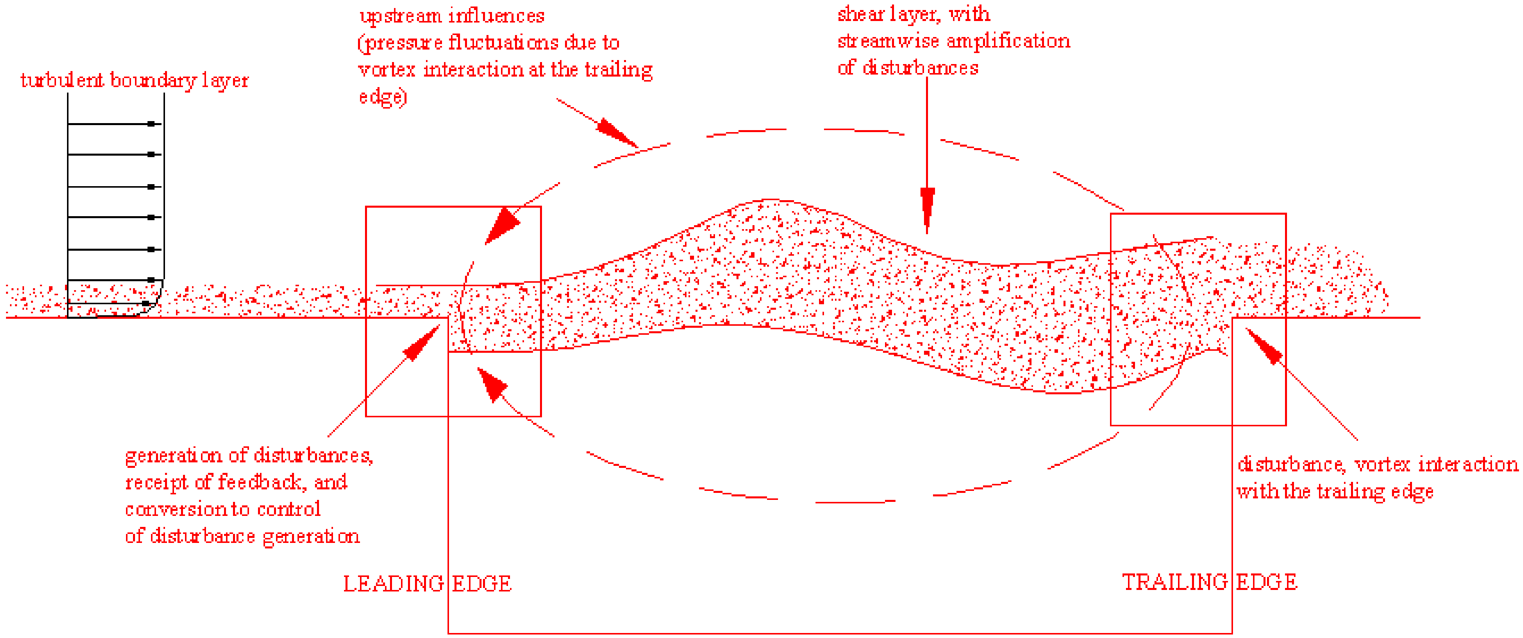

Figure 1.3. Schematic of a self-sustained oscillation mechanism over shallow cavities.

2. To identify geometries and flow conditions, that exploit the interaction between an enclosed cavity and the shear layer instability to generate high frequency, high amplitude pulses.
3. To study the relation between the presence of different modes and relative amplitudes on the basis of geometric and flow parameters.
4. Investigate thoroughly the flowfield of the Axial Jet Actuator's (AJA) mixing layer with emphasis on the formation, interaction and breakdown of the flow structures in the near field using experimental and numerical means.

1.6 Organization of The Study

Chapter 2 presents details of the experimental set-up, geometries studied and the different measurement techniques used in this study. Chapter 3 presents a brief background on the numerical methods employed by CFDACE solver and details of the grid used for this study. Chapter 4 presents the results and its analysis of data. The presentation of results begins with a study of natural axisymmetric turbulent jets. The following two sections presents results from two different configurations used for exciting a base flow in this study. Chapter 5 presents the conclusions derived from this study. Appendix A discusses a heat separation phenomenon observed in the course of this study.

Chapter 02

EXPERIMENTAL APPARATUS AND DATA ANALYSIS

As previously mentioned, the objective of this study is to investigate the effect of axisymmetric cavities on the growth and mixing characteristics of axisymmetric jets. Detailed measurements were made to evaluate different model configurations by comparing their centerline velocity decay, shear layer growth rate, entrainment ratio, turbulent intensity maps, topology of vortical structures in flowfield and spectral content of the pressure field. The measurements performed are comprised of flow visualizations, static and total pressure measurements, and mean, phase averaged and instantaneous velocity field measurements.

2.1 Jet Testing Setup

A schematic of the jet testing arrangement is shown in Figure 2.1. High-pressure air supply source is a set of reservoir tanks having a storage capacity of about 750 ft^3 at 3000 psi. Air from the reservoir was regulated into a 3-inch diameter pipe approximately 30 ft. long using control valves. This line acted as the settling chamber and can support a maximum line pressure of 150 PSI. The 3-inch line was reduced in two steps to a 1-inch line using standard pipe reducers. Different model configurations can be connected to the end of the 1-inch line. An orifice meter with an orifice diameter of 0.5-inches on the 2-inch pipe segment was used to measure the mass flow rate. The uncertainty estimate for an orifice meter having a beta ratio (ratio between the orifice diameter to the pipe inside diameter) between 0.2 and 0.7 is ±0.5%. Minimum uncertainty occurs between 0.2 and 0.6 beta ratios and Reynolds numbers above 1,000,000. The orifice plate was designed for a mass flow rate range of 0.05 – 0.2 lbs/sec having a turndown ratio of 4 to 1. Mass flow rate was controlled using a control valve on the 1-inch line. Honeycombs and screens were installed in the final leg of the 1-inch line to condition the flow. The final leg is longer than 30 times the diameter of the pipe thus ensuring that the flow is symmetrical and closely approaching a fully developed turbulent pipe flow. Tests were performed over a Reynolds number, based on jet exit diameter, range of 40,000 to 225,000 in low to high subsonic jet flow conditions.

2.2 Test Models

A number of models were designed and tested to study the effect of cavity (axisymmetric and asymmetric) geometrical parameters and flow parameters. Results chosen from the tested models and presented in this report include baseline turbulent jets and baseline turbulent jets passing through different axisymmetric cavities placed at the exit of the jet. Each model is briefly described in the following paragraphs.

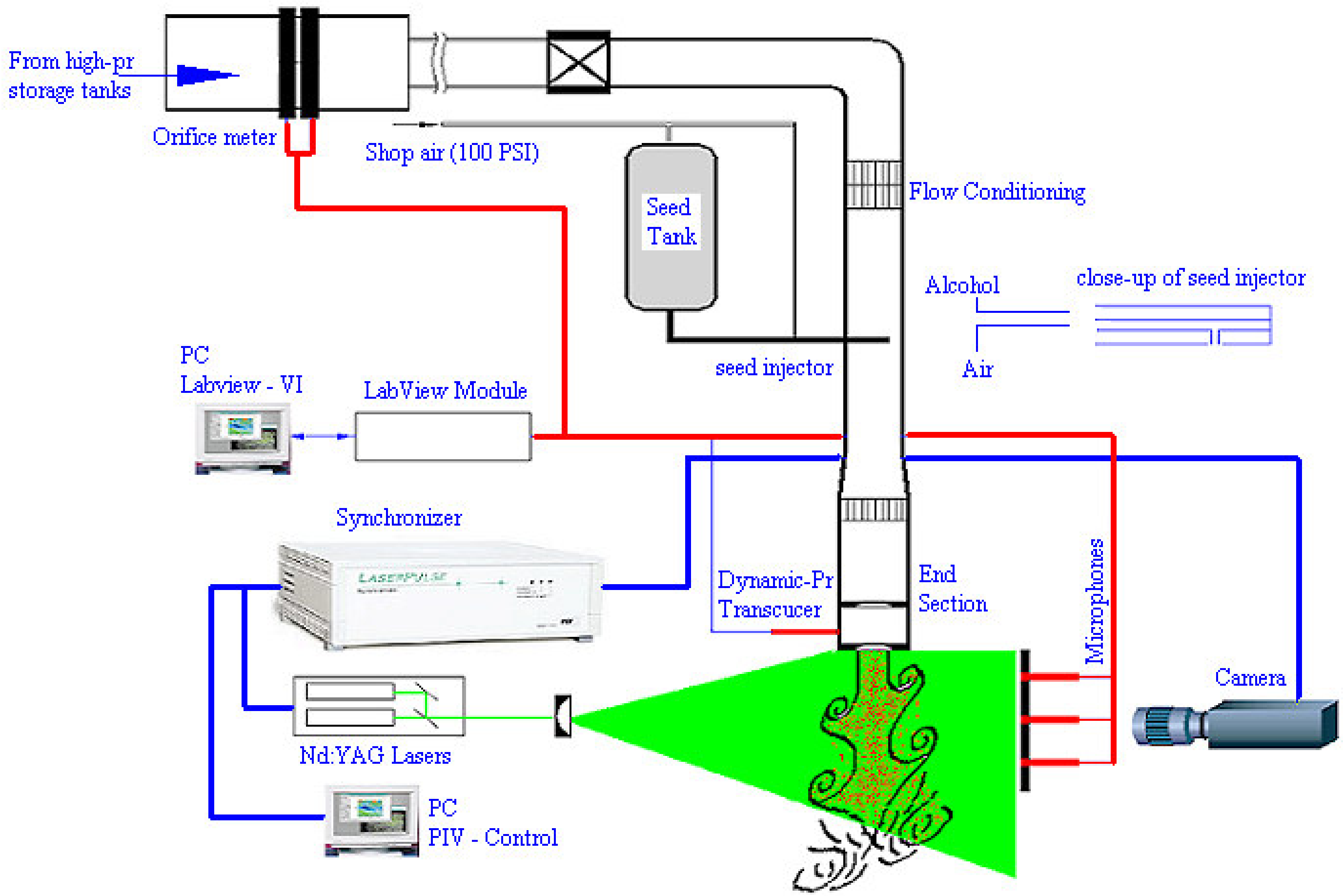

Figure 2.1. Schematic of jet test equipment and data acquisition systems

2.2.1 Baseline

The baseline turbulent jet was a short pipe attached to the supply line as shown in Figure 2.2a. It is a smooth aluminum pipe extending four jet diameters upstream of the exit. To study the natural processes in the growth of a jet, different exit geometries were also studied. An orifice jet shown in Figure 2.2b had a finite lip thickness of 0.0625 inches and a bevel (flat surface facing the jet). After studying different orifice plates, it was decided to use a bevel with 30˚ from the jet flow direction. A contoured nozzle and a diffuser (contoured nozzle placed in the opposite direction) were also tested. Different orifice sizes were also tested. Details of the geometries are descibed in Table 2.1. Other investigators have extensively studied jets issuing from a contoured nozzle and constant diameter pipes jets. In order to make a uniform comparison between the excited jets from different models, the pipe jet was used as the baseline jet.

2.2.2 Hole-Tone Actuator

A schematic of a hole tone actuator is shown in Figure 2.2c. We refer to this model as the radially unconfined cavity with infinite depth. A baseline turbulent jet is directed upon a baffle with an orifice. The distance between the jet exit and the baffle can be varied. The downstream baffle plate is supported through 4 thin plates around the circumference and fastened to the upstream body. This type models have been studied extensively in the literature a few decades ago [*Chaunad* 1965, *Umeda* 1987]. Studies using flow visualization and point-wise velocity spectra have allowed us to gain a good understanding of many aspects of the problem. This problem was revisited in this study for a number of reasons. One reason is that, this configuration allows us to study the axisymmetric cavity as a reduced order model with only the effect of axial distance (not the pipe diameter or the cavity depth) playing a major role. Another reason is, the relatively uncomplicated optical access available in the region between the exit and the baffle. A survey of current literature did not show any evidence that this case has been studied using advanced global measurement techniques that can confirm and improve our current understanding of the flow development. All tested configurations are described in Table 2.1.

2.2.3 Axial Jet Actuator (AJA)

In this configuration, a confined cavity is placed at the jet exit. The inlet/exit boundaries of the cavity could be a baffle with an orifice (same as the baffles used for orifice jet in baseline studies) or a short pipe (the baseline geometry as discussed in the baseline model description). Two configurations extensively tested and discussed in the results are shown in Figures 2.2d and 2.2e. Configuration in Figure 2.2d shows baffles with orifices used as the inlet/exit boundaries of the cavity. Here, the impingement surface (trailing edge of the cavity) is also the exit. Therefore, the source of excitation is very close to the most sensitive region of the jet. Configuration in Figure 2.2e has a short pipe as the exit boundary of the cavity. In this case the impingement surface is four jet diameters away from the exit surface. Different L_c/D_c ratios and different D_j/D_e ratios were tested. All tested configurations are shown in Table 2.1.

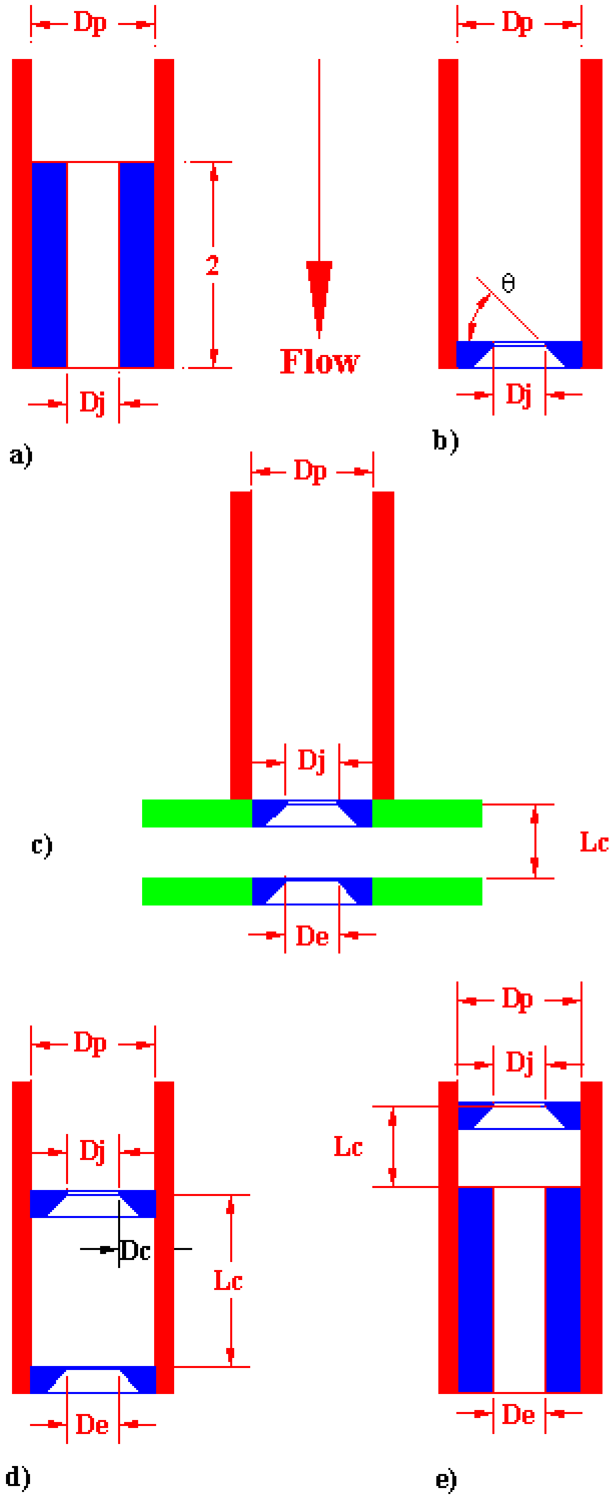

Figure 2.2. Generic geometry of tested models, a) Baseline – pipe jet, b) Baseline – orifice jet, c) Hole-tone actuator, d) Axial jet actuator – orifice boundary and e) Axial jet actuator – pipe exit boundary

Table 2.1. Description of the geometries tested

Model Type	D_p"	D_j/D_p	D_j/D_e	L_c/D_j	L_c/D_c	T_u"	T_d"	θ_u°	θ_d°	PIV
Baseline	1.2	0.333				0.125		60		
	1.2	0.358				0.125		60		
	1.2	0.375				0.250		30		
	1.2	0.375				0.250		60		
	1.2	0.417				0.125		60		
	1.2	0.417				0.250		30		
	1.2	0.417				0.250		60		x
	1.2	0.458				0.250		30		
	1.2	0.500				0.250		30		
	1.2	0.417				2.000		90		x
Hole Tone	1.2	0.375	0.900	1.042	1.250	0.250	0.250	30	30	x
	1.2	0.375	0.900	1.375	1.650	0.250	0.250	30	30	x
	1.2	0.375	0.900	2.264	2.717	0.250	0.250	30	30	x
	1.2	0.417	1.000	1.225	1.750	0.250	0.250	30	30	x
	1.2	0.417	1.000	1.600	2.286	2.000	0.250	90	30	x
AJA	1.2	0.333	0.930	1.000	1.000	0.125	0.125	60	60	
	1.2	0.333	0.930	2.000	2.000	0.125	0.125	60	60	
	1.2	0.333	0.889	1.000	1.000	0.125	0.250	60	60	
	1.2	0.333	0.800	1.000	1.000	0.125	0.125	60	60	
	1.2	0.333	0.800	2.000	2.000	0.125	0.125	60	60	
	1.2	0.333	0.800	1.000	1.000	0.125	0.250	60	30	
	1.2	0.333	0.800	1.000	1.000	0.125	0.250	60	60	
	1.2	0.333	0.800	2.000	2.000	0.125	0.250	60	60	
	1.2	0.333	0.667	1.000	1.000	0.125	0.250	60	30	
	1.2	0.333	0.667	2.000	2.000	0.125	0.250	60	30	
	1.2	0.358	1.075	1.500	1.500	0.125	0.125	60	60	
	1.2	0.358	0.860	1.500	1.500	0.125	0.125	60	60	
	1.2	0.375	1.125	1.000	1.000	0.250	0.125	30	60	x
	1.2	0.375	1.125	1.750	1.750	0.250	0.125	30	60	x
	1.2	0.375	1.047	1.000	1.000	0.250	0.125	30	60	x
	1.2	0.375	1.047	1.750	1.750	0.250	0.125	30	60	x
	1.2	0.375	0.900	1.000	1.000	0.250	0.125	30	60	x
	1.2	0.375	0.900	1.750	1.750	0.250	0.125	30	60	x
	1.2	0.375	0.900	1.250	1.250	0.250	0.250	30	30	x
	1.2	0.375	0.900	1.750	1.750	0.250	0.250	30	30	x
	1.2	0.375	0.900	2.500	2.500	0.250	0.250	30	30	x
	1.2	0.375	0.900	3.000	3.000	0.250	0.250	30	30	
	1.2	0.375	0.900	3.500	3.500	0.250	0.250	30	30	
	1.2	0.375	0.900	4.000	4.000	0.250	0.250	30	30	

Table 2.1. Continued

Model Type	D_p"	D_j/D_p	D_j/D_e	L_c/D_j	L_c/D_c	T_u"	T_d"	θ_u°	θ_d°	PIV
AJA	1.2	0.375	0.900	1.250	1.250	0.250	0.250	30	60	x
	1.2	0.375	0.900	1.750	1.750	0.250	0.250	30	60	x
	1.2	0.375	0.900	2.500	2.500	0.250	0.250	30	60	
	1.2	0.375	0.900	3.000	3.000	0.250	0.250	30	60	
	1.2	0.375	0.900	4.000	4.000	0.250	0.250	30	60	
	1.2	0.417	1.250	1.000	1.000	0.125	0.125	60	60	
	1.2	0.417	1.163	1.000	1.000	0.125	0.125	60	60	
	1.2	0.417	1.163	1.750	1.750	0.125	0.125	60	60	x
	1.2	0.417	1.111	1.500	1.500	0.125	0.250	60	30	x
	1.2	0.417	1.111	1.000	1.000	0.125	0.250	60	60	x
	1.2	0.417	1.111	1.500	1.500	0.125	0.250	60	60	x
	1.2	0.417	1.000	1.000	1.000	0.125	0.250	60	30	
	1.2	0.417	1.000	1.500	1.500	0.125	0.250	60	30	x
	1.2	0.417	1.000	1.750	1.750	0.125	0.250	60	30	x
	1.2	0.417	1.000	1.000	1.000	0.125	0.250	60	60	
	1.2	0.417	0.909	1.500	1.500	0.125	0.250	60	30	x
	1.2	0.417	0.833	1.000	1.000	0.125	0.250	60	30	
	1.2	0.417	1.111	1.750	1.750	0.250	0.250	30	30	x
	1.2	0.417	1.000	1.750	1.750	0.250	0.250	30	30	x
	1.2	0.417	1.000	2.500	2.500	0.250	0.250	30	30	
	1.2	0.417	1.000	3.000	3.000	0.250	0.250	30	30	
	1.2	0.417	1.000	4.000	4.000	0.250	0.250	30	30	
	1.2	0.417	1.000	5.000	5.000	0.250	0.250	30	30	
	1.2	0.417	1.000	0.500	0.500	0.250	2.000	30	90	
	1.2	0.417	1.000	1.000	1.000	0.250	2.000	30	90	x
	1.2	0.417	1.000	1.500	1.500	0.250	2.000	30	90	x
	1.2	0.417	1.000	1.750	1.750	0.250	2.000	30	90	x
	1.2	0.417	1.000	2.000	2.000	0.250	2.000	30	90	
	1.2	0.417	1.000	2.500	2.500	0.250	2.000	30	90	
	1.2	0.500	1.200	2.000	2.000	0.250	0.125	30	60	x
	1.2	0.500	1.000	1.500	1.500	0.250	0.250	30	30	x
	1.2	0.500	1.000	2.000	2.000	0.250	0.250	30	30	x
	1.2	0.417	1.000	1.000	1.000	2.000	0.250	90	30	x
	1.2	0.417	1.000	1.750	1.750	2.000	0.250	90	30	x

D_p – Pipe diameter, D_j – Jet diameter, D_e – Exit diameter, L_c – Cavity length, D_c – Cavity depth, T_u – Upstream baffle thickness, T_d – Downstream baffle thickness, θ_u – Upstream baffle bevel angle, θ_d – Downstream baffle bevel angle

2.3 Instrumentation and Data Acquisition

2.3.1 Pressure Measurement System

Pressure signal within the cavity, spectral content of sound radiated into the ambient and the corresponding sound pressure levels were measured to identify the geometric parameters influencing oscillations setup in the flow field. Pressure spectra were recorded using dynamic pressure transducers and microphones. An Endevco® Model 8510C-50 miniature, high sensitivity piezoresistive pressure transducer, flush mounted on the sidewall of the cavity, was used to record pressure data inside the cavity. The transducer was always 0.25 inches upstream of the trailing edge of the cavity or baffle in the baseline cases. It had a full-scale output of 170 mV with a rated sensitivity of 3.41 mV/psi. The resonant frequency of this transducer was specified at 320 kHz giving a nominally flat frequency response within ±0.34 dB up to 64 kHz. The transducer contains a four-arm strain gage bridge ion implanted into a sculpted silicon diaphragm and operates with a 10 Vdc excitation voltage.

Microphone probes of 0.25 in. diameter were used to record sound pressure radiated from the jet into the ambient medium. The condenser microphones used were Bruel & Kjaer® 4938 along with Bruel & Kjaer® 2670 preamplifiers. In the frequency range between 20 and 10 kHz, their frequency response was nominally flat within ±0.25 dB and within ±1dB from 10 kHz to 70 kHz. The upper limit of dynamic range was 172 dB below which the distortion of sound pressure level was less than 3%. The microphones were connected to the data acquisition system through Bruel and Kjaer® microphone multiplexer Type 2822. A polarization voltage of 200V was applied. The microphones were calibrated using a sound level calibrator providing 94 dB and 114 dB re 20 μPa sound levels at 1 kHz. The microphones were located about 4 inches away from the centerline of the jet at different locations downstream of the jet (usually at 2D, 4D and 6D).

LabView® based instrumentation simulation system was setup to acquire data from the pressure transducer and microphones. National Instruments® PCI 6023E Multifunction DAQ card was used. It is a 12 bit, 16 analog input channels card capable of a maximum sampling rate of 200 kS/s. Data from the transducers were recorded at a sampling rate of 40000 Hz giving a bandwidth of 20,000 Hz. A total number of 20,000 data points were obtained for each channel resulting in a frequency resolution of 2 Hz. The Labview® VI (virtual instrument) was also programmed to do a real time Fast Fourier Transform (FFT) on the pressure data and display it on the screen. Mass flow rate, temperature and raw pressure data was also continuously monitored. For each data acquisition, 20 sets of 20,000 data points were taken and averaged to reduce noise from the system and in the pressure field.

2.3.2 Velocity Measurement System

Particle Image Velocimetry (PIV) was applied to measure instantaneous, mean and phase averaged two-dimensional velocity fields in streamwise and cross-stream planes of the jet. Particle Image Velocimetry is a non-intrusive global velocity measurement technique, which can be used to identify instantaneous flow structures and compute spatial quantities such as vorticity and the instantaneous contribution of Reynolds stress that are almost impossible to obtain using point based measurement techniques. A descriptive background on this technique is presented below.

Principle of Operation

PIV is based on the fundamental definition of velocity $u(x,t) = \frac{\Delta x(x,t)}{\Delta t}$ where Δx is the ensemble average displacement of flow markers located within a small grid around 'x' at time 't' over a short interval Δt separating observations of the marker images. This Lagrangian velocity of the marker is equated to the Eulerian velocity at that location. The accuracy of the measurement depends on how accurately the marker follows the flow. A planar laser sheet is formed to illuminate the flow and images of the seeded flow are taken. The elapsed time between each recording of the seeded flow is accurately recorded. The images are then correlated to determine the displacement vector and the velocity field. Each of these steps, as used in this study, will be described briefly in the following sections.

Components and Operation

A schematic of the PIV system and its arrangement is shown in Figure 2.1. The PIV system used two pulsed Nd:YAG lasers (Continuum® PIV-Lite) providing 200 mJ per pulse at a wavelength of 532 nm (green light) to form a thin planar laser sheet using spherical and cylindrical lenses in the desired planes of interest. The thickness of the laser sheet was about 1 mm at the waist. TSI® PIVCAM 10-30, an 8-bit digital camera with a 1008 (H) x 1018 (V) light sensitive pixel CCD chip was used for image captures. The camera has a frame rate of 30 frames per second. Despite the low frame rate, this cross-correlation camera has the unique ability to capture sequential PIV images with a very short time between them. Using a "Frame Straddling" technique, two laser pulses are captured on consecutive video frames. Laser pulse separations down to less than 0.3 microseconds can be achieved. Frame Straddling is a technique in which the first laser pulse is pulsed and hence the image captured at the end of the first video frame and the second laser pulse is at an appropriate time (user specifiable pulse separation time) in the second video frame. A sequence of the Frame Straddling technique is shown in Figure 2.3. In this study, the pulse separation time varied from 0.5 to 1 μs (mostly at 0.8 μs. TSI® model 610032 laser pulse synchronizer controls the camera and the laser. The synchronizer, laser and camera can be externally triggered individually or through the synchronizer. The measurements were triggered and evaluated by TSI® Insight software. This is a user-friendly graphical user interface, which allows the operator to define all laser, camera and data recording options. It also allows for image spatial domain calibration so that the calculated velocity vectors could be expressed in useful engineering units (m/s). The spatial domain of the image is calibrated by taking the image of a calibration scale placed in the region of interest. The number of pixels between identified points is then measured to give the calibration in terms of μm/pixel. The dimensions of the investigated areas were about 50 mm x 50 mm. The magnification scale of the images taken for this study

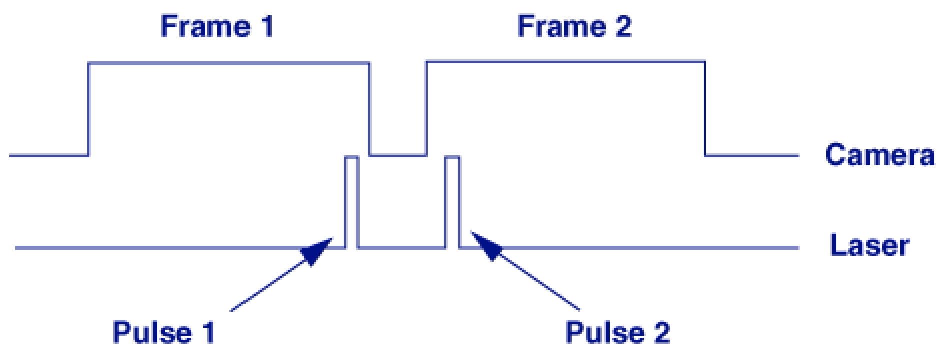

Figure 2.3. Principle of Frame Straddling technique

ranged from 20 μm/pixel to 100 μm/pixel. Dimensions of the investigated areas also vary with the magnification scale.

Seeding

Uniform distribution and high density of flow seeding are the most critical elements in PIV experiment. PIV actually measures the velocity of the tracer rather than the velocity of the fluid itself. The accuracy of the velocity field is ultimately determined by the ability of the scattering particles to follow the instantaneous motion of the continuous phase. The choice of optimal diameter for seeding particles is a compromise between an adequate tracer response of the particles in the fluid, requiring small diameters, and a high signal-to-noise ratio (SNR) of the scattered light signal necessitating large diameters. Tracer particle diameter up to 2-3 μm is acceptable for a moderate frequency response of 1 kHz. Particles present in the flow only need to respond to the changes in velocity directed on it by the growth and decay of eddies and not as measured by a stationary probe. The required frequency response of the particle is much less than the fluctuating frequencies measured the stationary probe. However, how much less is still unknown. In the present case, 90% isopropyl alcohol mixed with a fluorescent material was used for seeding. Shop air at 100 PSI is applied to a seeding tank to force liquid through a small tube. Within this tube is another tube, which is also connected to the shop air. Near the end of tube concentric orifices on both tubes are present. As air exits out of the orifice, liquid is sucked into the flow breaking it into small particles. We do not use an impactor that could remove large size particles. So the seeding would be a polydisperse spray contaminated with some large size particles rather than monodisperse, which is ideal for these measurements. No measurements were made to find the particle size. Based on past experience at similar high-speed flows, we believe that the seeding is good enough to faithfully follow the flow.

Evaluating Velocity Vector

The captured image pairs were evaluated by doing a cross-correlation analysis on the raw images. Correlation techniques generally used are auto-correlation and cross-correlation. In the auto-correlation technique, two sequential images are taken in the same frame. Auto-correlation produces symmetric peaks. This results in directional ambiguity, requiring image-shifting techniques to resolve it. Also, there is a limit on the minimum distance that the seeds should travel between frames severely limiting the maximum velocity that could be measured.

In a cross-correlation analysis method, two sequential pictures are taken in different frames and analyzed, thereby eliminating any directional ambiguity. The images are divided into small sub-sections called interrogation spots. The interrogation spot from each image frame I_1 and I_2 are cross-correlated with each other pixel by pixel. The correlation produces a signal peak, identifying the average particle displacement within the interrogation spot.

$$C(s) = \iint_{IA} I_1(x).I_2(x-s)dx$$

where, C(s) is the cross-correlation between interrogation spots of two sequential image frames I_1 and I_2.

The interrogation size used in this study was 32 x 32 pixels with a 70 % overlap to obtain more number of vectors. Usually a 50% overlap related to the Nyquist criterion is used. Using a higher overlap only increases the number of vectors and not the scales that could be truly resolved. That dynamic spatial range is basically fixed by the image size and interrogation spot size. This interrogation process is repeated to cover the entire image frame. Detailed studies have shown that cross-correlation methods perform much better than any other method in terms of signal-to-noise ratio and flexibility of choosing parameters for PIV imaging. A schematic of the cross-correlation process is shown in Figure 2.4.

Spatial Resolution and Dynamic Range

In setting the spatial resolution, the balance to be achieved is between the size of the flow structures to be resolved against the interrogation spot size and image magnification. The size of particles recorded on the image is usually larger than the corresponding size after magnification. This increase in size comes from different parameters including diffraction limit of the recording optics and the experiment specific intensity of image. The diffraction limit spot diameter d_s can be evaluated using a simple expression.

$$d_s = 2.44(1+M)f^{\#}\lambda$$

The optical image size prior to being recorded is then given by:

$$d_e = \sqrt{M^2 d_p^2 + d_s^2}$$

The recorded image diameter d_τ is given by :

$$d_\tau^2 = d_e^2 + d_r^2$$

Here, M is the magnification of the lens, $f^{\#}$ is the aperture used, λ is the wavelength of the light used (532nm for green), d_p is the actual tracer particle's size and d_r is the resolution of a pixel in the recording device. As mentioned above, this is only the effect due to the optics and the actual image size is substantially higher than what is predicted by this expression (usually an order of magnitude higher). Optimizing the optical system is an important factor in getting good quality data. As a rule of thumb for spatial resolution, the displacement of particles due to the maximum gradient present in an image should not exceed 5% of the interrogation spot size.

The dynamic range as reflected by the maximum velocity that can be measured by the system is constrained by particles traveling further than the interrogation spot size and resulting in improper correlation values. So, choosing the right time interval dT between images and the right interrogation spot size is necessary to cover the maximum velocities that are expected in the flow. Investigators have established standards that require the displacement due to the maximum velocity be limited to 25% of the interrogation spot size. More details on the dynamic spatial and velocity range is discussed in the error analysis section.

Post-Processing

Post processing of the raw vector field involves removal of the outliers using range, local median, standard deviation and mean filters. The eliminated vectors were filled through interpolation.

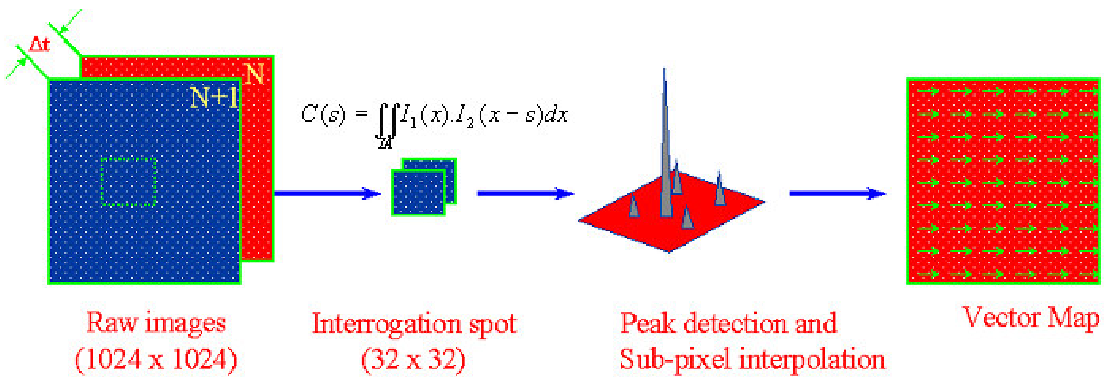

Figure 2.4. Cross-Correlation analysis of image pairs to obtain velocity vectors

The vector field was then smoothed using a Gaussian smoothing with exponent $p = 1.3$. A typical sequence of the post processing steps is shown in Figure 2.5.

Phase-locked Measurements

Due to the limited frame rate of the imaging system (maximum frame rate of 10 Hz), it is impossible to resolve the dynamics of the flow temporally. Therefore to study the temporal evolution of the jet, phase locked measurements were made. Triggering of the PIV image capturing sequence was accomplished using signal from the dynamic pressure transducer present inside the cavity. A typical signal obtained from the pressure transducer within the cavity, before amplification, is shown in Figure 2.6. The dynamic signal from the pressure transducer was amplified and fed to a phase locking circuitry, which produces a TTL signal at the same frequency and phase. The phase of the output signal can be varied in reference to the input signal. Variations from -180° to 180° from the actual signal were possible. The regions of measurement of pressure and velocity are different and hence there is a finite phase difference. No attempt was made to directly relate the pressure signal to the velocity field even though it should be possible because the phase relation between the two regions is fixed.

Results presented in this report include both phase and time averaged data. Time averaging is defined as the averaging of each point in the field over a time period. The total number of images used for time averaging varied between 300 to 900 images for different conditions. Definitions for the time averages of different properties using N images are given below.

$$U(x, y) \equiv \frac{1}{N}\sum_{i=1}^{N} u_i(x, y)$$

$$V(x, y) \equiv \frac{1}{N}\sum_{i=1}^{N} v_i(x, y)$$

$$\omega(x, y) \equiv \frac{1}{N}\sum_{i=1}^{N} \omega_i(x, y)$$

$$u'(x, y) \equiv \frac{1}{N}\left\{\sum_{i=1}^{N}\left[u_i(x, y) - U_i(x, y)\right]^2\right\}^{\frac{1}{2}}$$

$$v'(x, y) \equiv \frac{1}{N}\left\{\sum_{i=1}^{N}\left[v_i(x, y) - V_i(x, y)\right]^2\right\}^{\frac{1}{2}}$$

$$u'v'(x, y) \equiv \frac{1}{N}\left\{\sum_{i=1}^{N}\left[u_i(x, y) - U_i(x, y)\right]\left[v_i(x, y) - V_i(x, y)\right]\right\}$$

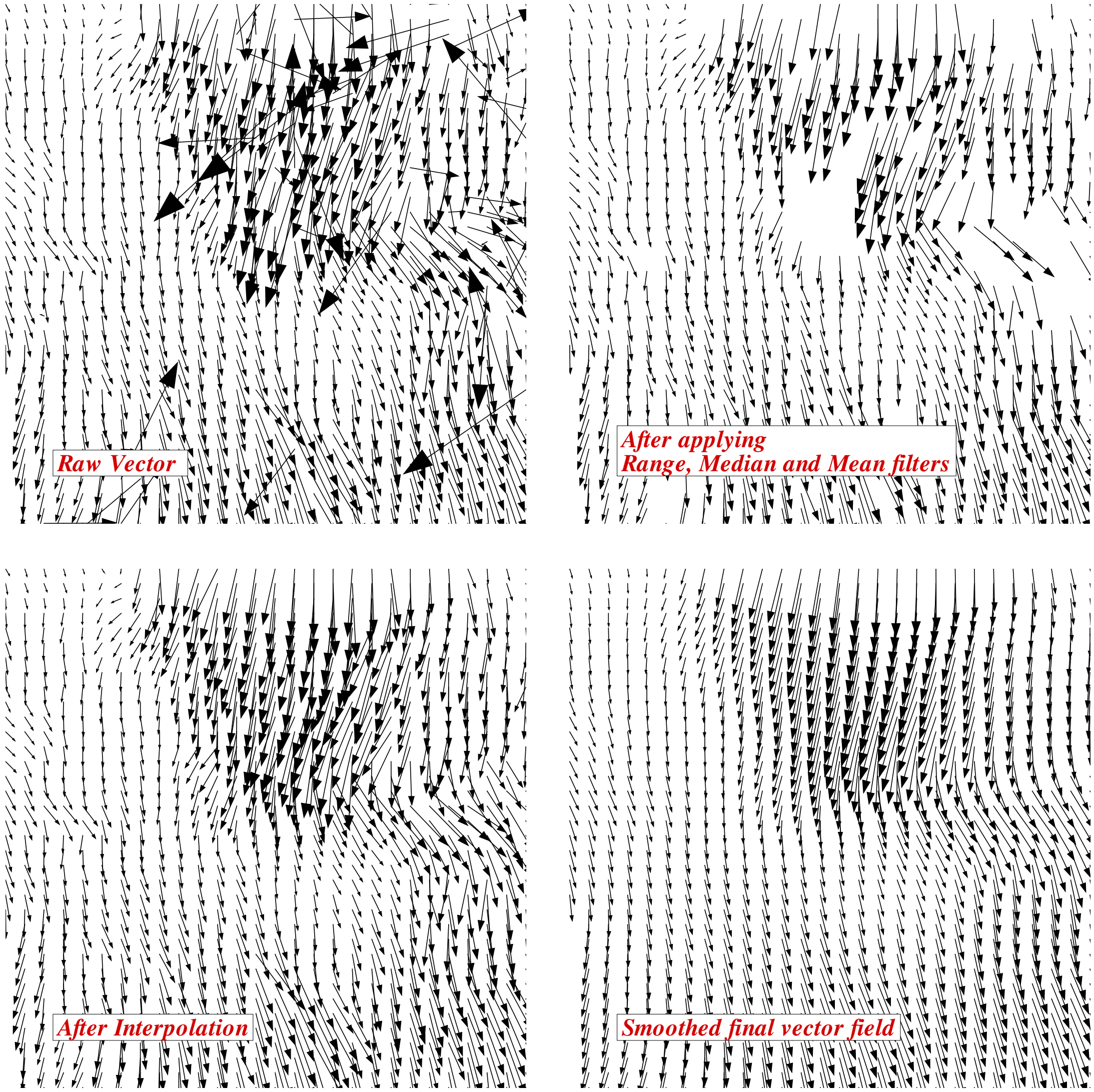

Figure 2.5. Post processing to remove bad vectors, fill by interpolation and smoothing of the vector field.

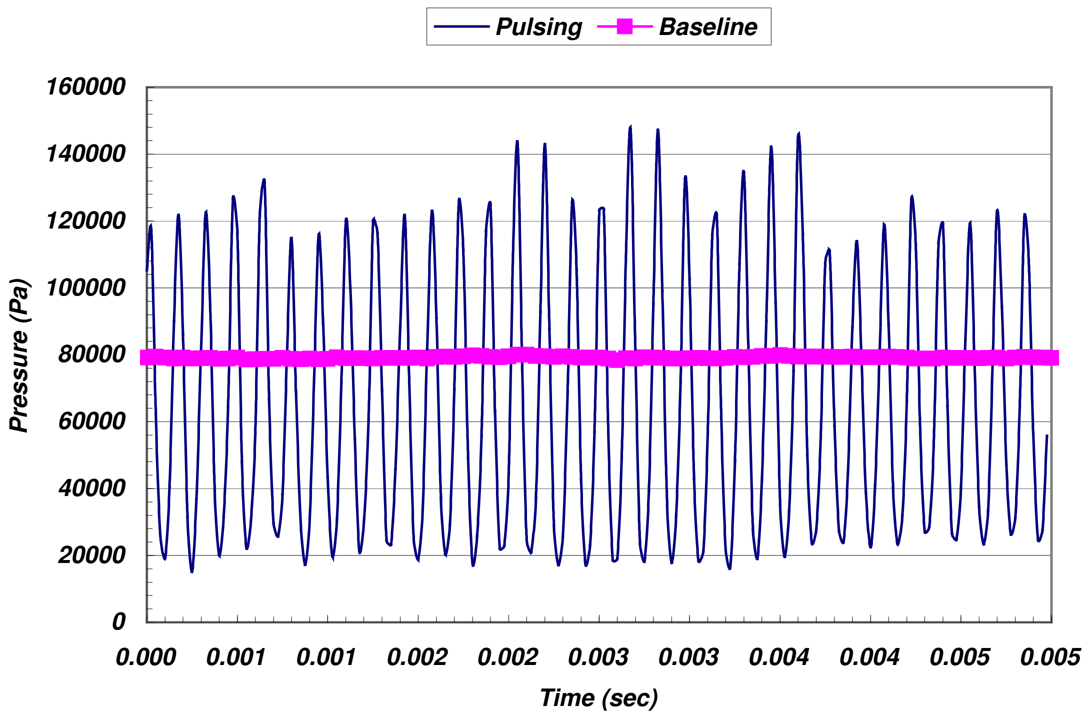

Figure 2.6. Typical pressure data used for phase locked measurements of a pulsed jet at $U_j \approx 250$ m/s (baseline at similar conditions shown for comparison)

Phase averaging is defined as the averaging of each point in the field taken at the same phase condition over a time period. Definitions very similar to time averages are given below for the phase averages of different properties using N images.

$$U_p(x,y) \equiv \frac{1}{N}\sum_{i=1}^{N} u_{i,p}(x,y)$$

$$V_p(x,y) \equiv \frac{1}{N}\sum_{i=1}^{N} v_{i,p}(x,y)$$

$$\omega_p(x,y) \equiv \frac{1}{N}\sum_{i=1}^{N} \omega_{i,p}(x,y)$$

$$u'_p(x,y) \equiv \frac{1}{N}\left\{\sum_{i=1}^{N}\left[u_{i,p}(x,y) - U_{i,p}(x,y)\right]^2\right\}^{\frac{1}{2}}$$

$$v'_p(x,y) \equiv \frac{1}{N}\left\{\sum_{i=1}^{N}\left[v_{i,p}(x,y) - V_{i,p}(x,y)\right]^2\right\}^{\frac{1}{2}}$$

$$u'v'_p(x,y) \equiv \frac{1}{N}\left\{\sum_{i=1}^{N}\left[u_{i,p}(x,y) - U_{i,p}(x,y)\right]\left[v_{i,p}(x,y) - V_{i,p}(x,y)\right]\right\}$$

The corresponding averaging method used will be made clear in context.

2.3.3 PIV Resolution and Error Analysis

Resolution

For all images, an interrogation spot size of 32 x 32 pixels was used. The distance between any two adjacent vectors was 10 pixels. The calibration of the images was around 50 um/pixel for most cases. Based on this, the resolution of the vector map is 0.5 mm. In order to determine what minimum size vortex structures can be visualized, we have to decide how many data points are needed to determine a structure. We set the threshold that at least 3 x 3 vectors are needed to properly identify a vortex structure. For the parameters mentioned above, we could identify all structures above a radius of 1mm can be identified.

When studying turbulence characteristics, the dynamic spatial range and the dynamic velocity range are more important than the spatial resolution as defined above. This actually sets the minimum limit on the size of the structures and the minimum velocity fluctuations that could be resolved for a particular setup. The following discussion is based on the analysis procedure proposed by Adrian [*Adrian* 1997]. The dynamic spatial range (DSR) is defined as the field-of-view in the object space divided by the smallest resolvable spatial variation.

$$DSR = \frac{l_x}{\Delta x_{p\max}} = \frac{L_x / M}{\Delta x_{p\max}}$$

where, $u_{max} = \Delta x_{pmax}/\Delta t$ is the magnitude of the full-scale velocity, l_x is the recording dimension in the object plane, L_x is the dimension in the recording plane, M is the magnification of the optics and Δx_{pmax} is the particle displacement associated with the maximum velocity. The minimum resolvable scale is at least Δx_{pmax}, so DSR is at least the value given by the expression above. The dynamic velocity range (DVR) is defined as the ratio of maximum velocity to the minimum resolvable velocity and is given by,

$$DVR = \frac{l_x}{\sigma_u} = \frac{M\Delta x_{p\max}}{c_\tau d_\tau}$$

where σ_u is the rms error that defines the minimum resolvable velocity fluctuations, c_τ is a constant that depends on the ability of the analysis procedure to determine the displacement between the images. Typically c_τ varies between 1-10% of the image diameter. Westerwheel estimates that usually the error in resolving the location of a correlation peak is in the order of 0.1 pixels.

The expressions for DSR and DVR can be combined to result in

$$(DSR\}(DVR) = \frac{L_x}{c_\tau d_\tau}$$

This expression states that the capability of a PIV system to have both a large dynamic velocity range and a large spatial range is determined by a dimensionless constant $L_x/c_\tau d_\tau$. PIV systems having large values of $L_x/c_\tau d_\tau$ are well suited for turbulence research, and measurements in higher Reynolds number flows too require larger values of this constant. Typical values of this constant ranges from a few thousand for standard video to over 450000 for 8" x 10" high-resolution films. Assuming a particle diameter of 2 µm, for a maximum velocity of 300 m/s with dT = 0.8µs, we get DSR = 208 and DVR = 39.68. Since we assumed the particle size, Table 2.2 shows the variation of DSR and DVR with different tracer particle sizes. It shows that for particle size diameters between 0.2 and 16 microns, DVR is above 30, which implies that, if the experiment is setup carefully, we can resolve velocities in the range 300 - 10 m/s confidently. We used the higher limit of 10% of the image diameter as the ability of the analysis procedure to determine the displacement between images accurately. If this value can be lowered to 1% of the image diameter, DVR can be extended to range from 300m/s to less than 1 m/s.

Errors in PIV

A number of factors can produce errors in a PIV measurement. They can be broadly classified into

a. Errors in PIV hardware

These errors are related to the hardware of the PIV system such as the timing between different frames, aberrations inherent in the optics, and damaged pixels in the CCD. Timing circuits have reached a stage of very high accuracies that the error in the timing for most flows can almost be ignored except at very high speeds, well into the supersonic regime. However, using a larger separation time within the maximum possible dT for a particular flow condition and interrogation sampling size is recommended.

Table 2.2. Variation of Dynamic Velocity Range (DVR) with particle size

$\mathbf{d_p}$ (μm)	$\mathbf{d_s}$ (μm)	$\mathbf{d_e}$ (μm)	$\mathbf{d_\tau}$ (μm)	**DVR**	**DSR**	**(DSR)(DVR)**
0.2	6.127	6.128	10.89	39.68	208.33	8266.05
0.5	6.127	6.131	10.89	39.67	208.33	8264.73
1.0	6.127	6.142	10.90	39.65	208.33	8260.03
2.0	6.127	6.185	10.92	39.56	208.33	8241.31
4.0	6.127	6.358	11.02	39.20	208.33	8167.68
8.0	6.127	7.004	11.40	37.88	208.33	7891.72
16.0	6.127	9.144	12.83	33.67	208.33	7014.59
32.0	6.127	14.895	17.40	24.82	208.33	5171.57
64.0	6.127	27.836	29.25	14.77	208.33	3076.46
128.0	6.127	54.650	55.39	7.80	208.33	1624.95
256.0	6.127	108.784	109.16	3.96	208.33	824.51
512.0	6.127	217.310	217.50	1.99	208.33	413.80

d_p – Particle diameter

d_s – Diffraction limited spot diameter

d_e – optical image diameter before being recorded

d_τ – recorded image diameter

DVR – Dynamic Velocity Range

DSR – Dynamic Spatial Resolution

b. Errors in experimental setup

Experimental setup errors include calibration errors, non-optimal choice of tracer particles and laser sheet alignment. The necessity to choose proper seeding materials and systems has already been discussed. Setting up the system precisely and carefully can reduce experimental errors significantly.

c. Errors in computation

Computational errors include truncation errors, detection errors, and precision errors. Truncation errors are very similar to truncation error in numerical analysis caused by approximations using numerical discretization. Most PIV algorithms use a simple forward differencing interrogation scheme in which the velocity at time t is calculated using particle images recorded at time t and t+Δt, given by

$$U(t) = \left.\frac{d\vec{X}}{d\tau}\right|_{\tau=t} = \frac{\vec{X}(t+\Delta t) - \vec{X}(t)}{\Delta t} + \left.\frac{\Delta t}{2}\frac{d^2\vec{X}}{d\tau^2}\right|_{\tau=t} + \ldots$$

This approximation is accurate to order Δt. Krothapalli [Krothapalli, 2000] shows that the maximum accuracy with which velocity may be evaluated includes at best second order terms for the location corresponding to the half point between the initial and final position of the laser. Other investigators [Meinhart, 2001] have implemented a second order accurate central difference scheme. Detection errors are due to the improper correlation peak identification. This error cannot be completely eliminated due to the inherent nature of correlation PIV. Random correlation between particles that don't belong to the same pair can influence the peak-searching algorithm. Achieving a high SNR would help in reducing this improper identification. Precision errors are due to the inability of the analysis procedure to perform highly accurate sub-pixel interpolation. Calculating centroids or curve fitting procedures are used to perform sub-pixel interpolation. This procedure introduces additional bias errors. Westerwheel shows that the error for similar conditions of image size and algorithms, the uncertainty in subpixel interpolation is about ±0.1 pixels. Effect of this on the range of velocities is shown in Table 2.3. Particularly note the error introduced at the lower speeds, which will be important for our case because of the wide range of velocities possible from the jet core to the edges of the shear layer. Further discussion of this will be taken up in the results section.

d. Errors in derivatives (Vorticity)

Vorticity is obtained by evaluating the velocity derivatives with a suitable finite difference scheme (second order central difference scheme in our case). Lourenco and Krothapalli [Lourenceo., L, 1995] show that two components of error arise from this scheme. One is the truncation error associated with the finite differences of order Δx^2, Δy^2 and the other uncertainty comes from the uncertainty in the velocity measurement and is of order $1/\Delta x$, $1/\Delta y$. Also, note that these errors proceed in opposite directions.

Table 2.3. Effect of sub pixel interpolation resolution on velocity uncertainty

Velocity (m/s)	Pixel Size (μm)	Sub pixel interpolation precision (±pixels)	±% Uncertainty
300	9	0.1	0.38
250	9	0.1	0.45
200	9	0.1	0.56
150	9	0.1	0.75
100	9	0.1	1.12
50	9	0.1	2.25
25	9	0.1	4.50
20	9	0.1	5.63
15	9	0.1	7.50
10	9	0.1	11.25
5	9	0.1	22.50
4	9	0.1	28.13
3	9	0.1	37.50
2	9	0.1	56.25

Increasing grid size increases truncation error while decreasing the uncertainty in velocity. It also shows the importance of setting up and acquiring good quality data for an accurate velocity estimate in the first place.

Chapter 03

NUMERICAL ANALYSIS SETUP

CFD methods are an alternate way to predict the full flow field and study them thoroughly. 2D axisymmteric models of the axisymmetric cavity geometries were modeled using commercially available software called CFDACE®. It uses a finite volume technique to predict flow fields. In a finite volume technique, the solution domain is divided into a number of cells known as control volumes. The governing equations are then numerically integrated over each of these computational cells or control volumes. The average value of any quantity within a control volume is given by its value at the cell center. The approach used by the software is given in CFDACE user manual [*CFDACE user manual* 2004] and is briefly presented below.

3.1 Governing equations

3.1.1 Mass Conservation

Conservation of mass requires that the time rate of change of mass in a control volume be balanced by the net mass flow into the same control volume (outflow - inflow). This can be expressed as:

$$\frac{\partial \rho}{\partial t} + \nabla \bullet \left(\rho \vec{V}\right) = 0$$

The first term on the left hand side is the time rate of change of the density (mass per unit volume). The second term describes the net mass flow across the control volume's boundaries and is called the convective term.

3.1.2 Momentum Conservation

The x-component of the momentum equation is found by setting the rate of change of xmomentum of the fluid particle equal to the total force in the x-direction on the element due to surface stresses plus the rate of increase of x-momentum due to sources:

$$\frac{\partial(\rho u)}{\partial t} + \nabla \bullet \left(\rho \vec{V} u\right) = \frac{\partial(-p + \tau_{xx})}{\partial x} + \frac{\partial \tau_{yx}}{\partial y} + \frac{\partial \tau_{zx}}{\partial z} + S_{Mx}$$

Similar equations can be written for the y- and z-components of the momentum equation.The momentum equations, given above, contain as unknowns the viscous stress components $\tau_{i,j}$. A model must be provided to define the viscous stresses. Solutions of the three momentum equations yield the three Cartesian components of velocity. Even though pressure is an important flow variable, no governing PDE for pressure is presented. Pressure-based methods utilize the continuity equation to formulate an equation for pressure. In CFD-ACE®, the SIMPLEC (Semi-Implicit Method for Pressure-Linked Equations Consistent) scheme has been adopted. It is an inherently iterative method. A pressure field is initially guessed or the latest available pressure in an iterative procedure is used to find the velocity field. Correction to pressure and velocity are found so that an improved solution is obtained.

3.2 Turbulence Modeling - Large Eddy Simulations

Large Eddy Simulations (LES) are considered somewhere between the model-free Direct Numerical Simulations (DNS) and Reynolds Averaged Navier-Stokes Simulations (RANS) with respect to both physical resolution and computational costs. LES partly inherits the robustness and universality of DNS, allowing accurate prediction of the coherent structures in turbulent flows. The cost for LES is lower than for DNS because the resolution requirements for LES are of the same order as those for RANS. In most turbulent flows of practical interest the motion on the order of the dissipation scale cannot be evaluated explicitly due to limitations on the available computational resources required to resolve the physics of the flow. To overcome this limitation, the governing equations have to be altered in such a way that the activity at the level of unresolved scales is mimicked by a proper model, and only the large-scale fluctuations are explicitly taken into account. In LES, a smoothing (low pass) filter of constant kernel width achieves separation of scales, decomposing a given field into a resolved component and a residual component (also called subgrid fluctuations). Operationally, the filtering is described by the convolution:

$$\bar{f}(x,t) = \int_D f(x',t)G(x-x',t,\Delta_f)dx'$$

where $\overline{f}$ represents the filtered value of the field variable *f*, *G* denotes the filter, which is a symmetric function with compact support and Δf is the filter width (assumed constant in the standard LES formulation). In variable density flows, it is desirable to use Favré (density weighted) filtering. Applying the filtering operation, the Navier-Stokes equations for the evolution of the large-scale motions are obtained. The filtered equations contain unknown terms such as $\tau_{ij} = \overline{u_i u_j} - \overline{u}_i \overline{u}_j$ (velocity-velocity correlation) arising from the filtering of nonlinear terms and are known as subgrid scale (SGS) stresses. The SGS eddy viscosity is computed based on the grid spacing and local strain rate:

$$\gamma_t = (C_s \Delta)^2 \left| \tilde{S}_{ij} \right|$$

where Δ is the filter (grid) width. The constant of the model follows from the isotropy-of-the-small-scales assumption. A value of 0.1 was used.

3.3 Geometry and Mesh generation

Axisymmetric cavities of three experimentally tested models were simulated. The first geometry was a cavity of infinite depth with its periphery open. The second geometry was an enclosed cavity placed at the exit of the jet with orifice inlet/exit boundaries. The third geometry was an enclosed cavity placed at the exit of the jet with a short pipe of constant diameter extending up to four jet diameters upstream of the jet exit. The computational domain showing the geometry, boundary conditions and a closer view of the grid used in the cavity region for the first geometry (hole tone actuator) is shown in Figure 3.1. The domain extended up to 10D from the exit. The total number of nodes was approximately 176000 for each case. The grid resolution was about 0.125 mm x 0.125 mm.

3.4 Discretization scheme and Solution control

Second order schemes with a blending factor of 0.2 were used for velocity and density terms. The original idea of this scheme is to evaluate the cell face value by using linear interpolation of values at two upstream cells, instead of one. For turbulence a first order upwind scheme was used. The Algebraic Multi-Grid (AMG) solver available in CFDACE is used in this study. Inlet boundary conditions were specified as fixed mass flow rates with an estimated value for the turbulence quantities. Pressure outlet boundary conditions were used at the exit. Default relaxation parameters available in the code were used. A RANS simulation provided the initial condition to the model. During LES analysis convergence at each time step was ensured.

Monitor points were placed at the cavity exit plate and near the jet exit to get time histories of pressure and other data. A typical pressure signal at the monitor point until steady oscillations occur is shown in Figure 3.2. Vorticity and other parameters were calculated from the data and animations of different quantities were created to study the problem.

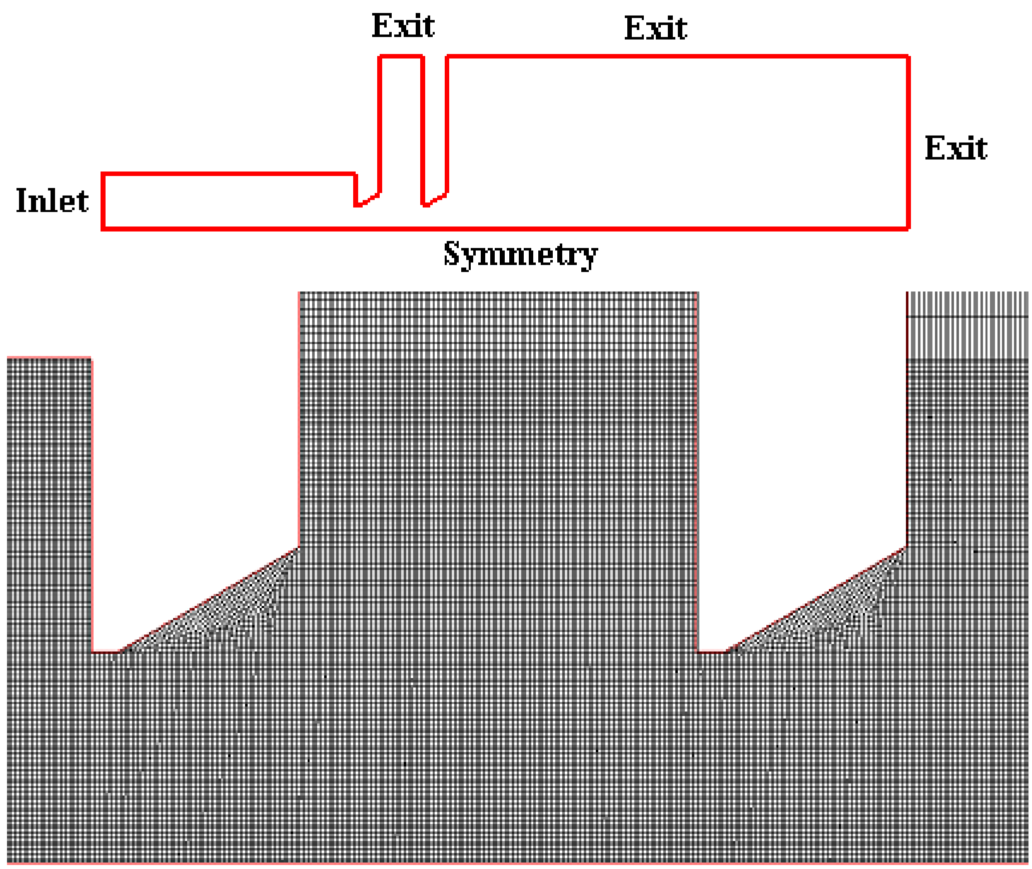

Figure 3.1. Computational domain showing the boundary conditions used and a closer view of the grid used for the hole tone geometry

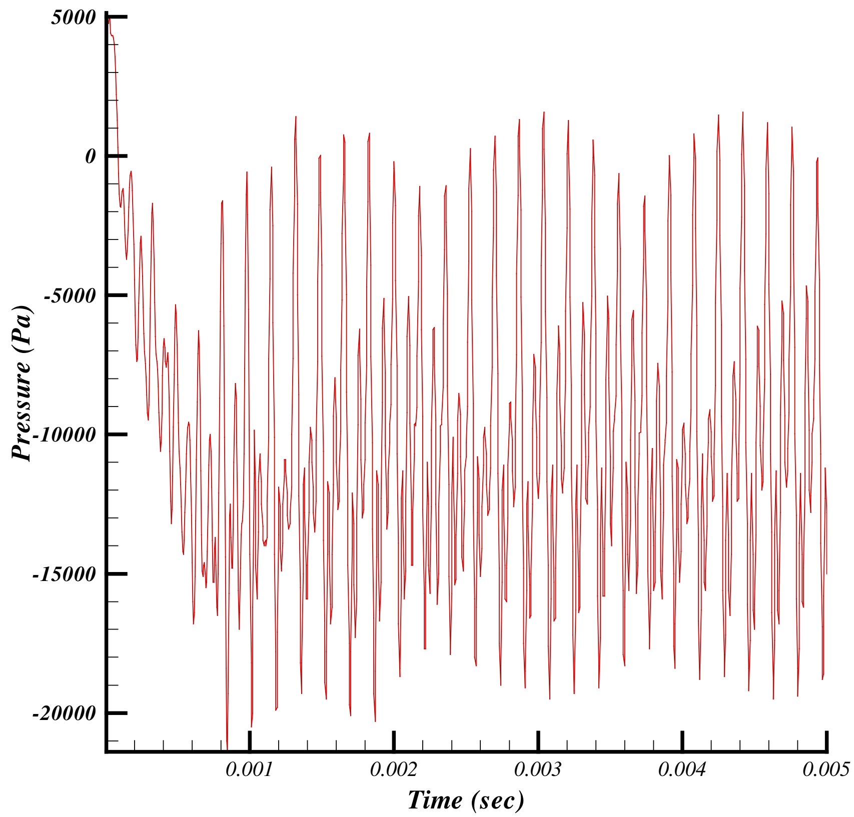

Figure 3.2. Pressure data at a monitor point within the cavity from CFD analysis (Axial Jet Actuator with orifice inlet and exit boundaries, U_j = 300 m/s

Chapter 04

RESULTS AND DISCUSSIONS

The presentation of results from this work begins with a study of natural axisymmetric turbulent jets. The purpose of this is to establish a baseline case against which other excited jets can be compared. Another objective is to establish and document naturally occurring processes that affect the growth of a jet. This could then be used to study how various excitation techniques exploit these processes. The following sections present results from two different configurations used for exciting a baseline turbulent jet flow in this study. The first configuration is a hole tone device which will be referred here as a radially unconfined cavity. The second configuration is a confined cavity placed deep inside the pipe. The effect of different inlet and exit boundaries are also presented. Experimental and numerical results are presented together for each tested configuration.

4.1 Natural Axisymmetric Turbulent Jets

4.1.1 Introduction

Many investigators [*Michalke* 1965, 1972, *Ho* 1982, 1984, *Cohen & Wygnanski* 1987] have conducted excellent studies and reviews on free axisymmetric turbulent jets exiting from a nozzle with smooth contraction. As the term ‘free’ implies, the flow is remote from walls and the turbulent flow is because of mean-flow differences. The region very close to the exit of the jet is dominated by a linear instability mechanism. The basic vorticity distribution, which possesses a maximum at the exit, is inviscidly unstable to small perturbations via the Kelvin-Helmholtz instability governed by Rayleigh’s equation. The shear layer that emanates from the nozzle lip with instability frequency f_n has a length scale of θ, which denotes the initial momentum thickness of the shear layer. An estimate of the most amplified frequency f_n (shear layer mode frequency) can be predicted by $St = f_n\theta/U_j = 0.017$ where, U_j is the mean velocity measured at the jet exit. The initial momentum thickness is proportional to $U_j^{-1/2}$ and hence $f_n \propto U_j^{3/2}$. Beyond the region of exponential growth, Kelvin-Helmholtz instability waves rolls up into coherent structures that merge and are convected downstream. In a planar mixing layer, these recirculating regions are usually referred to as Kelvin cat’s eyes. Thin vorticity layers or braids connect them to each other. The process of successive vortex merging causes the shear layer to spread and the vortex passage frequency to decrease. Farther downstream, these vortices become large-scale structures producing perturbations that feedback to the trailing edge. The large-scale structures are characteristic of the column mode of instability (f_p). The dimensionless frequency $St = f_pD/U_m$ for the preferred mode lies between 0.25 and 0.5. Here D is the diameter of the jet exit. This strouhal number is dependent on the initial momentum thickness at low jet velocities and becomes constant and equal to 0.44 for higher flow rates [*Lucas* 1997]. The preferred mode is present even when the successive vortex merging process does not take place.

Baseline measurements for axisymmetric jets can be made on three different types of geometries.

1. Contraction Jet, a jet issuing through a smoothly contracting nozzle.
2. Pipe Jet, a jet exiting from a constant diameter tube (0.5 inches diameter tube extending up to 4 jet diameters upstream of the exit in the present work).
3. Orifice Jet, a jet exiting through an orifice plate (0.5 inches diameter in the present work).

Experiments were conducted on all of the above mentioned exit geometries. In this study, the pipe jet would be used for baseline measurements. Reason for this would be discussed in the following sections. In all cases, supply line for the exit geometries was 1.2 inches in diameter. Initially results from the pipe jet would be presented in detail and then different exit conditions would be compared against it.

4.1.2 Mean Velocity Field

The mean flow field of a round jet at $Re_D = 2.1 \times 10^5$ is shown in Figure 4.1.1a-d. Figure 4.1.1a shows the axial velocity contour. The axial velocity is normalized using the jet exit velocity U_j. This composite image is an average of about 500 instantaneous snapshots per zone in the region $X/D_j = 0 – 9$ and about 50 images per zone for $X/D_j > 10$.

The jet flow field can be divided into three distinct zones: the potential core region, a transition zone and a self-similar zone. Potential core is the region where the axial velocity remains constant. In our case, this region extends till about $5D_j$. This value is comparable to values in the literature for jets with high Reynolds number and significant perturbations in the shear layers near the exit. The length of the potential core depends on the state of the flow at the exit. At lower Reynolds number, the incoming flow is generally laminar and hence they tend to have a larger potential core length. Stromberg [*Stromberg* 1979] reported a potential core length of about $7D_j$ for a low Reynolds number flow ($Re_D = 3600$) at Mach 0.9. The transition zone is the region where the axial velocity starts to decrease. In the self-similar zone, the transverse velocity profiles exhibit self-similarity and the velocity keeps decreasing linearly.

Figure 4.1.1b shows the mean axial vorticity field (ω_z). Near the end of the potential core, the vortex structures generated in the shear layer begins to interact and merge. The effect of this interaction is that the large scale eddies in the shear layer are broken into smaller scale turbulence. From a mixing application point of view, the smaller the potential core length, the higher the mixing. For an application where deeper penetration is required, merging of the shear layer and hence the interaction of eddies must be delayed, which requires the potential core length to be longer. Figure 4.1.1c shows the velocity profiles at various locations in the axial direction. Figure 4.1.1d shows a closer view of the region1 ($X/D_j = 0 – 4$). Figure 4.1.1c clearly show that the velocity decreases in the axial direction as the lateral width of the profile increases. If this region has achieved self-similarity, then the decay of axial velocity and the growth of jet width must be linear.

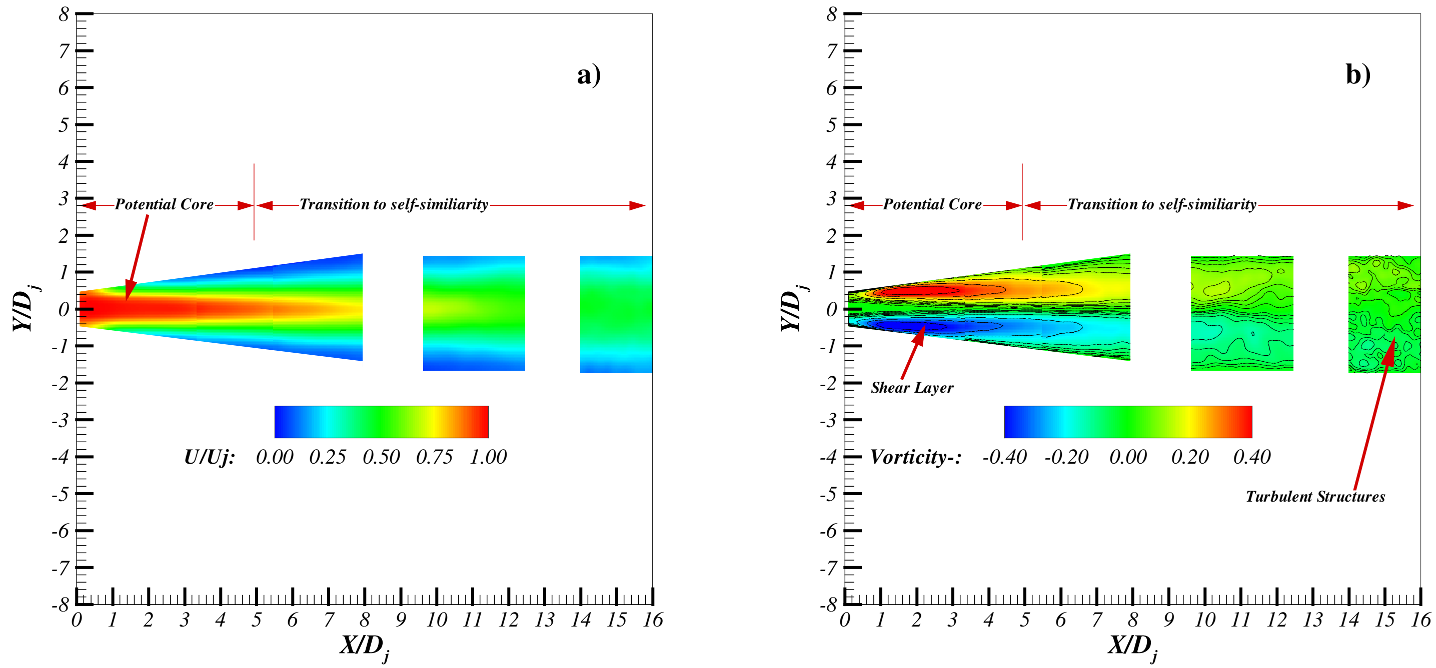

Figure 4.1.1. Flow field of an axisymmetric jet issuing from a short pipe of constant diameter ($Re_D = 2.1 \times 10^5$). a) normalized mean axial velocity b) vorticity field

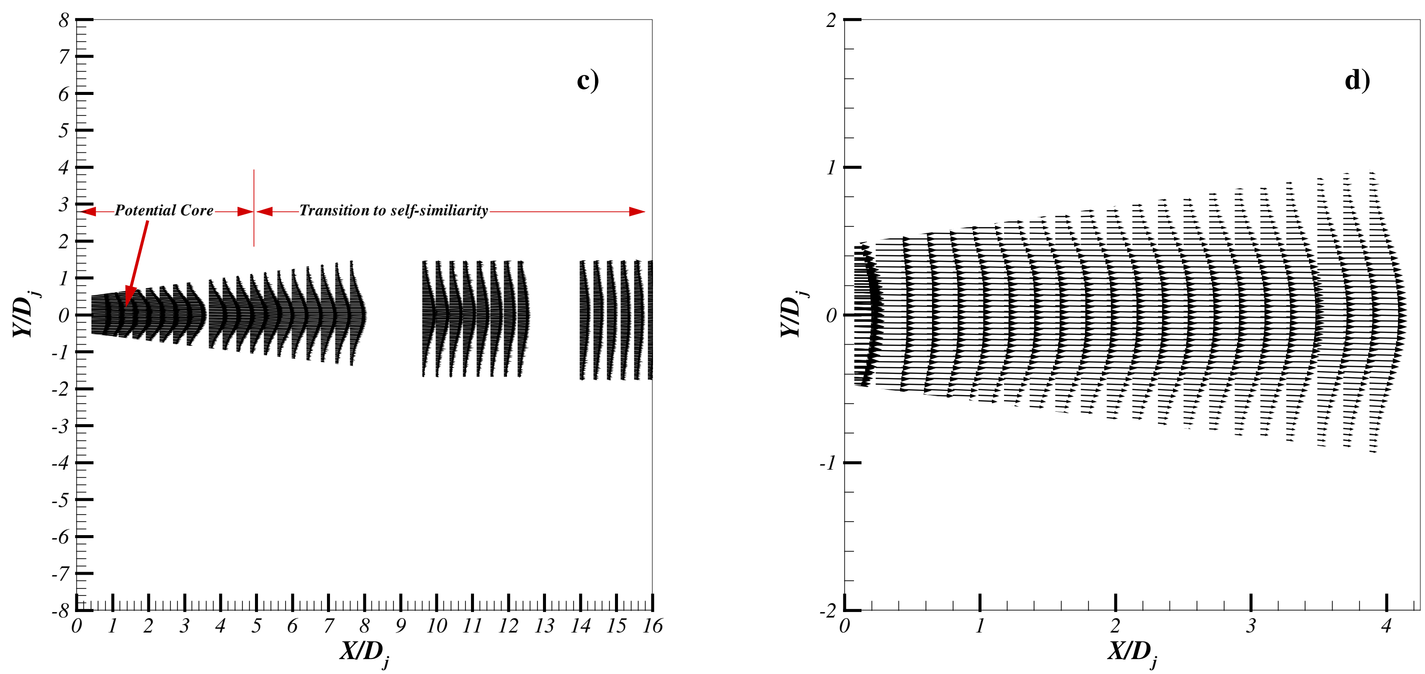

Figure 4.1.1. Continued. c) mean velocity profiles d) close view of the velocity profiles up to $4D_j$

Scaling

A brief look into the scaling properties of the axisymmetric turbulent jet is presented before specific results are present. There is a point source of momentum with momentum flux J_o in the axial direction. The jet fluid and ambient fluid both have density, ρ, and viscosity, ν. In the self-similar region, the mean velocity will have the form

$$u(x,r) = u_c(x) f(\eta), \quad where\ \eta = \frac{r}{y_{1/2}(x)}$$

meaning that the shape of the mean velocity profile is given by the function f(η), width of the profile given by $y_{1/2}(x)$ and the magnitude of the profile given by the mean centerline velocity $u_c(x)$.

We are interested in finding how $y_{1/2}$ and u_c varies as the jet progress. $y_{1/2}$ depends on x, J_o, ρ, and ν. In turbulent flows, the importance of molecular viscosity is basically confined to the smaller scales and while considering large-scale properties effects of viscosity can be ignored. Considering the units of the remaining parameters,

$$y_{1/2} \Rightarrow L, \quad x \Rightarrow L, \quad J_o \Rightarrow \frac{ML}{T^2}, \quad \rho \Rightarrow \frac{M}{L^3}$$

where, M – Mass, L – length, and T – Time. Comparing the units, the only parameter that can be used is x. And we have the relation,

$$y_{1/2} = \text{Constant} * x$$

Dependence of u_c on x can be found by using the conservation of momentum. The momentum flux through any arbitrary x = constant surface has to be constant and equal to J_o.

$$J_o = J(x) = \rho \int_0^{2\pi} d\theta \int_0^{\infty} u^2 r dr$$

$$= 2\pi\rho u_c^2 \int_0^{\infty} f^2 y_{1/2}^2 \eta d\eta$$

$$= 2\pi\rho u_c^2 y_{1/2}^2 \int_0^{\infty} \eta f^2 d\eta$$

For the integral to be a constant $u_c^2 y_{1/2}^2$ has to be a constant which implies

$$u_c = \text{Constant} / x$$

Centerline Velocity Decay

The normalized axial velocity variation along the centerline of the jet axis is shown in Figure 4.1.2. The axial velocity is normalized using the local centerline velocity. Both coordinates X/D_j and U_{CL}/U_j are represented in logarithmic scale. The centerline velocity starts decreasing rapidly after the end of the potential core. This decay of the axial velocity is usually modeled using a simple decay equation with a $1/x$ decay profile.

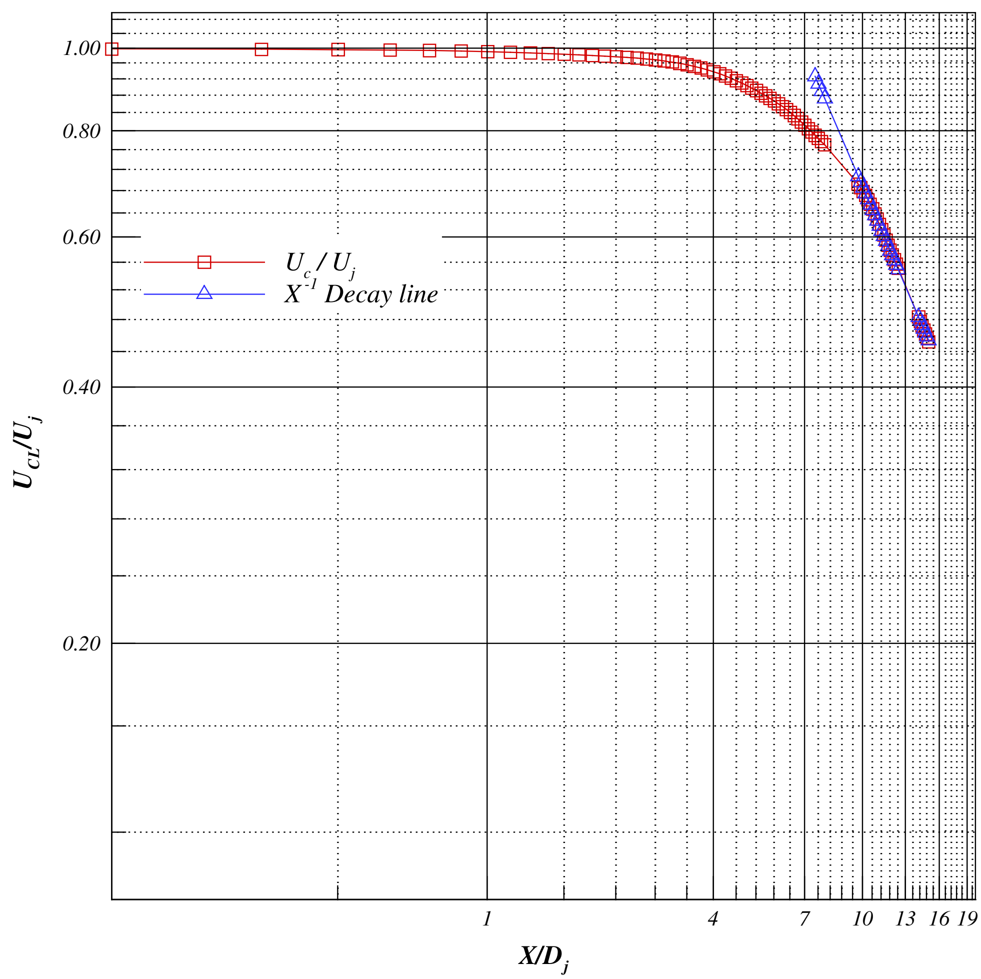

Figure 4.1.2. Axial mean velocity decay along the centerline of the baseline jet ($Re_D = 2.1 \times 10^5$)

$$\frac{U_{CL}}{U_j} = \frac{BD_j}{x - x_0}$$

where, U_{CL} is the local mean centerline velocity in the *x*-direction along the axis of the jet, B is the velocity decay rate coefficient, *x* is the coordinate in the axial direction and x_o is the distance of the virtual origin from the jet exit. Fitting the data using least squares, the velocity decay rate coefficient for the pipe was B ≈ 6.3. A comparison with data from other researchers is given in Table 4.1. The efficiency of the mixing process decreases with increasing values of B. Evidence from various research papers [*Panchapakesan & Lumley* 1993, *Wygnanski & Fiedler* 1969] show that the value of B depends on the initial conditions of the jet. Compared to pipe jet, a contraction jet (a jet issuing from a contoured nozzle) has a smaller value of B, which generally lies between 5 and 6. One possible explanation for this would be that the pipe jets have a fully developed turbulent velocity profile at the exit (in contrast to a top hat velocity profile of a contraction jet) and hence a thicker initial momentum thickness. A shear layer having a thicker initial momentum thickness is more stable than a thin shear layer. The total energy available at the jet exit is distributed to an increasing area as the jet moves forward and instabilities in the shear layer is a process through which this distribution takes place. The virtual origin, *x*-intercept of the linear growth rate, lies $x_0 \sim 1D_j$ in front of the exit. The value of x_0 varies between $-2.5D_j$ to $4D_j$ in the literature. This value depends on a number of parameters like Reynolds number, initial conditions and their effect on the potential core.

Lateral Spread Rate

Figure 4.1.3 shows the longitudinal evolution of jet-width normalized with exit diameter D_j. The width is close to 0.5 up to $x = 4D_j$ and then spreads linearly. This linear growth could be modeled as:

$$\frac{Y_{1/2}}{D_j} = \frac{A}{D_j}(x - x_0)$$

A = tanβ where, β is the spread angle. For the pipe jet in this experiment, A = 0.0925 which compares to values in the literature. For a jet with Gaussian velocity profile, a 'top hat' velocity profile at the exit, and a constant streamwise momentum flux, the decay rate coefficient B is related to the jet spread angle β as:

$$B = \frac{(0.5\ln 2)^{1/2}}{\tan\beta}$$

Even though our velocity profile at the exit is not a top hat velocity profile, this relation between B and A is satisfied indicating that a Gaussian distribution could model the jet's transverse profile in the self-similar zone. This could be expected because, by definition, a self-similar zone is insulated from the effects of the initial conditions (i.e., the effects of initial conditions has already been played out). As a jet proceeds downstream, it drags previously still fluid from the surroundings along with it. This process is referred to as entrainment. The mass flow rate through a surface of constant *x*, is given by:

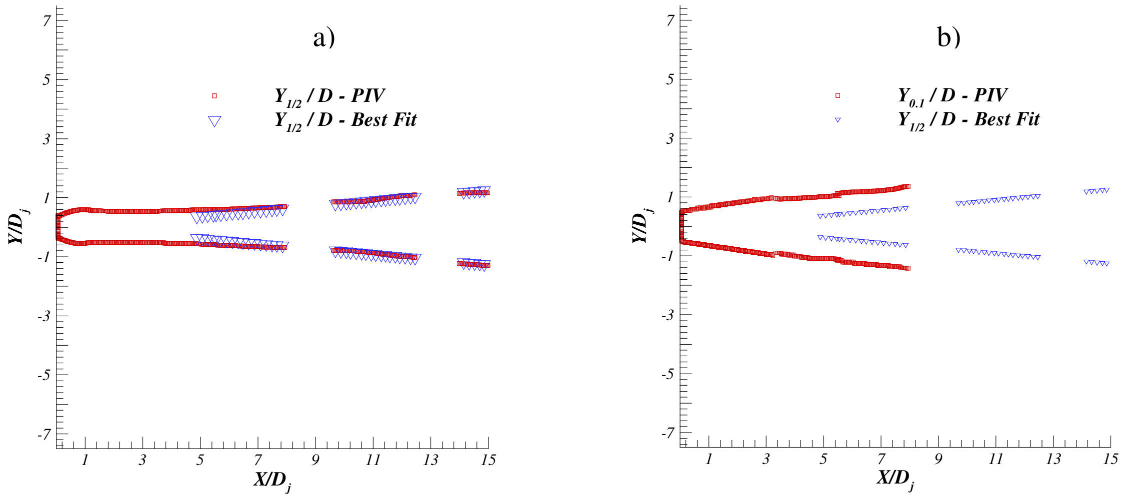

Figure 4.1.3. Locus of jet width of the baseline axisymmetric jet ($Re_D = 2.1 \times 10^5$). a) 50% of the centerline velocity b) 90% of the centerline velocity

Table 4.1. Comparison of mean flow parameters with data from literature

ReD	B	A	Reference
8.6×10^4	5.4	0.086	[Wygnanski 1969[1]]
1.1×10^4	6.1	0.096	[Panchapakesan 1993[1]]
9.5×10^4	5.8	0.094	[Hussein 1994[1]]
2.4×10^3	5.9	0.095	[Boersma 1998[2]]
6.5×10^4	5.5	0.096	[Bogey 2003[3]]
2.1×10^5	6.3	0.093	present study[1]

1 - Experiments, 2 – DNS, 3 – LES

$$\dot{m} = \int_0^{2\pi} d\theta \int_0^{\infty} \rho u(x,r)\ r\ dr$$

$$= 2\pi\rho\, u_c\, y_{1/2}^2 \int f\ \eta\ d\eta$$

Since $y_{1/2} \propto x$ and $u_c \propto x$, mass flow rate varies linearly with x

$$\dot{m}(x) \propto x$$

If the jet source properties are assumed constant, the rate at which surrounding fluid is drawn into the jet varies linearly with *x*. In some instances, a jet width based on 10% of the centerline velocity is used to compare different jets and to get a complete picture of the effective spreading due to mixing. Figure 4.1.3b shows the shear layer width based on 10% centerline velocity.

Based on the discussions above, we can show that the volume flow rate at any axial location *x* is linearly proportional to *x*:

$$\frac{Q}{Q_j} = \int_S \frac{U}{U_j} dS \approx \sum \pi\left(\Delta r^2 + 2r\Delta r\right)\left(\frac{U}{U_j}\right)$$

$$\frac{Q}{Q_j} = \frac{2}{B}\frac{x - x_0}{D_j} = C\frac{x - x_0}{D_j}$$

where, Q is the volume flow rate at any axial location, Q_j is the volume flow rate at the exit, S is the area of the jet cross-section (r-θ) over which the velocity profile is integrated to get the flow rate, Δr is the step between two velocity vectors in the flow field obtained through PIV and C is the volumetric flow coefficient.

Figure 4.1.4 shows the evolution of the mean volume flow rate in the axial direction. Unlike centerline velocity decay and lateral spreading, volume flow rate starts growing from a very early stage. This indicates that entrainment of surrounding fluid starts right from the exit boundary. The evolution of volume flow rate based on the value of C derived from B and x_o is also shown as the C = 0.32 profile. The difference between the experimental and calculated values is because the region of PIV studies at larger X/D_j (> 7) is smaller than the actual jet width and hence some part of the profile is lost resulting in a lower volume flow rate. At lower X/D_j, the growth is not linear and this equation cannot be applied.

Reynolds Number based on the exit diameter D_j ($Re = U_jD_j/\nu$) is proportional to the square root of the momentum flow rate. Therefore,

$$Q_x = \frac{\pi}{4} C\nu \operatorname{Re}\left(x - x_0\right)$$

Here, ν is the kinematic viscosity. If B and x_0 are the same, all jets with the same Reynolds number will have the same volume entrainment at identical axial locations. Or, for jets having the same Reynolds number, volume flow rate and hence the entrainment and mixing performances can be altered by changing two parameters,

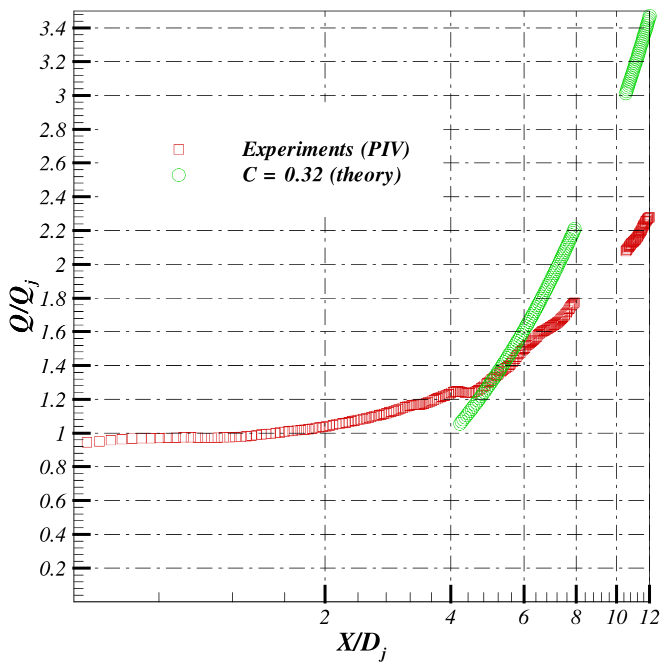

Figure 4.1.4. Axial volume flow rate for the baseline axisymmetric jet ($Re_D = 2.1 \times 10^5$)

1. The location of virtual origin
2. The velocity decay rate

Convergence

Before we discuss the mean velocity and turbulent components of the flow field in detail, convergence of these values are presented. Single point velocity measurement techniques like hotwire or LDV can take data at very high frequencies. Thousands of data points can be taken allowing a very accurate estimate of mean velocity and turbulence quantities. Particle Image Velocimetry technique while allowing global instantaneous measurements is limited by the maximum frame rate at which images can be taken. Also storage capacity, processing and computing time puts a limit on the maximum number of images that can be processed with the best possible resolution and within a reasonable time period. In the present case the frame rate is limited to 10Hz and the maximum number of images to a few hundred for each case. About 500 images of the initial region ($0 < X/D_j < 3.5$ was used for this convergence study) of the pipe jet were processed and averaged. Evolution of the averaged U, V, u', and v' components are shown in Figures 4.1.5a-d. Figure 4.1.5a shows that the mean axial velocity has converged at around 100 images. When compared to the final averaged value, after averaging 100 images, the differences are less than 5% for the whole region including the shear layer. For data near the jet axis, at 100 images, deviations from the final value are less than 1%. Figure 4.1.5b shows a similar plot for the mean radial component reaching a steady state after around 250 images. The radial component is a very small fraction of the axial velocity and it introduces additional experimental uncertainty especially when the setup is tuned based on the axial velocity. The deviations after averaging 250 images is about 10% at the jet axis and higher (20-40%) in the outer shear layer regions. Figure 4.1.5c,d shows that the turbulence components are not yet fully converged. The trend of the evolution of convergence suggests that after 500 images, the data is very close to reaching a steady state even for the turbulence quantities.

Mean U, V Velocities

Figure 4.1.6a shows the streamwise velocity profiles (not normalized) at different axial locations of the jet. At the jet exit, velocity profiles have a shape resembling a flat developing pipe flow. A fully developed pipe flow requires an inlet length of about $25 – 40D_j$, which is not available in our case. As the flow moves away from the exit, the shape of the velocity profiles quickly transform to a Gaussian type profile. It also shows the lateral growth of the profile. Figure 4.1.6b shows the normalized streamwise velocity profiles at different axial locations between $1 – 14D_j$. Normalization was done using the local centerline velocity and the local half-width of the jet. After a few jet diameters form the exit, the velocity profiles collapse very closely to a single curve. As mentioned earlier, this curve can be represented by a Gaussian profile given by [*Malmstrom* 1997]:

$$\frac{U}{U_{CL}} = e^{-\ln 2\eta^2}$$

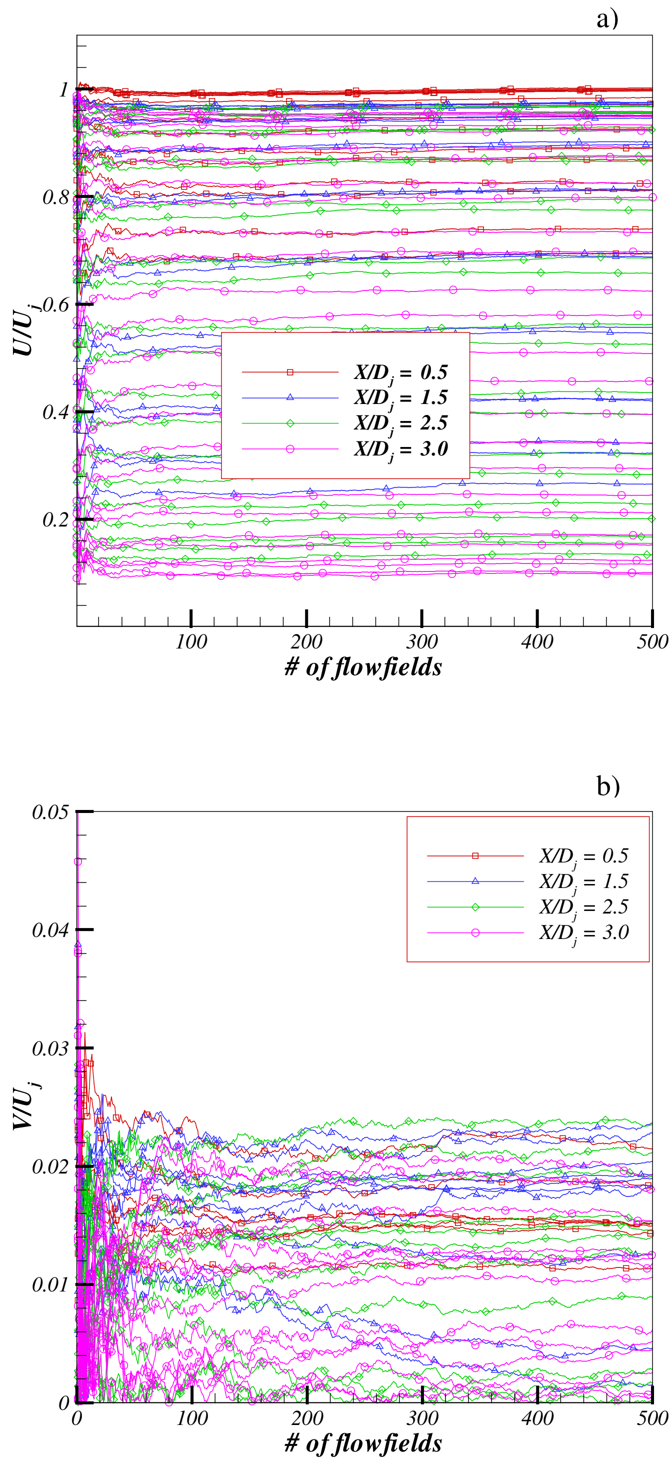

Figure 4.1.5. Convergence of velocity statistics obtained using PIV. a) mean axial velocity b) mean radial velocity

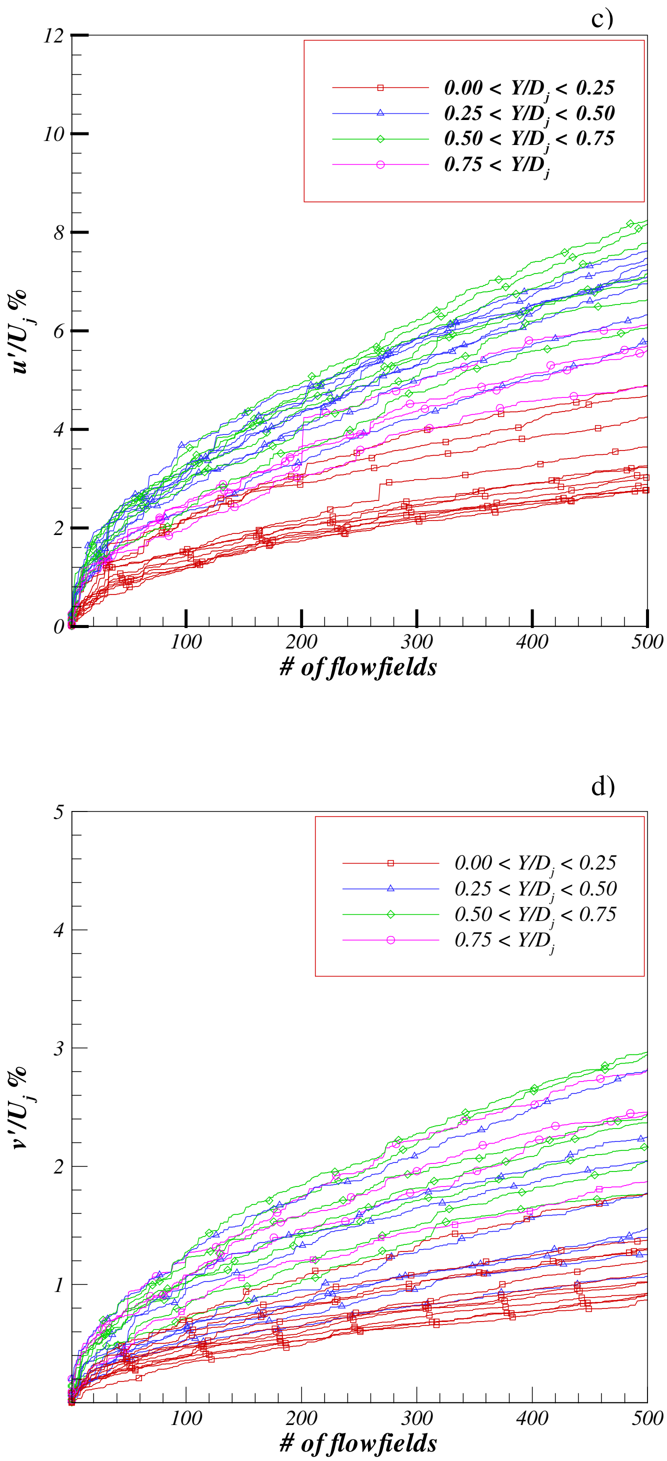

Figure 4.1.5. Continued. c) mean axial rms fluctuating velocity d) mean radial rms fluctuating velocity

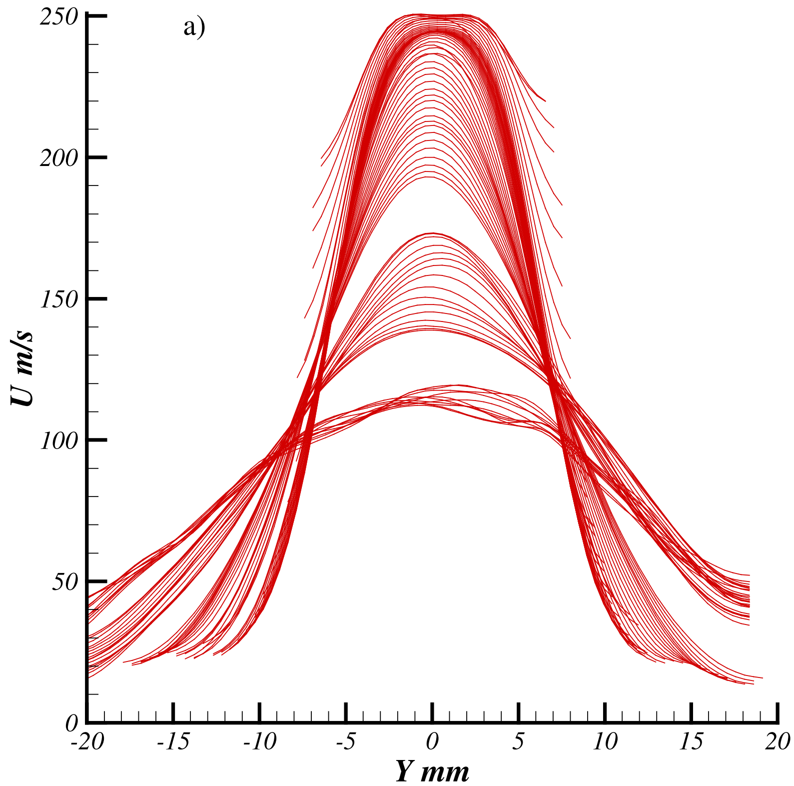

Figure 4.1.6. Streamwise velocity profile for the baseline axisymmeric turbulent jet. a) actual axial velocity

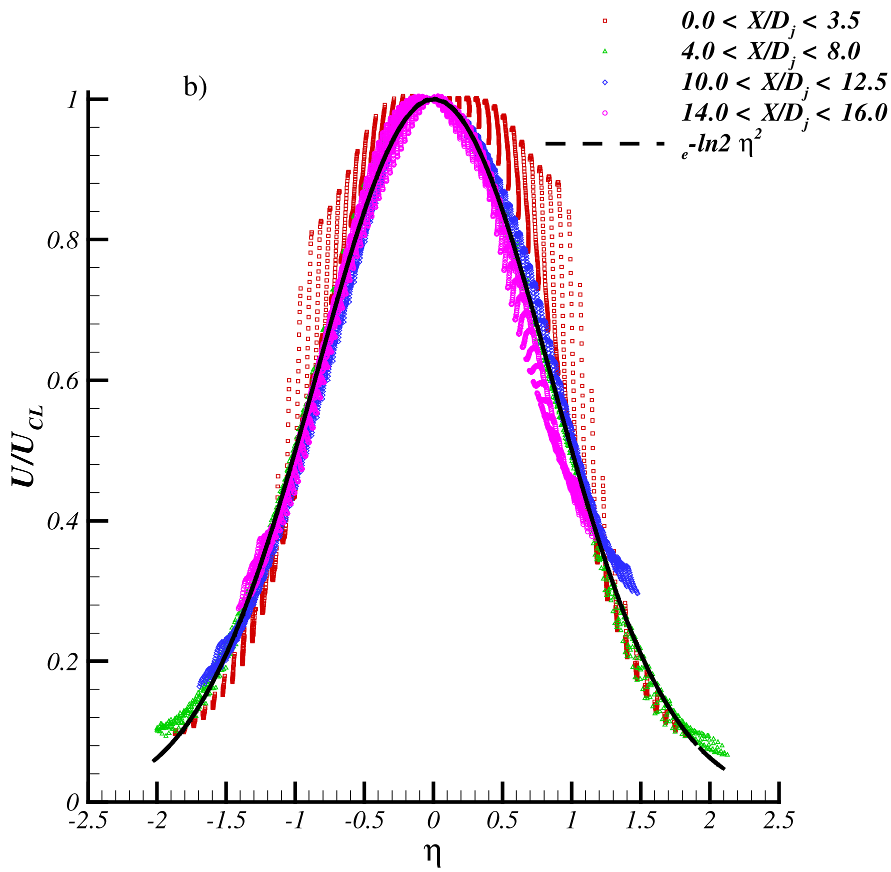

Figure 4.1.6. Continued. b) normalized axial velocity. (data in Figure 4.1.6a normalized based on the local centerline velocity)

where, $$\eta = \frac{y}{y_{1/2}}$$

A typical subsonic turbulent axisymmetric jet attains self-similarity in its mean velocity components at $X/D_j > 20$. Turbulent components of the velocity take a longer distance to attain similarity. A jet is completely self-similar only if all the mean and turbulent components have achieved similarity. It is believed that the approach to a completely self-similar jet takes place in steps. The mean axial velocity becomes self-similar leading to a certain level of turbulence production. After reaching self-similarity in the axial turbulence components, other directions tend towards similarity. In this work, the farthest measurement point was in the region of about 15-16D_j. As can be seen from Figure 4.1.6b, after about 4D_j, the mean axial velocity component is very close to a self-similar profile.

The measured radial velocity, V, normalized by the local centerline axial velocity U_{CL} is plotted in Figure 4.1.7. The radial component of the velocity in the near field is a very small fraction (about 4%) of its axial counterpart. As mentioned during the discussion of convergence, because of the large difference between the ranges of axial and radial velocity components, there is an increased uncertainty in the accuracy of the radial components. Also in the region of measurements ($X/D_j < 8.0$), the radial velocity has not yet reached self-similarity. However, it clearly shows good qualitative agreement as compared to an expected profile in the self-similar region. In the region near the jet axis, there is an outflow of fluid. This outward velocity, which is very close to zero at the axis, increases to a maximum before decreasing and at sufficient distance away from the axis, becomes an inward flow that is usually associated with entrainment. The reason for this outward flow is the decay in the centerline velocity. This decay is associated with a decrease in the axial volume flux for a small control volume centered at the axis. The excess volume exits the lateral sides of the control volume resulting in a lateral outflow near the jet axis. If the control volume is extended to include the whole jet, there is a net increase in the axial volume flux that is associated with the inward flow at the edges. As we move away from the jet exit, the point of maximum outward velocity moves towards the axis. The radial velocity profile in the similarity zone (shown in the insert) is obtained by substituting a Gaussian profile for U/U_{CL} in the continuity equation [*Agrawal & Prasad* 2003].

$$\frac{V}{U_{CL}} = \frac{A}{2\eta}\left(-1 + \exp\left(-\eta^2\right) + 2\eta^2 \exp\left(-\eta^2\right)\right)$$

This profile reveals that $V/U_{CL}=0$ at $\eta=0$. It reaches an outflow maximum at $\eta=0.54$ and declines back to zero at $\eta=1.12$. Inward flow reaches its maximum at $\eta=2.08$ and asymptotes to 0 as $\eta\to\infty$. Comparing the profiles of U/U_{CL} and V/U_{CL}, it is clear that $U/U_{CL}\to 0$ much faster than V/U_{CL}. This implies that the central portion of a jet is dominated by the axial component of velocity and the radial component is more important far away from the axis. Agrawal [*Agrawal & Prasad* 2003] suggests that it would be advantageous to use the V/U_{CL} profile to determine the spread rate A. The location and height of the extrema can be unambiguously determined from a V/U_{CL} profile. However, as mentioned earlier experimental uncertainty in V/U_{CL} can be very substantial.

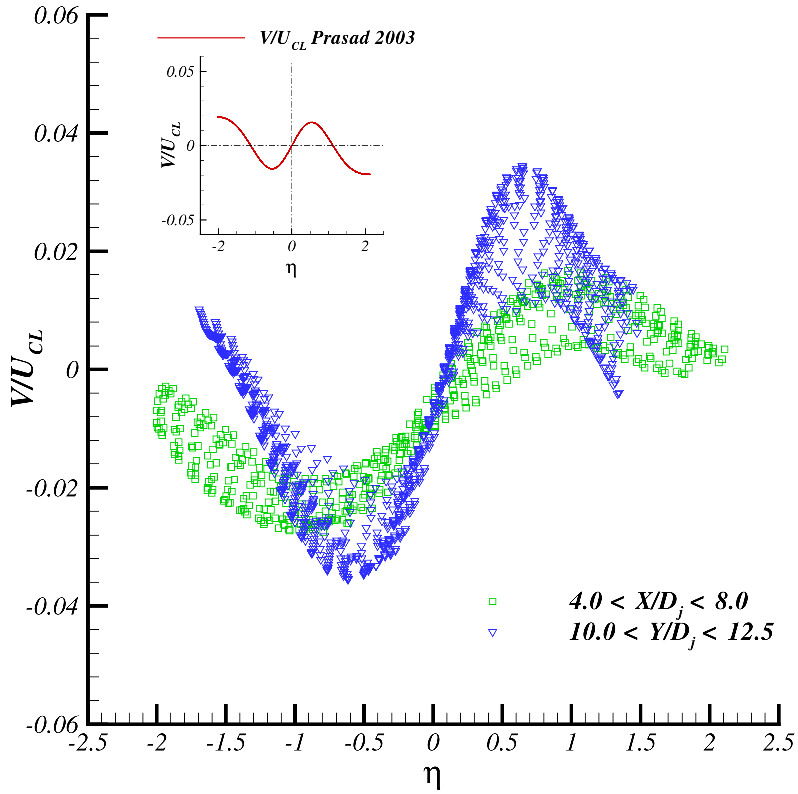

Figure 4.1.7. Normalized radial velocity profile for the baseline axisymmetric turbulent jet (same flow conditions as in Figure 4.1.6)

4.1.3 Mean Turbulent Quantities

Mean u, v Fluctuations

The rms values of the two components of velocity fluctuations on the centerline of the jet are shown in Figure 4.1.8. Both u' and v' varies sharply along *x* away from the jet. These values are normalized using the local centerline velocity. The variation of both u' and v' confirms the same trend as observed by many researchers. The variation of u' with *x* has been observed to depend on the initial boundary layer at the jet exit. Hill [*Hill* 1976] and Bradshaw [*Bradshaw* 1966] found that when the initial boundary layers are laminar, u' increases sharply near the exit, reaches a maximum, then decreases, and increases again gradually. Krothapalli [*Krothapalli* 1979] observes that this type of behavior is present in jets that have a laminar boundary layer at the exit plane and which go through a transition before it becomes a turbulent jet. On the other hand, when the boundary layers are turbulent, u' varies monotonically with *x*. In the present case, the initial boundary layer is turbulent. As can be expected, the magnitude of v' is smaller than u'. v' shows a similar behavior as u'.

Several investigators have observed that coherent large-scale structures in the jet shear layer when the exit boundary layer was laminar. When the exit boundary layer was turbulent, such structures that could be observed through simple visualization techniques were not observed. This is not to say that there would not be any structures, but that they are poorly correlated spatially and temporally. We illustrate this with two PIV images in Figure 4.1.9. The image in the left has a laminar initial layer and the one on the right is turbulent. It is very clear from the images that the image on the left has large recognizable vortices while the image on the right doesn't have organized structures even though presence of non-coherent structures is evident from the variations of the image seeding intensity.

Figure 4.1.10 and 4.11 show the contours of u' and v' along with extracted profiles at downstream X/D_j=3 and 7. The profiles indicate that until $8D_j$ downstream of the exit, geometrical similarity has not been achieved. Closer to the jet exit and near the axis, both u' and v' have low turbulence and starts increasing very sharply away from the axis. It reaches a maximum before declining. The maximum is approximately near the half-width of the jet. At sufficient distance far away from the exit, the axial turbulence level catches up with the turbulence level in the shear layers. Considering the profiles at $7D_j$, we can conclude that u' is much closer to achieving similarity than v'. At $7D_j$, v' has a much larger deficit in the jet core than u'. In a subsonic turbulent jet, fluctuations in the radial component take a longer distance to reach similarity. While the axial component reaches similarity at $X/D_j > 40$, radial component reaches similarity at $X/D_j > 70$. The radial component is lower than the axial component in all regions of the flow field. Turbulence quantities are important parameters in determining the mixing characteristics of a jet. Higher turbulence intensities can be directly related to a higher mixing performance. Variation of the total turbulence intensity $(u'^2+v'^2)^{1/2}$ is shown in Figure 4.1.12. The steepest increase in turbulence intensity is along the centerline of the jet. This will have a direct effect on the rate at which the centerline velocity decays.

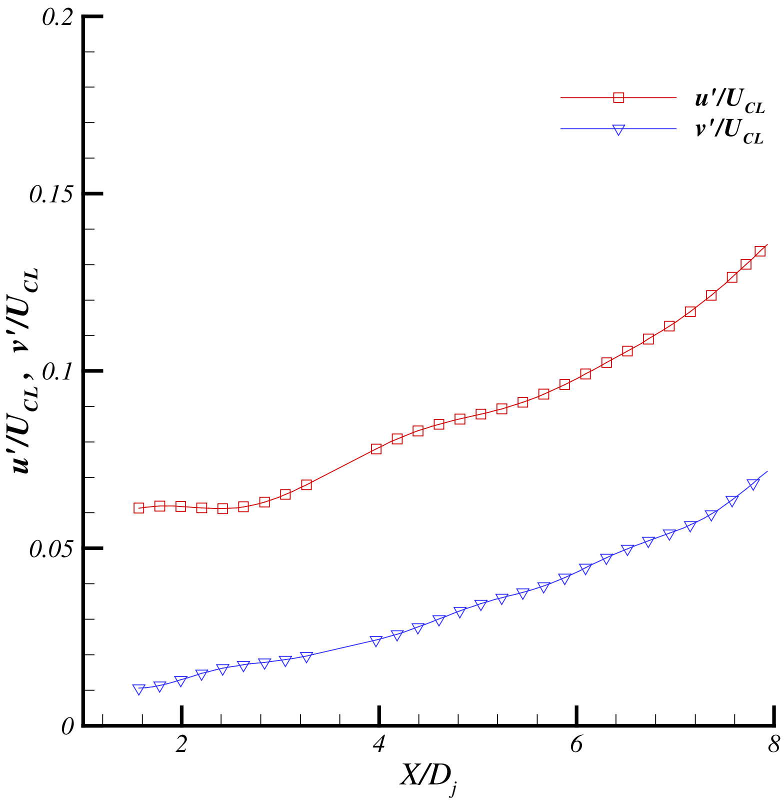

Figure 4.1.8. Velocity fluctuations along the centerline of the baseline axisymmetric jet

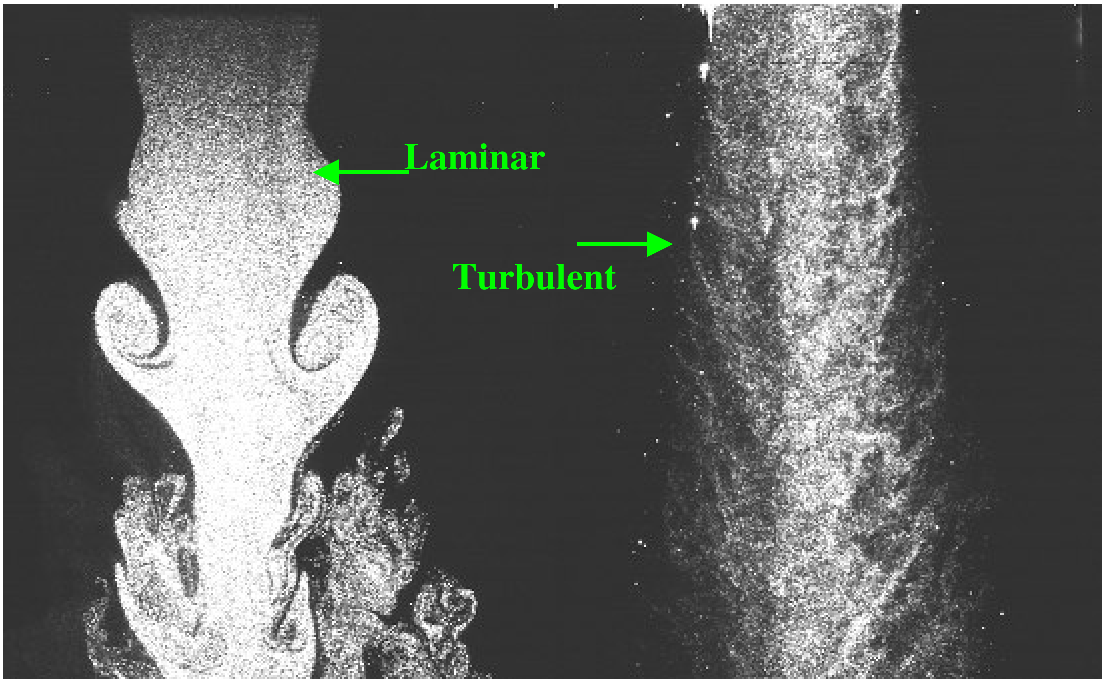

Figure 4.1.9. Coherent structures in laminar and turbulent jets (Δt for both images = 0.8 μs)

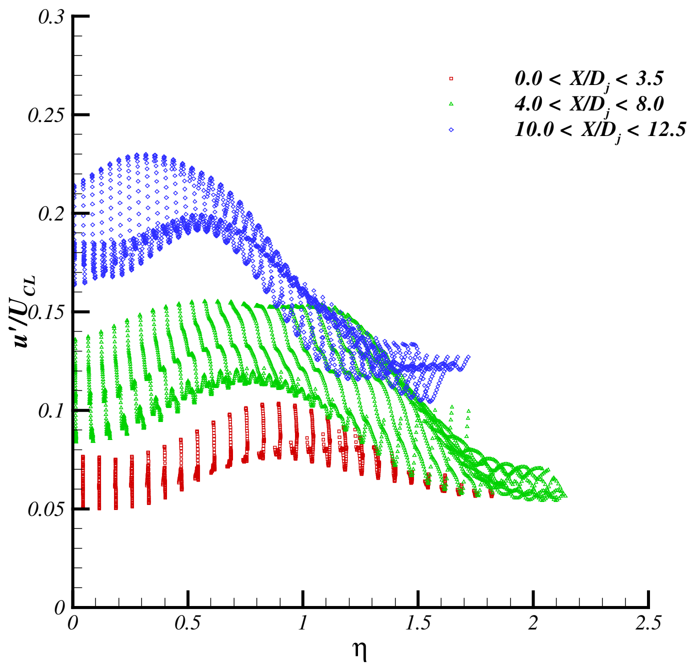

Figure 4.1.10. Axial velocity fluctuations for the baseline axisymmetric jet

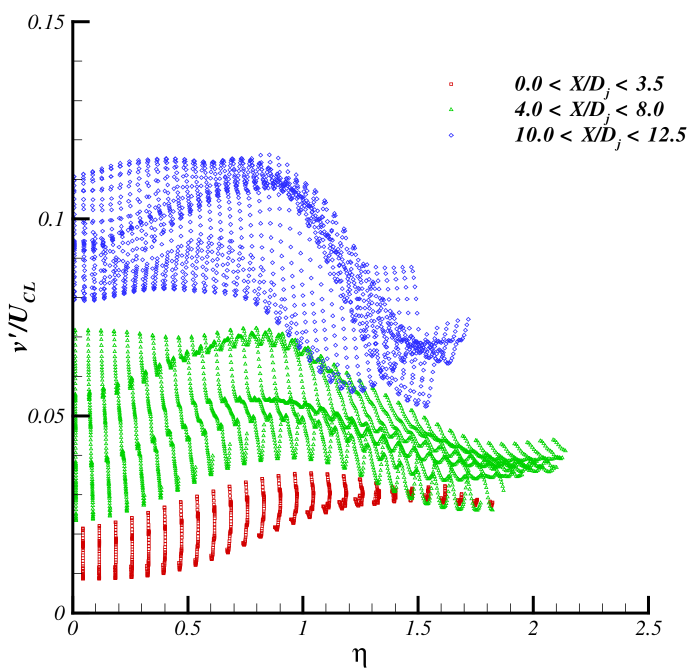

Figure 4.1.11. Radial velocity fluctuations for the baseline axisymmetric jet

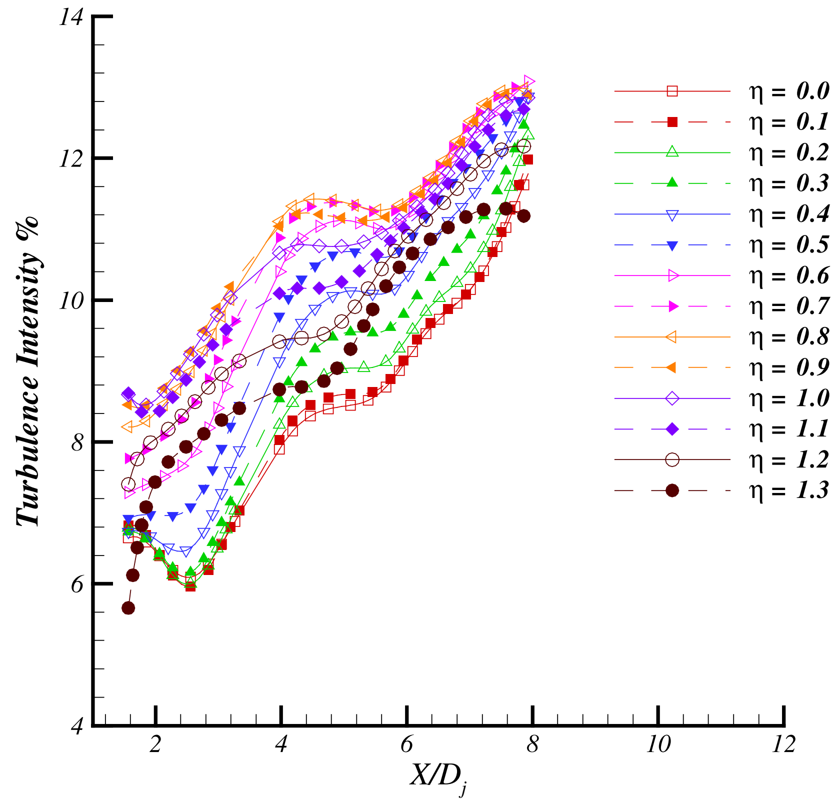

Figure 4.1.12. Percent turbulent intensity variation in the axial direction for a baseline axisymmetric jet

As mentioned earlier, a rapid decay of U_{CL} indicates enhanced mixing. Increased mixing should also advance the location where self-similarity is achieved in different quantities.

Turbulent Shear Stress

The normalized turbulent shear stress (Reynolds stress) at different downstream locations is shown in Figure 4.1.13. The stress values are normalized with respect to the square of the local centerline velocity. Extracted profiles at locations $1D_j$, $2D_j$ and $3D_j$ are shown in the insert. As with u' and v', the turbulent shear stress has not reached self-similarity within the measurement region. An explicit expression for the shear stress can be obtained by inserting the time-averaged profiles for U and V into the streamwise momentum equation.

$$\frac{\overline{u'v'}}{U_{CL}^2} = \frac{c}{2\eta}\left(\exp\left(-\eta^2\right) - \exp\left(-2\eta^2\right)\right)$$

This profile is also shown in the insert in Figure 4.1.13. The maximum for Reynolds stress lies at $\eta = 0.58$. The shear stress near $\eta = 0$ is negligible for a jet having a 'top hat' shaped profile at the exit or a Gaussian profile in the self-similar zone. The velocity gradient in the crosswise direction for these profiles, $\partial U/\partial y = 0$ within the potential core region and consequently the Reynolds stress is negligible. However, in the vicinity of $\eta=0$ and near the exit, we observe a linear distribution of the shear stress in the experimental data. This is consistent with the expected linear distribution for a pipe flow type profile with finite velocity gradients at the centerline.

Kinetic Energy

The mean kinetic energy and the turbulent kinetic energy given by $[(U/U_j)^2+(V/V_j)^2]/2$ and $[(u'/U_j)^2+(v'/U_j)^2]/2$ are shown in Figure 4.1.14. The mean kinetic energy decreases away from the exit while the turbulent kinetic energy increases. The mean kinetic energy possesses a maximum along the centerline and drops off away from it whereas, the turbulent kinetic energy possesses a maximum away from the center and a minimum at the center for some distance away from the exit after which it catches up with the turbulence level in the edges. This also illustrates in a single picture the way energy is transferred between different regions of the jet.

Estimation of Momentum Thickness

The boundary layer displacement thickness, δ^*, is defined as

$$\delta^* = \int_0^{y_{99\%}} \left(1 - \frac{\rho U}{\rho_{CL} U_{CL}}\right) dy$$

and the momentum thickness, θ, as

$$\theta = \int_0^{y_{99\%}} \frac{\rho U}{\rho_{CL} U_{CL}} \left(1 - \frac{U}{U_{CL}}\right) dy$$

and ρ/ρ_c was found using the adiabatic relationship

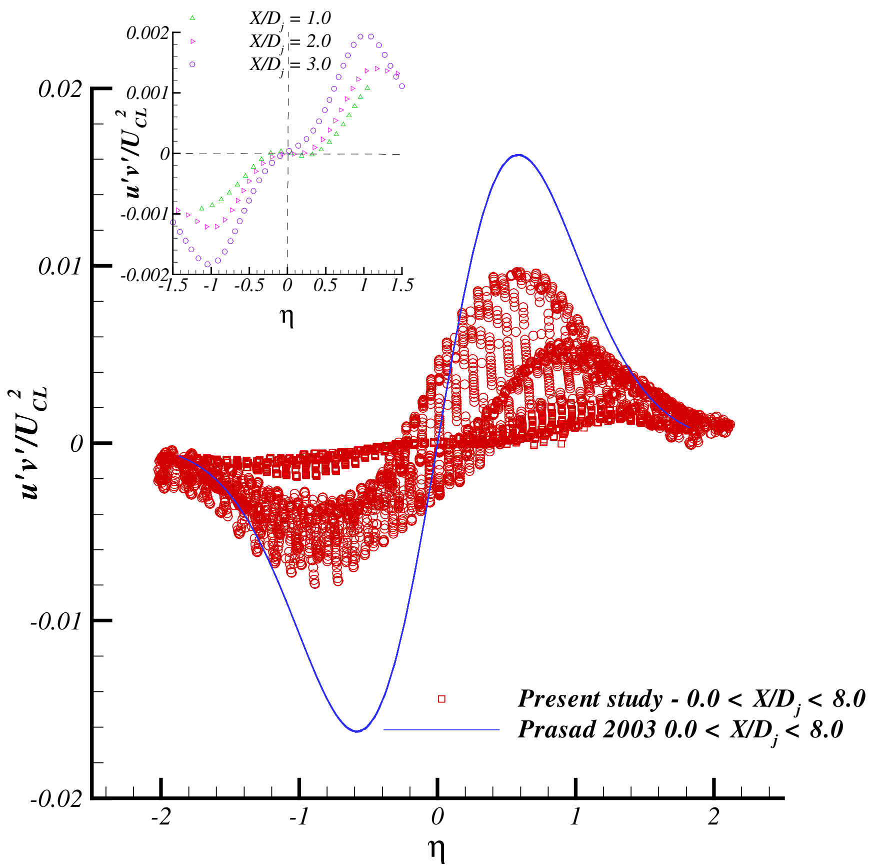

Figure 4.1.13. Turbulent shear stress profile for the baseline axisymmetric jet

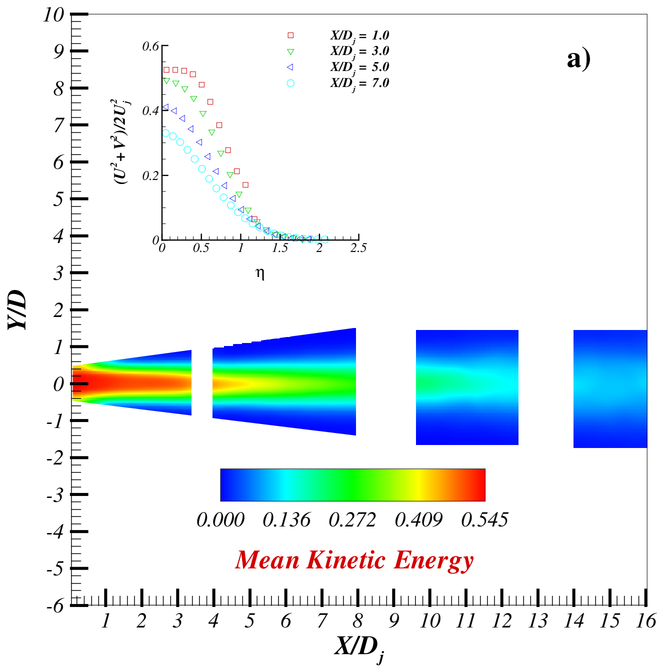

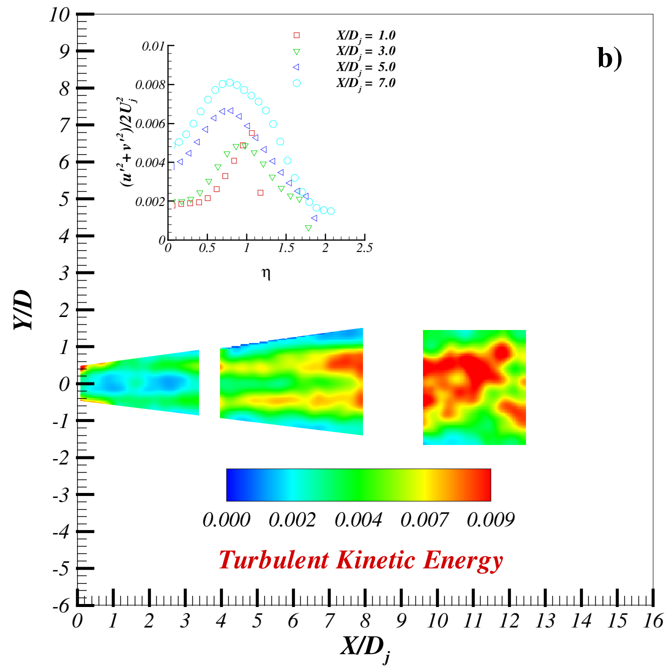

Figure 4.1.14. Kinetic energy contours and profiles for the baseline axisymmetric jet. a) mean kinetic energy b) turbulent kinetic energy

$$\frac{\rho}{\rho_{CL}} = \left(\frac{1 + \frac{\gamma - 1}{2} M_{Cl}^2}{1 + \frac{\gamma - 1}{2} M^2} \right)^{\frac{1}{\gamma - 1}}$$

The shape factor H is then defined as $H = \delta^* / \theta$.

The centerline velocity is used to estimate the local momentum thickness instead of the jet exit velocity. Figure 4.1.15 shows the growth of momentum thickness from $2D_j$ to $8D_j$. It shows the linear growth of the momentum thickness. It is expected that momentum thickness grows linearly right from the exit. Making velocity measurements using PIV at the exit is not possible for some configurations like the orifices because of the bevel. The exit momentum thickness could be found by fitting a straight through these points. For this case the value of θ/D_j at $X=2D_j$ is 0.14. As expected, this value is larger than that of a jet originating from a contoured nozzle. A larger initial shear layer thickness results in an increased potential core. As mentioned earlier, the initial shear layer instability frequency is inversely proportional to the boundary layer thickness.

Spectral Decay

Spectra from velocity components are used to study the presence of temporally coherent structures. Since we do not have a large uniformly spaced velocity data set (temporal) that would allow us to study its spectra using conventional methods, we rely on the near field acoustic data. Figure 4.1.16 shows the spectral decay obtained from a microphone placed at different downstream locations equidistant from the jet axis ($Y/D_j = 4$). Spectra of the first four locations ($X/D_j = 3, 5, 7$ and 9) are also shown separately. The first data point near the exit at $3D_j$ has a maximum at $St_D = 0.48$. This lies within the expected range for the column/preferred mode of a jet (0.2-0.5). The important feature is that the preferred mode is present even though the boundary layer from the exit may be turbulent at separation and is incapable of undergoing successive vortex merging characteristics of the thin shear layer. Further downstream the peak shifts towards lower frequencies. This indicates that energy is being transferred to progressively larger scales away from the exit.

4.1.4 Instantaneous Flow Field

Visualization of vortices

We now turn our attention towards the instantaneous flow field of the pipe jet. One of the important reason for studying instantaneous fields is the realization of the existence and crucial role played by large-scale, organized motions in turbulent flow in recent years. But, these structures are usually embedded in a seemingly random flow field. Therefore, it is important to have methods that could identify and quantify these structures and also allow us to understand the way they interact with the rest of the flow field. There are several methods available to educe structures out of a flow field. One method may be more desirable than another depending on the information that is sought (understanding statistical interrelationships or contribution of small

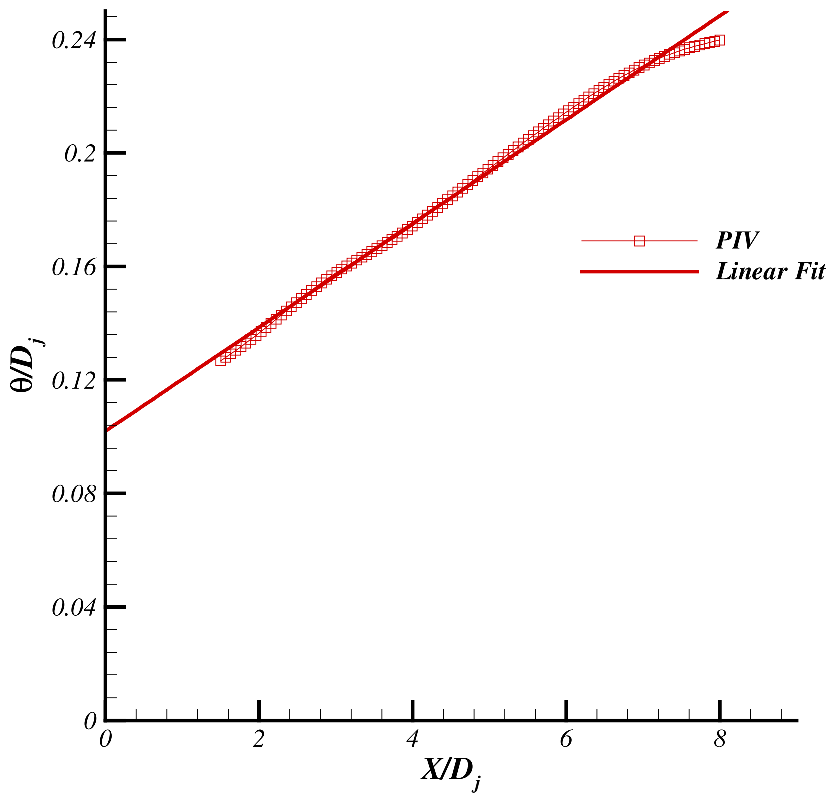

Figure 4.1.15. Momentum thickness growth for the baseline axisymmetric jet

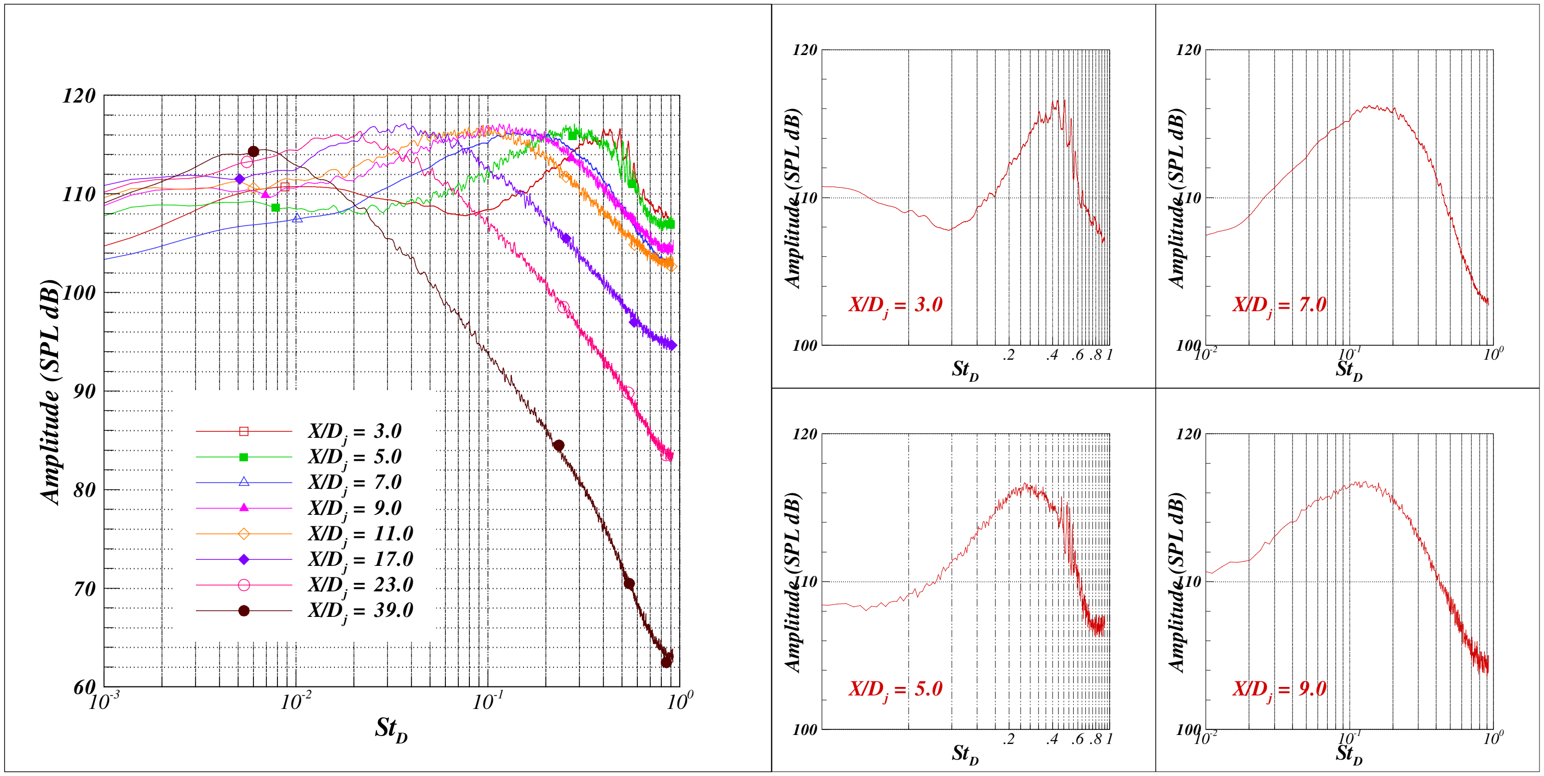

Figure 4.1.16. Spectral decay in the streamwise direction for the baseline axisymmetric jet (enlarged view of the first 4 locations also shown)

scale structures to the stresses on large-scale structures or understanding the coherent elements of the flow). And, often it might be necessary to use more than one method in tandem to validate the results or obtain more complete information. Some of the commonly used methods include:

a. Vorticity
b. Reynolds decomposition
c. Galilean decomposition
d. Swirling strength

Other methods used include LES decomposition and critical point analysis, Wavelet analysis / Pattern recognition techniques and Proper Orthogonal Decomposition methods. Before further discussing the instantaneous flow field of the pipe jet, some of the methods mentioned above are illustrated using a sample from this dataset. After much discussions, the fluid dynamics community has yet to arrive for a consensus on the definition of a vortex or an eddy. But a widely used definition especially in terms of identifying structures is the one offered by Kline and Robinson [*Kline and Robinson*, 1999]. "*A vortex exists when instantaneous streamlines mapped onto a plane normal to the core exhibit a roughly circular or spiral pattern, when viewed in a reference frame moving with the center of the core*". The two key conditions in this definition are that the reference frame must be moving with the center of the core and vorticity is concentrated in the core. In a turbulent field, many small-scale structures are embedded within large-scale structures. Based on the above definition, it would be possible to visualize such a vortex only if the velocity at the center of each small vortex is removed.

Vorticity

Vorticity is the most common method of studying rotational fields. In simple flows with vortices but negligible shear, vorticity directly gives the location and other estimates of the vortex (size, strength, etc.). However, in complex flows, such as in jets, shear is a significant part of the flow field and more often the vortex structures themselves are located within this shear regions. In such cases it is extremely difficult to identify vortices and to assess their contribution to the overall flow. Figure 4.1.17 shows a sample image in which eddy structures are present in a region of shear. Figure 4.1.17a shows the vorticity map and Figure 4.1.17b shows the corresponding velocity vectors. Examining the vorticity map shows that there are regions of very high vorticity in the shear layer. This could possibly imply the presence of a vortex core. But the region has comparable values of vorticity throughout the length. By examining the vorticity map and velocity vectors alone, one cannot conclude that there are eddies present within the shear layer. Reliable statistics about eddies cannot be obtained.

Galilean Decomposition

This is the simplest method of decomposition. A constant independent of space and time equal to the convection velocity of the vortices is removed from the vector field. Using the correct convection velocity will reveal vortices as described by the definition for vortices. Figure 4.1.18a-d shows the same vector field decomposed using different convection velocities (0.2, 0.4, 0.6, 0.8 the spatial average of the centerline velocity). Since all three vortices are of similar scale,

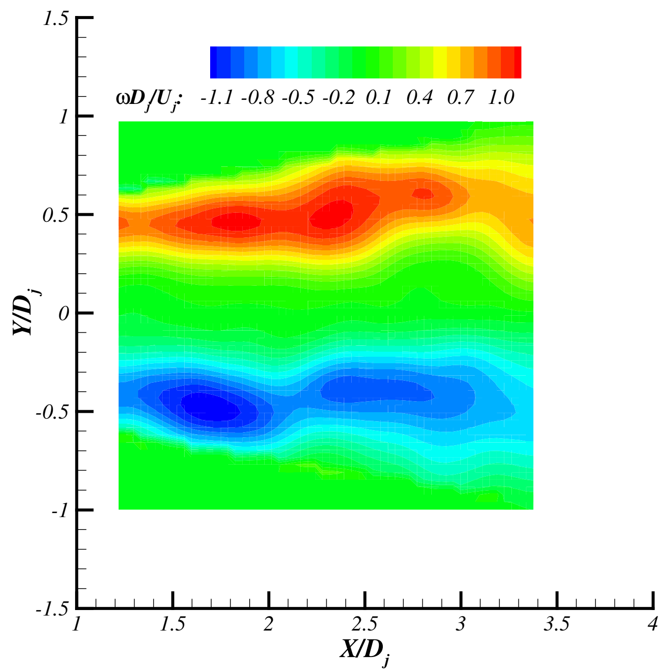

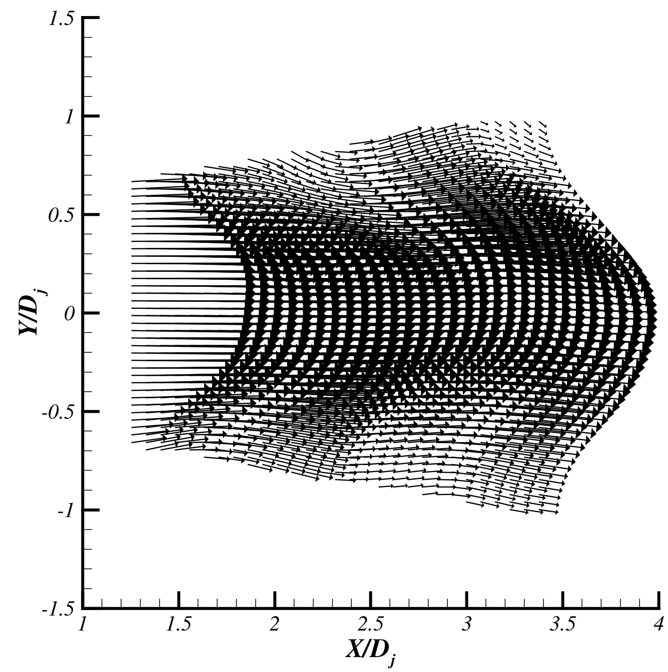

Figure 4.1.17. Vortex identification based on vorticity

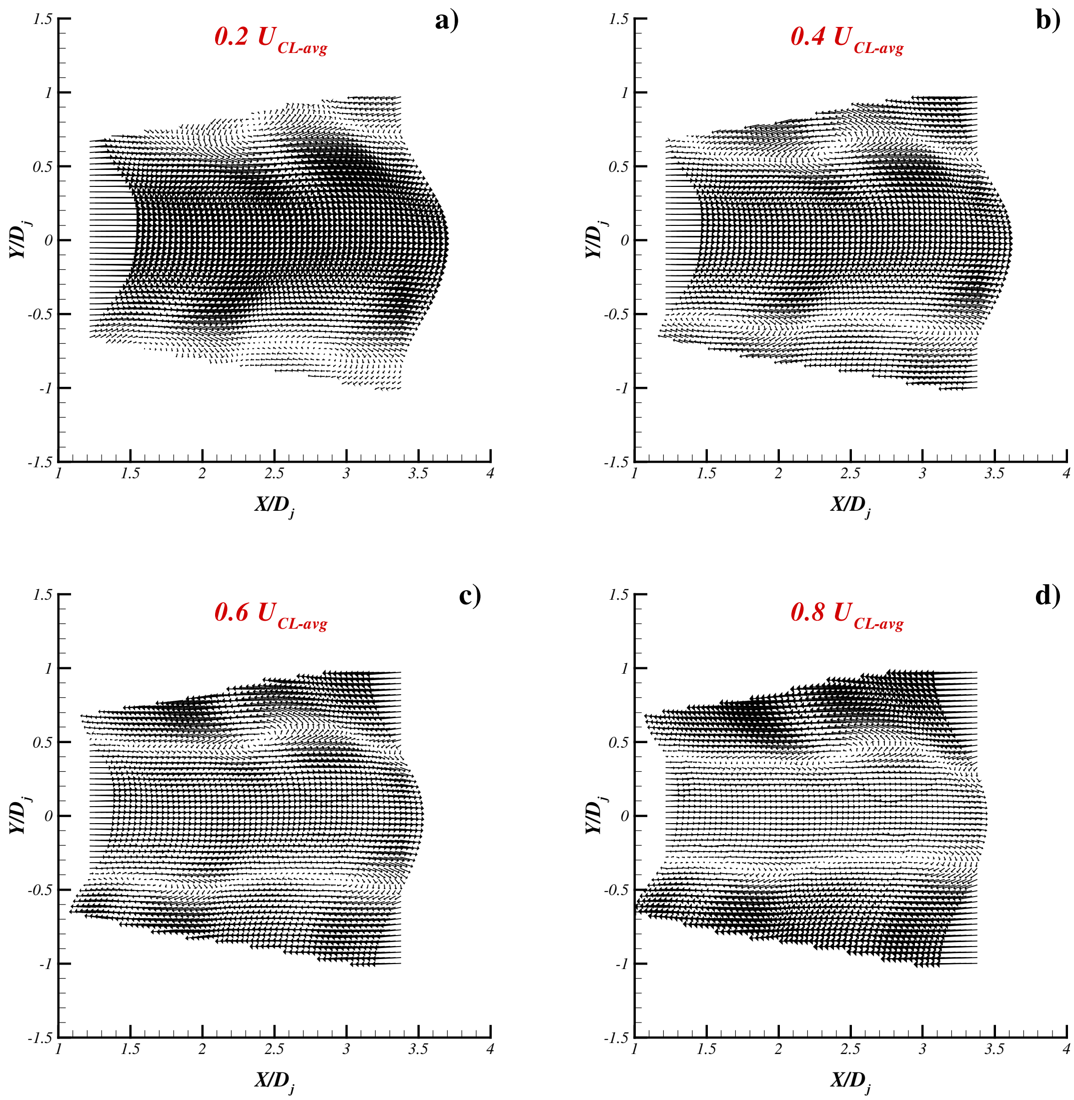

Figure 4.1.18. Vortex identification using Galilean transformation. a) 0.2 $U_{CL\text{-}avg}$ b) 0.4$U_{CL\text{-}avg}$ c) 0.6$U_{CL\text{-}avg}$ d) 0.8$U_{CL\text{-}avg}$

all are visible at the same time. In cases where different scales are present different convection velocities would reveal different vortices. Even though detection of vortices is not too sensitive to the convective velocity selected, the location and size of the vortex are very sensitive as can be seen from the figure. It clearly demonstrates this method's dependence on a correct reference frame. However, the advantage in this method is its simplicity and its ability to reveal most of the vortex cores if the velocity field is systematically cycled through different convection velocities.

Swirling strength

Vortex identification based on swirling strength is a frame independent method. It does not need a correct reference frame to visualize vortices. In three dimensions, the local velocity gradient tensor will have one real eigenvalue (λ_r) and a pair of complex conjugate eigenvalues ($\lambda_{cr} \pm\lambda_{ci}$) when the discriminant of its characteristic equation is positive. For this condition, particle trajectories exhibit a spiraling motion about the eigenvector corresponding to λ_r with a period λ_{ci}^{-1}. For pure shear flow, the particle trajectory is an infinitely long ellipse and hence the time period is infinite corresponding to $\lambda_{ci} = 0$. $\lambda ci > 0$ represents shorter and more circular ellipses, which are, eddies. Zhou [*Zhou et.al.*, 1996,1999] show that the strength of any local swirling motion is quantified by λ_{ci}, defined as the swirling strength. In addition to being frame independent, this method can also differentiate between pure shear and vortex structures. In a two dimensional velocity field, the reduced local velocity gradient tensor is

$$\begin{bmatrix} \frac{\partial u}{\partial x} & \frac{\partial u}{\partial y} \\ \frac{\partial v}{\partial x} & \frac{\partial v}{\partial y} \end{bmatrix}$$

In this case, the local velocity gradient tensor can have either two real eigenvalues or a pair of complex conjugate eigenvalues. And, vortices could be easily identified by plotting iso-regions of $\lambda_{ci} > 0$. When further reduced, we have the condition used,

$$\sqrt{\left(\frac{\partial v}{\partial y}+\frac{\partial u}{\partial x}\right)^2 - 4\left[\left(\frac{\partial v}{\partial y}\frac{\partial u}{\partial x}\right)-\left(\frac{\partial v}{\partial x}\frac{\partial u}{\partial y}\right)\right]} \quad > \quad 0$$

Figure 4.1.19a shows contours of the swirling strength shown in the relation above. Very strong swirling values are present at the expected locations of vortical structures. To check whether we can see vortices as per previous definition, we subtract the velocity at the center of these high swirling strength regions. Figure 4.1.19b shows vectors corresponding to vortices at each location. Figure 4.1.19c shows the iso-lines of swirling strength superimposed on vorticity contour. Vorticity identifies some of the vortices clearly (see the lower left eddy) but is not very clear regarding the other vortices. Also vorticity identifies local shear layers and does not differentiate them from coherent structures. This makes swirling strength method a very useful tool to identify eddies and calculating reliable vortex statistics. In this study, swirling strength will be used to identify eddies and the educed vortices will be validated by using local Galilean

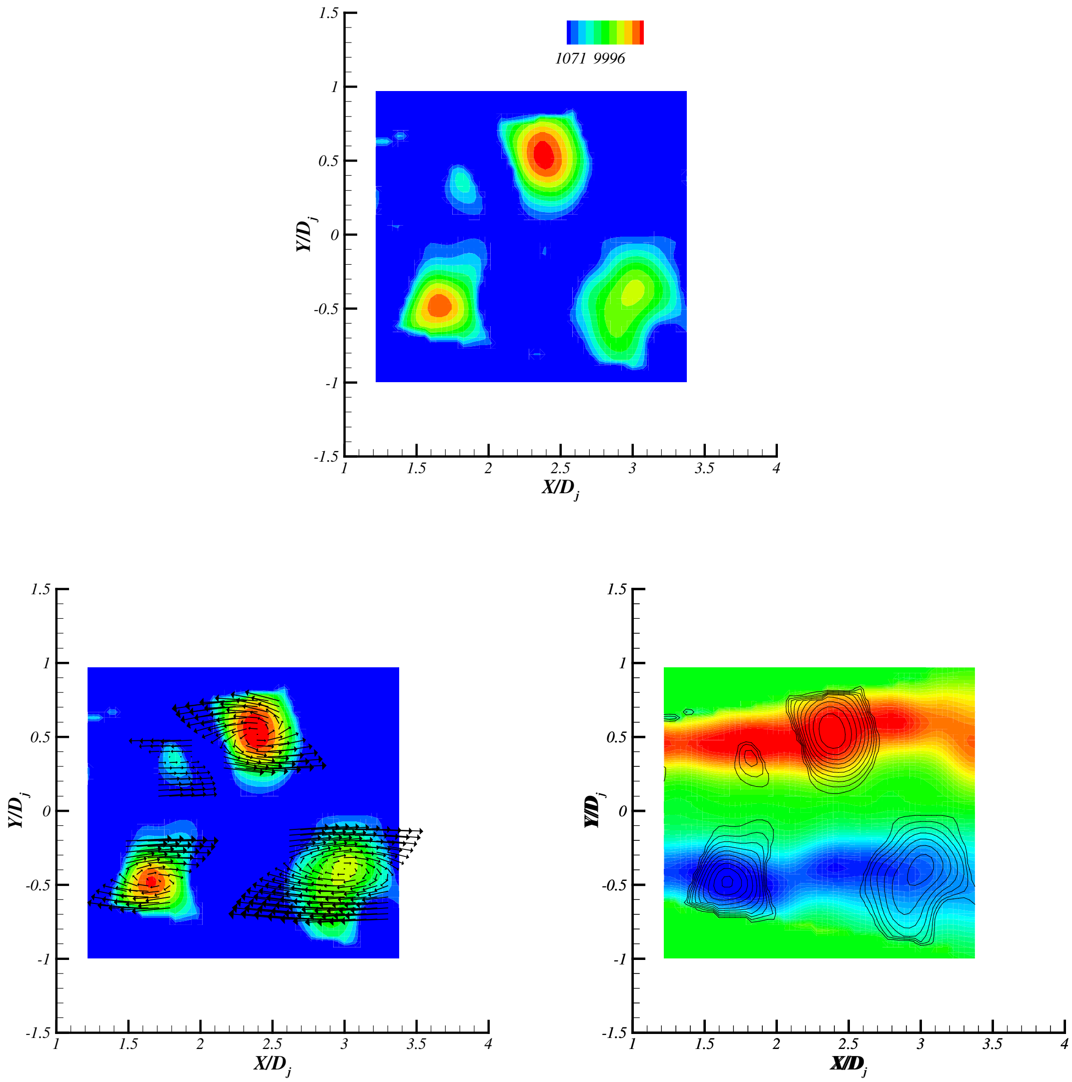

Figure 4.1.19. Vortex identification using frame independent swirling strength calculations

decompositions. Though it is possible to calculate detailed vortex statistics using this method, it is beyond the scope of this work at this time.

Reynolds Decomposition

This is the classical method of decomposing a turbulent velocity field. The total velocity vector $\vec{u}$ can be decomposed into two different portions having different scales of length or time given as:

$$\vec{u} = \vec{U} + \vec{u}'$$

where, $\vec{U}$ is the mean of the total velocity obtained by ensemble averaging, time averaging or spatially averaging in a statistically homogeneous direction, and $\vec{u}'$ is the fluctuating field. Depending on the averaging method, Reynolds decomposition can be viewed as decomposition by scale separating components of infinite time or space scale and components of lesser scales in time or space. Vortices frequently move at velocities close to the local mean velocity and by removing the mean velocity, vortices of different scales can be visualized. Figure 4.1.20 shows the fluctuating component of the Reynolds decomposition obtained by using a spatial average (velocity averaging was done in a direction normal to the direction of the component) on Figure 4.1.17. It shows the three expected vortices. One of the disadvantages of Reynolds decomposition is that it removes large-scales features associated with the flow. It can be very useful when statistics about the small-scale fluctuations are needed.

Organizational Modes and Vortical Structures

In this section, some of the naturally occurring processes that help mixing in a turbulent jet are examined.

Ring and Helical Modes

Several studies [*Michalke* 1977, *Batchelor* 1962] have predicted the presence of ring and helical modes in axisymmetric jets. Batchelor [*Batchelor* 1962] has shown that only the helical mode can produce amplified disturbances. Michalke [*Michalke* 1977] has shown that both ring mode and helical mode are equally unstable. Figure 4.1.21a-f show the presence of ring type vortices throughout the measurement region. The velocity fields have been Galilean transformed to educe the vortex structures. A constant velocity was removed from all fields rather than using different velocities optimal for each vortex. Figure 4.1.21a-b shows region between 0 - 4D_j. Figure 4.1.21c-d shows region between 2 - 6D_j. Figure 4.1.21e-f shows region between 4 - 8D_j. The locations of the vortices are noted as A-A to K-K. In Figure 4.1.21b, vortex ring C-C is visible partially. The sizes of the vortex rings are comparable in size to the local jet width. At least three different vortex rings are visible within the potential core. Figure 4.1.22a-f shows the presence of helical mode vortices present in the near field measurement regions. The vortices are marked A-Q. Figure 4.1.22a-b shows region between 0 - 4D_j. Figure 4.1.22c-d shows region between 2-6D. Figure 4.1.22e-f shows region between 4 - 8D_j. In both axisymmetric and helical modes, there is some evidence suggesting that the distance between the vortices increases

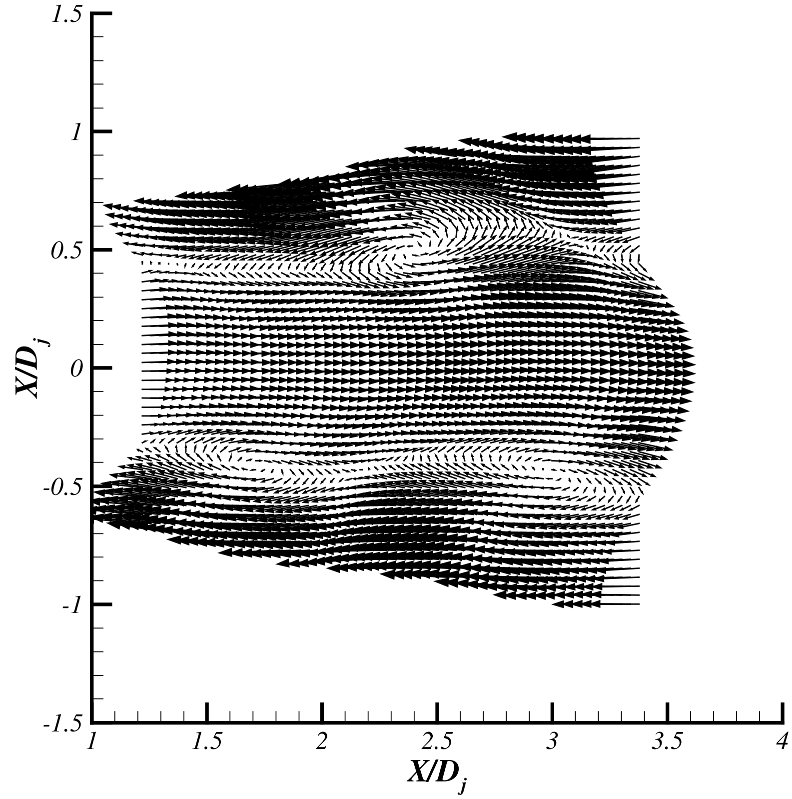

Figure 4.1.20. Vortex identification using Reynolds decomposition

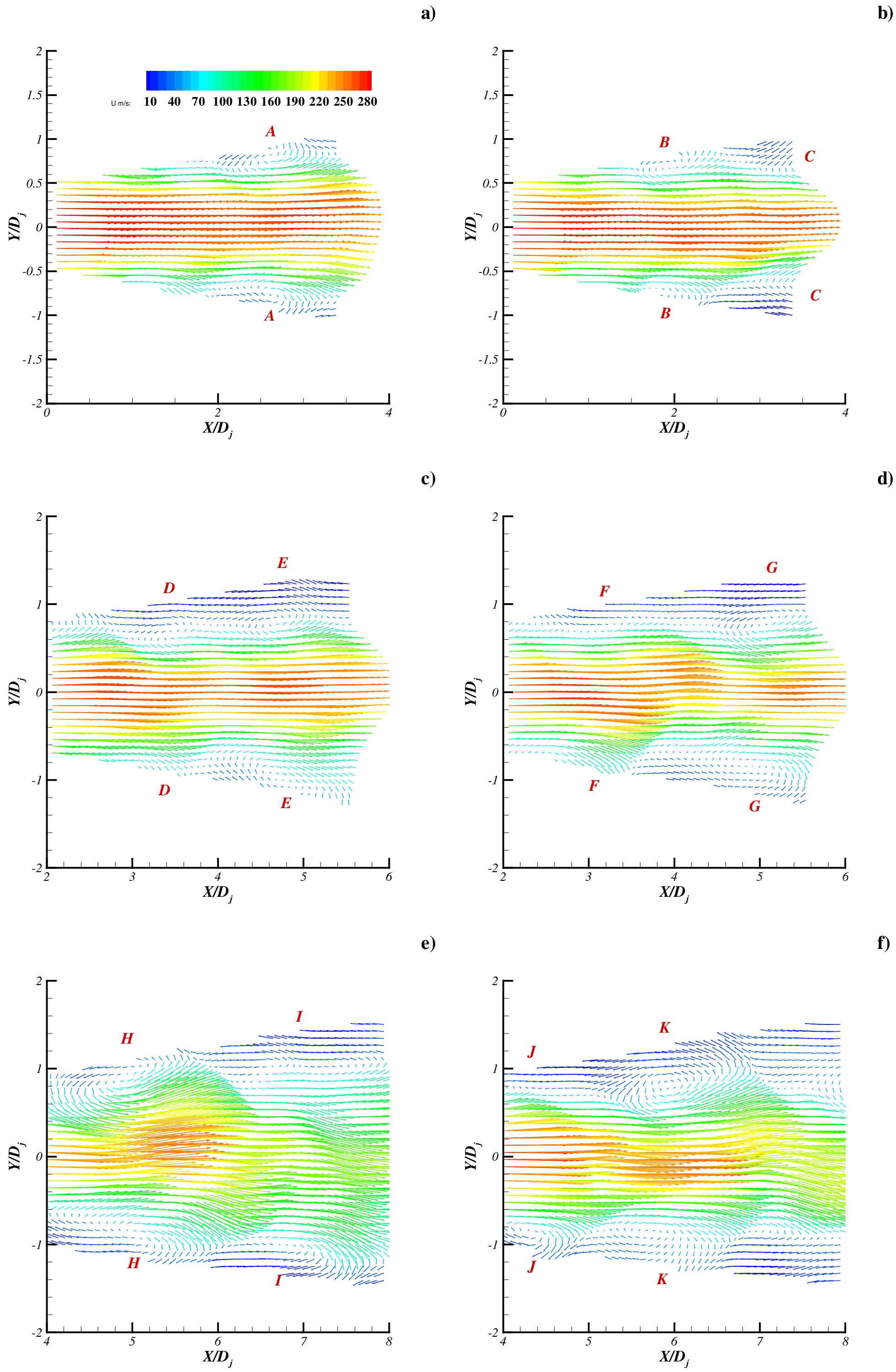

Figure 4.1.21. Ring mode vortices present in the near field of the baseline jet

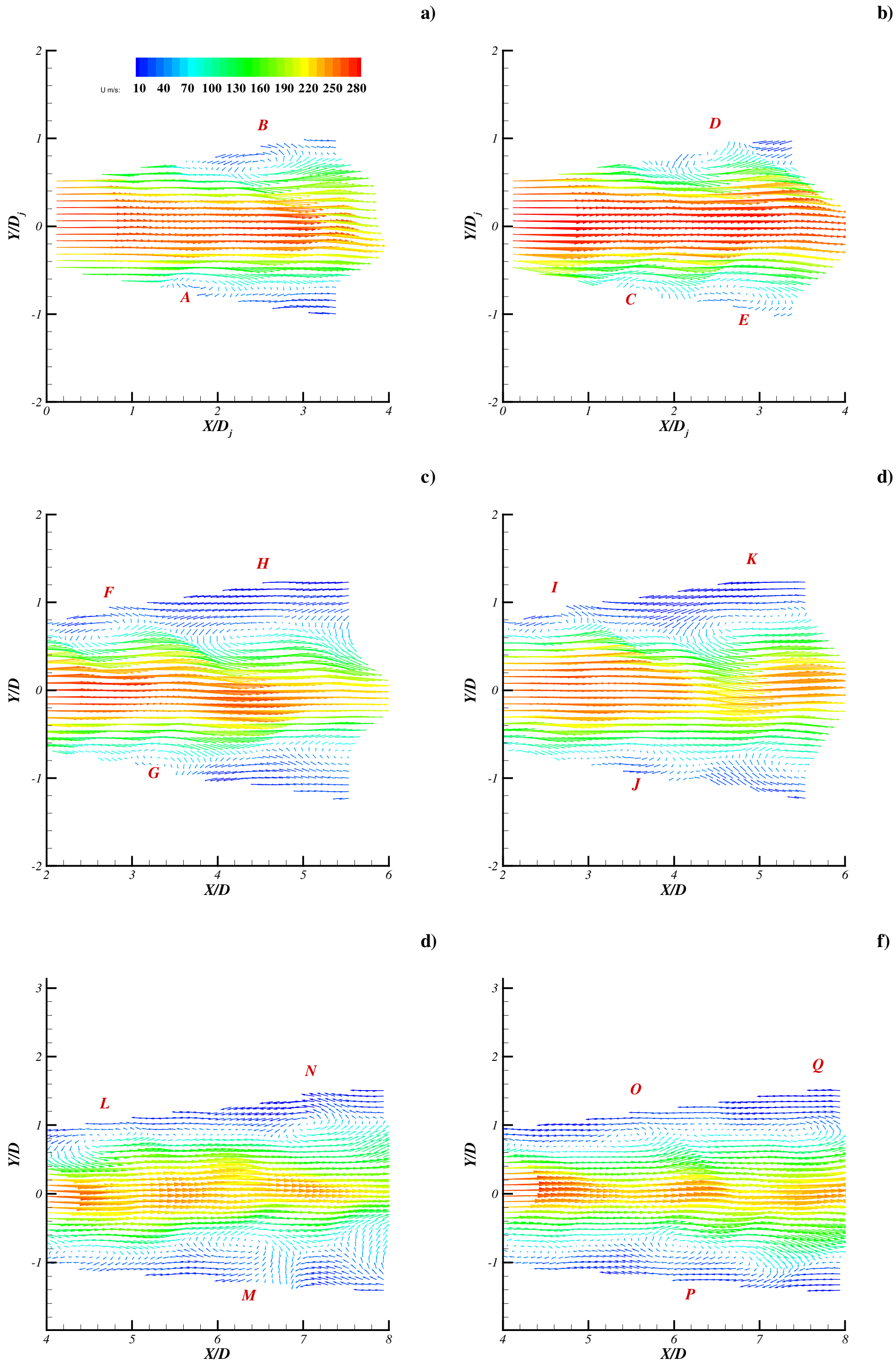

Figure 4.1.22. Helical mode vortices present in the near field of the baseline jet

downstream. In unforced jets, axial and helical modes have equal probability of occurring and a thorough examination of the dataset shows that it is much easier to find helical mode than ring mode. Also, in some cases, an initially axisymmetric ring tilts in one direction due to its own induction or of an adjacent vortex. Other researchers have also described the presence of such structures. These type rings would also be counted as helical modes and probably skewed the probability of occurrence towards helical modes.

The presence of ring or helical modes is important from the viewpoint of mixing or momentum transfer. They play an important role in bringing ambient fluid in contact with the jet fluid. This is the first step in any type of transfer (mass, momentum or energy). Two possible mechanisms of the process or rather the effect of these vortices is described below. Figure 4.1.23a-b show the first process. Figure 4.1.23a shows the actual velocity field and Figure 4.1.23b shows the Galilean transformed field. They show conical or arrowhead shaped structures present in the flow field. At the base of each conical structure, Figure 4.1.23a shows a large influx of fluid into the jet and this influx increases downstream. Figure 4.1.23b confirms the presence of vortex rings at the base of these structures. This indicates that the large influx caused by the vortices forces these arrowhead structures or vice versa. Figure 4.1.24a-b show a second process called jet meandering. Figure 4.1.24a shows the actual velocity field and Figure 4.1.24b shows the Galilean transformed field. Jet meander refers to the movement of the whole jet away from the centerline. It is similar to flapping motions in non-circular jets. As can be seen from Figure 4.1.24a, this process also produces large influxes into the jet much larger than the previous one. Figure 4.1.24b shows the Galilean transformed field and the vortices associated with this process. From this figure, it seems that the interaction of azimuthal instabilities with an axial instability could be responsible for this process.

Vortex merging

Several experiments have shown vortex merging as the mechanism that causes the shear layer to grow and produce momentum transfer. It has also been shown that vortex merging can produce pressure disturbances that will propagate upstream to force the shear layer forming a feedback loop. This feedback mechanism is governed by the feedback equation

$$\frac{X_i}{\lambda_{DPW}} + \frac{X_i}{\lambda_{UPW}} = N$$

where, X_i is the location of the i^{th} vortex merging from the trailing edge, λ_{DPW}, λ_{UPW} are the downstream and upstream propagating waves given by U_c/f_i, a/f_i respectively, U_c is the convection speed of the vortices, a is the speed of sound, f_i is the frequency after the i^{th} merging, and N is an integer. At each vortex merging the frequency is halved. Therefore,

$$f_i \approx f_o / 2^i$$

where, f_o is the initial instability frequency. This gives a relation between the i^{th} and the $i-1^{th}$ merging locations.

$$\frac{X_i}{X_{i-1}} \approx 2$$

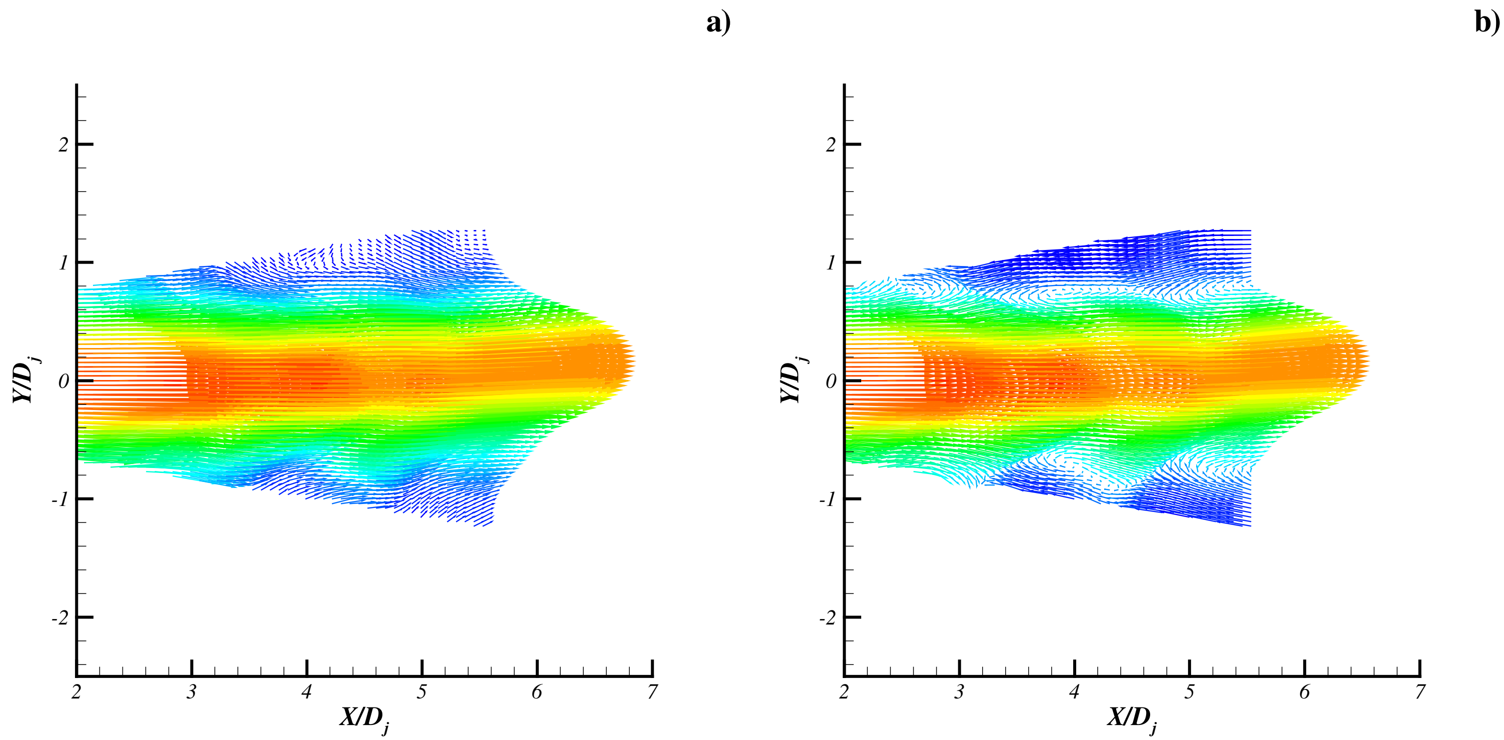

Figure 4.1.23. Arrowhead shaped structures in the near field of the baseline jet. a) actual vector field b) Galilean transformed vector field

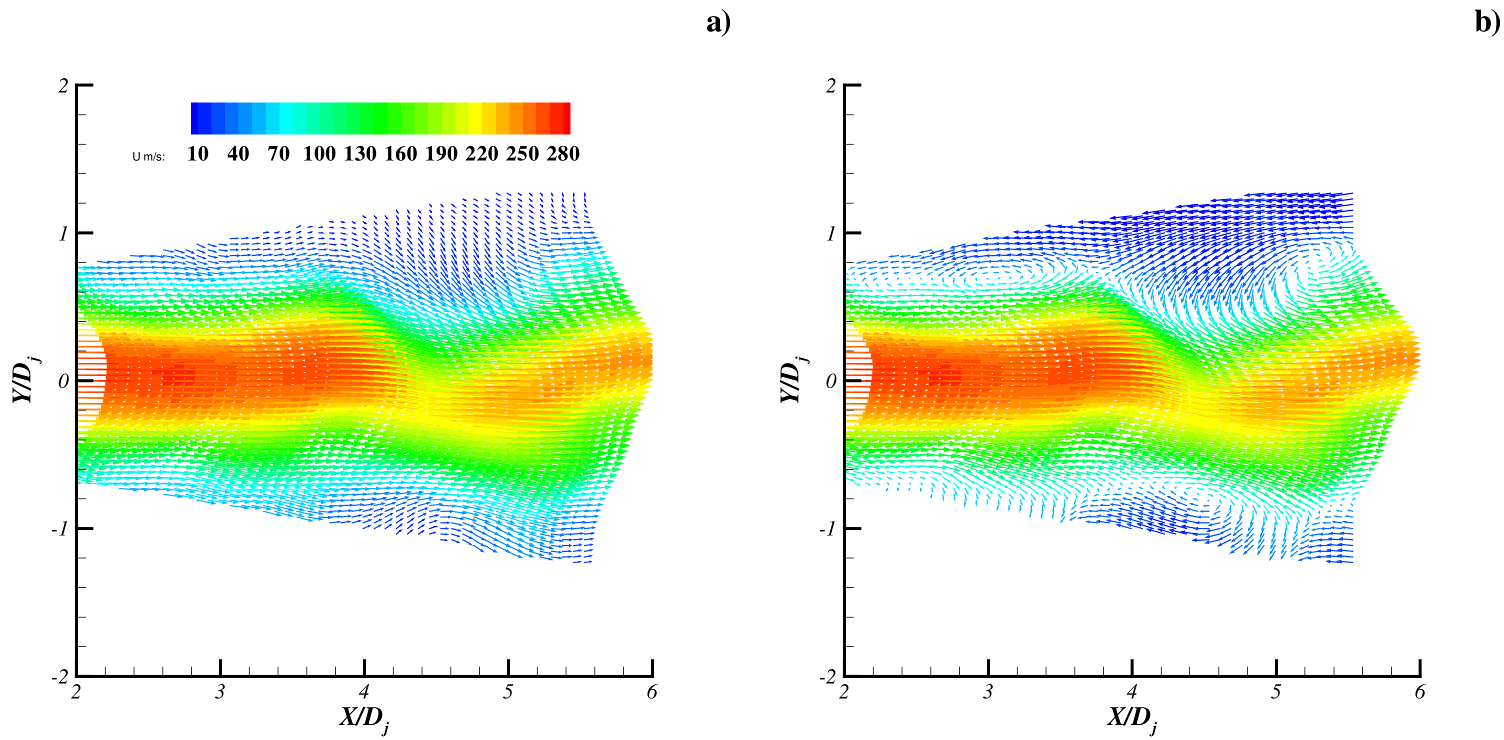

Figure 4.1.24. Jet meandering resulting in asymmetric velocity profiles in the near field of the baseline jet. a) actual vector field b) Galilean transformed vector field

This implies that the vortex merging locations has to be an even number of initial instability wavelengths. In an axisymmetric jet, the last vortex merging appear at the end of the potential core, which is approximately four to six exit diameters. For a potential core length of 5D, the next-to-last merging should take place approximately near 2.5D and the one before that near 1.25D. Figure 4.1.25a-f shows the shear layer thickness in the measurement regions. Normalized vorticity contours ($\omega D/U = -1$ to -0.4) representing one side of the shear layer is shown. Figure 4.1.25a-b show the first two merging locations. At the vortex merging locations, the thickness of the shear layer doubles. Figure 4.1.25c-f show the last merging location at the end of the potential core and also the subharmonic evolution introduced by Ho [Ho 1982]. The amplifying subharmonic laterally displaces vortices from the initial instability wave. Due to the velocity gradient, vortices within the high-speed region travel faster and catch up with the vortices in the low speed side. Finally, the two vortices merge into a single coherent structure. A set of carefully chosen images is shown in Figure 4.1.26 to demonstrate this process.

4.1.5 Effect of Initial Conditions

A smooth contoured nozzle is the preferred jet exit for most studies. But it involves a more difficult manufacturing process. Orifices are used in many studies because of the ease of manufacturing as compared to a contoured nozzle especially with noncircular exits. Long pipes are also a very common type of exit condition in practical applications. The initial condition of an orifice jet would be very different from that of a pipe jet or a contoured nozzle. Different studies have arrived at contradictory conclusions about the mixing performance of an orifice jet. Quinn [*Quinn* 1989] compared a smooth nozzle to an orifice and found that the jet from the nozzle spread much faster than the orifice jet. He suggested that non-parallel exit flow is the reason for this. Vakili and Chang [*Vakili* 1991] studied the effect of different exit conditions on the evolution of a vortex ring and found that a vortex ring from an orifice exit traveled further than a ring from a pipe jet. A deeper penetration of a vortex ring indicates less mixing (more suited for momentum transfer) with the ambient fluid and provides support to Quinn's study. Recently Mi [*Mi* 2001] compared a contoured nozzle, an orifice plate and a pipe and found that the orifice jet had the highest mixing rate followed by the contoured nozzle and the pipe jet. They also show that even though an orifice jet has less coherent structures than the contoured nozzle, the higher three dimensionality of the structures in the near field of the orifice jet is responsible for the increased mixing. This indicates that the performance of an orifice also depends on geometrical parameters other than the exit diameter. This would include the lip thickness, the angle and orientation of the bevel and the ratio between the orifice diameter and the diameter of the pipe to which it is connected.

Sample image frames from a pipe jet and orifice jet at very low speeds is shown in Figure 4.1.27a-b. Figure 4.1.27a is the pipe jet and Figure 4.1.27b is the orifice jet. Both show the same physical process of a shear layer rolling up into distinct vortex structures and breaking down after some distance. The difference is in the location at which the vortex structure rolls up and the features of the vortex. In an orifice jet, the first vortex structure rolls up almost at the exit itself

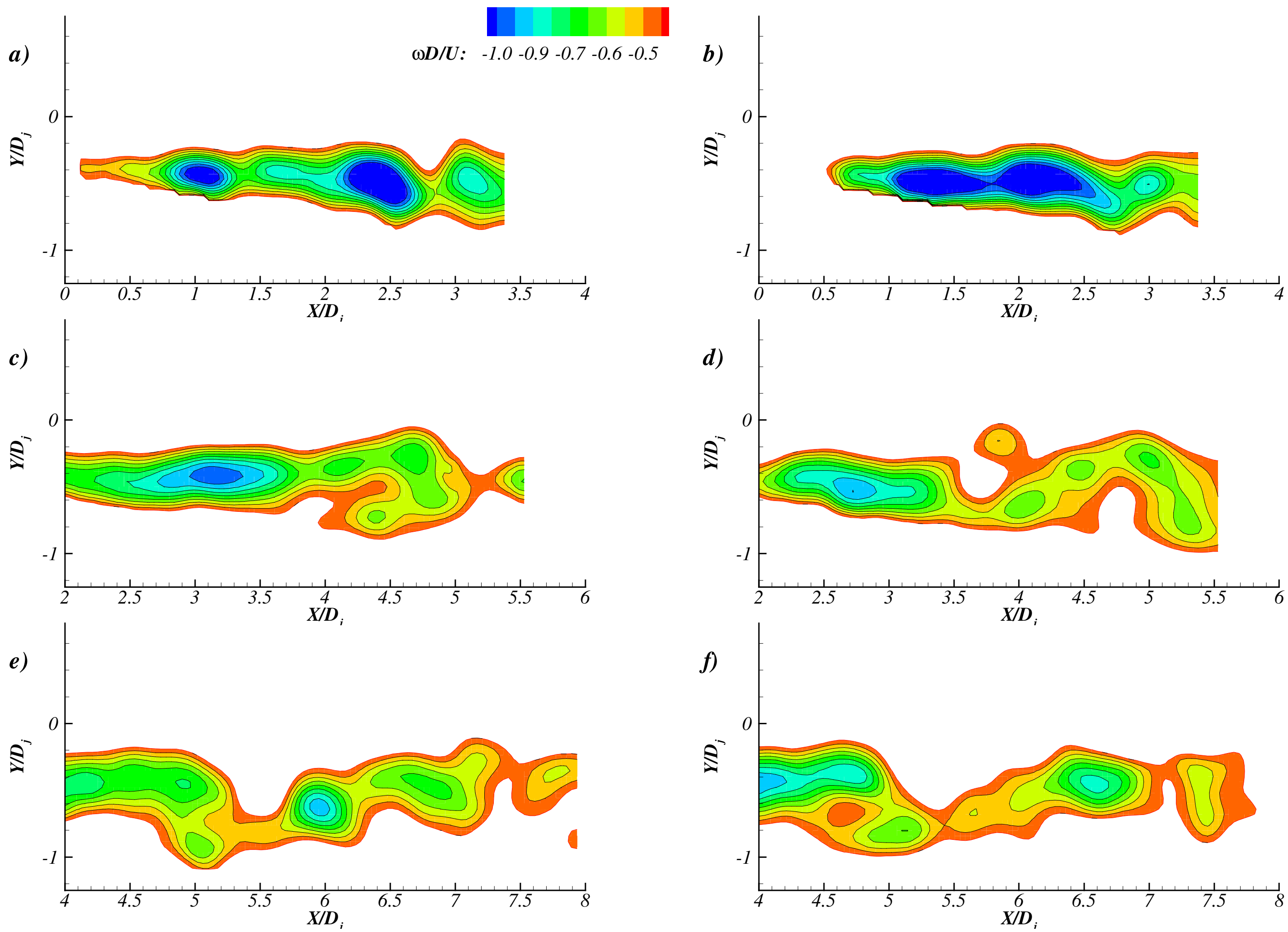

Figure 4.1.25. Instantaneous velocity fields showing vortex merging

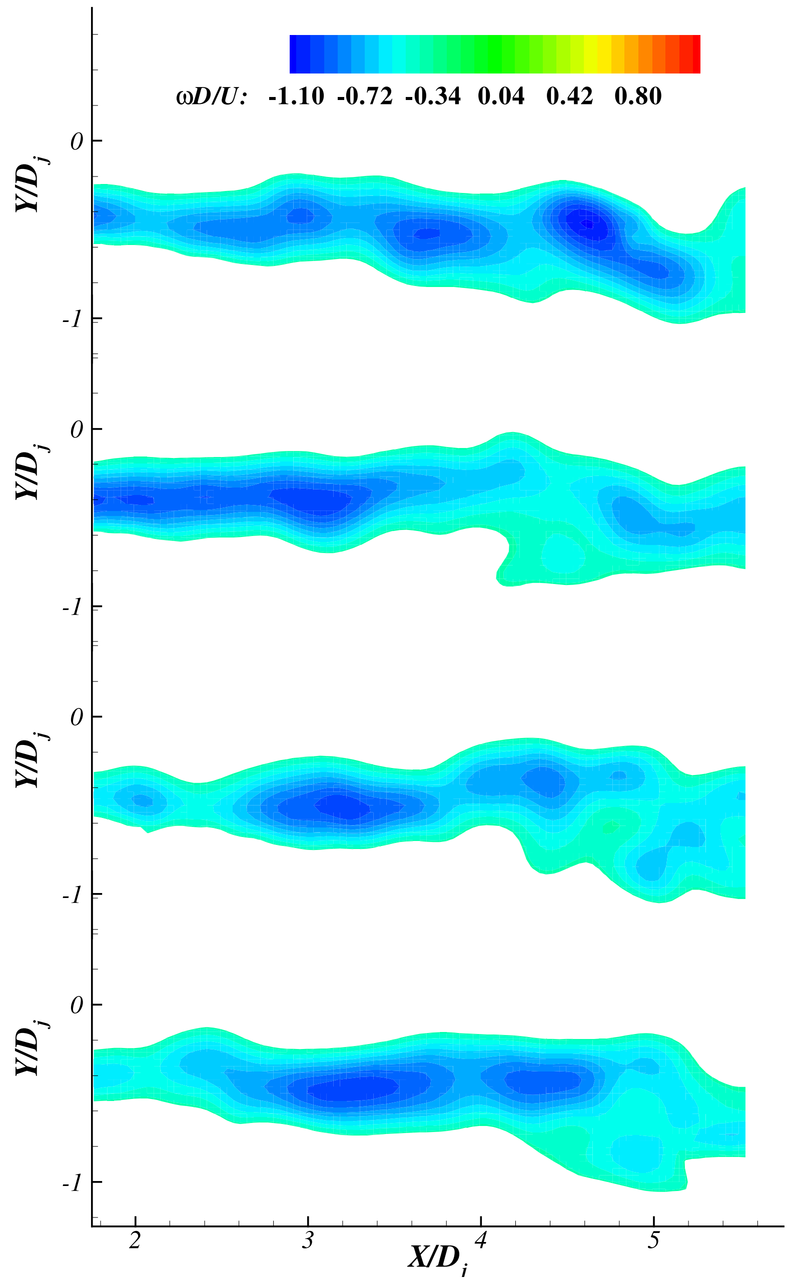

Figure 4.1.26. Sub-harmonic evolution

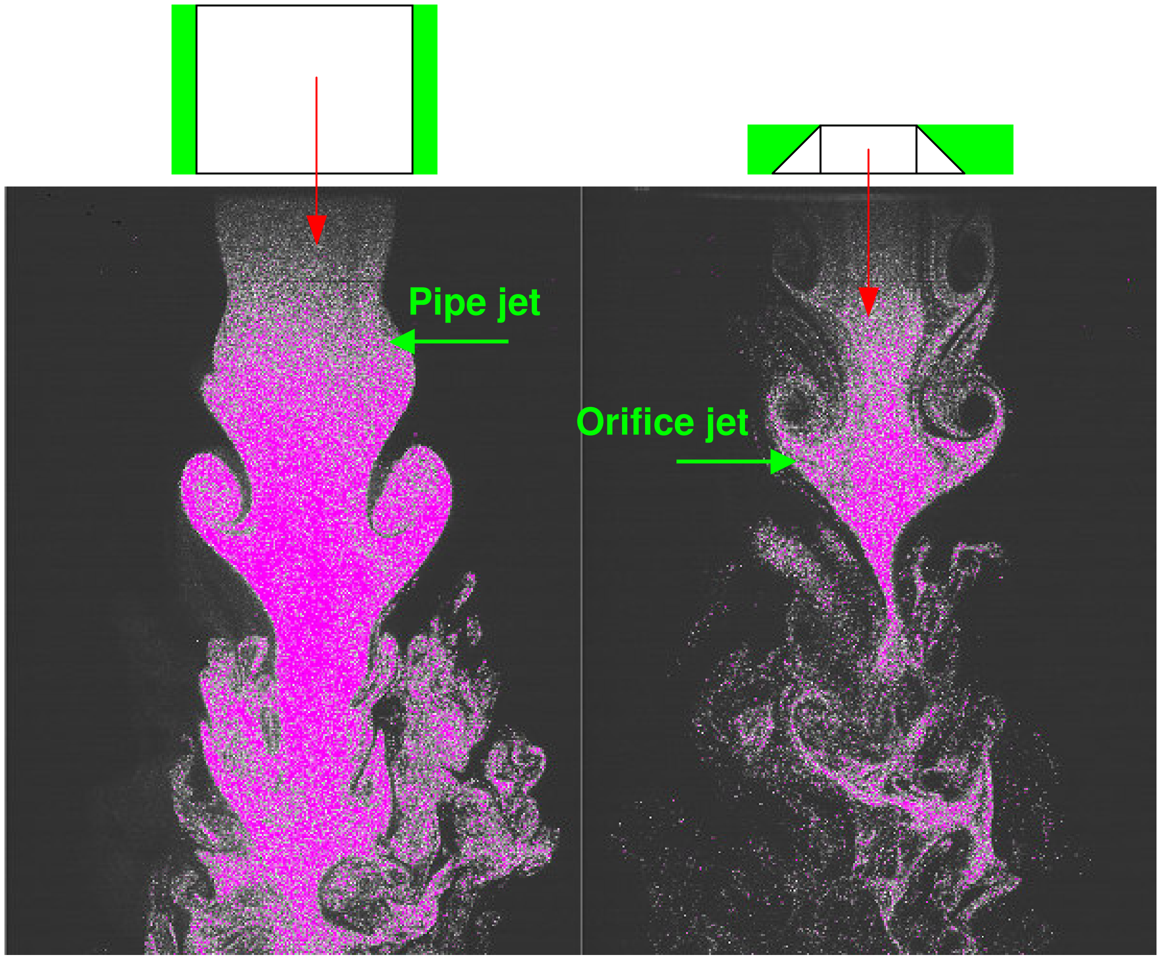

Figure 4.1.27. Comparison between a pipe jet and an orifice jet at low Reynolds number (both images were taken at similar Reynolds numbers)

whereas in the pipe jet, the first roll up is at some distance downstream. The vortex ring of the pipe jet is almost comprised of the jet fluid itself. The vortex ring of an orifice jet shows dark regions indicating a large amount of ambient fluid present within the vortex. There are two major differences between these two jets. The first difference is the thickness of the shear layer. A pipe jet has a much thicker shear layer than an orifice jet. A pipe jet has a thicker boundary layer because it has a growing boundary layer for some distance upstream of the exit. In an orifice jet, the boundary layer starts at the exit in addition to any effects of the boundary layer of the orifice plate walls. A thin shear layer is more unstable as compared to a thick shear layer. The second difference is due to the effect of vena contracta in an orifice. There is an increase in the velocity gradient that contributes to the out-of-plane vorticity. The initial vorticity available is more than what would be available in a pipe jet of similar upstream conditions. Also note the presence of arrowhead shaped structures discussed in previous sections in both jets and its sharpness in the orifice jet. The study of these images indicates that the orifice jet might have more mixing capability than a pipe jet.

Jets issuing from a pipe, an orifice, a contoured nozzle and an inverted contoured nozzle were studied. It has to be mentioned that the contoured nozzle is not a perfectly smooth nozzle. Due to manufacturing limitations, it was not possible to make a perfectly smooth nozzle. The nozzle had sudden changes in the slope. Figure 4.1.28a-c show averaged images of the above mentioned four configurations at about 275 m/s. Figure 4.1.28e-g show averaged images of the pipe, orifice and nozzle exits at about 130 m/s. The orifice jet shows a slightly larger lateral spread than the pipe jet. Some imperfection of the contoured nozzle is noticeable in the image near the exit. The initial profile does not look like that of a top hat profile expected for a nozzle and indicates possible separation. The effect of this was very clearly demonstrated when the nozzle was inverted. It generated multiple tones above certain velocities. Figure 4.1.28d,h shows this case at different velocities. Figure 4.1.28d is for 275 m/s and Figure 4.1.28h is at about 230 m/s, the velocity at which the screeching tones had their highest amplitude. In both cases the spread of the jet is much larger than any of the other configurations. Velocity contours normalized by their exit velocity for conditions corresponding to Figure 4.1.28a-d are shown in Figure 4.1.29a-d. The velocity contours have been truncated at 10% of centerline velocity. It confirms the same conclusions arrived at using the averaged images. The difference in the spread rate in the near field is very small as shown by the 10% and 90% profiles of the centerline velocity in Figure 4.1.30. Also note the centerline velocity dropping faster in the case of an orifice and even faster in the inverted nozzle. The profound effect of this screeching is shown in Figure 4.1.31 corresponding to the conditions of Figure 4.1.29h. The centerline velocity has fallen very rapidly and the potential core length has been reduced to less than one jet exit diameter. This process deserves further study not possible at this time. Because of this phenomenon, the contoured nozzle will not be used for comparison or as a baseline in evaluating the axial jet actuators. Between the pipe jet and the orifice jet, it was decided to use the pipe jet as the baseline for reasons mentioned in previous paragraphs regarding its sensitivity to geometrical parameters.

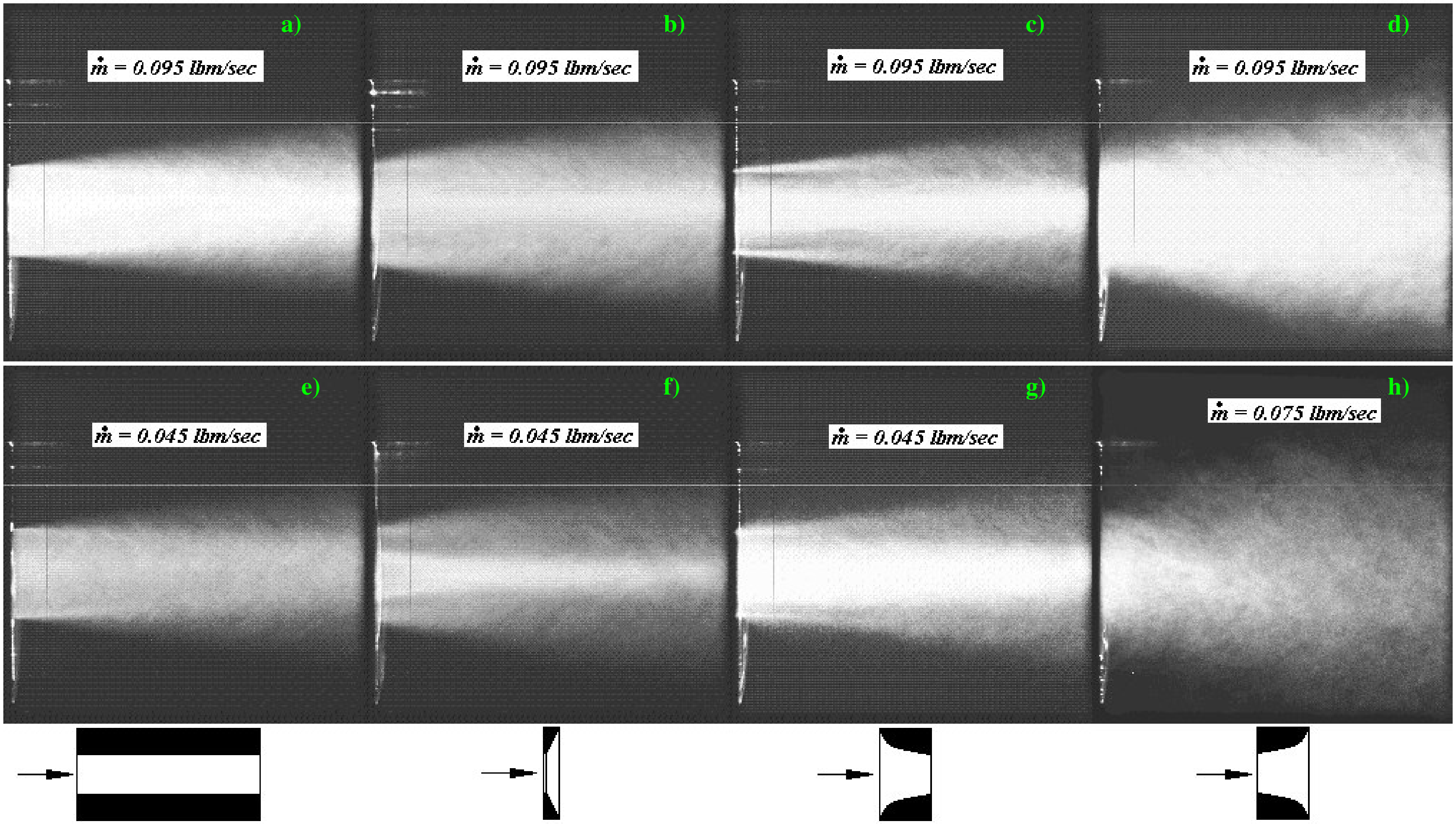

Figure 4.1.28. Averaged images of the baseline jet issuing from different exit boundaries at two different speeds. a-d) $U_J \approx 275$ m/s; e-g) $U_J \approx 130$ m/s and h) $U_J \approx 230$ m/s

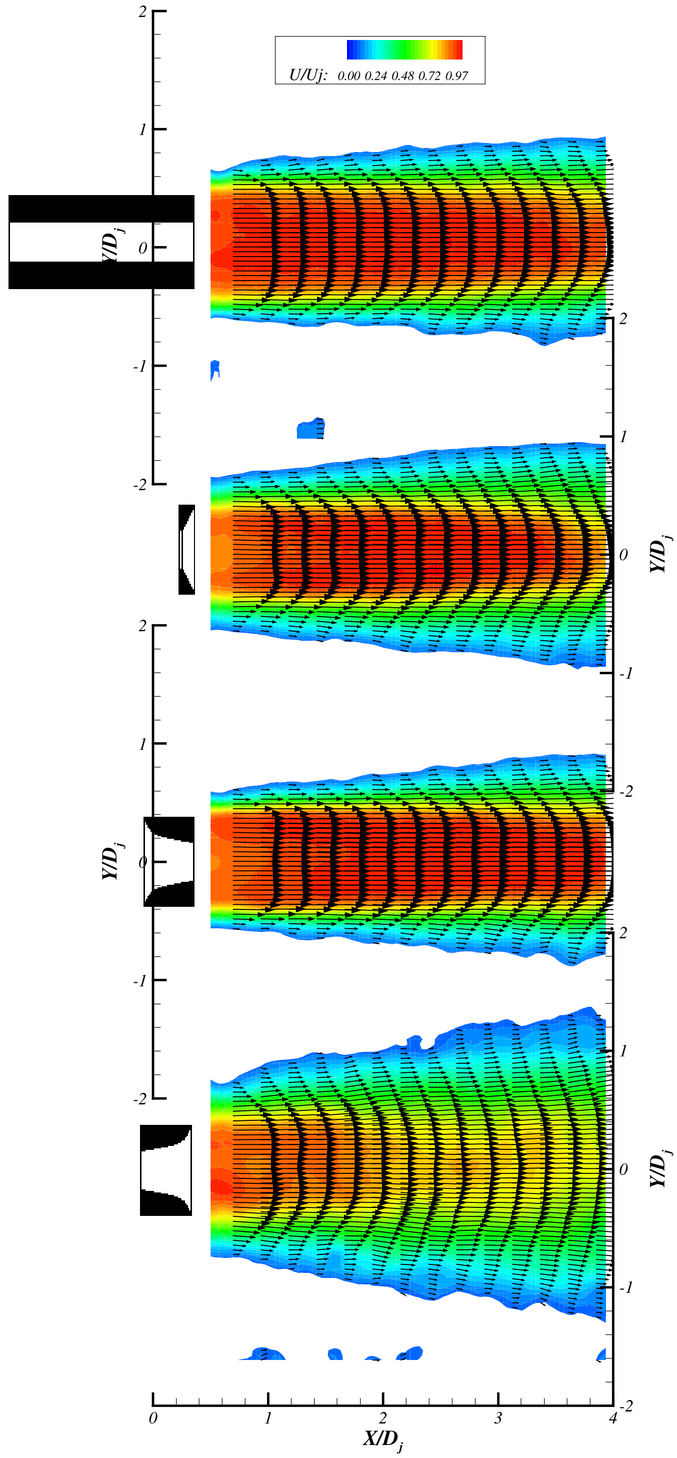

Figure 4.1.29. Normalized mean velocity contours of the baseline jet issuing from different exit boundaries ($U_J \approx 275$ m/s)

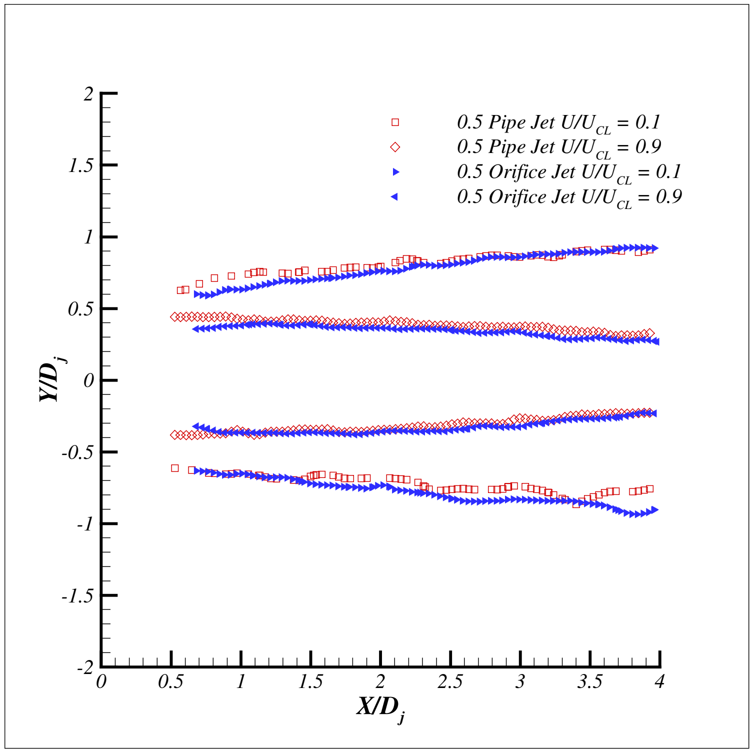

Figure 4.1.30. Comparison of the profiles of 10% and 90% centerline velocities for jets issuing from a short pipe and an orifice

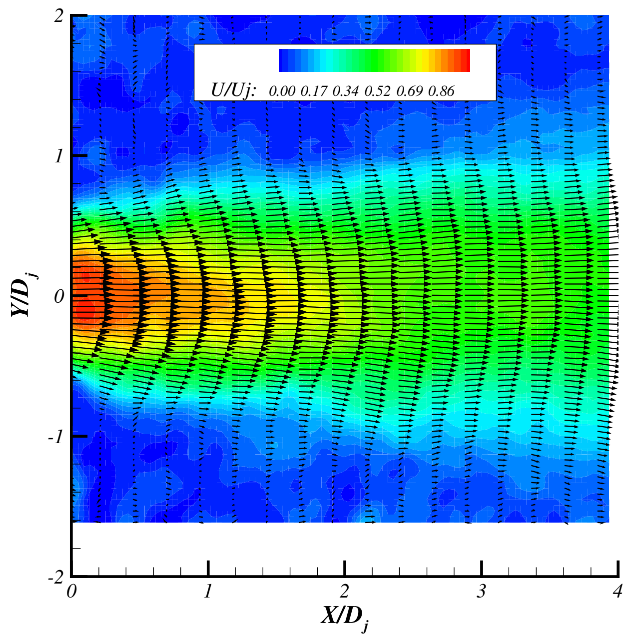

Figure 4.1.31. Mean velocity contours of a jet issuing from an expanding nozzle (condition corresponds to maximum screech – Figure 4.1.28h)

4.2 Hole Tone Actuator

4.2.1 Introduction

A hole tone is characterized by the instability of an axisymmetric jet forming vortex rings and the subsequent interaction of these vortices with a solid boundary in the flow field. A common example of this process can be observed in a whistling teapot. Vapor escaping from the teapot passes through two concentric circular orifices separated by a small distance. The first orifice produces a jet that has to pass through the second orifice. Whenever there is sufficiently high flow rate through the orifices, a discrete tone is produced. Another common example is the human whistling.

The first reported study of a hole tone is attributed to Sondhauss [*Sondhauss* 1854]. He found from his experiments that the tone frequency (f) increased with increasing jet velocity (U_j) and decreased with increasing length (L_c) between the orifices.

$$f \propto \frac{U_j}{L_c}$$

Rayleigh [*Rayleigh* 1945] studied hole tones as a convenient source to produce sounds of high frequencies (about 50000 Hz). Using dynamic and geometric similarity he showed that

$$f = \frac{U_j}{L_c} g\left(\frac{D_j}{L_c}, \mathrm{Re}\right)$$

$$where\ \mathrm{Re} = \frac{U_j D_j}{\upsilon}$$

He observed that the sound emitted was uniform through a wide angle indicating that the disturbance of the jet accompanying this emission is symmetrical. He also concluded that viscous forces could not play any major role in determining the frequency of the tone. He explained the process as follows. "*When a symmetrical excrescence reaches the second plate, it is unable to pass the hole with freedom, and the disturbance is thrown back possibly with the velocity of sound, to the first plate, where it gives rise to a further disturbance, to grow in its turn during the progress of the jet*".

Chanaud and Powell [*Chanaud & Powell* 1965] conducted a thorough investigation of the hole-tone mechanism over a range of L_c/D_j of 2 to 8 and upto a Reynolds number of 2500. They noted that the operation of a hole tone shows marked similarity to that of an edge tone with one major difference regarding the symmetric nature of the disturbances. In an edge tone, the disturbances are asymmetric. Figure 4.2.1 shows a schematic of the hole-tone system and Figure 4.2.2 shows the physical mechanism as proposed by Chanaud and Powell. Direct feedback is the pressure disturbance generated at the exit orifice. Indirect feedback refers to any reflecting mechanism present in the system. These feedback paths can be from upstream, downstream or from the radial boundaries of the system. Any one of the four feedback paths (1 direct and 3 indirect) can dominate and control the oscillations depending on their relative amplitudes. Similar to an edge tone, they concluded that the hole-tone both with and without indirect feedback would

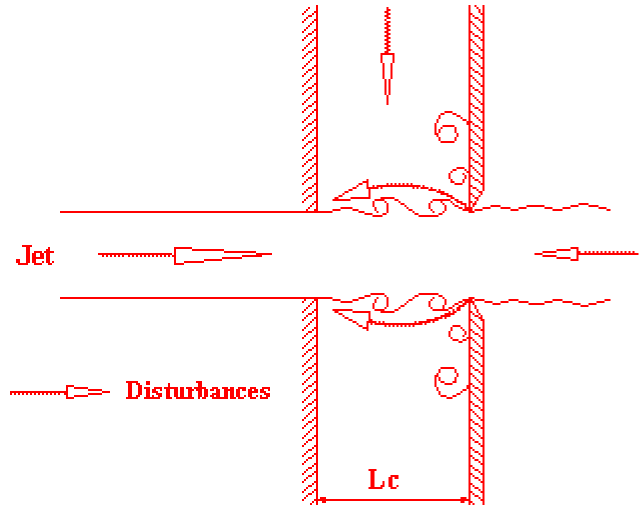

Figure 4.2.1. Schematic of a hole-tone system and its operation mechanism

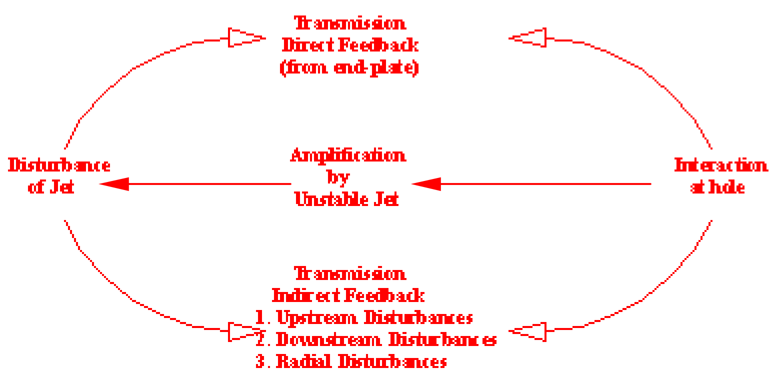

Figure 4.2.2. Possible feedback mechanisms in a hole-tone system (adapted from Chanaud 1965)

operate only within the unstable region of an axisymmetric jet. Thus, there is a minimum plate distance and a minimum velocity below which, the hole tone will not work. For a given plate distance, the frequency increases proportional to increasing velocity. At certain velocities, a sudden jump to higher frequencies occurs. And the frequency starts increasing with velocity until the next jump occurs. Each of this region of continuous operation is referred to as a stage. They also showed a hysterisis effect present in the operation of this system. When the velocity is decreased, frequency also decreases and falls back to lower stages at different velocities. But their jump to lower stages is not at the same conditions as their jump to higher stages. It is interesting to note that the Strouhal number based on the spacing between the nozzle and the plate remains approximately constant in each stage. Their investigations also indicated that the sound generated at the end plate is mainly of monopole type if the end plate diameter is larger than the acoustic wavelength and mainly of dipole type if it is smaller. A monopole type sound source is due to the unsteady volume flow through the hole and a dipole type source is due to the unsteady fluid forces on the plate.

A simple feedback model can be used to predict the possible frequencies. This is done by an estimate of the time required for the hydrodynamic disturbance wave to cross the spacing between the plates and the time required for the acoustical wave to travel back to the leading edge (jet exit). This estimate is given by the criterion

$$\frac{n}{f} = \frac{L_c}{u_c} + \frac{L_c}{a}$$

where, ‘n’ is the mode number, ‘f’ is the frequency, ‘L_c’ is the spacing between the plates, u_c is the convection velocity and ‘a’ is the speed of sound. The mode number n is usually an integer. But recent investigations have shown that both integer and non-integer numbers are possible. Integer mode numbers correspond to cases where vortex rings are shed at every half cycle when the pressure perturbations are positive. Values between $0.5U_j$ and $0.6U_j$ are typically used for the shear layer convection velocity.

Most studies of hole tones are motivated by practical applications such as the solid propellant rocket motors, automobile intake and exhaust systems, ventilation systems, gas distribution systems and musical instruments. And consequently, the range of velocities studied is limited to very low subsonic speeds (mostly Re < 10000). In this report, Reynolds number varies from 60000 to 230000 and L_c/D_j ratio varies from 1 to 2.25. Results from pressure and acoustic measurements are presented followed by a discussion of the velocity measurements and numerical simulations.

4.2.2 Frequency and Amplitude Analysis

Adaptive control requirements could be of two different types. One could require different frequencies at different operating conditions or different frequencies might be required for the same flow conditions. Either changing the geometrical parameters or a constant geometry providing different frequencies can achieve these requirements. So, a thorough knowledge of the effect of different flow conditions for a given geometry and the effect different geometrical parameters have for a given flow condition is necessary. For that reason, variations of frequency and amplitude for different flow conditions and geometrical parameters were studied.

Frequency Characteristics

Figure 4.2.3a,b shows the spectra obtained from a pressure transducer present in the cavity (L_c/D_j = 2.26) at two different Reynolds numbers (41000 and 157000 respectively). At low speeds, axisymmetric vortex shedding from the first orifice seems to be the dominant source of instability. When the shed vortex interacts with the second plate, strong hole tones are radiated in the upstream direction. Figure 4.2.3a shows the presence of a strong discrete tone and its harmonics. At higher Reynolds numbers, the same mechanism still produces hole tones. But as shown in Figure 4.2.3b, the pressure signal is amplitude modulated by a second sound source present in the system. Peaks f_{0-1} and f_{0-2} represent the hole tones. Peak f_m is the modulating frequency produced as a result of the superposition of frequencies f_0 and f_{1-L}. The effect of this modulation is shown in the presence of the sidebands f_{1-L} and f_{1-R}. Peaks f_{1-L} and f_{1-R} are separated by a value of f_m. Spectrogram analysis of the pressure signal indicated that the modulation is not a frequency modulation. A typical spectrogram is shown in Figure 4.2.4. Analysis regarding the source of this peak will be discussed in the following sections.

Effect of Reynolds Number

Frequency of the hole tone oscillations produced generally increased with increasing jet speed. Figure 4.2.5-7 shows the variation of frequency with Reynolds number for cavity length to jet exit diameter ratios 1, 1.375 and 2.26. In these graphs, the thickness of the line varies according to the amplitude of the corresponding frequency. So, the thicker regions denote peaks. As jet speed is increased, frequency increases and at certain conditions jumps to a higher level and continues to rise again. Based on the feedback relation discussed before, as jet speed increases, convection velocity also increases and reduces the time period of each oscillation. The jump in frequency is due to changes in the number of major vortices accommodated between the cavity plates. Under certain conditions due to vortex merging, the number of vortices can be reduced and the oscillations fall back to a lower stage. Figure 4.2.8-10 shows corresponding variation in Strouhal number. Strouhal number based on the exit diameter shows a near constant or slowly varying Strouhal number operation. Strouhal number for the hole tone frequencies varied between 0.4 and 0.8 for all L_c/D_j ratios. These plots indicate that the cavity tends to oscillate at higher stages for smaller cavity lengths even from low Reynolds number flow conditions. This could be explained based on the velocity between end plates. Orifices have their highest velocity about one jet diameter away from the exit due to vena contracta and for smaller cavity lengths, this means an increased average velocity and hence higher convection velocities and frequencies.

Figure 4.2.11 plots hole tone frequencies for an L_c/D_j ratio 2.26 along with calculated frequencies from the feedback relation. The trend of the frequency variation with jet speed is in agreement with the feedback relation. For this case, oscillations started in the first mode and then jumped to the second stage and operated at that stage for the conditions tested thereafter.

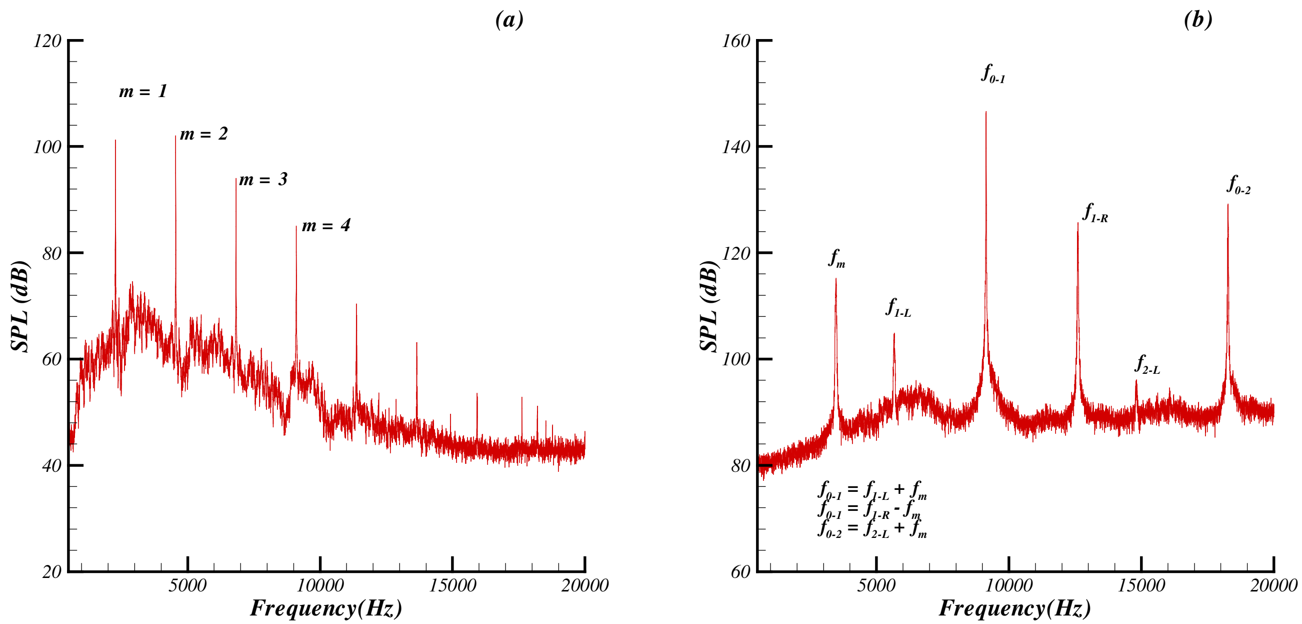

Figure 4.2.3. Pressure spectra obtained from a pressure transducer in the cavity for a hole-tone device ($L_c/D_j = 2.26$) at different Reynolds numbers. a) $Re_D = 41000$, b) $Re_D = 157000$

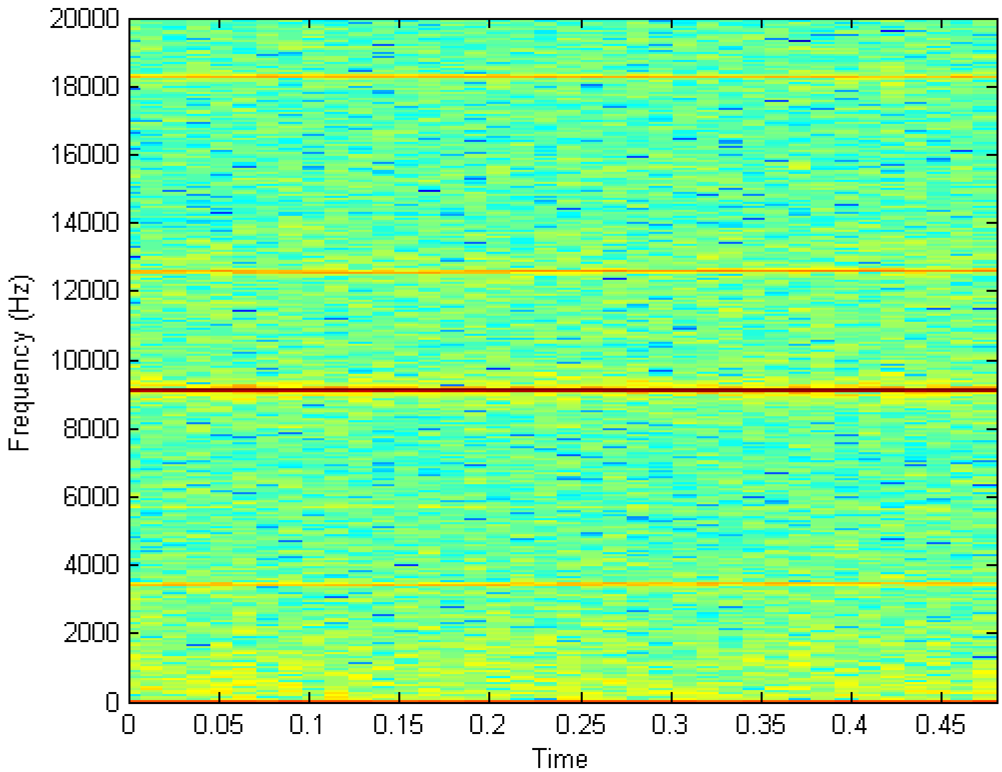

Figure 4.2.4. Spectrogram of the pressure signal from a hole-tone device (L_c/D_j = 2.26, Re_D = 157000, different number of FFTs were studied-only one showed as an example)

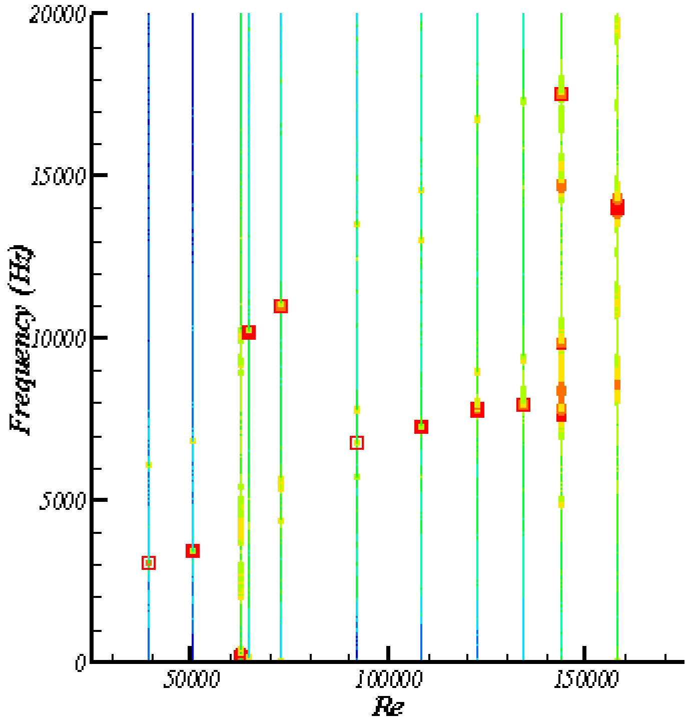

Figure 4.2.5. Variation of frequency with Reynolds number for a hole-tone device (L_c/D_j = 1.04, inlet to exit diameter ratio D_j/D_e = 0.9)

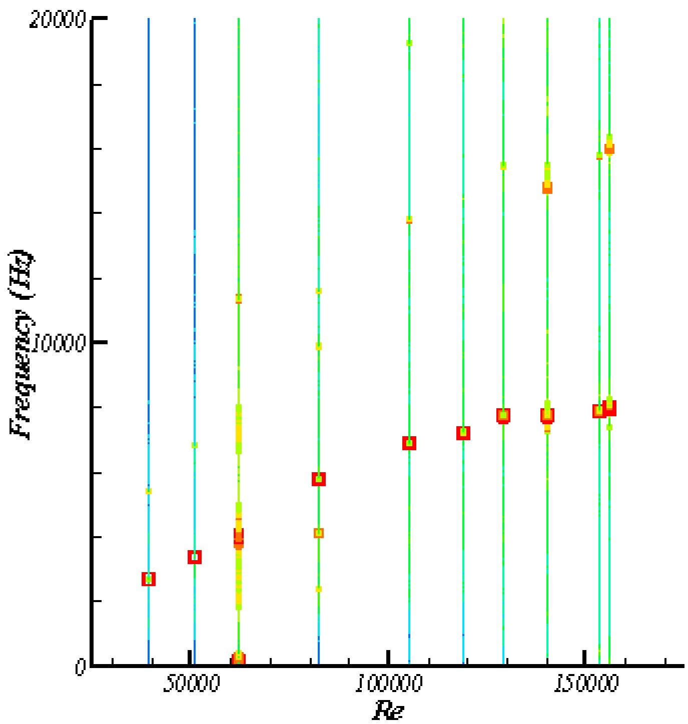

Figure 4.2.6. Variation of frequency with Reynolds number for a hole-tone device (L_c/D_j = 1.375, inlet to exit diameter ratio D_j/D_e = 0.9)

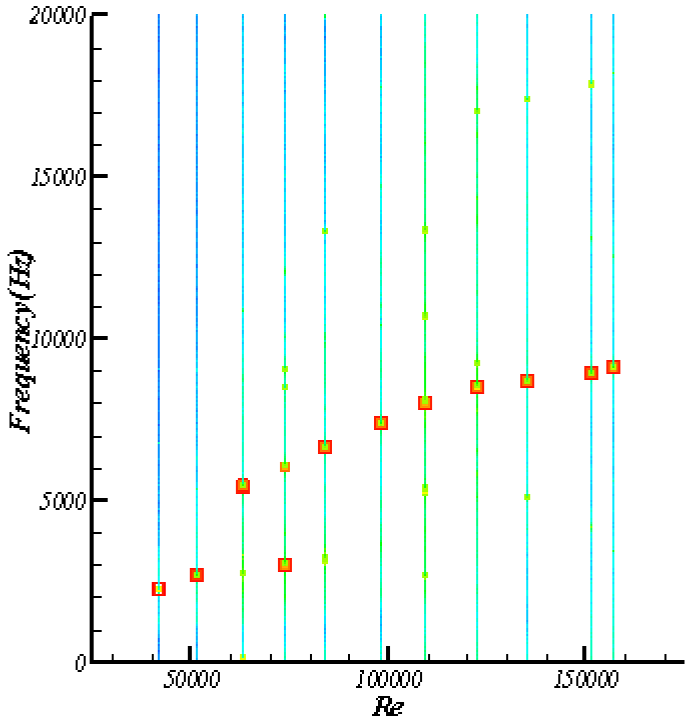

Figure 4.2.7. Variation of frequency with Reynolds number for a hole-tone device (L_c/D_j = 2.26, inlet to exit diameter ratio D_j/D_e = 0.9)

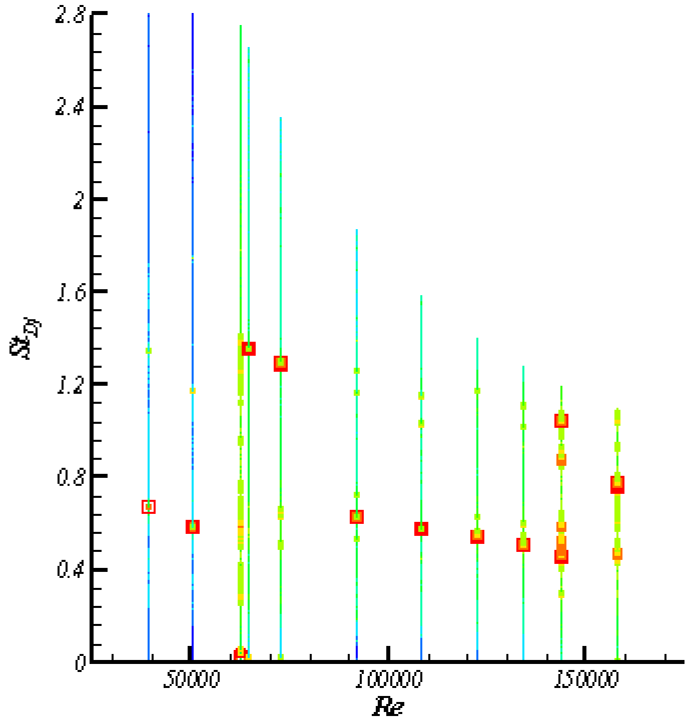

Figure 4.2.8. Variation of St_D with Reynolds number for a hole-tone device (L_c/D_j = 1.04, inlet to exit diameter ratio D_j/D_e = 0.9)

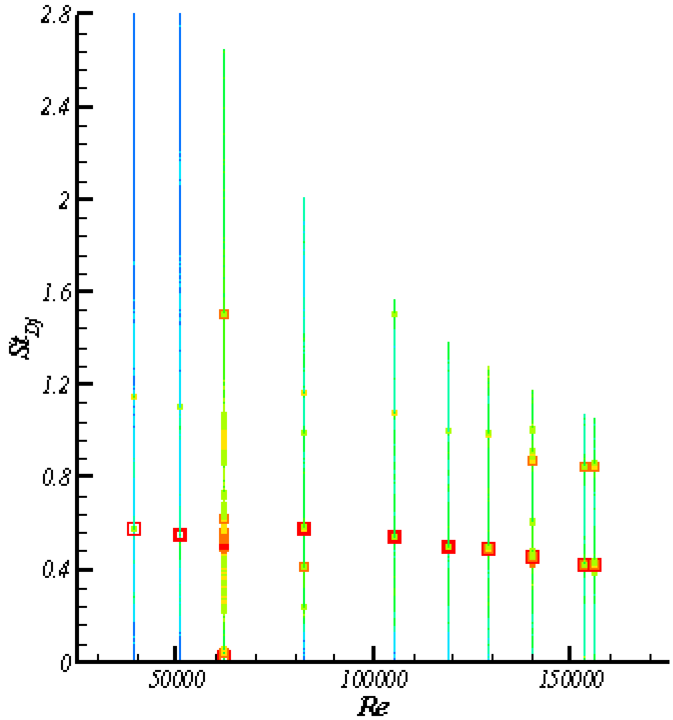

Figure 4.2.9. Variation of Frequency with Reynolds number for a hole-tone device (L_c/D_j = 1.375, inlet to exit diameter ratio D_j/D_e = 0.9)

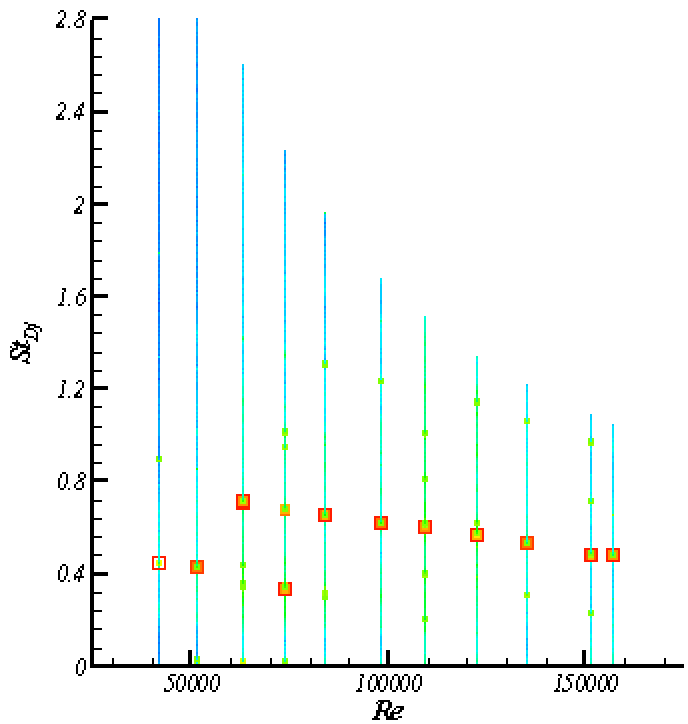

Figure 4.2.10. Variation of St_D with Reynolds number for a hole-tone device (L_c/D_j = 2.26, inlet to exit diameter ratio D_j/D_e = 0.9)

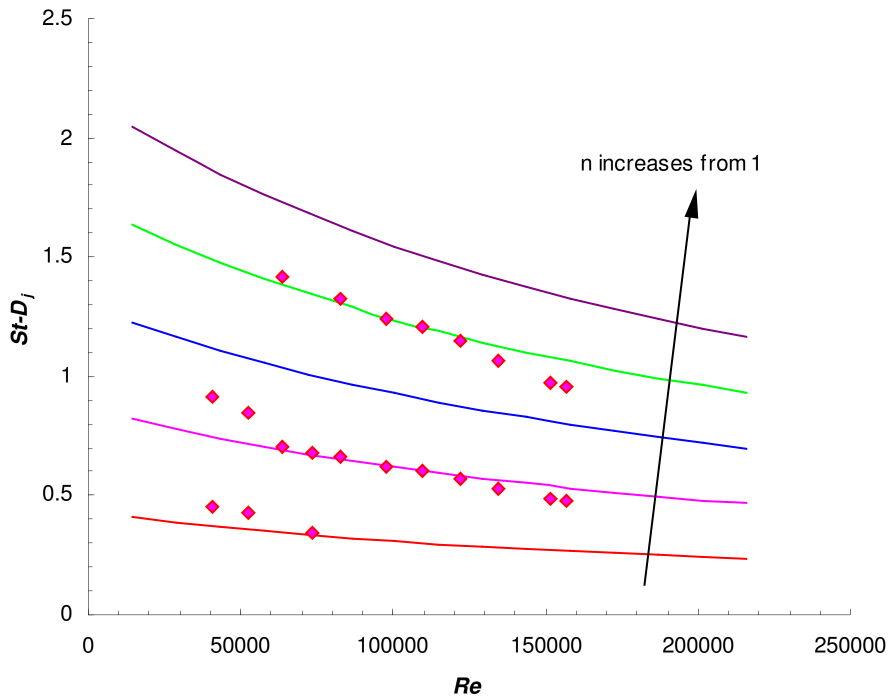

Figure 4.2.11. Comparison of experimental hole tone frequencies with the feedback relation (L_c/D_j = 2.26, inlet to exit diameter ratio D_j/De = 0.9)

Effect of L/D

Figure 4.2.12 shows the effect of the cavity length to jet diameter ratio on the oscillation frequencies at two different jet velocities. Frequency decreases with increasing length to jet diameter ratios. When L_c/D_j increases and U_c is assumed to be a constant ratio of mean velocity, one can reformat the feedback relation described in the previous section as

$$\frac{1}{St_D} = \frac{1}{n}\left(\frac{(L_c/D_j)}{K} + \frac{(L_c/D_j)}{M}\right)$$

So an increase in L_c/D_j leads to an increased time period and hence lowers the Strouhal number for the oscillations. But it is not very clear whether the ratio of convection velocity to mean velocity is a constant. To evaluate, possible dependency on oscillation mode and jet speed, calculated convection velocity ratio based on the above relation is shown in Figures 4.2.13a,b respectively. U_c/U_j is plotted against Strouhal number in Figure 4.2.13a and it shows that convection velocity ratio increases with increasing Strouhal number. Also, this ratio (U_c/U_j) increases with increasing L_c/D_j ratio. Figure 4.2.13b shows that this ratio (U_c/U_j) is a generally decreasing function of Reynolds number.

Effect of Inlet to Exit diameter ratio

The ratio between inlet and exit diameters determines the portion of the jet that can pass directly through the exit. When the inlet diameter is much smaller than the exit diameter, the jet can pass through the exit without much hindrance. When the inlet diameter is much larger than the exit diameter, the exit plate blocks a large portion of the jet. In a system, where the oscillating mechanism is due to the interaction of elements in the jet with the trailing edge, this is an important parameter to be considered. Inlet to exit diameter ratios of 0.9 and 1.0 were studied. Its effect on the frequencies is shown in Figure 4.2.14. It shows that with lesser blockage for the jet, oscillations have higher frequencies. A reason for this is that the vortices are not as restricted as in the case where a bulk of the jet has to interact with the plate and asymmetric instabilities sets in. Asymmetric instabilities usually operate at higher modes.

Variation of SPL

Variation of the amplitude of oscillations with inlet to exit diameter (D_j/D_e) ratio, Reynolds number and Strouhal number are shown in Figures 4.2.14,15,16 respectively. SPL increases with Reynolds number except during certain flow conditions. Smaller length to depth ratios appears to have higher amplitudes until a particular jet speed and drops of after that most possibly due to other processes that reduce the oscillations. All three L/D ratios appear to exhibit some correlation between the dropping off amplitude and switching to a different stage. This needs to be further studied before a complete explanation can be provided. Higher Strouhal number oscillations results in decreased sound pressure level. Maximum amplitudes were obtained for St_D between 0.4 and 0.6. This range is also very close to the preferred mode of a jet. Higher amplitudes were obtained for smaller inlet to exit diameter ratios. This could be expected

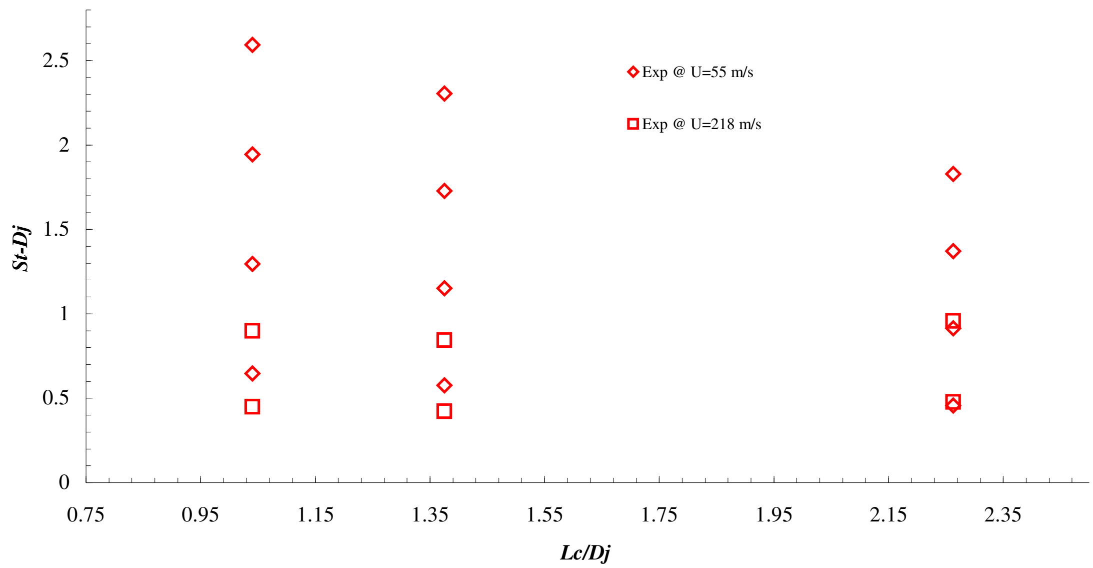

Figure 4.2.12. Variation of hole tone frequencies with L_c/D_j (inlet to exit diameter ratio D_j/D_e = 0.9)

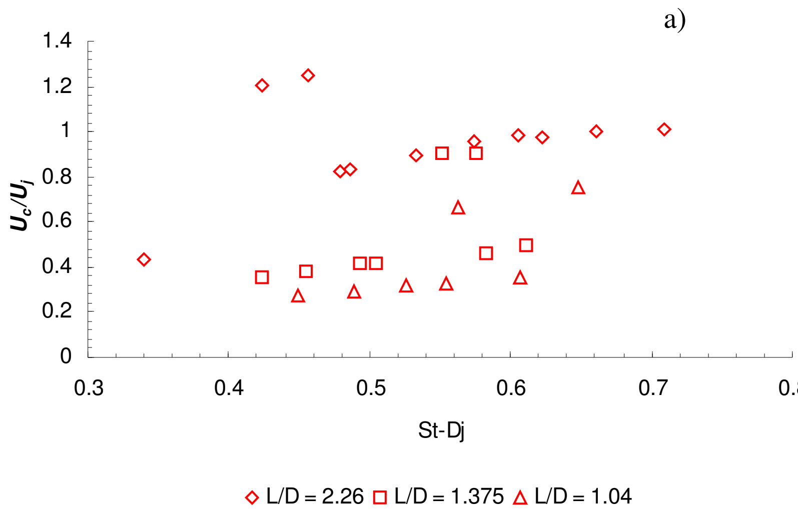

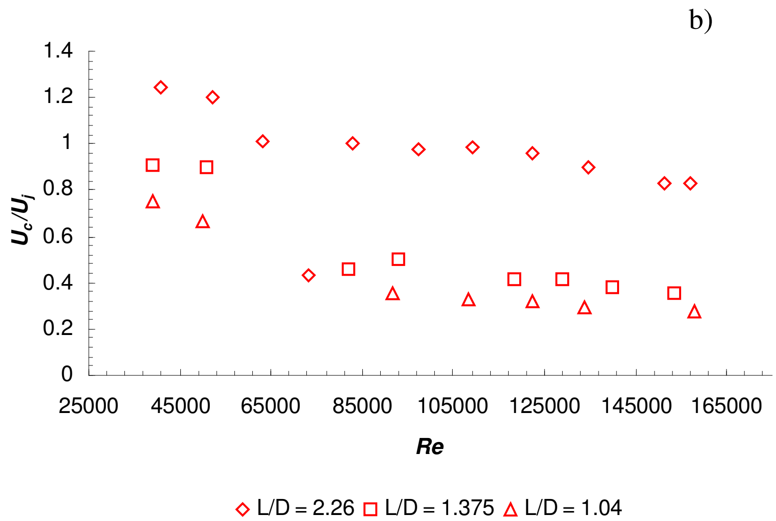

Figure 4.2.13.Variation of convection velocity to mean velocity ratio (U_c/U_j). a) with Strouhal number b) with Reynolds number

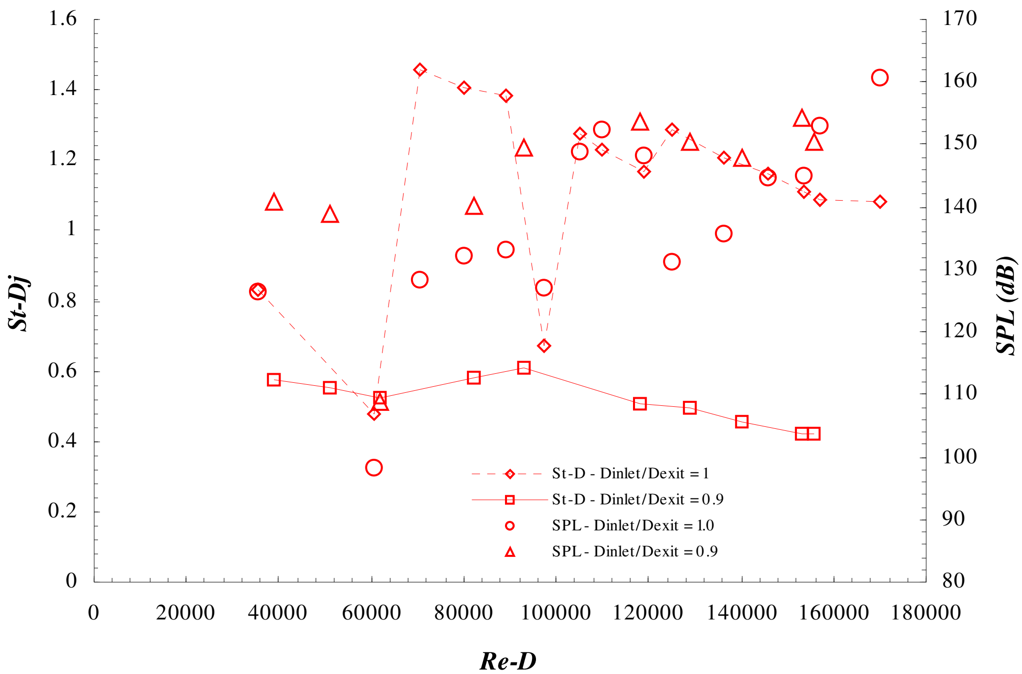

Figure 4.2.14. Effect of inlet to exit diameter ratio (D_j/D_e) on hole tone frequencies and oscillation amplitudes

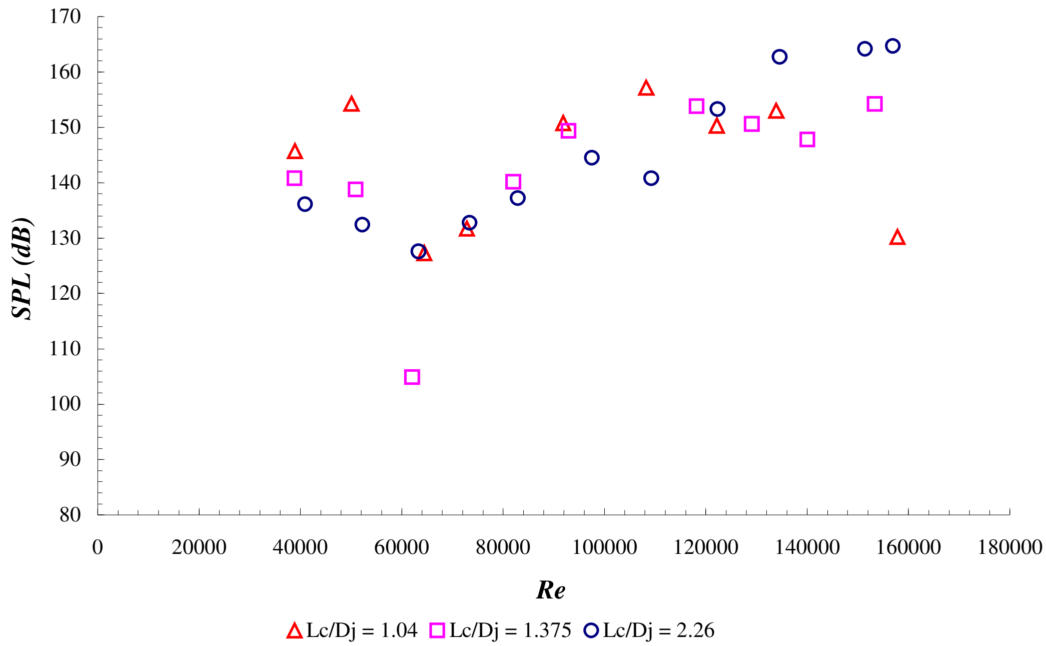

Figure 4.2.15. Variation of sound pressure level with Reynolds number in a hole-tone device

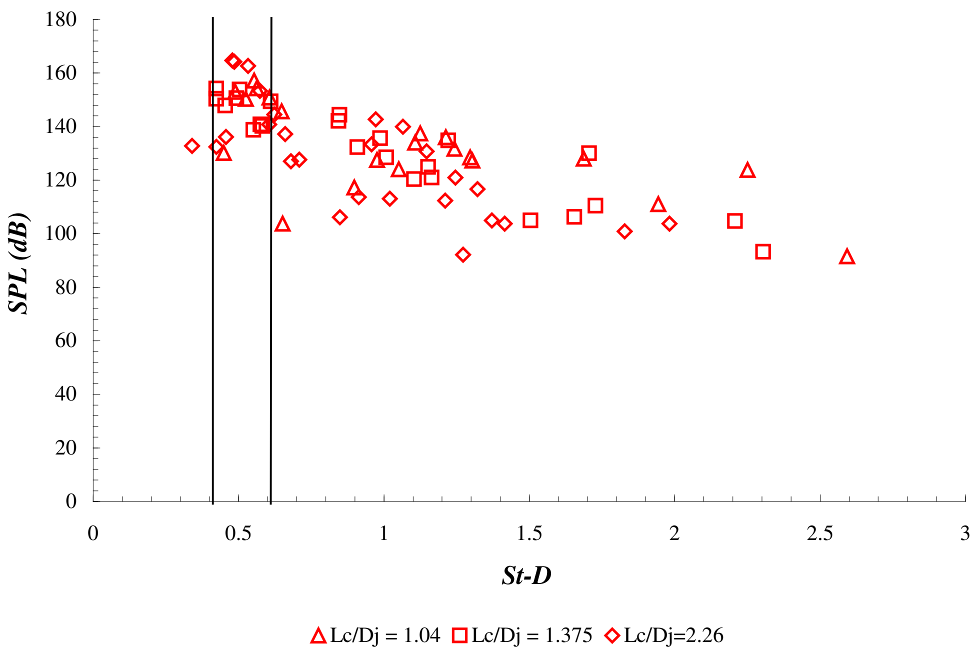

Figure 4.2.16. Variation of sound pressure level with Strouhal number in a hole-tone device

from results obtained before. It was shown before that large inlet to exit diameter ratios (D_j/D_e) allow for oscillations at higher stages and hence higher Strouhal numbers.

Effect of Inlet Boundary Condition

Comparison was made between using a constant diameter pipe and an orifice at the leading edge of the cavity. It has already been shown in the previous section on baseline turbulent jets, a pipe jet produces lesser coherent structures in the near field than an orifice jet. Figure 4.2.17 shows that a pipe jet produces similar frequency response as an orifice jet. But the amplitudes are lower than the orifice jet especially at lower speeds. It should be noted for this case, the amplitude of the orifice inlet is higher than the pipe inlet even though the former is operating at a higher stage. It has been shown before that at higher stages, the amplitude of oscillations is reduced. Figure 4.2.18 shows images obtained for orifice inlets and pipe inlets at similar conditions. In the case of orifices, it is much easier to see the rolled up vortices. These vortices also make the effective width of the jet impacting on the exit plate much larger than the actual jet diameter.

4.2.3 Velocity Measurements

2D velocity measurements made on this configuration allowed to visualize the flow field inside the cavity. Instantaneous images from PIV measurements showed the roll up of vortices within the cavity. Figure 4.2.19 shows typical images obtained for different conditions. Figure 4.2.19a corresponds to an L_c/D_j ratio of 1.25 and inlet to exit diameter ratio of 1. Figure 4.2.19b,c corresponds to an L_c/D_j ratio of 1.0 and inlet to jet exit diameter ratio (D_j/D_e) of 0.9. Figure 4.2.19d corresponds to an L_c/D_j ratio of 2.0 and inlet to jet exit diameter ratio (D_j/D_e) of 0.9. All figures correspond to the same mass flow rate. Both symmetric (Figures 4.2.19a,d) and asymmetric (Figures 4.2.19b,c) vortex rings were observed. At lower speeds, only symmetric vortex rings were observed. Even very small inclination between the end plates tended to create asymmetric vortex rings. This can be expected because the upstream pressure wave traveling back from the exit plate will be starting at different times along the circumference of the exit hole. It can also be noted that Figures 4.2.19a,d shows a single vortex ring while Figures 4.2.19c,d shows at least two rings within the cavity. The number of these vortices indicates the mode at which oscillations are taking place. Also there seems to be a correlation between asymmetric vortex rings and operation at higher modes.

Phase locked measurements were made by using total pressure signal from a transducer located at the exit plate. The pressure signal was amplified and used to produce a signal to trigger camera and laser firings. The pressure signal was good enough to reliably use it as a trigger signal. Figure 4.2.20 shows few images taken within a particular phase. These figures show good agreement between different pictures at the same phase even though a careful analysis would reveal slight difference in position between different images. For our purpose of studying the oscillation mechanism, it was good enough to capture different stages of an oscillation cycle. In oscillations of these type, there will always be some cycle to cycle variations and phase averaged study would help in focusing on the major features of the cycle. Figure 4.2.21 shows averaged

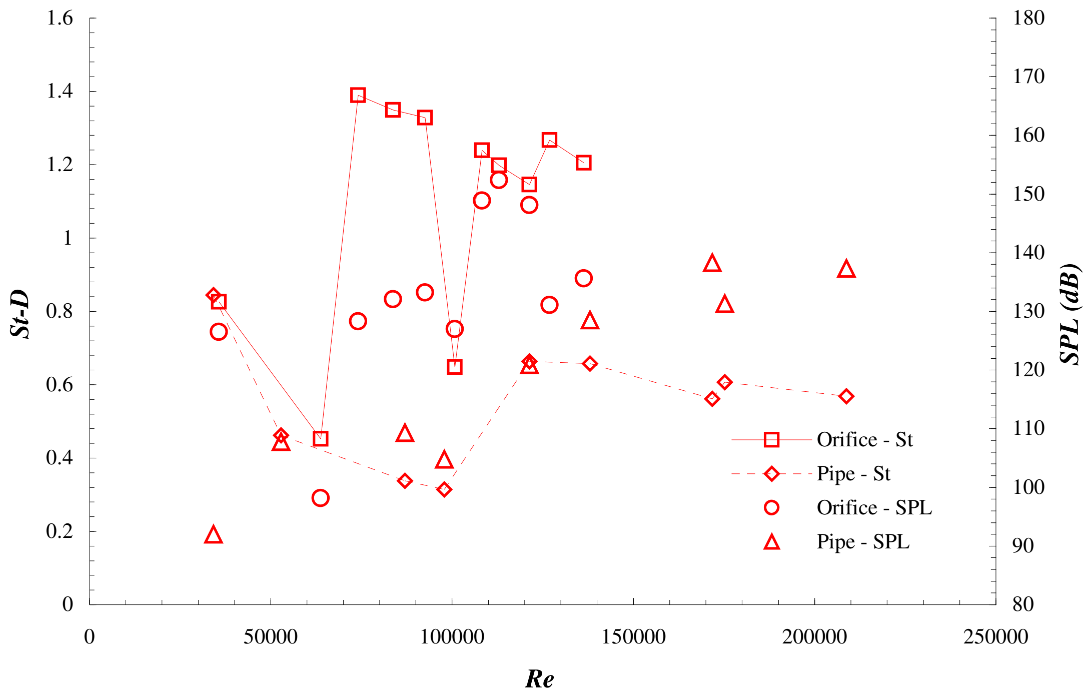

Figure 4.2.17. Effect of cavity inlet boundary conditions (Lc/Dj = 2.26 for orifice inlet and 1.6 for pipe inlet)

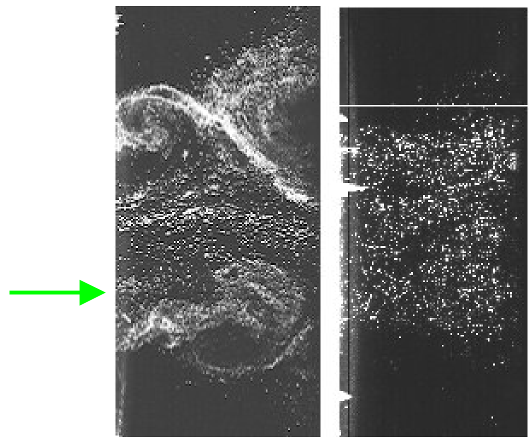

Figure 4.2.18. Effect of cavity inlet boundary conditions (Lc/Dj = 2.26 for orifice inlet and 1.6 for pipe inlet)

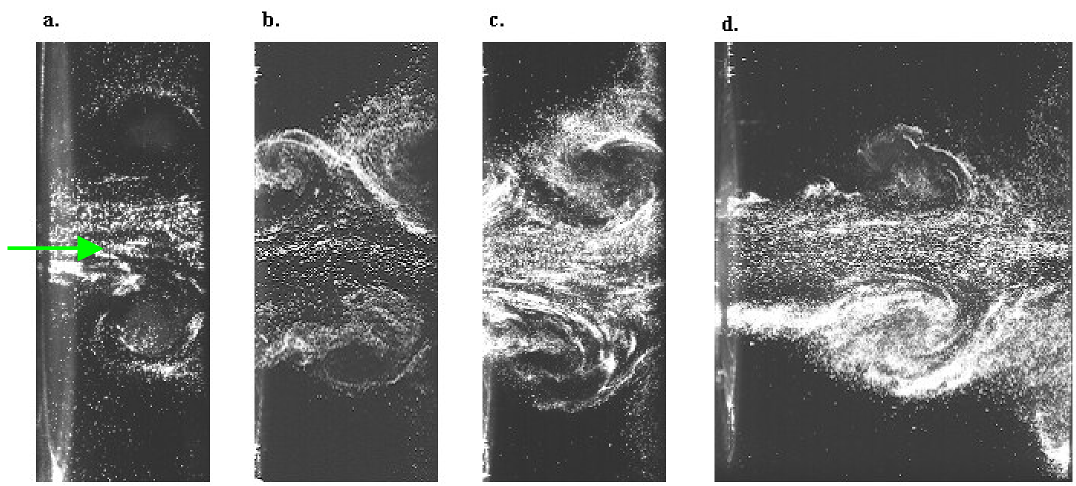

Figure 4.2.19. Roll up of vortices in the cavity. (mass flow rate for all conditions remain the same – high subsonic conditions), a) L_c/D_j = 1.25, inlet to exit diameter ratio D_j/D_e = 1, b) and c) L_c/D_j = 1.0, diameter ratio = D_j/D_e = 0.9, d) L_c/D_j = 2.0 diameter ratio D_j/D_e = 0.9

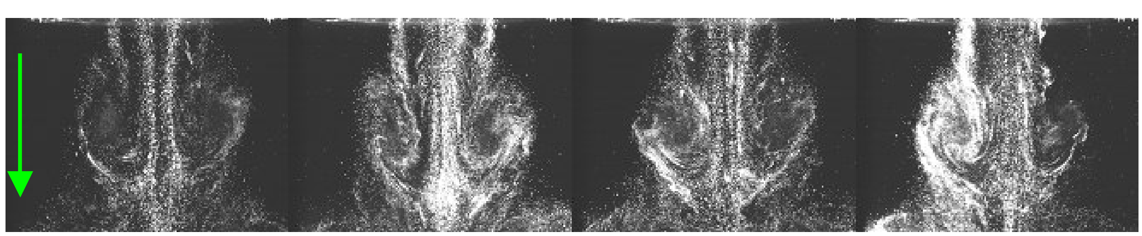

Figure 4.2.20. Representative instantaneous images within one phase condition. (L_c/D_j = 2.0, diameter ratio D_j/D_e = 0.9)

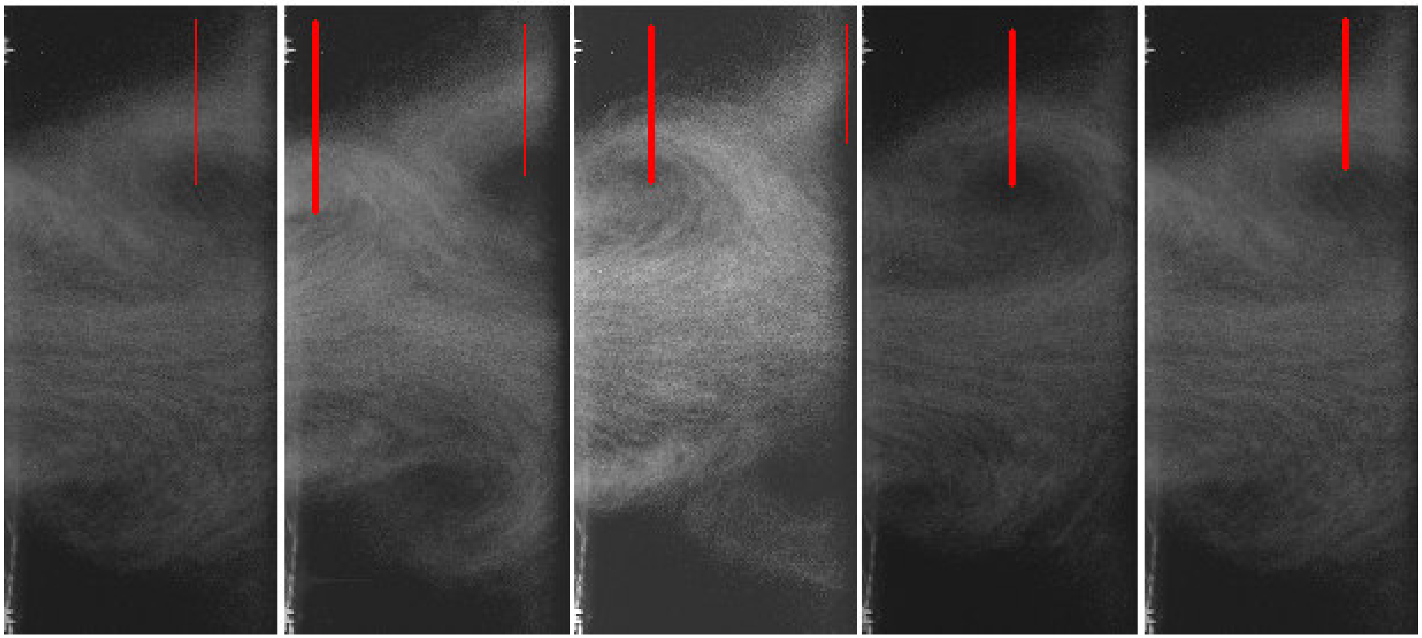

Figure 4.2.21. Phase averaged images show an oscillation cycle. Images are separated by 90˚ from neighboring images. Lines of different thickness track different vortices ($L_c/D_j = 1.0$)

images taken at different phases. These images were taken for an L_c/D_j ratio of 1.75 and exit to inlet diameter ratio (D_j/D_e) of 0.9. Each image is separated by 90˚ from adjacent images and corresponds to conditions of 0˚, 90˚, 180˚, 270˚ and 360˚. The first image starts with a vortex ring impinging at the trailing edge and the cycle shows the process as this ring passes through the exit and another ring originating at the leading edge reaching the exit plate. Figure 4.2.22 shows corresponding velocity vectors and Figure 4.2.23 shows corresponding vorticity contours for the case in Figure 4.2.20. Figure 4.2.24 and Figure 4.2.25 shows velocity vectors and vorticity fields for an L_c/D_j ratio of 2.0 and an inlet to exit diameter ratio (D_j/D_e) of 0.9.

Figures 4.2.26,27 show selected typical instantaneous velocity vectors and the corresponding vorticity contour for the case in Figure 4.2.22. Figures 4.2.28,29 shows similar plots for the case in Figure 4.2.24. As could be expected there was some cycle-to-cycle variation in the instantaneous images and it is suspected that the modulating frequency discussed previously might also be having some phase modulation effects on the oscillations.

4.2.4 Numerical Simulations

2D LES analysis of an axisymmetric model of the hole tone devicewas performed for an L/D ratio of 1 and inlet to exit diameter ratio of 1. These simulations provided a much clearer picture of the oscillation process. A pressure and velocity monitor was placed inside the cavity corresponding to the experimental pressure transducer location. A constant time step of 1μs was used. At each time step, it was made sure that the solution converged. A typical reading from the pressure monitor is shown in Figure 3.2. The frequency of the oscillations appears to be very similar to the experimental frequencies. Since, the data set obtained through CFD has very small number of data points and a very high equivalent scan rate, ordinary Fourier analysis won't have the necessary resolution or accuracy. Advanced signal processing techniques are needed to evaluate the frequency of the oscillations. The solution was run until the pressure oscillations were sustained. Different stages of an oscillation cycle as obtained from the numerical simulation are shown in Figure 4.2.30. Vorticity contour is plotted. Vortex rings formed within the cavity upon interaction with the exit plate was divided and one part traveled through the exit and another part traveled along the inner wall of the exit plate. The vortices traveling along the wall continued to grow through subharmonic evolution. For this case, the vortex reached a diameter equivalent to the length of the cavity. After reaching this size, it appears to become a stationary vortex. This could provide a length scale for the transverse oscillations and could possibly be a source for the second peak. PIV measurements showed the traveling vortices along the wall. But the measurement region did not include the whole length of the plate. Further measurements have to be made to confirm this. Also it remains to be verified whether the location of the stationary vortex varies with different jet speeds. Pressure contours showed the upstream traveling wave and its reflections between the cavity sidewalls. By nature of the axisymmetric simulations, the vortex rings formed were axisymmetric and any type of asymmetric vortex shedding was not observed. Therefore 3D simulations with higher order accuracies capable of capturing the vortex structures and also the acoustic features of the flowfield are necessary.

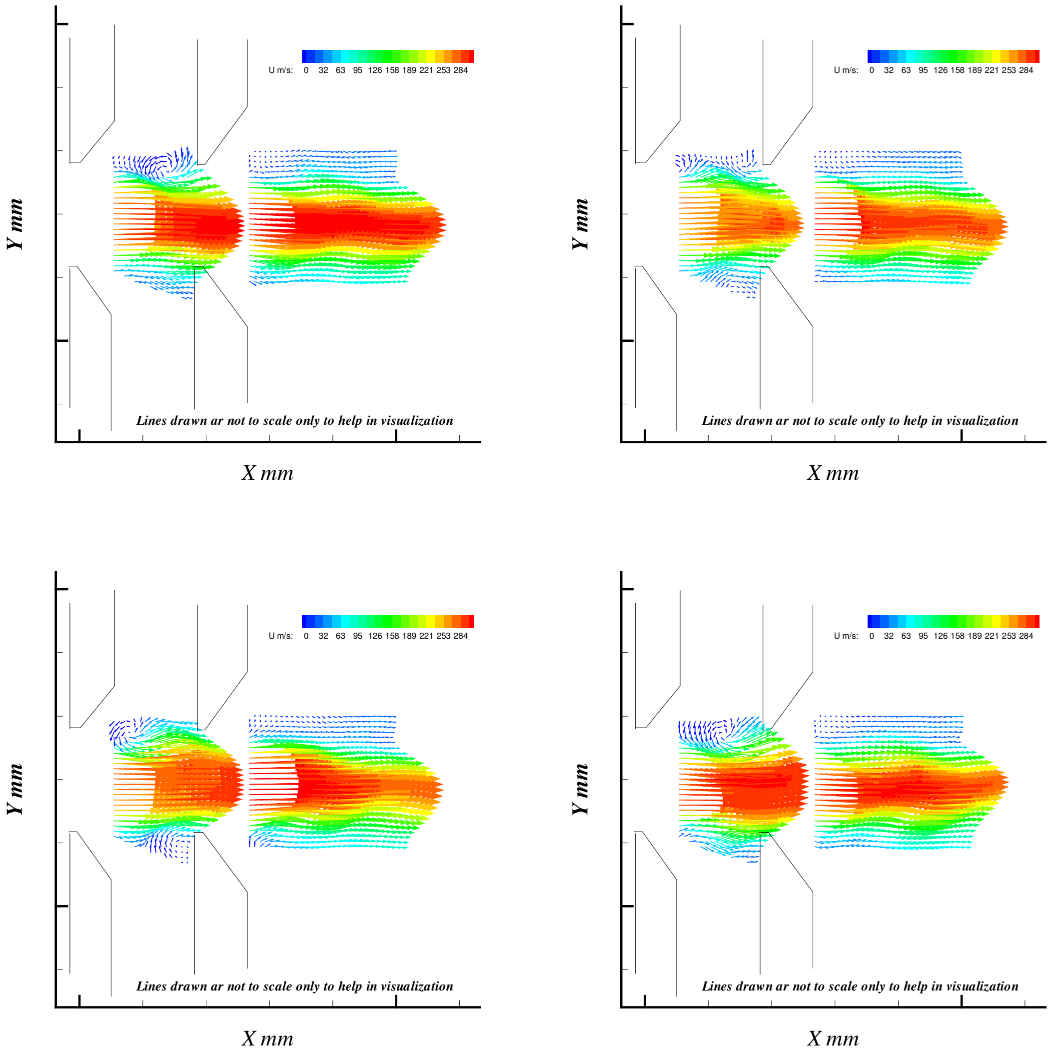

Figure 4.2.22. Mean velocity vectors at different phase conditions of the pressure signal for L_c/D_j = 1.0 (images arranged clockwise with each image separated from its neighbor by 90˚)

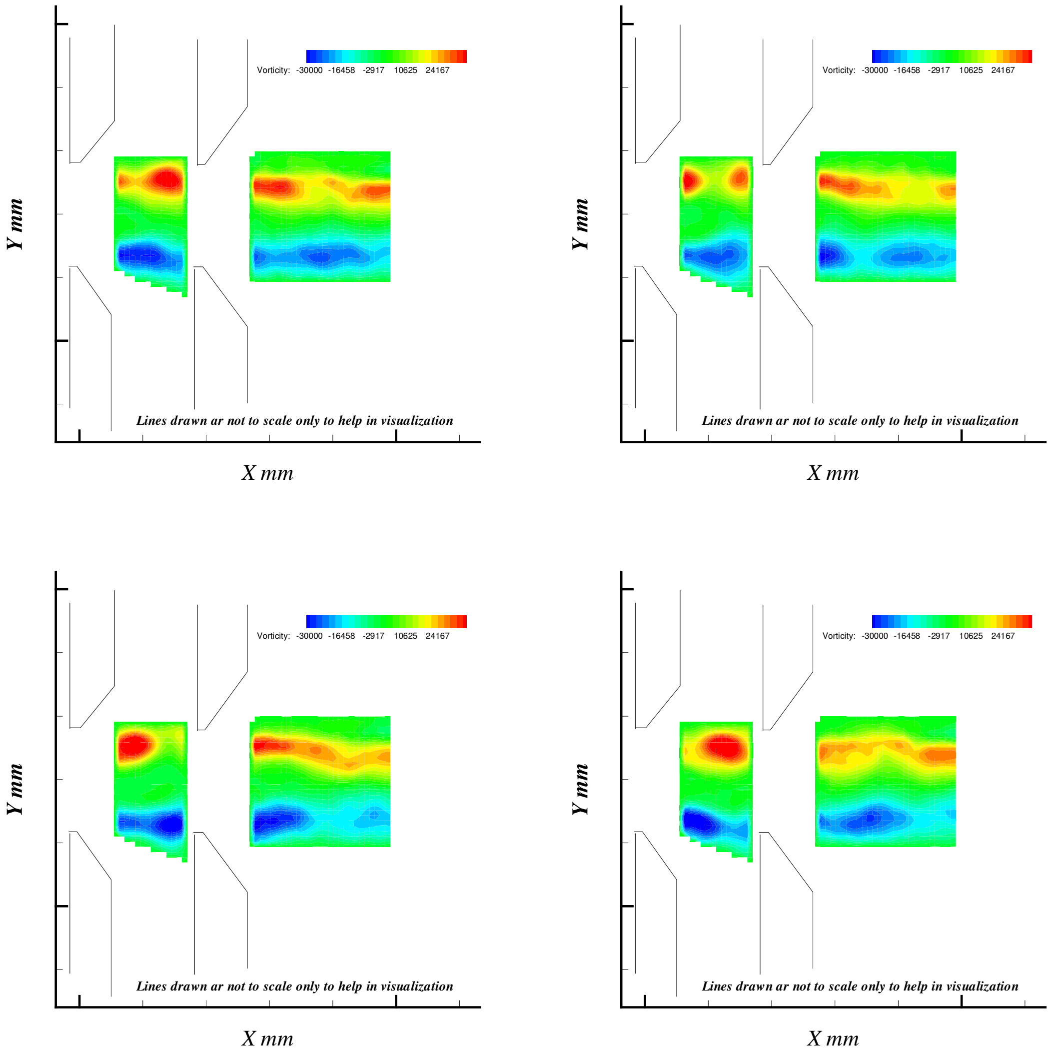

Figure 4.2.23. Mean vorticity contours at different phase conditions of the pressure signal for L_c/D_j = 1.0 (images arranged clockwise with each image separated from its neighbor by 90˚)

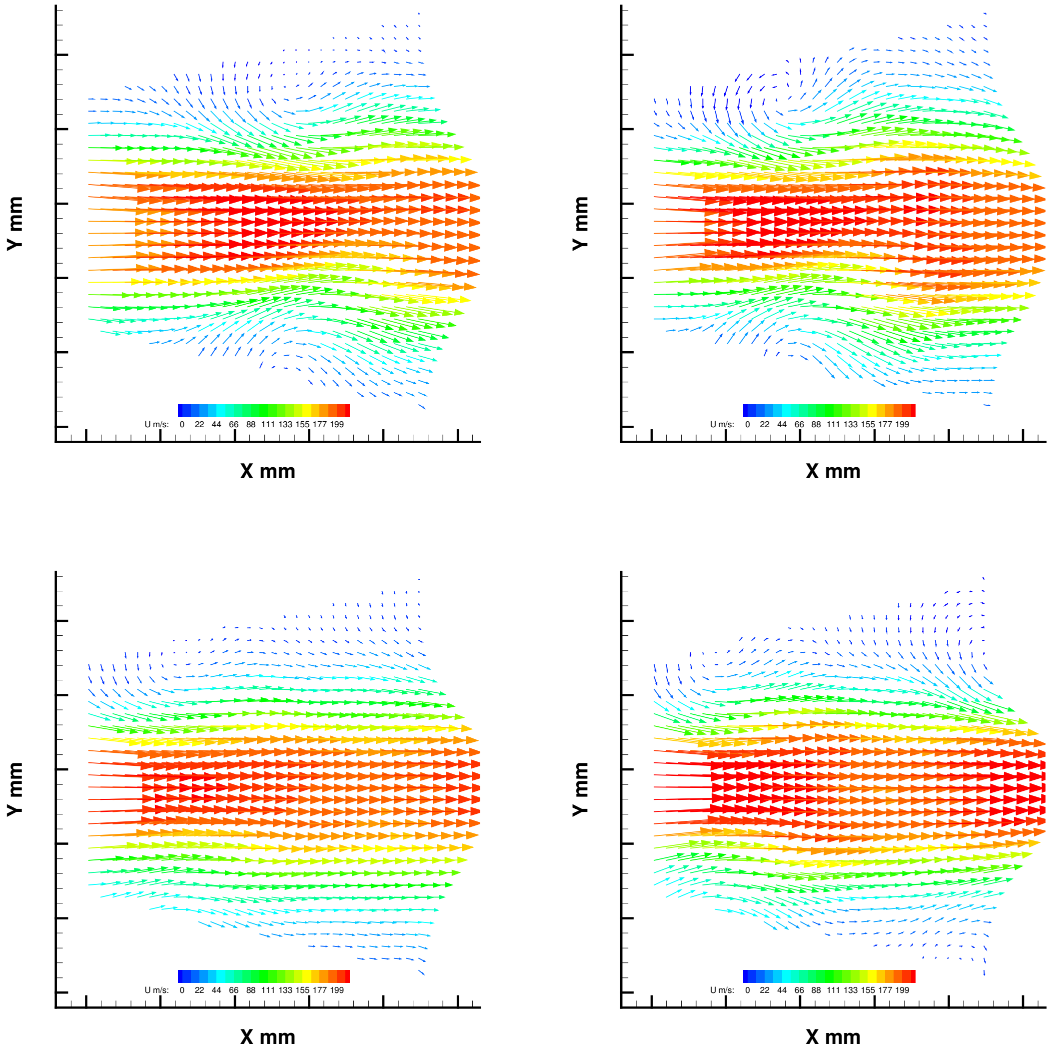

Figure 4.2.24. Mean velocity vectors at different phase conditions of the pressure signal for L_c/D_j = 2.0 (images arranged clockwise with each image separated from its neighbor by 90˚)

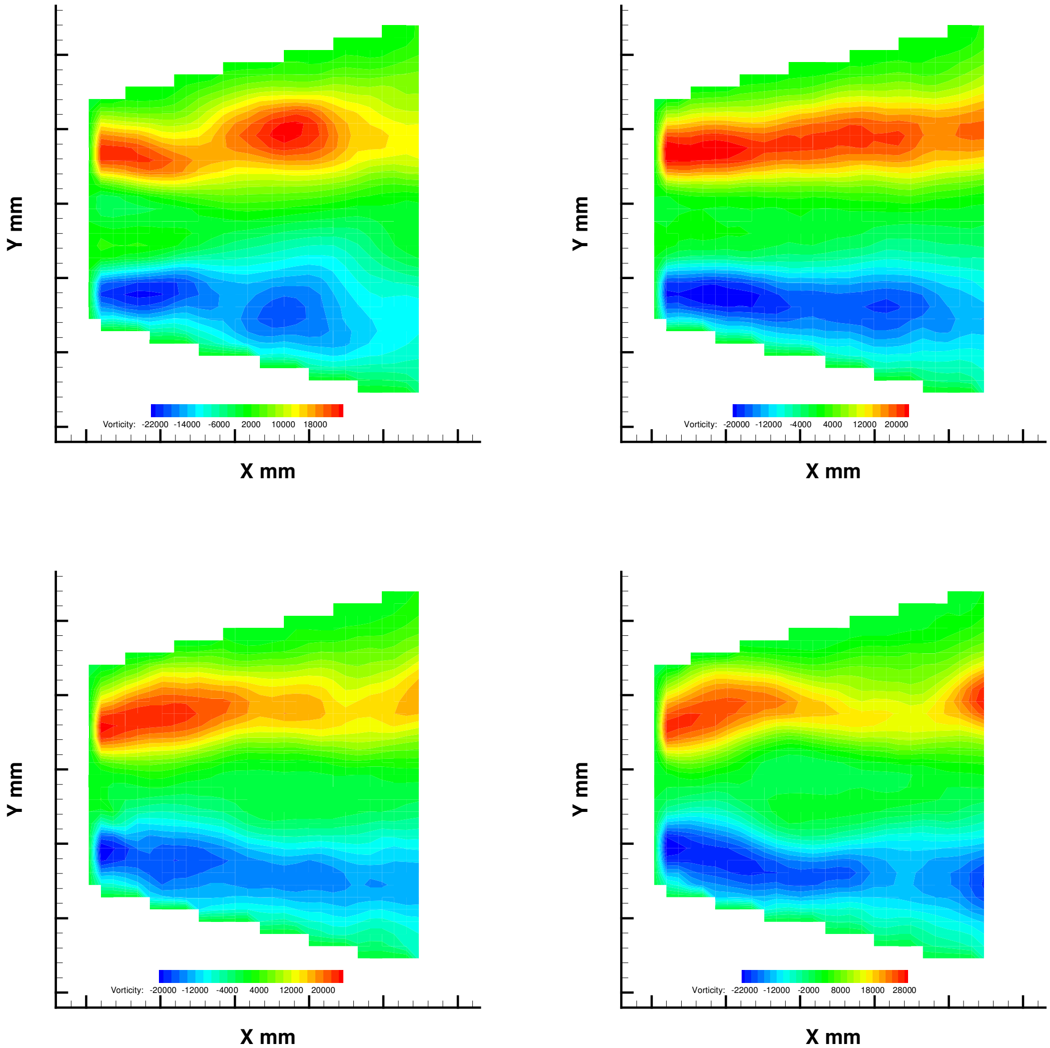

Figure 4.2.25. Mean vorticity contours at different phase conditions of the pressure signal for $L_c/D_j = 2.0$ (images arranged clockwise with each image separated from its neighbor by 90˚)

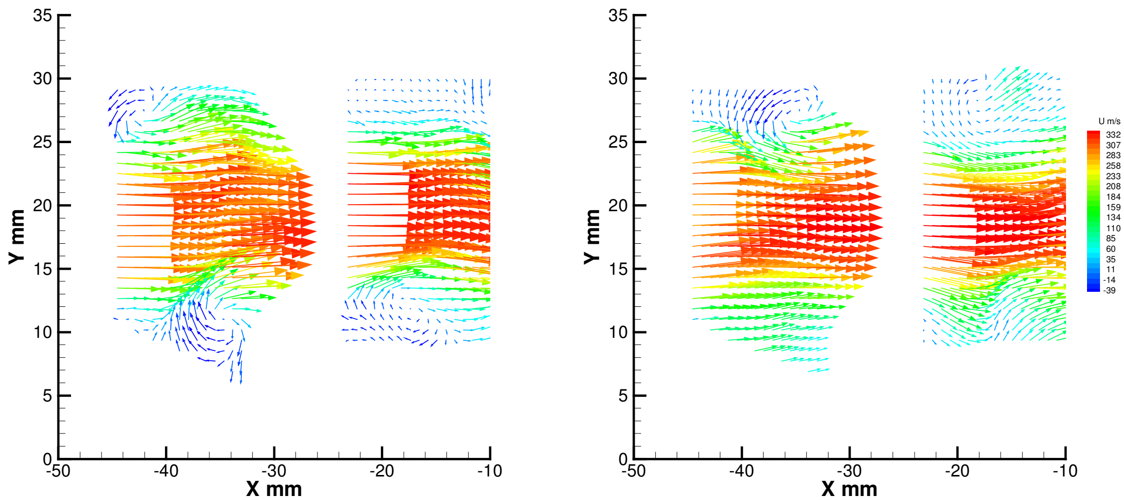

Figure 4.2.26. Representative instantaneous velocity vectors for $L_c/D_j = 1.0$

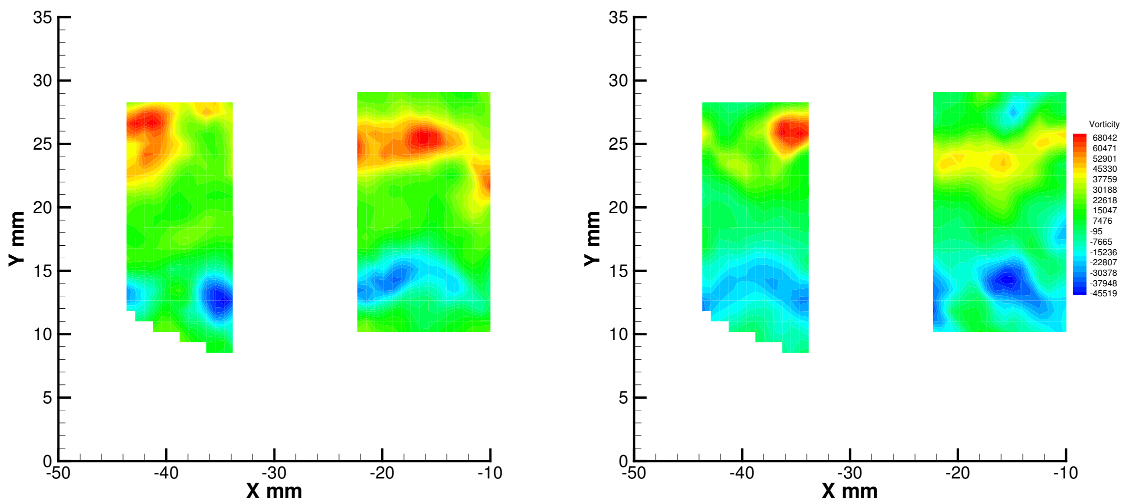

Figure 4.2.27. Representative instantaneous vorticity contours for $L_c/D_j = 1.0$

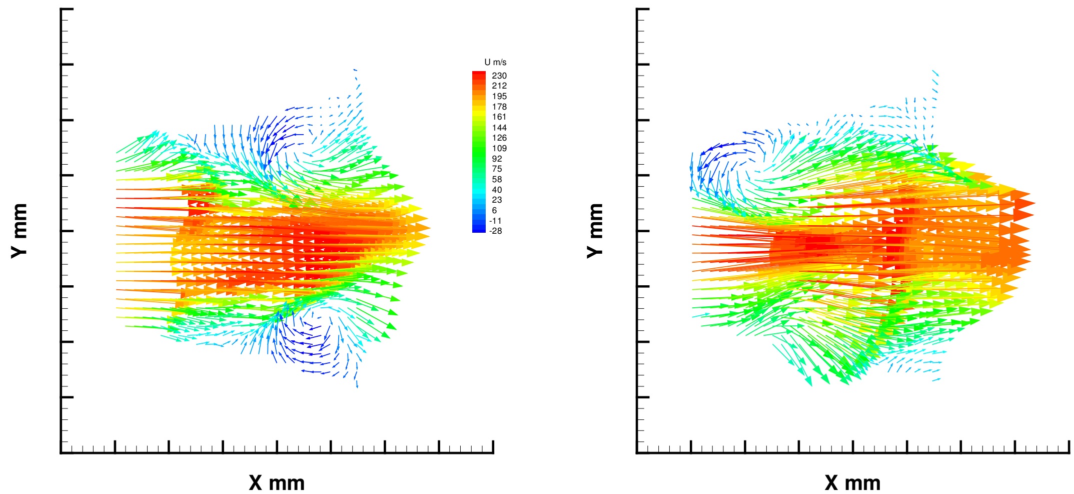

Figure 4.2.28. Representative instantaneous velocity vectors for $L_c/D_j = 2.0$

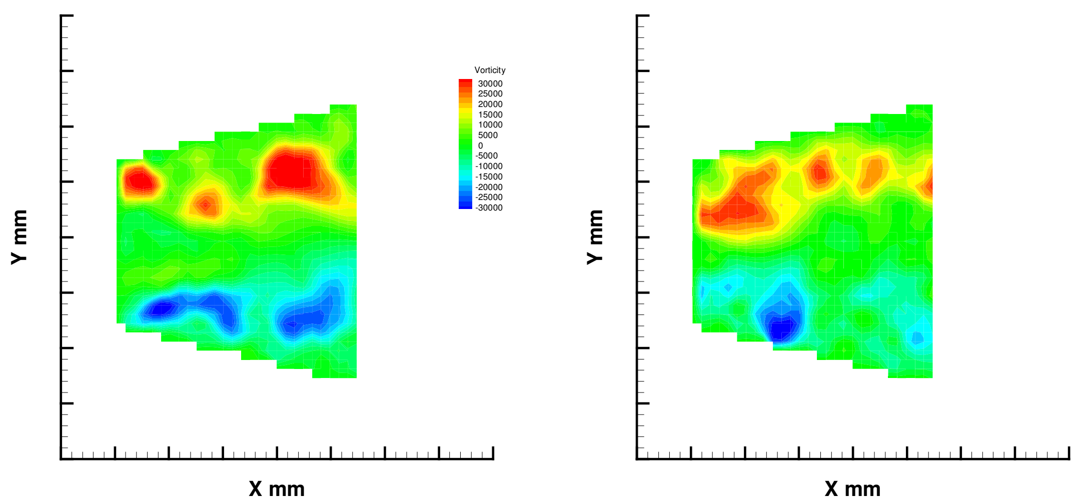

Figure 4.2.29. Representative instantaneous vorticity contours for $L_c/D_j = 2.0$

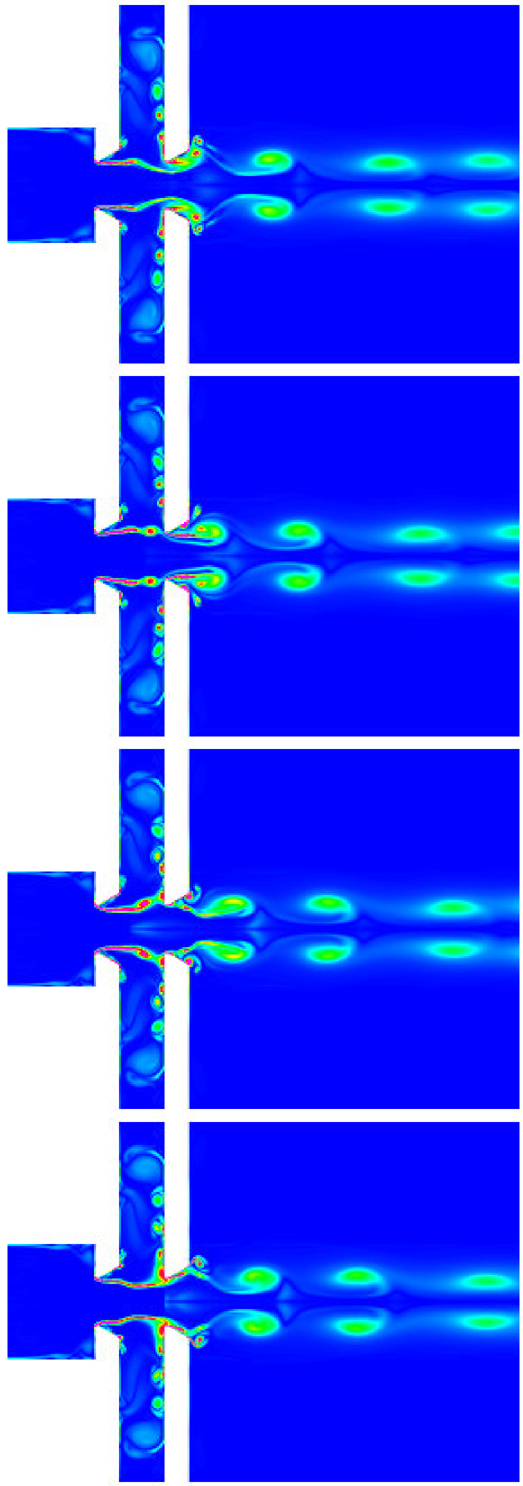

Figure 4.2.30. Hole-Tone oscillation cycle obtained from numerical calculations (L_c/D_j = 1.0, D_j/D_e = 1.0)

4.3 Axial Jet Actuator

4.3.1 Introduction

Axisymmetric cavities of finite depth (with the peripheries closed) were placed at the exit of baseline jets. Several geometrical parameters of interest were studied. They include the length to depth ratio of the cavity (L_c/D_c), jet to pipe diameter ratio (D_j/D_p) also called the expansion ratio and cavity inlet to cavity exit diameter ratio (D_j/D_e). Different L_c/D_c ratios between 1 and 5 were tested. Different D_j/D_p ratios between 0.33 and 0.5 were tested. Cavity inlet to cavity exit diameter ratio D_j/D_e varied between 0.67 and 1.5. Reynolds number based on the cavity inlet diameter varied between very low subsonic speeds to high subsonic speeds. During each run for a particular configuration (L_c/D_c, D_j/D_p and D_j/D_e being fixed), mass flow rate through the geometry was changed slowly from very low flow rates to high flow rates. Data were taken at several intermediate flow conditions. Only selected results are presented in this discussion. Cavity inlet and exit boundaries were varied from the two geometries available (orifice baffles of different sizes and a short pipe of constant diameter extending 4 jet diameters in length). Usage of the parameter L/D denotes the cavity length to depth ratio L_c/D_c unless otherwise specified.

4.3.2 Frequency Analysis

Effect of Reynolds number

Spectral data obtained for an L_c/D_c ratio of 1.75, D_j/D_p ratio of 0.375 and inlet to exit diameter ratio (D_j/D_e) of 0.9 is shown in Figure 4.3.1. Each line represents the complete pressure spectra for that particular Reynolds number. Thickness of the line varies according to the power spectral density of the corresponding frequency at each point. Color of the line indicates the amplitude, varying from blue to red for minimum to maximum. At low speeds ($Re_D < 50000$), the frequency characteristic of this configuration is very similar to that of a hole tone device. At low speeds, one can hear very distinct tones over the flow noise. Oscillation frequency (thick regions of the line) increases with jet speed very similar to that of the hole tone. In the previous section regarding hole tones, an axisymmetric cavity with its length scale dominating, produced well-defined tones. Based on those results, it was suspected that vortex rings formation within the cavity and their impingement on the inner surface of the exit wall could be the dominant mechanism of oscillation at these flow conditions. Further referring to Figure 4.3.1, at higher speeds ($Re_D > 50000$), a completely different response can be observed. Frequency remains constant for a wide range of Reynolds numbers (from Re_D 75000 – 150000). This is a clear indication that some type of resonance mechanism has been set in the system and possibly associated with an acoustic mode of the cavity or the pipe. Within the range of Reynolds numbers where the frequency remained constant, the amplitude however varied. Strouhal number based on cavity inlet diameter (D_j) corresponding to data in Figure 4.3.1 is plotted in Figure 4.3.2. The total length of the lines decreases with increasing Reynolds number because the range of St_D for a given frequency bandwidth, decreases with increasing velocity, based on the relation $St_D = \frac{fD}{U}$.

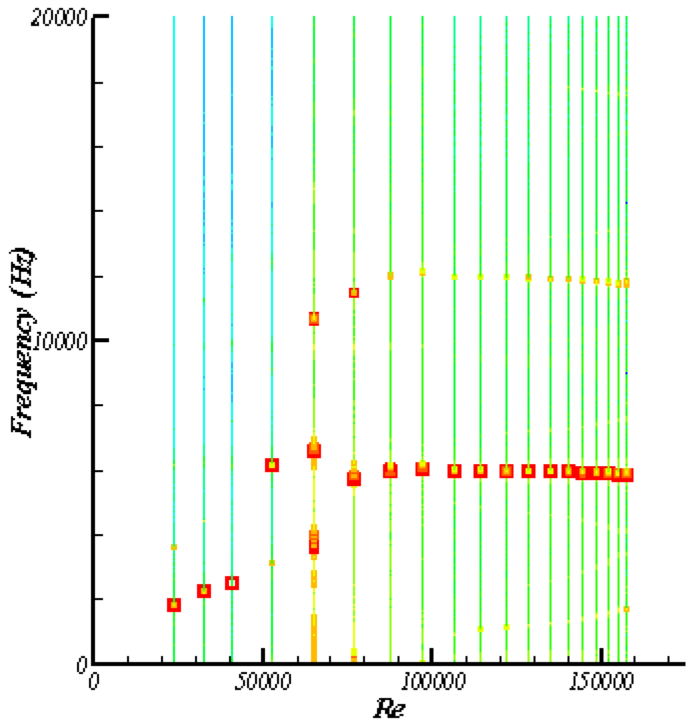

Figure 4.3.1. Variation of frequency with Reynolds number for L_c/D_j = 1.75, D_j/D_p = 0.375 and D_j/D_e = 0.9 (geometry - Figure 2.2d)

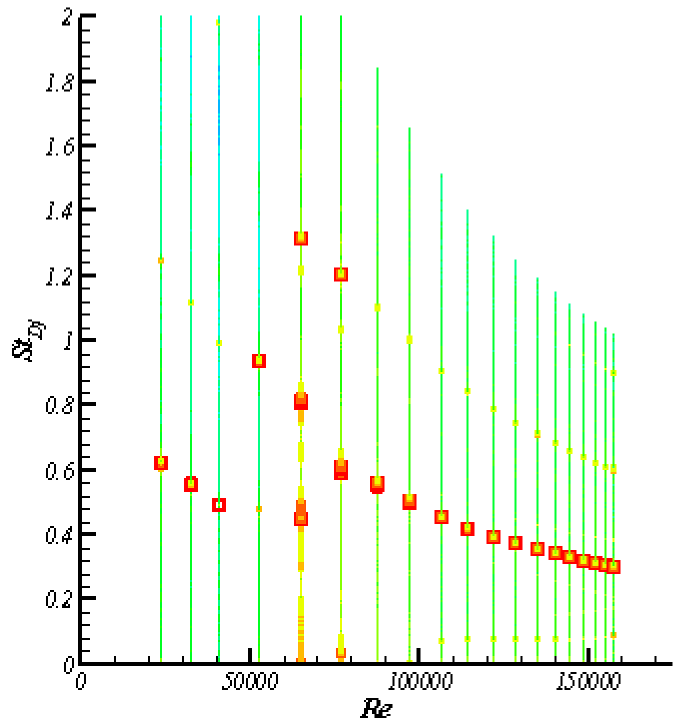

Figure 4.3.2. Variation of Strouhal number, based on cavity inlet diameter, with Reynolds number for L_c/D_c = 1.75, D_j/D_p = 0.375 and D_j/D_e = 0.9

As can be expected, St_D corresponding to the oscillating frequencies (thicker regions of the lines), decreases with increasing Reynolds number. To determine possible modes involved in the oscillation, results of Strouhal numbers from the case of Figure 4.3.1 are plotted against theoretical values of cavity modes and acoustic modes of the pipe. This is shown in Figure 4.3.3. Cavity modes are calculated based on the feedback relation discussed in the section on hole tones. It is repeated here for clarity. An estimate of the time required for a hydrodynamic disturbance wave to cross the cavity length and the time required for an acoustic wave to travel back to the leading edge (jet exit) is given by the criterion

$$\frac{n}{f} = \frac{L_c}{u_c} + \frac{L_c}{a}$$

where, 'n' is the mode number, 'f' is the frequency, 'L_c' is the spacing between the plates, u_c is the convection velocity and 'a' is the speed of sound. The mode number n is usually an integer. But recent investigations have shown that both integer and non-integer numbers are possible. Integer mode numbers correspond to cases where vortex rings are shed at every half cycle when the pressure perturbations are positive. Values between $0.5U_j$ and $0.6U_j$ are typically used for the shear layer convection velocity. Acoustic modes were calculated using standing wave solutions for a closed cylinder with rigid ends and is given by:

$$\omega = c\left[\left(\frac{j'_{m,n}}{r}\right)^2 + \left(\frac{q_z \pi}{L_c}\right)\right]$$

where, ω is the resonant frequency determined based on the azimuthal (m), radial (n) and axial (q_z) modes and $j'_{m,n}$ is the $(n+1)^{th}$ positive zero of the derivative of Bessel function.

At low speeds, the frequencies agree well with the first shallow cavity mode. This confirms that the primary mechanism is the feedback process from the impingement surface (trailing edge). But at higher speeds, the frequencies agree with the first acoustic radial mode based on the pipe diameter. It should also be pointed that the radial mode was present in the spectra even at low speeds. Figure 4.3.4 shows the pressure spectra for the same configuration at low Reynolds number flow. Even though the radial mode is present, its amplitude is less than the cavity mode by more than 20dB. The trend of the peaks at higher speeds follows the pattern of the theoretical value of the acoustic mode. A typical spectrum at high speed for the same configuration is shown in Figure 4.3.5. The major peak f_0 corresponds to the first radial acoustic mode of the pipe. Harmonics of f_0 shows significant energy present in them. This is a typical identifier of a process called wave steepening. Oscillations such as in this study have finite amplitudes and wave steepening could be expected. The questions of how such a process affects the oscillations by forming weak shock waves are not addressed in this study. It would be appropriate and important to examine this in future studies. Other peaks of interest are marked f_m, f_0-f_m and f_0+f_m. An animation of the pressure spectra for all the tested Reynolds number was made for this configuration. A collage of the frames in the animation is shown in Figure 4.3.6. Each frame represents a different Reynolds number corresponding to the mass flow rate shown in the

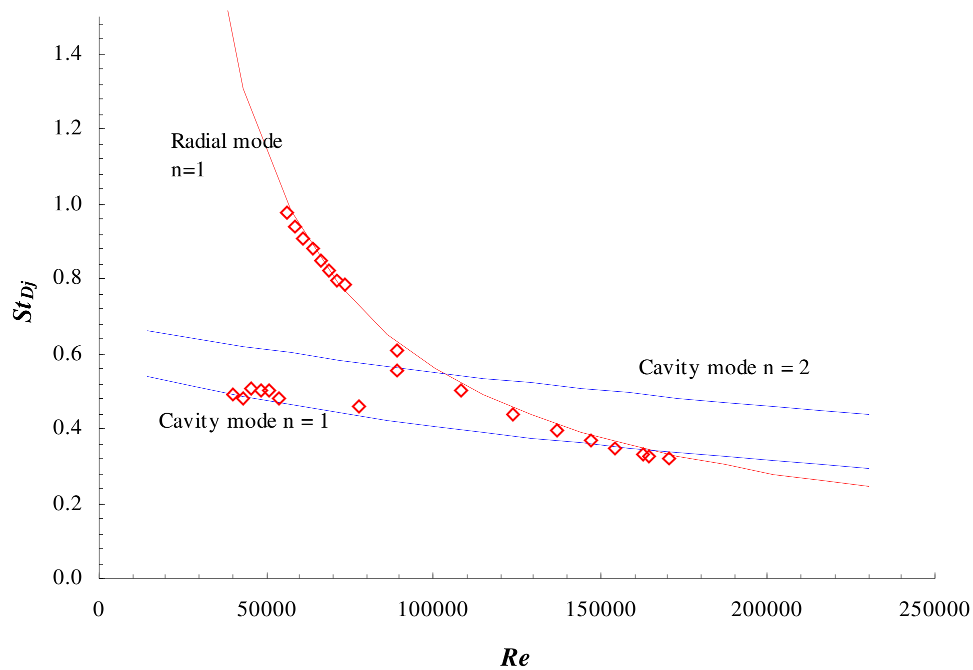

Figure 4.3.3. Comparison of frequencies of oscillation from experiments with theoretical cavity and acoustic modes (same configuration as in Figure 4.3.1)

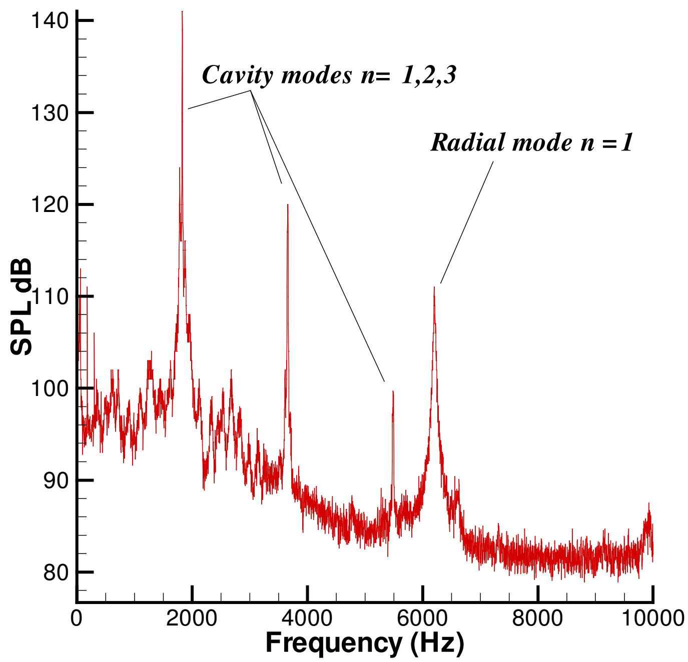

Figure 4.3.4. Pressure spectrum at low Reynolds number (configuration same as in Figure 4.3.1)

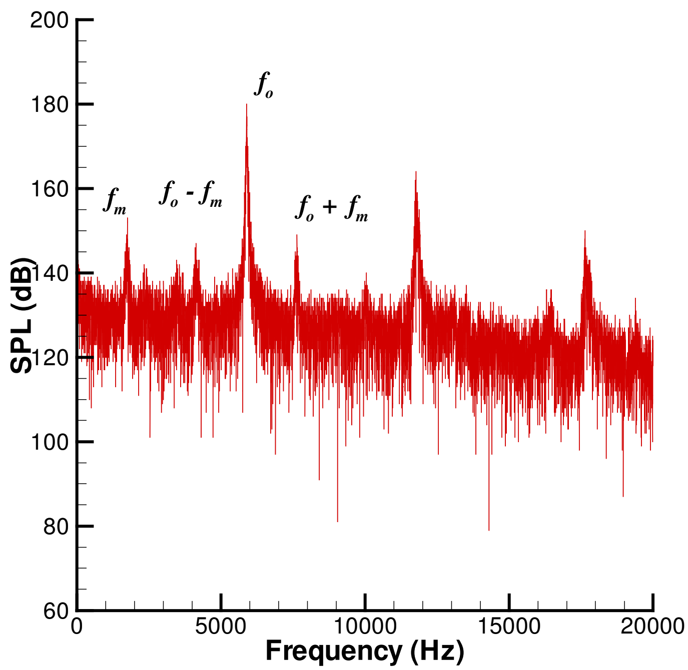

Figure 4.3.5. Pressure spectrum at high Reynolds number (same configuration as in Figure 4.3.1)

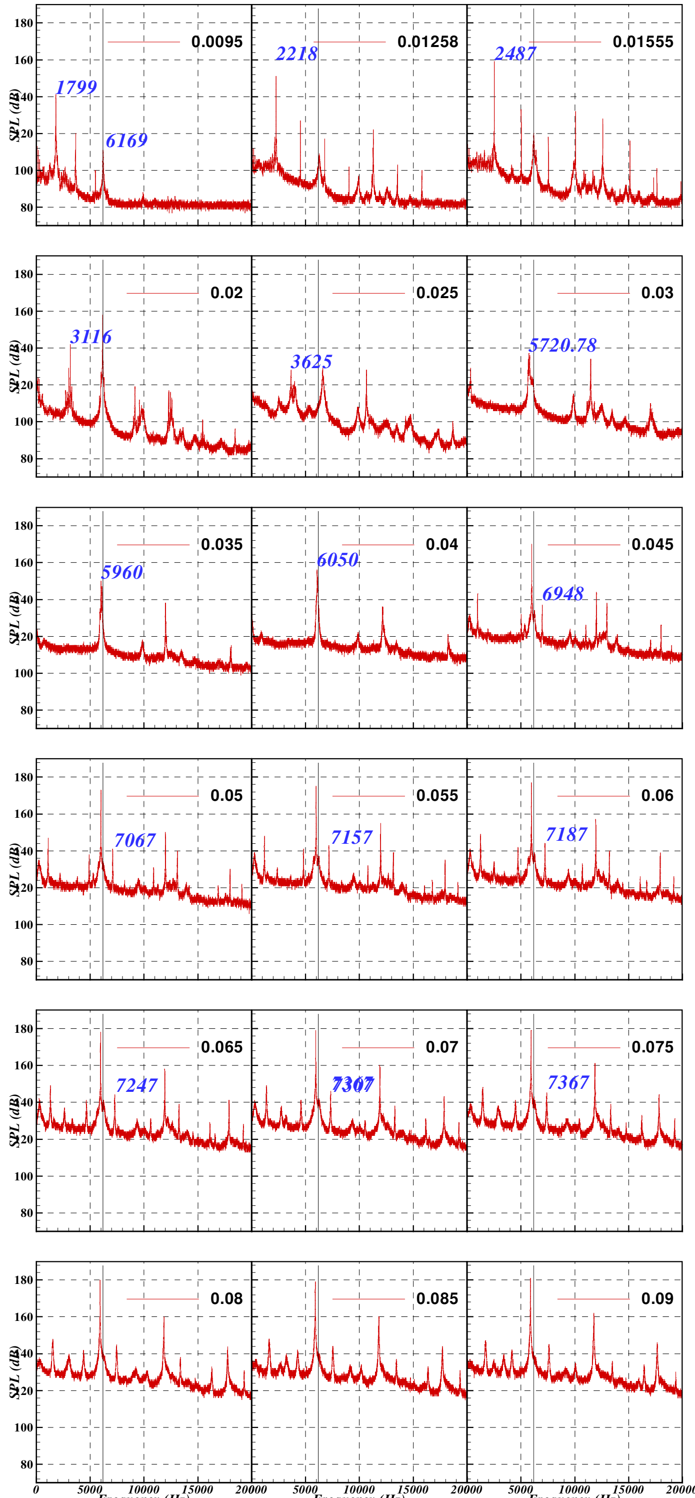

Figure 4.3.6. Pressure spectra showing the variation of cavity and acoustic modes

legend. The cavity modes and its frequency is also plotted. The straight line at about 6000Hz represents the acoustic radial mode. The animation clearly showed that both shallow cavity mode and the radial acoustic mode are present. But based on the flow condition, they modulate each other. At certain instances, the cavity mode was predominant. But in most cases within the range of this study, the radial mode was amplitude modulated and dominated the spectrum. The peak f_m is present in the spectrum due to the superimposition of the peaks f_0 and f_0+f_m or f_0-f_m. Based on this evidence, it is concluded that resonance is setup between the shallow cavity mode and the radial acoustic mode. This opens up a lot of opportunities that can be exploited to produce multi-frequency control mechanisms of a jet using a single passive geometry. The modulating frequency, the left and right hand side bands vary with velocity (another indication that it is dependent on convective mechanisms rather than just an acoustic mode which depends solely on the geometry). This variation is plotted in Figure 4.3.7. Maximum amplitude oscillations were observed when the cavity mode was within a small range from the acoustic frequency. Further study is necessary to carefully investigate this process and to be able reproduce it in a controlled manner so that it can be used to produce custom waveforms. Even though agreement with radial tones was obtained, it was evident during experiments that rotation was involved. At certain operating conditions, the baffles rotated despite having been fastened in place very tightly. It is not clear how axial and radial acoustic modes combine to produce helical or rotational fluid motions. Another possibility that needs further evaluation is that the frequency seen in the spectra is a composite frequency due to the combination of axial and helical modes. This resonance was observed in cavities with L_c/D_c values 1.5 to 2.0. Highest amplitudes were obtained for an L_c/D_c ratio of 1.75 and when inlet to exit diameters remained between 0.9 and 1. Sound pressure level inside the cavity reached in excess of 180dB for several cases. Highest amplitudes were observed when the flow conditions were such that the first cavity mode reached within range of the radial acoustic mode. Even though the second mode of the cavity oscillations raised the amplitude of the radial acoustic peak when it passed through, the peak amplitude was not as high as it was for the first cavity mode.

Testing at higher flow rates was restricted by a restraint on the transducer. Even though the transducer was rated for 50 PSID, at conditions above 25 psi, a phenomenon of very localized temperature rise due to the oscillations occurred that were high enough to burn the transducers (rated for 250˚C). Further details regarding this phenomenon are presented in Appendix A.

Effect of Geometric Parameters

Figure 4.3.8 shows the frequency of oscillations for different L_c/D_c ratios of the same configuration as in Figure 4.3.1. Corresponding Strouhal numbers are plotted in Figure 4.3.9. Based on the results in the previous section, the cavity length to depth ratio Lc/Dc should be able to produce oscillation in a range close to the radial acoustic mode of the pipe. Figure 4.3.8 and Figure 4.3.9 show that the resonant behavior is observed only for certain L_c/D_c ratios and under particular flow conditions. A complete analysis for many configurations showed that this resonant behavior is present only for L_c/D_c ratios between 1.5 and 2.5. At other conditions, resonance is

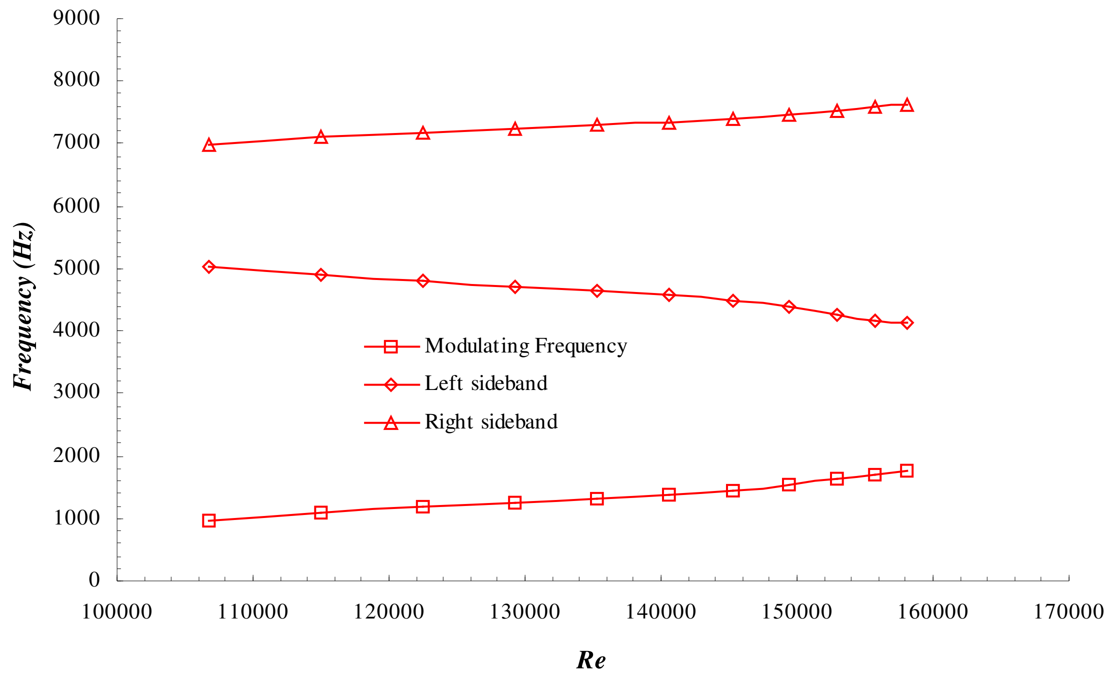

Figure 4.3.7. Variation of the modulating frequency and the side bands (same configuration as in Figure 4.3.1)

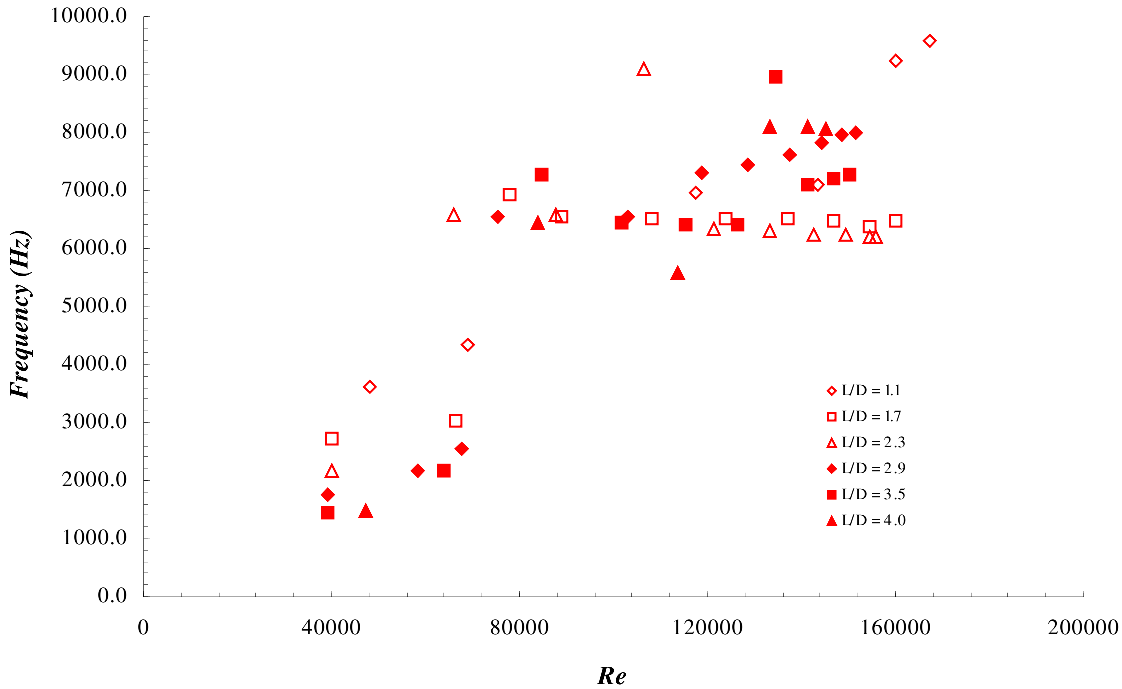

Figure 4.3.8. Variation of frequency of oscillation with L_c/D_j with different Reynolds numbers

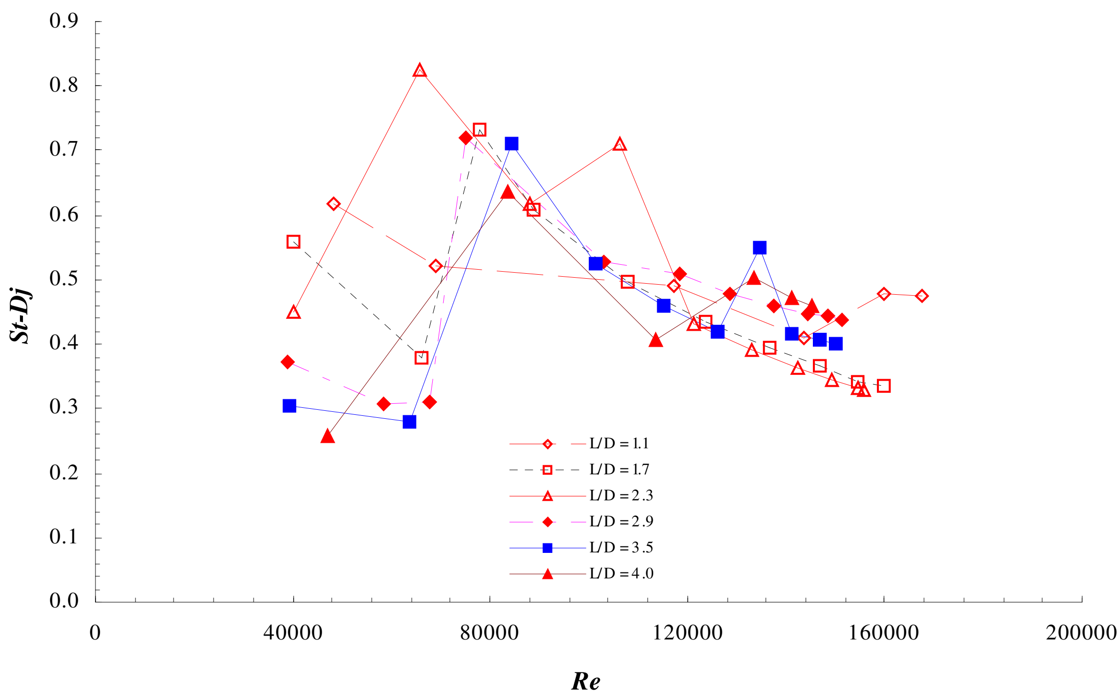

Figure 4.3.9. Variation of Strouhal number with L_c/D_j with different Reynolds numbers

either present for a very small period of time or the frequencies increases with jet speed. In cases where the frequencies continue to increase, the amplitude of the oscillations was not very high. Frequencies observed for L_c/D_c ratios of 1.75 and 2.3 are very close but different. This implies that even though the radial acoustic mode is excited, the resulting frequency in the pressure spectra has been modulated by the cavity mode. This is very clear in the high Reynolds number regime. Also note that at high Reynolds numbers, the frequency is lower for the larger L_c/D_c ratio of 2.3. Dependency on the length was very clearly shown when a baffle rotated during the oscillations. Figure 4.3.10 shows data from two cases. In the first case, the baffle started rotating during the oscillations resulting in an increased L_c/D_c ratio. When this rotation was noted, the run was repeated with the baffles securely fixed and making sure that the baffles does not move. Usually the exit baffle rotates. The inlet baffle rotates only when the exit baffle has been placed so tightly that it cannot rotate. Figure 4.3.10 clearly shows the dependence of oscillation frequency with length of the cavity even though it is a slowly varying function. For the non-rotating case, the frequency remained constant between 6500 and 6550 Hz in the Reynolds number range of 110000 to 170000. When the baffle was rotating increasing L_c/D_c ratio, the frequency starts shifting downwards going from about 6550 to 6250 Hz. Based on these results that the cavity length to depth ratio is an important parameter in terms of controlling the waveforms of excitation applied to the jet.

Effect of expansion ratio (D_j/D_p) is shown in Figure 4.3.11 respectively. For lower expansion ratios (not shown in figure), the range of mass flow rate during which any oscillations were observed was very small. Having larger expansion ratios extended the mass flow rate range during which oscillations can be observed. This is because the flow through smaller orifices chokes much quicker than the larger orifices. After the flow reaches the choking point, it was observed that the pressure spectra became relatively clean of any significant peaks. The experiments in this study did not isolate this parameter and any specific conclusions related to its effect on the frequency of the oscillations could not be made. Based on the discussions so far, it should not have a significant effect on the frequencies directly. However, it can have an effect indirectly by controlling the depth of the cavity that can be achieved for a particular configuration.

Effect of the cavity inlet to cavity exit diameter ratio (D_j/D_e) is shown in Figure 4.3.12. The ratio between inlet and exit diameters determines the portion of the jet that can pass directly through the exit. When the inlet diameter is much smaller than the exit diameter, the jet can pass through the exit without much hindrance. When the inlet diameter is much larger than the exit diameter, the exit plate blocks a large portion of the jet. In a system, where the oscillating mechanism is due to the interaction of elements in the jet with the trailing edge, this is an important parameter to be considered. D_j/D_e and D_j/D_p are inter-related based on the geometry and a more careful study with geometry designed specifically to isolate these parameters have to be employed in future studies.

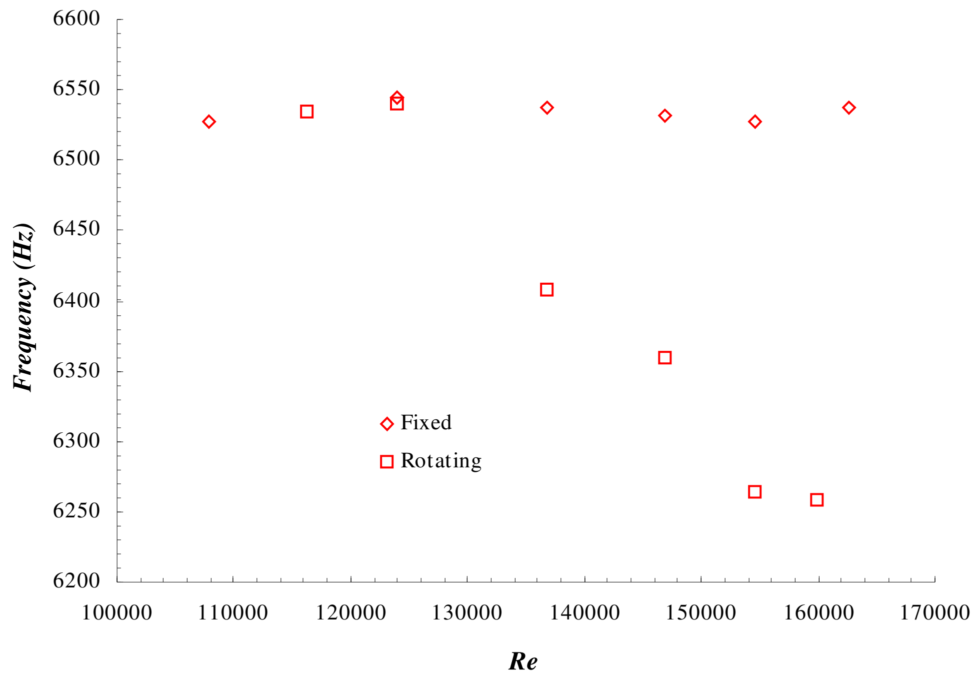

Figure 4.3.10. Variation of frequency with increasing cavity length (data taken when the exit baffle rotated and compared to the case when the baffle was not rotating – same configuration)

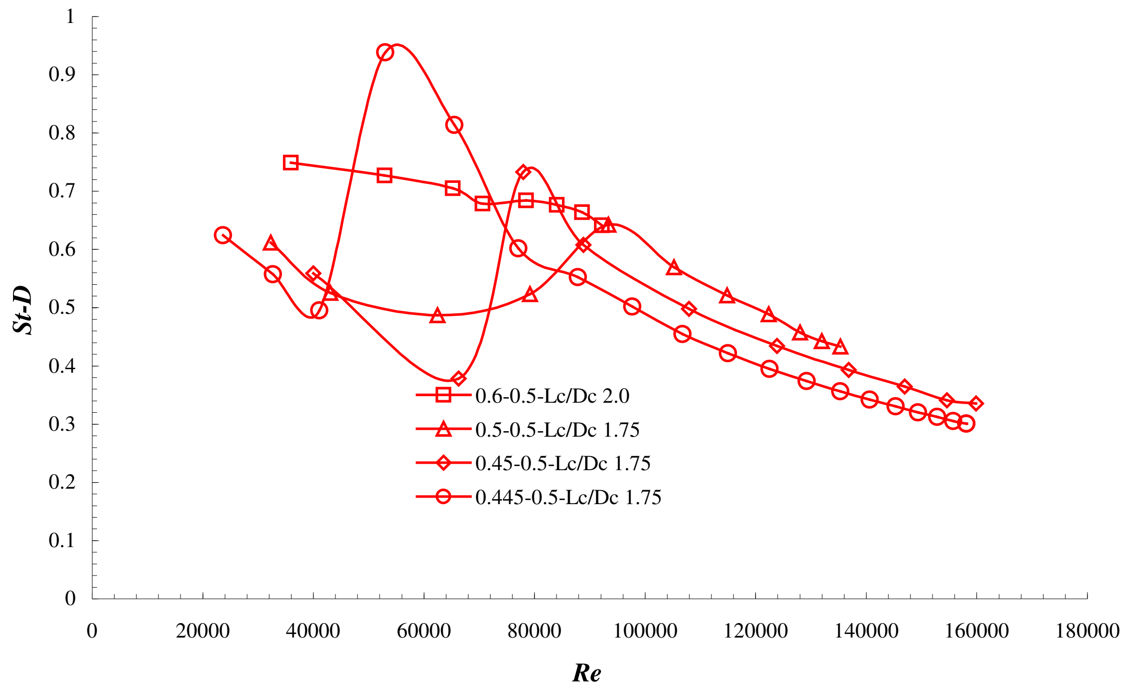

Figure 4.3.11. Effect of expansion ratio (D_j/D_p)

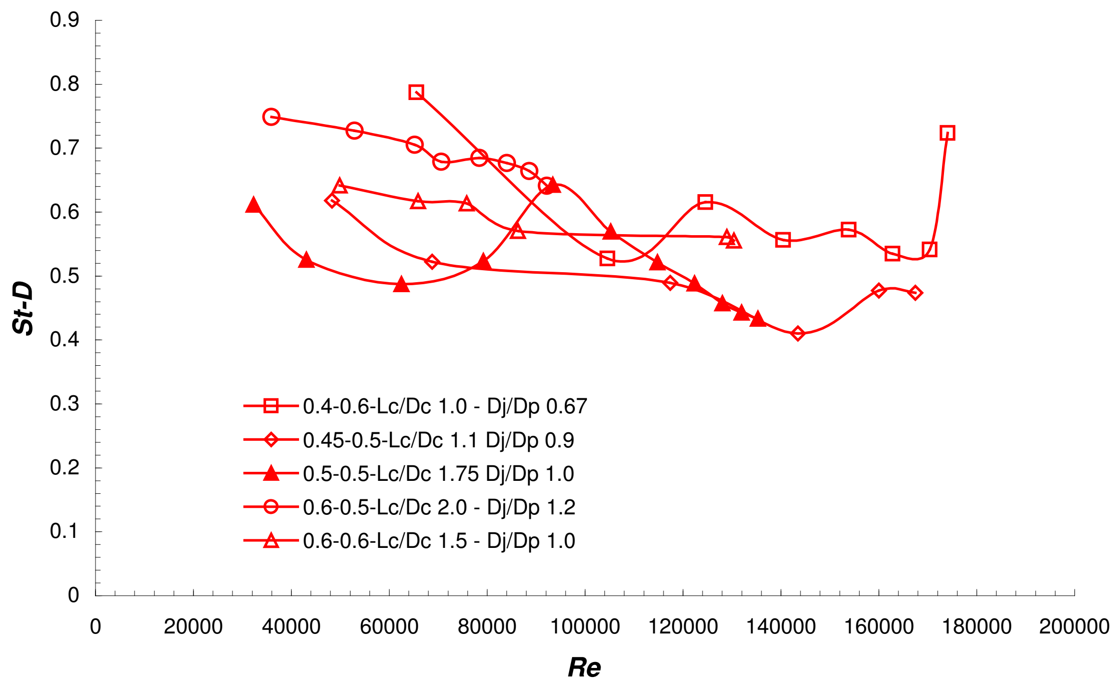

Figure 4.3.12. Effect of inlet to exit diameter ratio (D_j/D_e)

4.3.3. Amplitude Analysis

Variation of SPL

Figure 4.3.13 shows variation of the oscillation amplitude with Reynolds number for three L_c/D_c ratios, which exhibited the previously discussed resonance. Plotted values correspond to the sound pressure level of the major peak in the pressure spectra. Sound pressure level generally increases with Reynolds number. At certain regions, the SPL level drops before starting to increase again as observed in the hole tone cases. It also shows that L_c/D_c ratios 1.5 and 1.75 have significantly higher amplitudes than for L_c/D_c ratio of 2.0 even though it also exhibits the resonant condition. Cavities with L_c/D_c ratio 1.75 had oscillations in excess of 180 dB within the cavity. Peak to peak values were in excess of 100000 Pa (Figure 2.6).

Figure 4.3.14 shows variation of the oscillation amplitude with Strouhal number for three L_c/D_c ratios, which exhibited resonance. Higher amplitudes were observed for oscillations with St_D values between 0.2 and 0.6.

4.3.4 Flow Visualization and Velocity Measurements

Velocity measurements were taken using PIV in the near field of the jet for different configurations at selected Reynolds numbers. Instantaneous and Phase averaged measurements were taken to study and understand the flow structure in the jet and the growth of the jet. At low speeds, symmetric vortex rings were observed in the near field of the jet. This is consistent with the pressure measurements, which showed that the cavity mode dominates and the radial acoustic mode has much lower amplitude. As the mass flow rate is increased, the symmetric vortex rings become asymmetric or irregular. When resonance condition is set, the vortex structures become very complex. A selected few images for a configuration with $D_j/D_e = 0.9$ and $L_c/D_c = 1.75$ at jet velocity $U_j = 300$ m/s ($Re_D = 210000$) is shown in Figure 4.3.15. These figures clearly show that the vortex structures are no longer symmetric. Also note the significant widening of the jet and the asymmetry in the image of the jet.

Since these oscillations could have some cycle-to-cycle variations, Phase-averaged measurements were made so that the major features of the oscillation cycle are revealed. Figure 4.3.16 shows phase-averaged images for an L_c/D_c ratio 1.75. Images shown are from -90° to 90° from the reference signal. Figure 4.3.17 shows phase-averaged images for a different Reynolds number. The averaged images clearly show helical modes dominating the flow structures outside the cavity.

Figure 4.3.18a shows velocity vectors contours for L_c/D_c ratio 1.75 and D_j/D_e ratio 1.0. Figure 4.3.18b shows the corresponding vorticity contours. The degrees specified in the figures correspond to the phase difference of that particular phase condition with the reference signal from the cavity. Many images show a helical type vortex structure. Azimuthal instabilities have been shown to improve mixing characteristics of jets. They increase mixing by assisting in the break down of coherent structures. Unlike symmetric rings, they cannot transfer momentum to longer distances. It is evident from the figures that vortex merging and jet meandering, mechanisms identified with increased mixing are present.

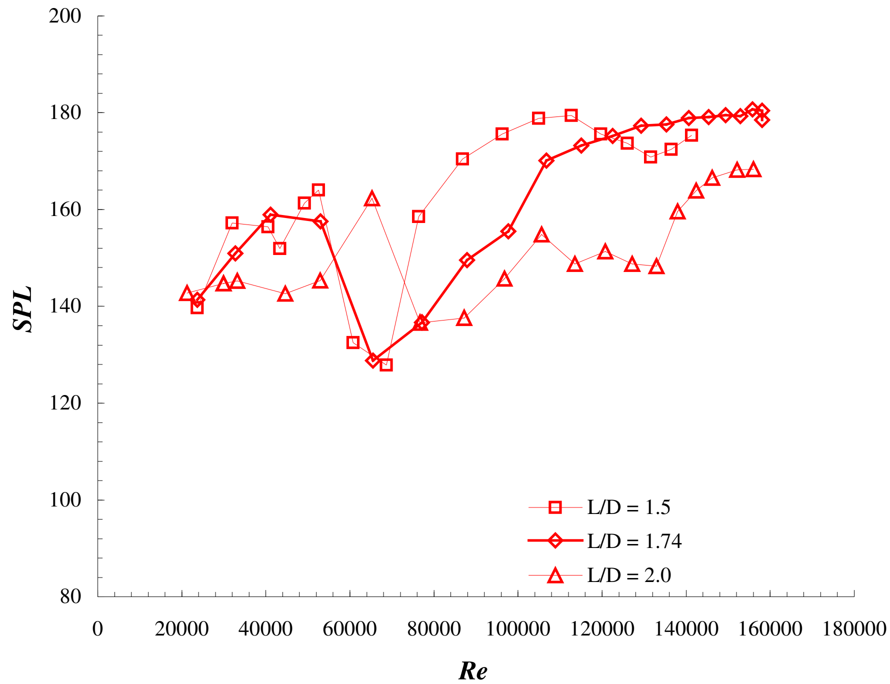

Figure 4.3.13. Variation of sound pressure level (SPL) with Reynolds number

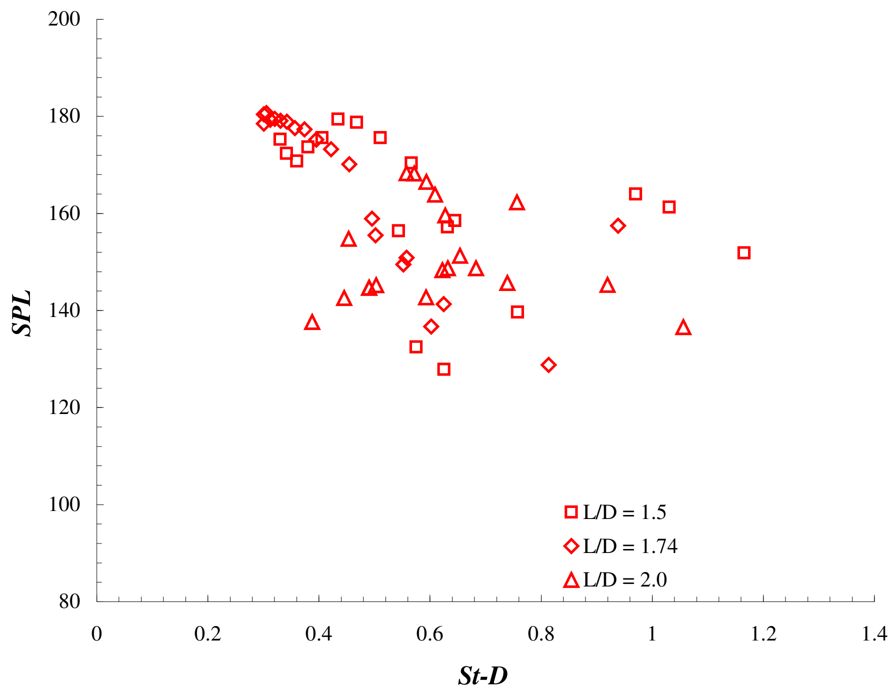

Figure 4.3.14. Variation of sound pressure level (SPL) with Strouhal number

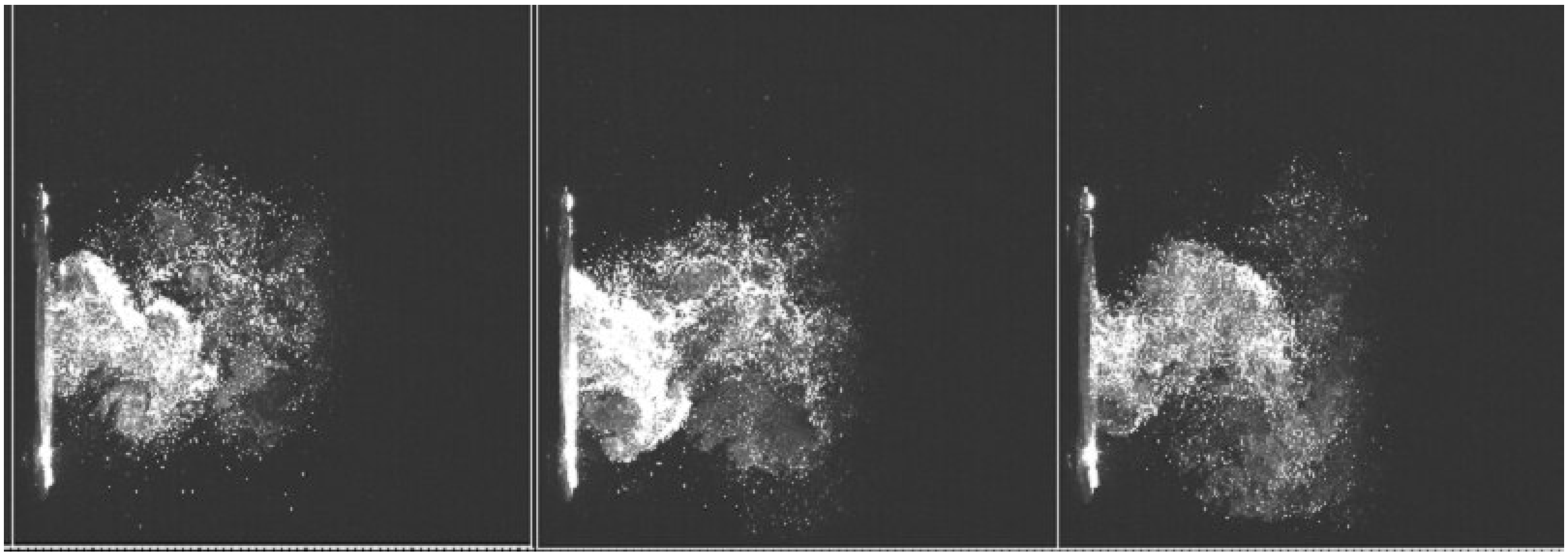

Figure 4.3.15. Typical instantaneous figures obtained from PIV ($L_c/D_c = 1.75, U_j = 210000$)

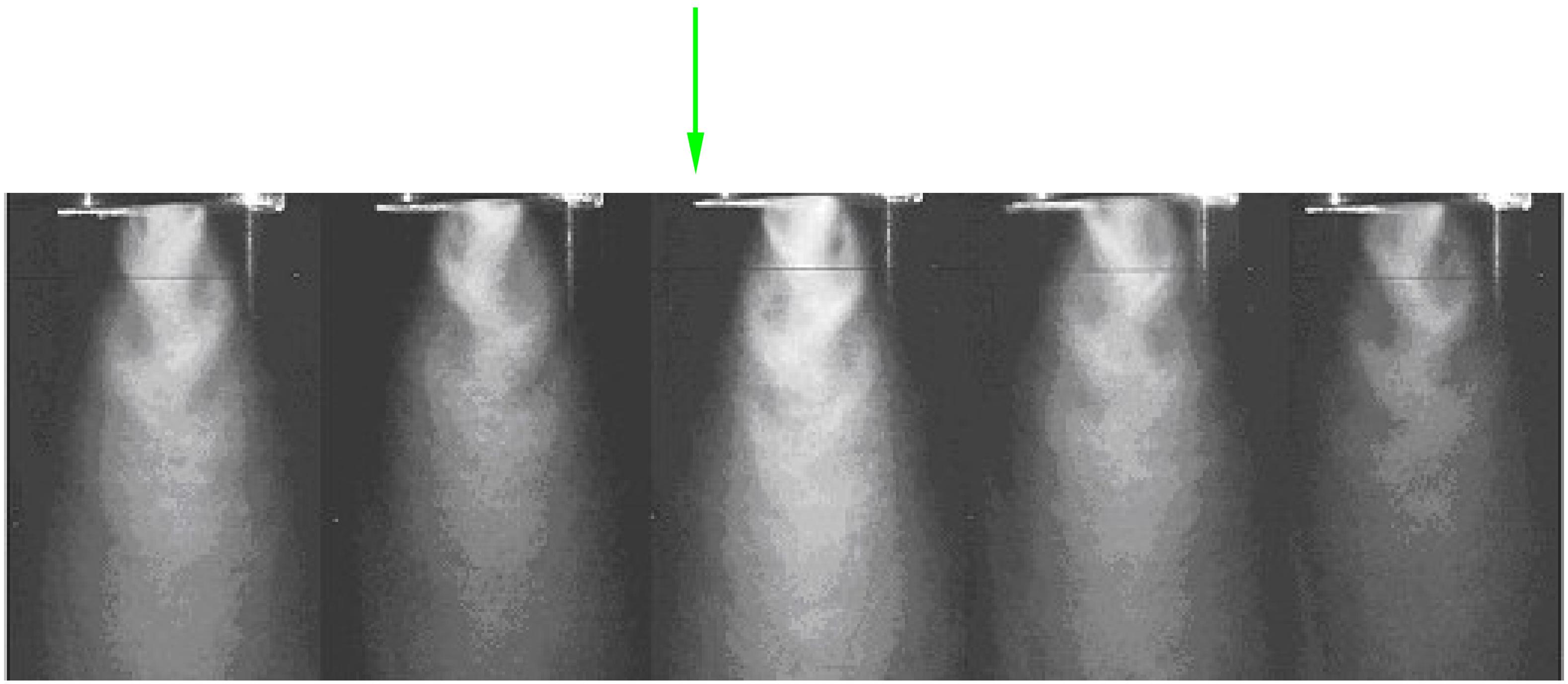

Figure 4.3.16. Phase-averaged images obtained from PIV. (L_c/D_c = 1.75,U_j = 250 m/s) Each figure separated from its neighbors by a phase angle of 90˚

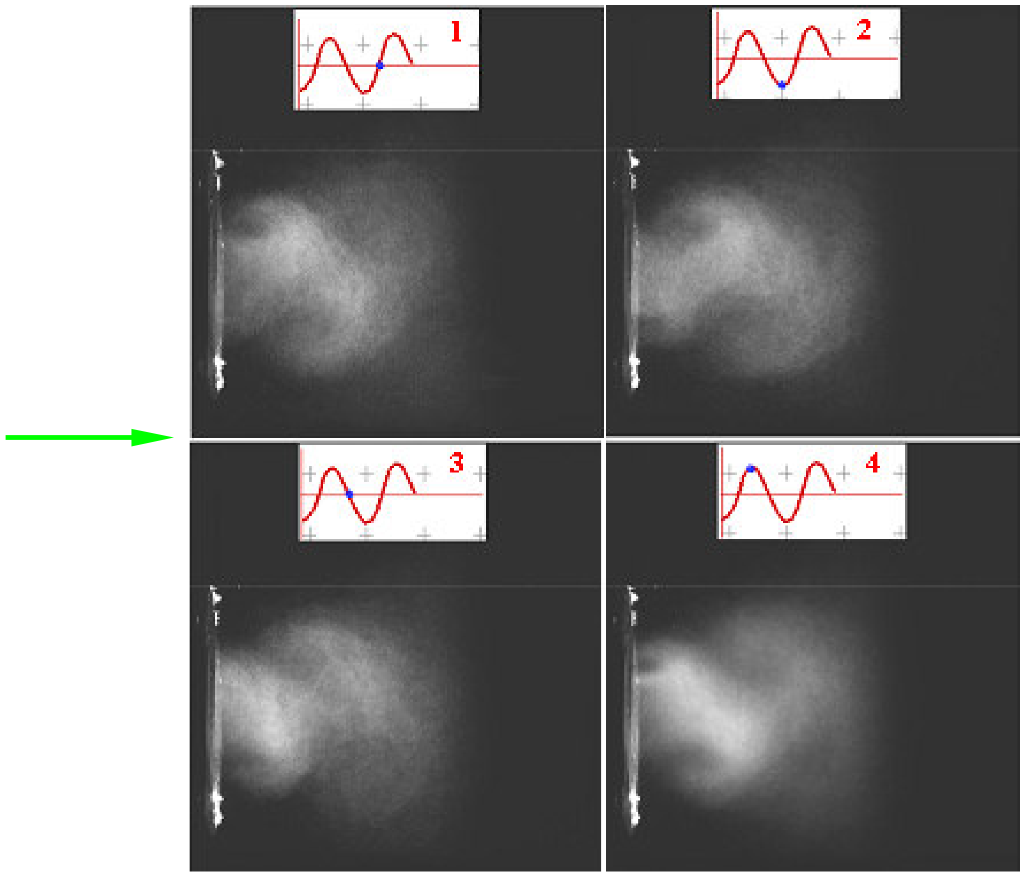

Figure 4.3.17. Phase-averaged images obtained from PIV. ($L_c/D_c = 1.75, U_j = 300$ m/s) Each figure separated from its neighbors by a phase angle of 90˚

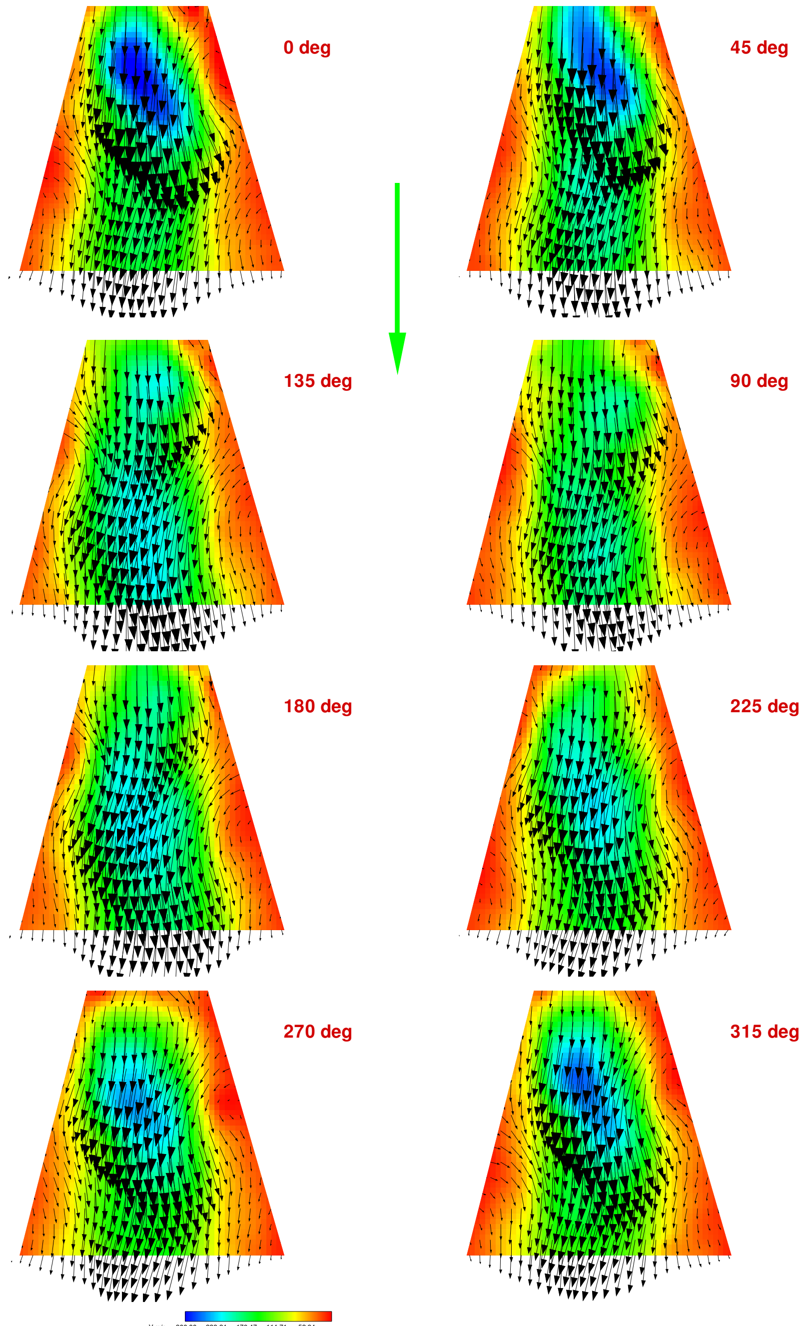

Figure 4.3.18. Phase-averaged flowfield in streamwise direction (L_c/D_c = 1.75,U_j = 300 m/s). a) axial velocity contours and vectors

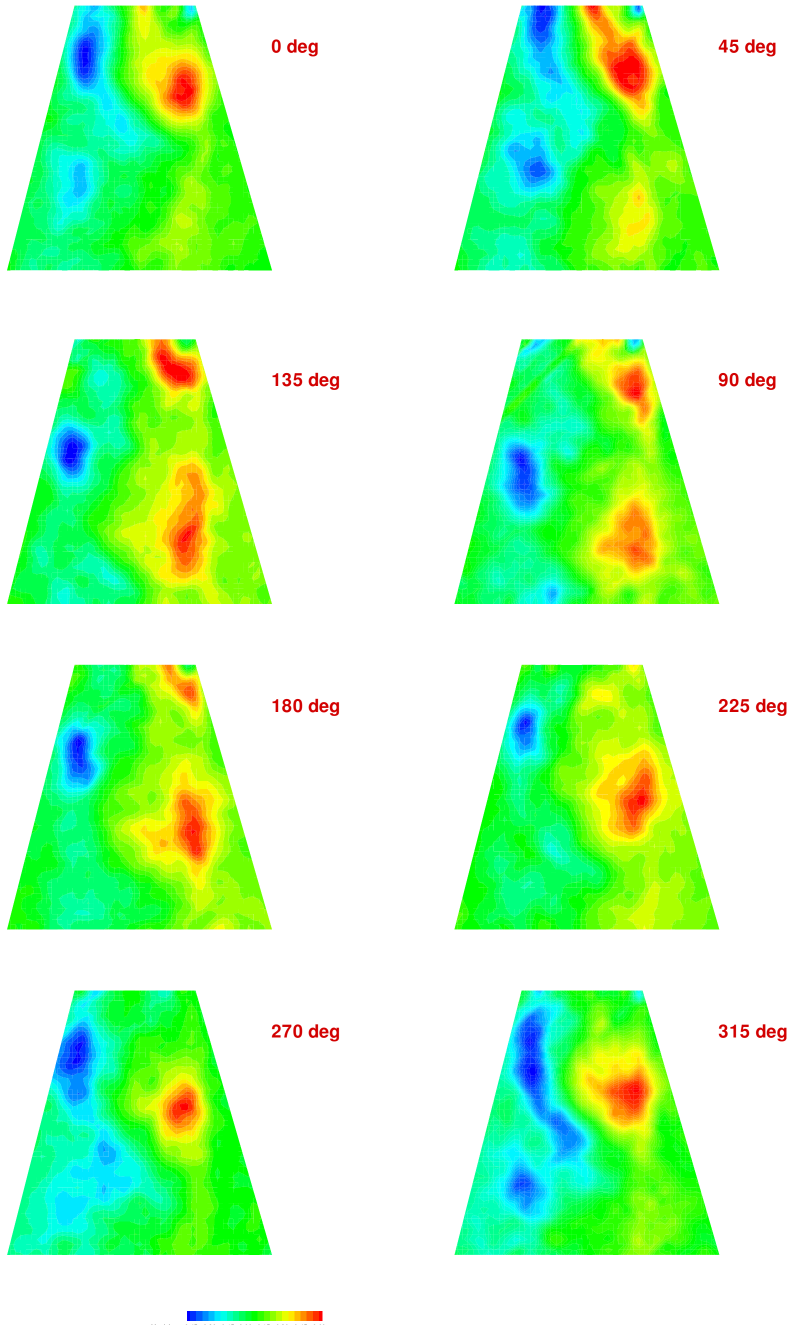

Figure 4.3.18. Continued. b) vorticity contours

To confirm that the jet is rotating or precessing, PIV measurements were taken along the cross section of the jet. Figure 4.3.19a show velocity vectors taken along the cross section o fthe jet about one jet diameter away from the exit. Figure 4.3.19b shows vorticity contours and two components of the velocity in the cross sectional plane. These figures clearly show that the vortices are rotating or precessing. It was not able to confirm whether the jet is precessing or rotating about the center of the jet. The rotational velocities are significant compared to the axial velocity. Both components have velocities about 10% of the axial velocity. Energy in the flow has to be used to drive this rotation. This should result in the decline of centerline velocity much quicker than if the rotation is not present.

Many investigators have used a combination of axial and azimuthal forcing to enhance mixing. Usually forcing is accomplished using powerful speakers very close to the jet exit. In this case, the cavity performs the function of the speaker. The cavity produces very high amplitude forcing waveforms that acts on the jet at the exit. As mentioned in the introductory chapter 1, the disadvantage in using speakers is that speakers capable of producing high amplitude oscillations in practical cases are not feasible at this time. Future goal of this work would be to effectively acquire control over the waveform available at the jet exit through a combination of axisymmetric cavity and the pipe diameter.

4.3.5 Effect of Inlet/Exit Boundary Condition

Different inlet and exit boundaries were used to form the axisymmetric cavities. The available geometries were orifices, a 0.5 inch constant diameter short pipe 2 inches long and a contoured nozzle. These geometries correspond to those discussed as the baseline configurations. The configurations discussed so far in regarding axial jet actuators had orifices for both the inlet and exit boundaries. For the first case, the inlet boundary was replaced with the short pipe. Pressure spectra showed that the oscillation frequencies were very similar to those of the orifice boundaries. Unlike in the hole-tone case, the amplitudes were also similar to that of the orifices. Figure 4.3.20 shows representative instantaneous images from this case. The flow structures also look very similar to those of the orifices discussed previously with helical mode structures in the near field.

The second variant of the axial jet actuator that was tested had the short pipe as the exit boundary. Pressure spectra showed that the oscillation frequencies were similar to that of the orifice boundaries. But their amplitude was slightly lower at most Reynolds numbers. But the flow structures showed marked differences especially at intermediate Reynolds numbers. Figure 4.3.21 show phase averaged images from this configuration for L_c/D_c ratio 1.75 at about 150 m/s. The flow structures show axisymmetric rings at all phases. As discussed previously, for many practical applications, the requirement is a trade off between concentrated momentum and distributed momentum. Axisymmetric vortex rings are capable of carrying momentum through large distances, which is attractive for applications requiring penetration through a cross-flow. Figure 4.3.22a shows velocity contours corresponding to the flow and geometric conditions in Figure 4.3.21. Figure 4.3.22b shows corresponding vorticity contours for different phases. The

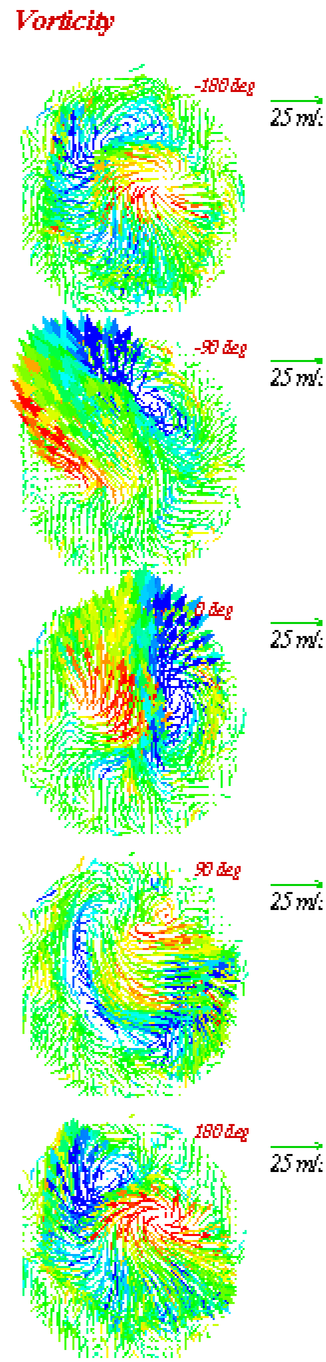

Figure 4.3.19. Phase averaged flowfield in the cross-section of the jet (L_c/D_c = 1.75 and U_j = 250 m/s, about $1D_e$ away from the exit). a) velocity vectors

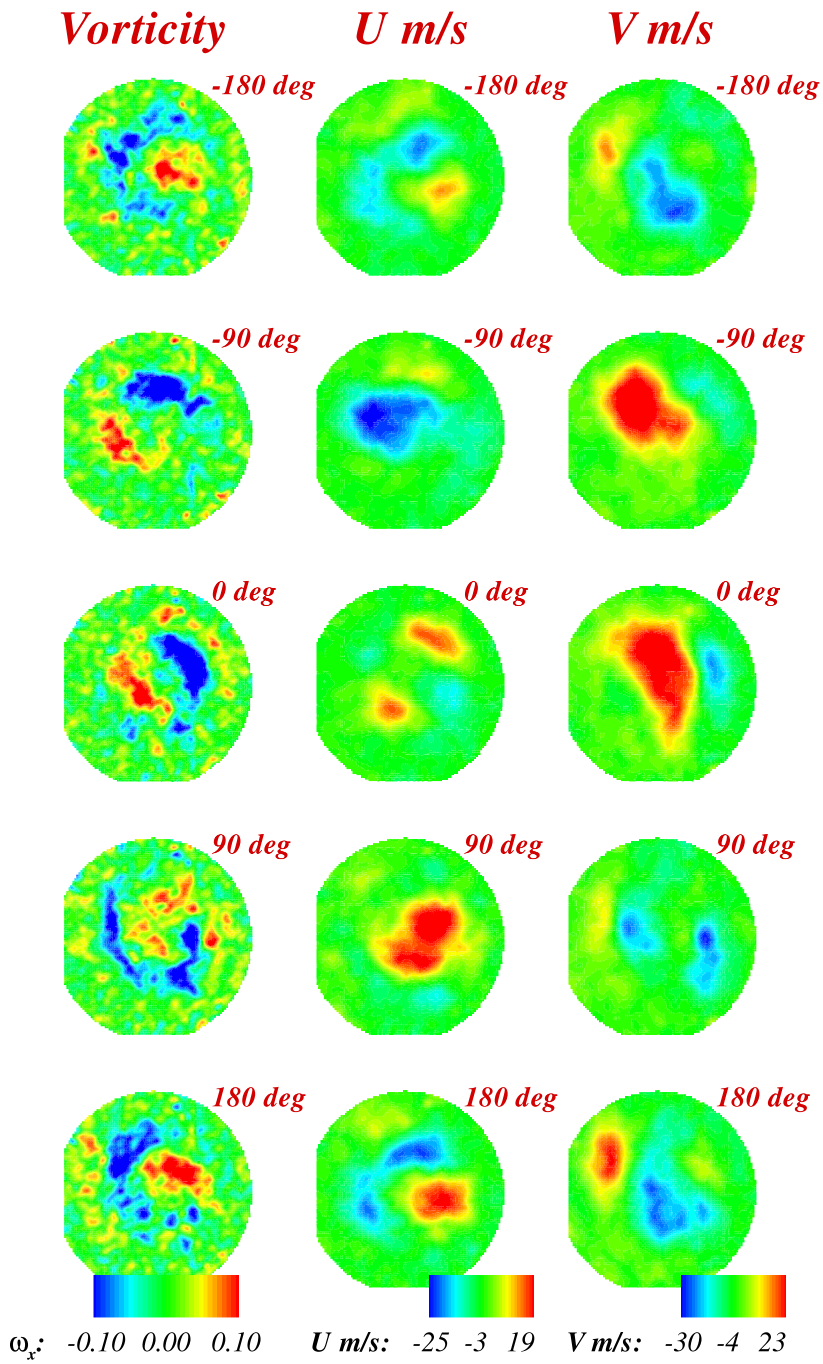

Figure 4.3.19. Continued. b) vorticity and velocity contours

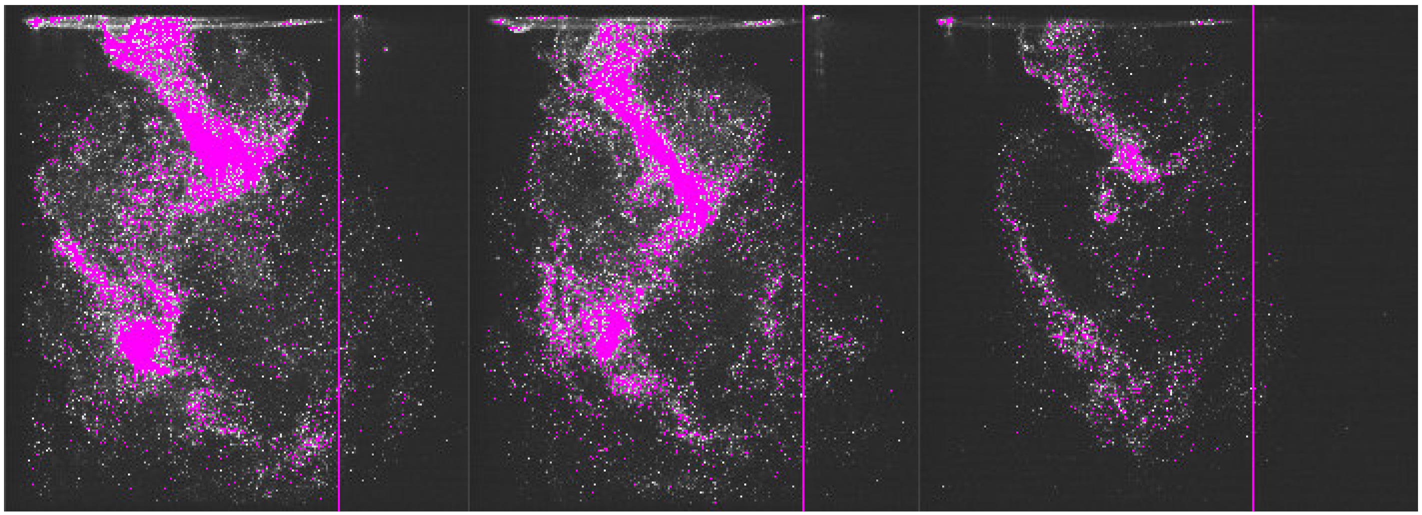

Figure 4.3.20. Representative instantaneous images for an axial jet actuator with a short pipe inlet and an orifice for the inlet exit boundaries of the axisymmetric cavity

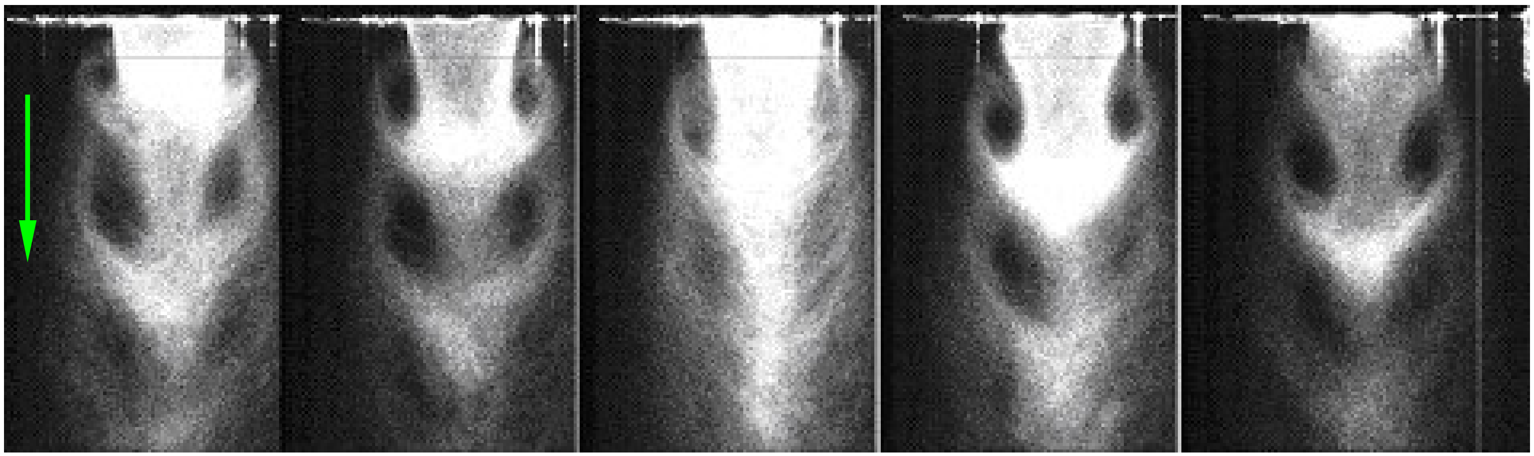

Figure 4.3.21. Phase-averaged images obtained from PIV. (L_c/D_c = 1.75,U_j = 150 m/s) Each figure separated from its neighbors by a phase angle of 90˚

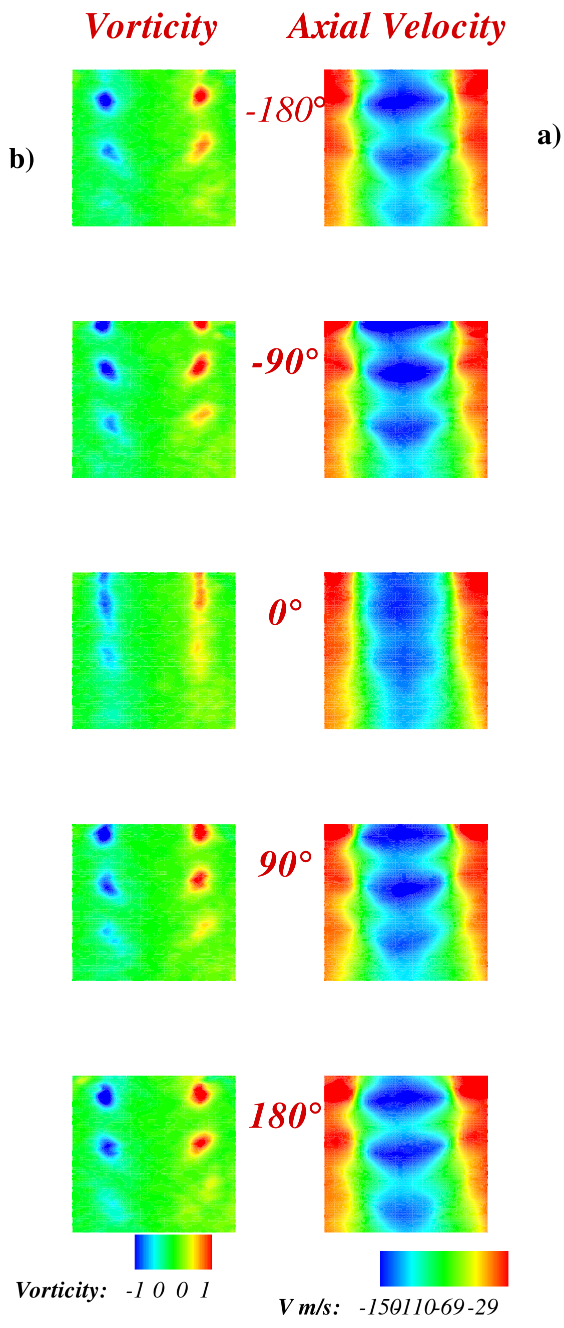

Figure 4.3.22. Phase-averaged vorticity and velocity contours for an axial jet actuator with a short pipe as the exit boundary (L_c/D_c = 1.75, U_j = 150 m/s)

presence of symmetric rings and the puffs of high velocity regions are very clear from the figures. At higher Reynolds numbers, the vortex rings were not as large and visible as in the low speed conditions. However, when the swirling strength technique was used to find the presence of vortices, one could find symmetric vortex rings in the shear layer. Figure 4.3.23 shows this using the phase-averaged image of one phase condition. Figure 4.3.23a shows the vorticity contour. The rings are not discernible in the vorticity contours. Figure 4.3.23b shows contours of swirling strength. The axisymmetric rings present in the shear layer are clearly shown.

The reason why a constant diameter pipe removes the helical modes could be because they the momentum carried by helical structures are distributed much quicker than an axisymmetric vortex ring. If the axial jet actuator with orifice boundaries could be analogous to an acoustic driver placed very close to the jet exit, an axial jet actuator with a short pipe of constant diameter as the exit boundary could be analogous to an acoustic driver placed far away from the jet exit (usually at the opposite end of the pipe). The reason why the oscillations are not as pronounced at high Reynolds number is not clear. The short pipe jet tested in this study had a fixed length of 4 jet diameters. The effect of its length in filtering the helical mode has to be further studied if at all there is a dependency.

Images taken in the cross-section of the jet revealed the rings very clearly as shown in Figure 4.3.24. In the case of orifice boundaries, such rings were not visible even though one could see helical type vortex structures in the images and velocity field in the streamwise direction.

4.3.6 Comparison with Baseline

Comparison with baseline is made using PIV images of the actuated jets. Figure 4.3.25 shows averaged images from the baseline (short pipe jet) and averaged images from the configuration in Figure 4.3.18. These images show that lateral jet spread has increased significantly due to these oscillations. Individual images of the baseline and the axial jet actuator were taken with similar velocity calibrations. So the images can be compared directly. Figure 4.3.26 shows the flow structures in the baseline, the axial jet actuator with orifice boundaries and the axial jet actuator with the pipe jet exit. These images were not taken with the same calibration. The axial jet actuator images are the phase averaged images of one phase condition and the baseline image is an ensemble average. The difference in flow structures and the different modes of forcing is apparent (no forcing/non-axial forcing/axial forcing).

Comparison with baseline is made using images taken along the cross-section of the jet at similar distances from the exit of the cavity. Figure 4.3.27 shows images from the baseline the axial jet actuator with orifice boundaries and the axial jet actuator with the pipe jet exit. All three images were taken with similar velocity calibration. So they can be compared directly. It is very clear that the size of the axial jet actuator with orifice boundaries has grown very significantly compared to the baseline jet. The axisymmetric vortex ring produced by the axial jet actuator is also clearly visible. Jet width of the non-axial forcing is much larger than the baseline and the axial forcing case.

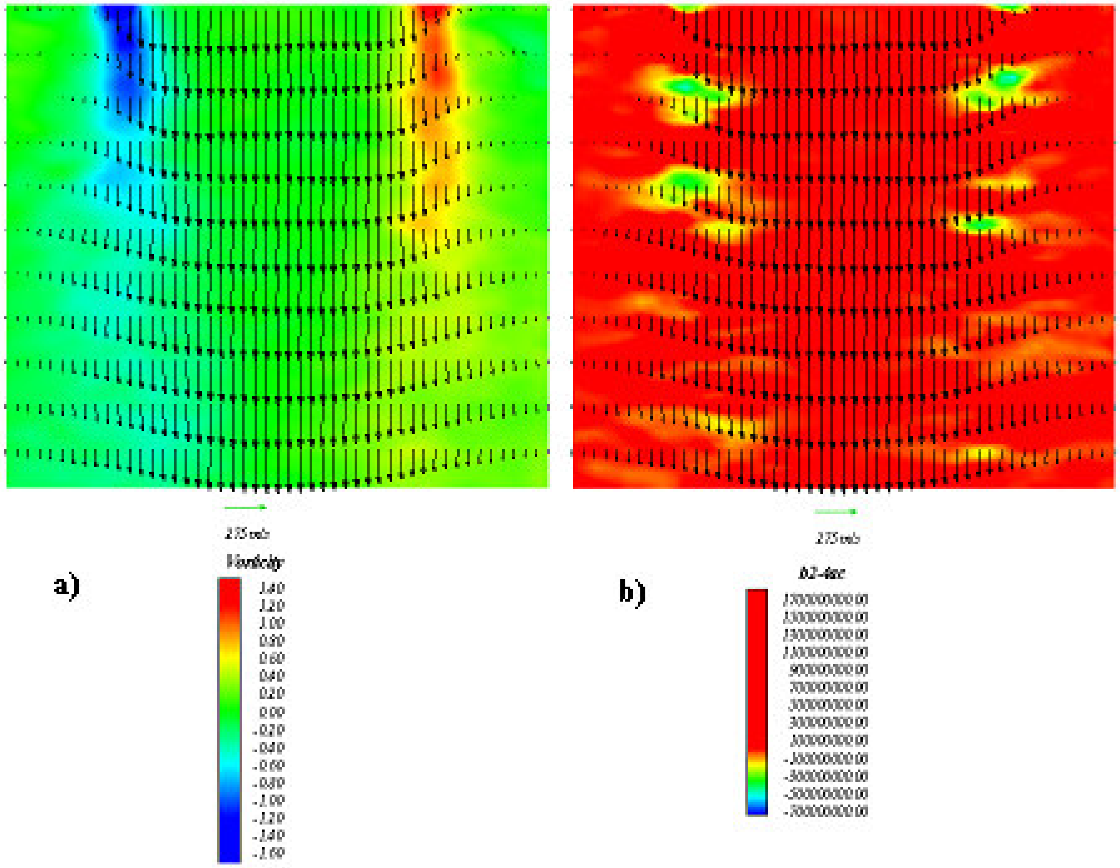

Figure 4.3.23. Presence of axisymmetric vortex ring at high Reynolds numbers. a) vorticity contour b) swirling strength

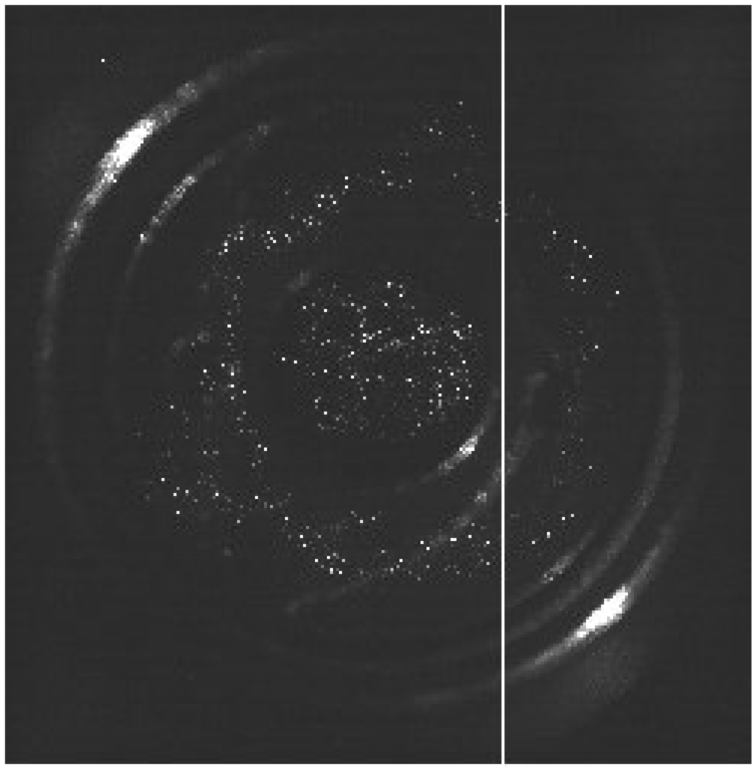

Figure 4.3.24. Axisymmetric vortex ring captured through an image in the cross section of the jet

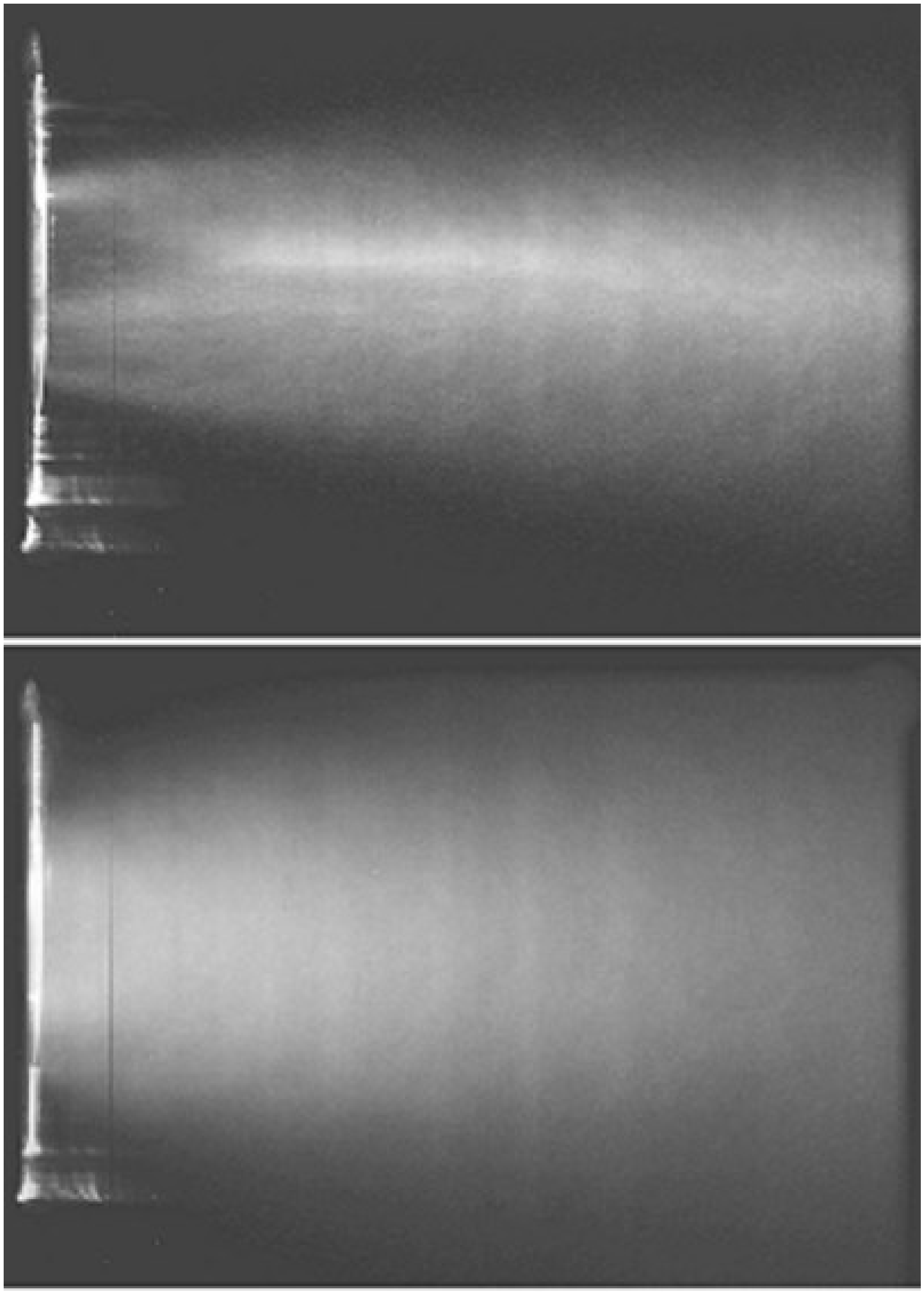

Figure 4.3.25. Comparison of axial jet actuator (geometry of Figure 4.3.1) and baseline ensemble averaged images. Exit diameters and mass flow rate same for both cases. (Figure on top – baseline)

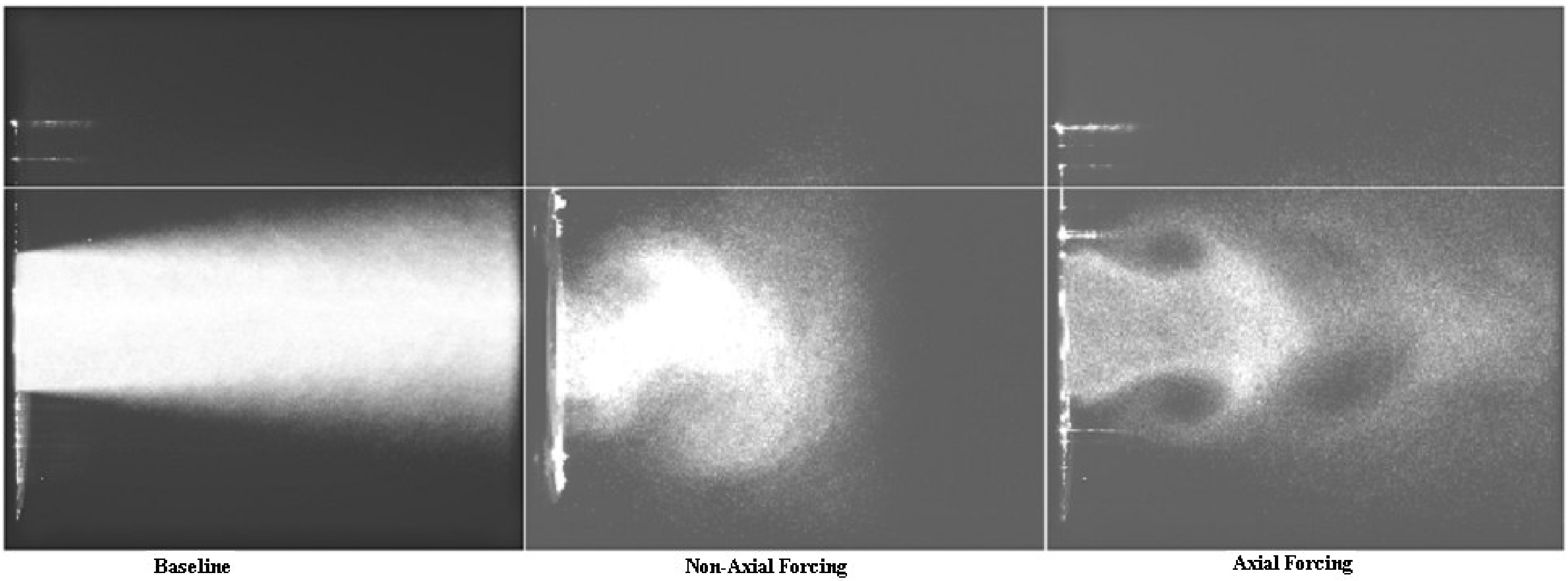

Figure 4.3.26. Flow structures in the baseline, non-axial forcing and axial forcing cases (streamwise direction)

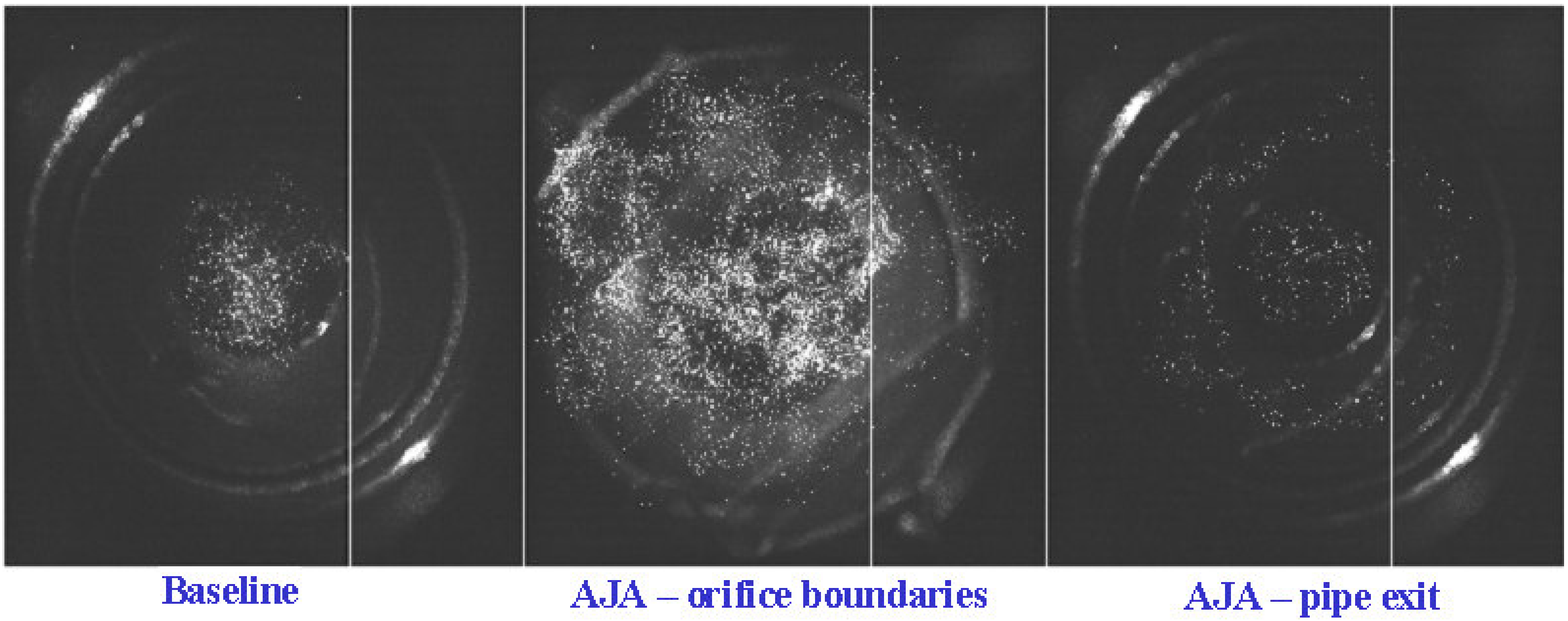

Figure 4.3.27. Flow structures in the baseline, non-axial forcing and axial forcing cases (along jet cross section)

As mentioned in the introduction, centerline velocity decay is a direct result of the jet spreading in the lateral direction and hence an increased mixing. Decay of centerline velocity for the baseline and the axial jet actuator with orifice boundaries is plotted in Figure 4.3.28. The centerline velocity of the axial jet actuator starts to decay from very close to the exit compared to the baseline jet. The baseline jet's potential core extends up to 5Dj whereas for the axial jet actuator the potential core length is less than 1D. However, it has to be noted that the decay rate after $X/D_e = 2.0$ appears to be similar to that of the baseline jet. This implies that the effect of the oscillation is most pronounced in the near field.

When the trailing edge of the cavity was replace by a contraction nozzle with the smallest diameter being upstream, at certain conditions, the jet started to precess in addition to the oscillations due to the cavity. This could be very suitable in certain applications. Figure 4.3.29 shows a few instantaneous images from this condition.

Based on the discussions, it can be concluded that the axial jet actuator with orifice boundaries performs the best in terms of jet entrainment. The cavity length to depth ratio that performed the best was for L_c/D_c ratio 1.75. Axial jet actuators with the short pipe as the exit boundary produced axial oscillations only.

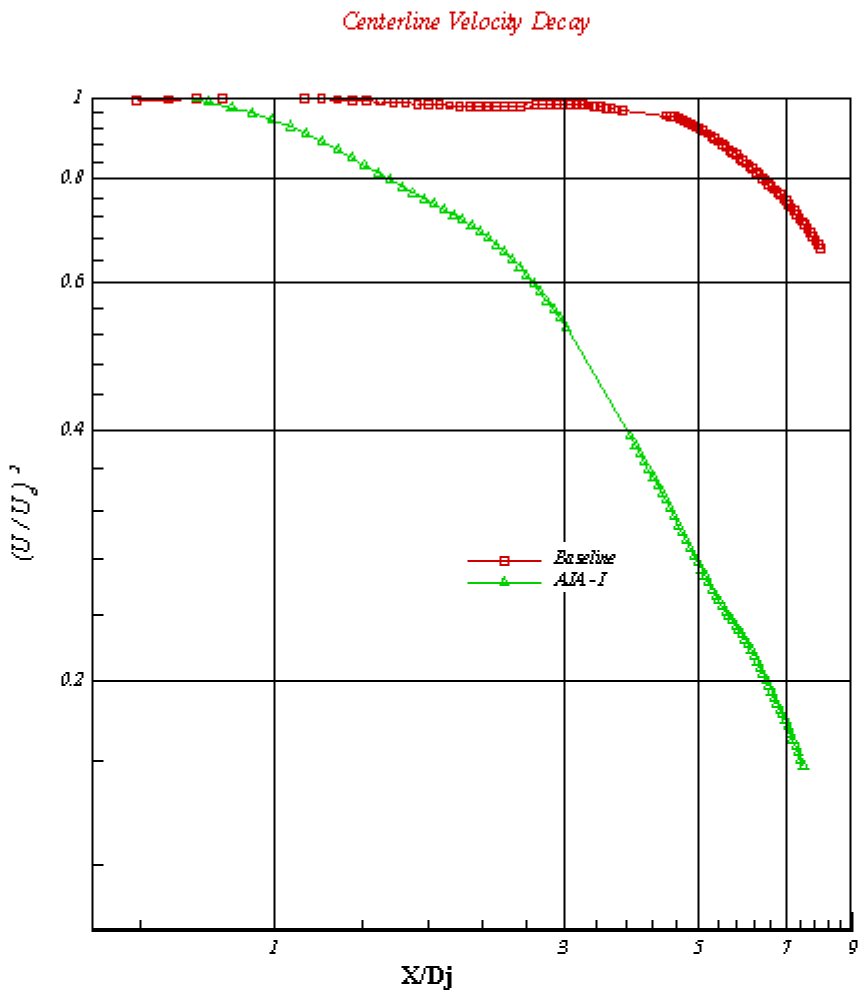

Figure 4.3.28. Comparison of velocity decay

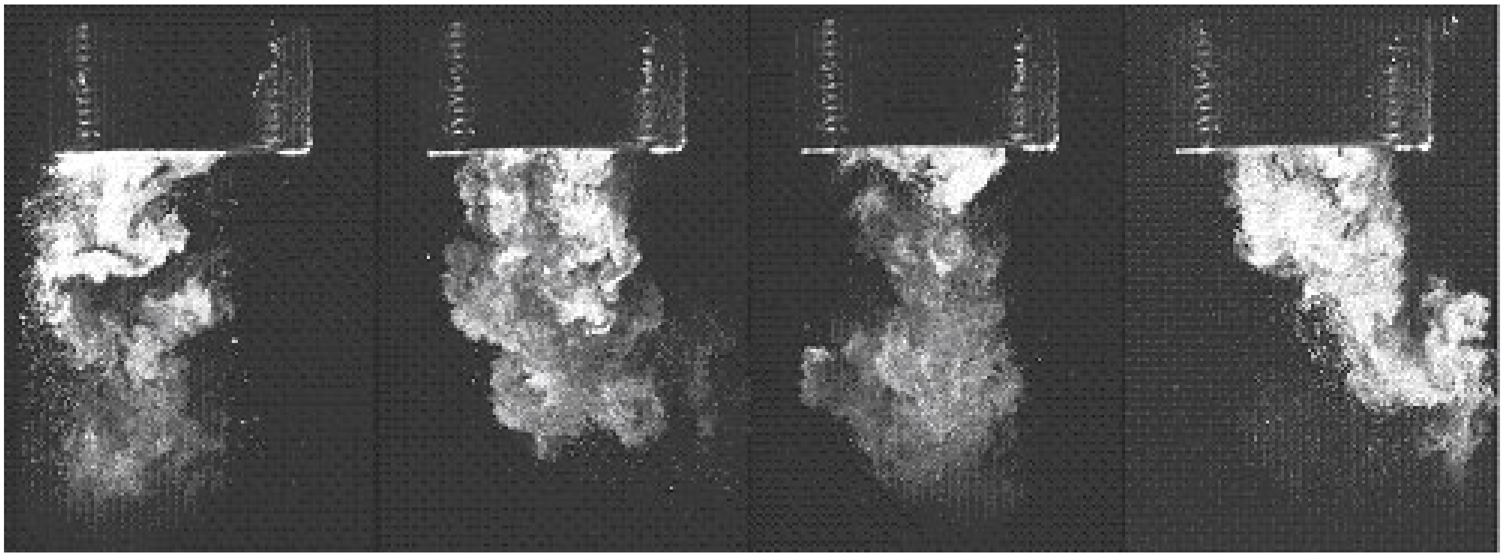

Figure 4.3.29. Precessing jet due to an axisymmetric cavity and an inverted contoured nozzle

Chapter 05

Conclusions

Flow of jets passing over axisymmetric cavities was studied and demonstrated as a potential jet actuation mechanism. Adaptive control can be achieved by varying cavity length to depth ratio and pipe diameter based on the desired forcing frequencies. Effect of geometrical length scales and boundary conditions of the cavity on the actuation frequency and amplitude were studied. Focus of the investigation was to understand basic physics behind the oscillations and their effect on turbulent jets so that results of this study may be used for either enhancing or suppressing relevant processes.

Tests were conducted on a) baseline turbulent, jet b) jet passing through open axisymmetric cavity (infinite depth) placed at the jet exit, c) jet passing through an enclosed axisymmetric cavity placed at the jet exit. Tests were performed with air over a Reynolds number, based on jet exit diameter, range of 40000 to 225000 in low to high subsonic jet flow conditions.

The following conclusions were drawn regarding naturally occurring processes (baselines) that help in the growth of turbulent jets:

1. Vortex rings/structures which are formed in the near field shear layer merge (coalesce) with adjacent rings and grow until they breakdown due to instabilities.
2. Both axial and helical instability modes were present, at different conditions and times, in the near field of the jet flow. The presence of these modes is important because they bring ambient fluid in contact with the jet fluid, a first step in any type of mass and momentum transfer.
3. Unsteady structures that have a large inward flux of ambient fluid at their tip regions and asymmetry in the velocity profile play an important role in the large scale mixing of jet and ambient fluids.
4. Orifice jet had the highest growth rate in the near field based on its shortest potential core length, centerline velocity decay, lateral spread rate, near field turbulent intensity and volumetric flow rate increase in the axial direction. A contoured nozzle and a short pipe jet had the second and third highest growth rates. The increased mixing in an orifice jet was found to be due to the presence of larger structures near the exit and their tendency to be quickly transformed into three-dimensional flow fields.

The following conclusions were drawn regarding an axisymmetric cavity with its periphery open (infinite depth cavity, or “hole-tone”).

1. Distinct tones were heard and corresponding peaks were present in pressure spectra. The major peak in the pressure spectra was well predicted by a feedback relation based upon vortices generated near the leading edge impinging on the trailing edge and the length scale being the cavity length.
2. PIV measurements (phase averaged and instantaneous) captured both symmetric and asymmetric vortex formations within the cavity. Asymmetric shedding occurred more consistently with shorter cavity lengths and with the slightest non-parallelism between the upstream and downstream plates.
3. Axisymmetric CFD analysis showed the impinging vortex dividing into two sections in greater detail. One section traveled through the orifice and the other traveled along the inner side of the downstream plate and continued to grow through sub-harmonic evolution. It is conjectured that the stationary vortex within the cavity (fed by the vortices traveling along the wall) provides a length scale and explain the presence of the amplitude modulating frequency in the experimental pressure spectra.

The following conclusions were drawn regarding the oscillations and the flow field of axisymmetric cavities of different L_c/D_c ratios with closed peripheries that were placed at the jet exit.

1. At low Reynolds numbers, shallow cavity tones were clearly present and the flow contained vortex ring structures in the near field of the jet, for a wide range of L_c/D_c ratios.
2. At low Reynolds number flows, frequency of the oscillation increases with increasing jet speed.
3. At higher Reynolds number flows, for cavity L_c/D_c ratios between 1.5 and 2.0, a resonant condition existed and the major peak in the pressure spectra remained constant for a wide range of speeds changing only in amplitude.
4. Resonance takes place when the axial shallow cavity mode is close to the radial acoustic mode of the axisymmetric cavity.
5. Amplitude of the oscillations at resonant condition was very high (in excess of 180dB within the cavity for L_c/D_c ratio 1.75).
6. Significant widening of the jet was observed in the near field at resonance.
7. Significant reduction in the length of the potential core of the actuated jet was observed (less than 1D for an actuated jet versus 5D for a baseline jet at similar flow conditions).
8. Flow structure in the near field depended on the inlet and exit boundaries of the cavity. Cavities with sharp orifice boundaries had complex helical mode structures in the jet flow direction. These structures were rotating about the jet axis as observed in phase averaged measurements.

9. Only symmetric vortex rings were observed when a short pipe was used for the exit boundary of the cavity.

The following recommendations are made to continue this investigation.

1. Further studies towards amplitude modulation processes could allow users to have multi-frequency control with a single complex geometry. Multi frequency control has the possibility to allow for custom waveforms of the oscillations.
2. High order of accuracy 3D modeling of the flow in these geometries are needed to simulate and study the formation and evolution of complex acoustic and vortical wave structures within the cavity and the near field.
3. Study finite amplitude flow oscillations and its relationship with possible shock formation and oscillations in the flow.
4. Further testing is recommended to study the heat separation phenomenon observed.

LIST OF REFERENCES

Agrawal A, and Prasad A, “Organizational Modes Of Large Scale Vortices In An Axisymmetric Turbulent Jet”, Flow, Turbulence and Combustion **68**: 359-377, 2002

Agrawal A, and Prasad AK. “Measurements Within Vortex Cores In A Turbulent Jet”, Journal of Fluids Engineering **125**(3): 561-568, May 2003

Agrawal A, Prasad AK, “Integral Solution Of The Mean Flow Profiles Of Turbulent Jets, Plumes And Wakes”, Journal of Fluid Engineering, **125**: 813-822, 2003

Bakewell P, and Lumley JL, “Viscous Sublayer And Adjacent Wall Region In Turbulent Channel Pipe Flow”, Physics of Fluids **10**: 1880–1889, 1967

Batchelor GK, and Gill AE, “Analysis Of The Stability Of Axisymmetric Jets”, Journal of Fluid Mechanics, **14**: 529-551, 1962

Binder G, and Didelle H, “Improvement Of Ejector Thrust Augmentation By Pulsating Or Flapping Jets”, Proc. AGARD conf. Fluid dynamics of jets with applications to V/STOL, Lisbon, Portugal **308**(22): 1-11, 1981

Boersma, BJ, Brethouwer G, and Nieuwstadt FTM, “A Numerical Investigation On The Effect Of The Inflow Conditions On A Self-Similar Region Of A Round Jet”, Physics of Fluids, **10**(4): 899-909, 1998

Bogey C, Bailly C, and Juve D, “Noise Investgation Of A High Subsonic, Moderate Reynolds Number Jet Using A Compressible Large Eddy Simulation”, Theoretical and Computational Fluid Dynamics, **16**: 273-297, 2003

Borisov YY, and Gynkina NM, “Acoustic Excitation Of High Velocity Jets”, Sov. Phys. Acous. **21**(3): 230-33, 1975

Bradshaw, P, “The Effect Of Initial Conditions On The Development Of A Free Shear Layer”, Journal of Fluid Mechanics, **26**: 225-236, 1966

Browand FK, and Weidman PD, “Large Scales In The Developing Mixing Layer”, Journal of Fluid Mechanics **76**: 127—144, 1976

Brown G, and Roshko A, “On Density Effects And Large Structure In Turbulent Mixing Layers”, Journal of Fluid Mechanics **64**: 775, 1974

Brown GL, and Roshko A, “The Effects Of Density Difference On The Turbulent Mixing Layer”, AGARD-CP-93, 23, 1971

CFDACE user manual, 2004

Chanaud RD, and Powell A, “Some Experiments Concerning The Hole And Ring Tone”, Journal of the Acoustical Society of America **37**: 902, 1965

Chang YK, and Vakili AD, 1995 "Dynamics Of Vortex Rings In Crossflow", Physics of Fluids **7**(7), 1995

Cohen J, and Wygnanski I, "The Evolution Of The Instabilities In The Axisymmetric Jet. Part 1. The Linear Growth Of The Disturbance Near The Nozzle", Journal of Fluid Mechanics **176**: 191-219, 1987

Crow SC, and Champagne FH, "Orderly Structure In Jet Turbulence", Journal of Fluid Mechanics **48**:547, 1971

Fiedler HE, "Coherent Structures In Turbulent Flows", Progress in Aerospace Science, **25**: 231, 1988

Fiedler, HE, "Flow Control Of Free Turbulent Shear Flows, Springer, 335–429, 1998

Glezer A and Amitay M, "Synthetic Jets", Annual Review of Fluid Mechanics, **34**, 2002

Gutmark E, and Ho CM, "Development Of An Elliptical Jet", Bulletin of the American Physical Society **27**(9): 1184, November 1982

Gutmark E, Bowman HL, and Schadow KC, "Flow And Acoustic Features Of A Supersonic Tapered Nozzle", Experiments in Fluids **13**: 49-55, 1992

Gutmark EJ, Schadow KC, and Yu KH, "Mixing Enhancement In Supersonic Free Shear Flows", Annual Review of Fluid Mechanics **27**: 375-417, 1995

Hak G, "Flow Control", Cambridge University Press, 2000

Hermanson JC, Wahba A, and Johari H, "Duty-Cycle Effects On Penetration Of Fully Modulated, Turbulent Jets In Crossflow", AIAA Journal **36**(10): 1935-1937, 1998

Hill WG Jr, Jenkins RC, Gilbert BL, "Effect Of The Initial Boundary Layer State On Turbulent Jet Mixing", AIAA Journal, **17**: 1055-1060, 1976

Ho CM, and Gutmark E, "Vortex Induction And Mass Entrainment In A Small Aspect Ratio Elliptic Jet", Journal of Fluid Mechanics, **179**: 383-405, 1987

Ho CM, and Huang LS, "Subharmonics And Vortex Merging In Mixing Layers", Journal of Fluid Mechanics **119**: 443-473, 1982

Ho CM, and Huerre P, "Perturbed Free Shear Layers", Annual Review of Fluid Mechanics **16**: 365-424, 1984

Hu H, Liu HX, Wu SS, "Experimental Investigation On The Aerodynamic Performance Of A 2D Exhaust Ejector System", ASME 96 GT-243, 1996

Hussain AKMF, "Coherent Structures And Studies Of Perturbed And Unperturbed Jets", Lecture Notes in Physics 136, 1980

Hussain AKMF, “Coherent Structures And Turbulence” Journal of Fluid Mechanics **173**: 303, 1986

Hussain AKMF, “Coherent Structures-Reality And Myth”, Physics of Fluids, **26**: 2816-2850, 1983

Hussein HJ, Capp SP, and George WK, “Velocity Measurements In High-Reynolds Number, Momentum Conserving, Axisymmetric, Turbulent Jet”, Journal of Fluid Mechanics, **258**: 31-75, 1994

Kibens V, and Gleezer A, “Excitation Of Supersonic Shear Layers By Piezoelectric Actuators”, Bulletin of the American physical society **37** (8): 1704, 1992

Koshigoe S, Gutmark EJ, and Schadow KC, “Initial Development Of Non-Circular Jets Leading To Axis Switching”, AIAA Journal **27**: 411, 1989

Krishnamurthy, K, “Acoustic Radiation From Two-Dimensional Rectangular Cutouts In Aerodynamics Surfaces”, NACA TN 3487, August 1955

Kurosaka, M, “Acoustic Streaming In Swirling Flow And The Ranque-Hilsch Effect”, Journal of Fluid Mechanics, **124**: 139–172, 1982

Lepicovsky J, Ahuja KK, Brown WH, and Morris PJ, “Acoustic Control Of Free Jet Mixing”, Journal of Propulsion power **2**(4): 323-30, 1986

Liepmann HW, “The Rise And Fall Of Ideas In Turbulence”, Am. Sci., **67**: 221–228, 1979

Longmire, Eaton EK, Elkins JK, and Christopher J, “Control Of Jet Structure By Crown-Shaped Nozzle Attachments”, AIAA-91-316, 1991

Lucas M, “Handbook Of The Acoustic Characteristics Of Turbomachinery Cavities” ASME Press, 1997

Malmstrom GT, “Centerline Velocity Decay Measurements In Low-Velocity Axisymmetric Jets”, Journal of Fluid Mechanics, **246**:363-377, 1997

Martens S, Kinzie KW, McLaughlin DK, “Wave Structure Of Coherent Instabilities In A Planar Shear Layer”, AIAA-94-0822, 1994

Mi J, Nobes DS, and Nathan GJ, “Mixing Characteristics Of Axisymmetric Free Jets Issuing From A Contoured Nozzle, An Orifice Plate And A Pipe”, ASME Journal of Fluids Engineering, **123**: 878-883, 2001

Michalke, A, “Instability Of Compressible Circular Free Jet With Consideration Of The Influence Of The Jet Boundary Layer Thickness”, NASA Technical. Memorandum 75190, 1977

Michalke, A, “On Spatially Growing Disturbances In An Inviscid Shear Layer”, Journal of Fluid Mechanics **23**: 521-544, 1965

Michalke, A, “The Instability Of Free Shear Layers”, Progress in Aerospace Science, **12**: 213-239, 1972

Panchapakesan N.R, Lumley J.L, “Turbulence Measurements In Axisymmetric Jets Of Air And Helium. Part 1. Air Jet”, Journal of Fluid Mechanics, **246**: 197-223, 1993

Power GD, McClure MD, and Vinh D, “Advanced IR Suppresser Design Using A Combined CFD/Test Approach”, AIAA-94-3215, 1994

Presz WM, Gousy R, Morin BL, “Forced Mixer Lobes In Ejector Designs”, AIAA-86-1614, 1986

Quinn W R, Militzer J, “Effects Of Nonparallel Exit Flow On Round Turbulent Free Jets”, International Journal of Heat and Fluid Flow, **10**: 139-145, 1989

Rayleigh JWS, “The Theory Of Sound”, **2**: 410-412, Newyork 1945

Reeder M, Samimy M, “The Evolution Of A Jet With Vortex Generating Tabs: Real Time Visualization And Quantitative Measurements”, Journal of Fluid Mechanics **311**: 73-118, 1996

Reynolds WC, Parekh DE, Juvet PJD, and Lee MJD, “Bifurcating And Blooming Jets”, Annual Review of Fluid Mechanics **35**: 295–315, 2003

Robinson SK, “Coherent Motions In The Turbulent Boundary Layer”, Annual Review of Fluid Mechanics **23**: 601-639, 1991

Rockwell D, Naudascher E, “Self-Sustained Oscillations Of Impinging Free Shear Layers”, Annual Review of Fluid Mechanics, **11**: 67-97

Rockwell D, and Naudascher E, “Review: Self-Sustaining Oscillations Of Flow Past Cavities” Journal of Fluids Engineering **100**: 152–165, 1978

Roshko, A, “Structure Of Turbulent Shear Flows: A New Look”, AIAA Journal **14**: 1349-1357

Rossiter, JE, “Wind Tunnel Experiments On The Flow Over Rectangular Cavities At Subsonic And Transonic Speeds”, ARC R&M No. 3438, October 1964

Sarohia V, “Experimental Investigation Of Oscillations In Flows Over Shallow Cavities”, AIAA Journal **15**(7): 984-991, 1977.

Sauerwein SC, and Vakili AD, “An Experimental Study Of Zero-Mass Jets In Crossflow”, AIAA-99-668, 1999

Schadow KC, Gutmark EJ, Parr DM, and Wilson KJ, ”Selective Control Of Flow Coherence In Triangular Jets”, Experiments in Fluids **6**:129-135, 1988

Schadow KC, Gutmark EJ, Wilson KJ, and Smith R, “Noncircular Inlet Duct Cross-Section To Reduce Combustion Instabilities”, Combustion Science and Technology, **73**: 537, 1990

Selerowicz, WC, Szumowski, AP, Meier, GEA, “Self-Excited Compressible Flow In A Pipe-Collar Nozzle”, Journal of Fluid Mechanics **228**: 465-85, 1991

Sfeir AA, “Investigation Of Three-Dimensional Turbulent Rectangular Jets”, AIAA Journal **17**: 1055-1060, 1979

Sforza PM, Steiger MH, Trentacoste N, “Studies On Three-Dimensional Viscous Jets” AIAA Journal **4**: 800, 1966

Smith LL, Majamak, AJ, Lam IT, Delabroy O, Karagozian AR, Marble FE, and Smith OI, “Mixing Enhancement In A Lobed Injector”, Physics of fluids **9**: 667-678, 1997

Sondhauss H, Pogg. Ann. **91**: 126 – 147, 1854

Stromberg JL, McLaughlin DK, and Troutt TR, “Flow Field And Acoustic Properties Of A Mach Number 0.9 Jet At A Low Reynolds Number”, Journal of Sound and Vibration, **72**(2): 159–176, 1979

Strykowski P, Krothapalli A, Forliti DJ, “Counterflow Thrust Vectoring Of Supersonic Jets”, AIAA Journal **34**: 2306-2314, 1993

Tam CKW, Block PJW, “On The Tones And Pressure Oscillations Induced By Flow Over Rectangular Cavities”, Journal of Fluid Mechanics **89**: 373–399, 1978

Tillman T, Presz W, “Thrust Characteristics Of A Supersonic Mixer Ejector”, AIAA-93-4345, 1993

Townsend A, “The Structure Of Turbulent Shear Flow”, Cambridge University press, 1952

Townsend AA, “Entrainment And The Structure Of Turbulent Flow”, Journal of Fluid Mechanics, **41**: 13–46, 1970

Townsend AA, “Equilibrium Layers And Wall Turbulence”, Journal of Fluid Mechanics **11**: 97–120, 1961

Trentacoste N, Sforza PM, “Further Experimental Results For Three-Dimensional Free Jets” AIAA Journal **5**: 885, 1967

Umeda Y, Maeda H, and Ishii R, “Discrete Tones Generated By The Impingement Of A High Speed Jet On A Circular Cylinder”, Physics of fluids **30**(8): 2380-88, 1987

Vakili AD, “Review Of Vortical Flow Utilization”, AIAA-90-1429, 1990

Vakili AD, Chang YK, and Wu JM, “Vortex Rings In Uniform Crossflow” AIAA-91-0522, 1991

Vakili AD, Sauerwein SC, and Miller DN. “Pulsed Injection Applied To Nozzle Internal Flow Control”, AIAA-1999-1002

Vakili AD, Wu JM, Chang YK, and Yu FM, “Pulsed Jets In Crossflow”, Intl Symposium on NonSteady Fluid Dynamics FED-Vol. 92

Winant CD, and Browand FK, “Vortex Pairing: The Mechanism Of Turbulent Mixing-Layer Growth At Moderate Reynolds Number”, Journal of Fluid Mechanics **63**: 237-255, 1963

Wu JM, Vakili AD, and Yu FM, “Investigation Of The Interacting Flow Of Nonsymmetric Jets In A Crossflow”, AIAA Journal **26**:8, 1988

Wygnanski I, and Fiedler H, “Some Measurements In The Self-Preserving Jet”, Journal of Fluid Mechanics, **38**(3): 577-612, 1969

Yu KH, Gutmark E, Smith RA, and Schadow KC, “Supersonic Flow Mixing And Combustion Using Ramp Nozzle”, AIAA-92-3840, 1994

Zaman KBMQ, Reeder M, Samimy M, “Control Of An Axisymmetric Jet Using Vortex Generators”, Physics of Fluids **6**: 778-92, 1994

Zaman KBMQ, “Effects Of Tabs On The Evolution Of An Axisymmetric Jet”, NASA TM 104472, 1991

APPENDIX

Appendix A

HEAT SEPARATION

During the course of this study, it was observed that under certain flow conditions, especially when resonant behavior (discussed in chapter 4) is present, a significant increase in temperature occurs in certain parts of the flow. This rise in temperature was high enough to be felt when the operator stands closer to the jet. However if one exposes their palm towards the jet, the heat could not be felt except in the small gap between the fingers. The temperature increase was so high that one could not bear for more than a few seconds. This heat appeared to be from radiated flow away from the flow. The increase in temperature between the fingers could not be felt in all locations but only along certain locations along the jet. However, for a particular axial and radial location away from the jet exit where this phenomenon is present, it was observable all the way in the circumferential direction. The necessity of a fine mesh was confirmed through another observation. When the pressure inside the axisymmetric cavity was increased above 25 psi, the pressure transducer placed flush with the cavity wall failed. After initial suspicions, that the failure might be due to the high amplitude oscillations were ruled out, it was suspected (based on the observation earlier regarding the rise in temperature between the finger and through clothes) that the failure was because the temperature of the transducer had risen beyond its limit. The transducer was rated to operate between -54˚C and +121˚C. The transducer had a mesh screen right in front of the diaphragm. A thermocouple was placed in the same location as the transducer (without any screen) and no increase in temperature was observed. When a fine screen was placed in front of the thermocouple and placed at the same location, temperature rose above the limits of the transducer. Based on these observations, it was concluded that two criterions are necessary for the phenomenon.

1. Presence of the oscillations (For the baseline cases, there was no rise in temperature even at much higher pressures).
2. Presence of a fine mesh.

The following sections try to raise possible processes involved in this phenomenon. Two processes that are suspected are:

1. Ranque-Hilsch effect
2. Acoustic streaming

The Ranque-Hilsch tube is a simple device (shown in Figure A.1a), which can produce hot and cold air streams simultaneously at its two ends from a source of compressed air and without any moving parts. The basic process is as follows. Air is supplied to the main tube tangentially and passes towards the hot air exhaust as an outer vortex. Some part of the air turns back and flows towards the cold air exit as an inner vortex along the center of the tube. There are a number of theories explaining why the inner vortex loses heat ranging from loss of angular momentum to

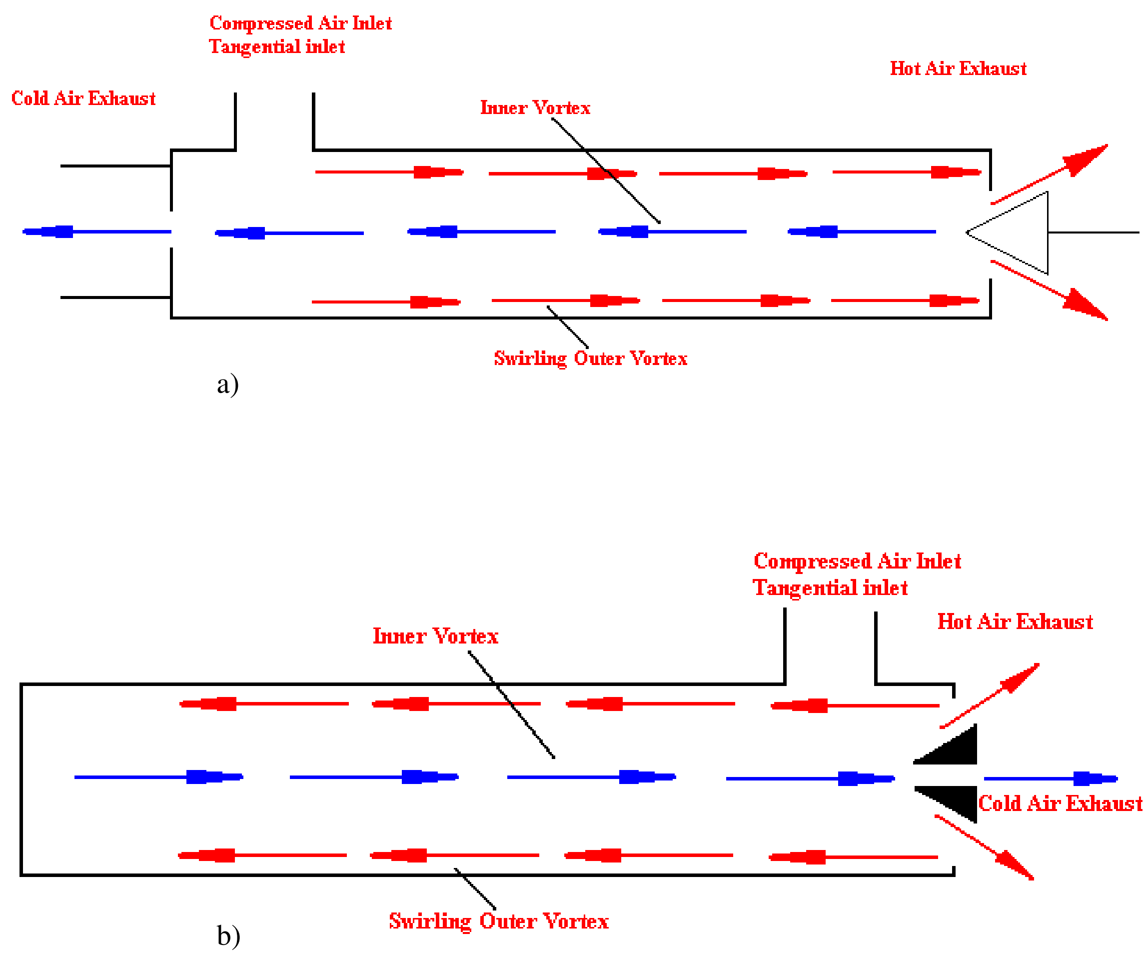

Figure A.1. Schematic of a Ranque-Hilsch tube. a) with two ends b) with a single end random radial migration of fluid lumps. A Ranque-Hilsch tube could also have just one end through which both hot and cold air is taken out (Figure A.1b).

Acoustic streaming describes a steady flow field superimposed upon the oscillatory motion of a sound wave propagating in a fluid. It is a non-linear effect, taking place due to the presence of boundaries or because of attenuation of the wave. Acoustic streaming velocities are normally small compared to the velocity of the oscillatory fluid motion (<10%). There are two basic types of acoustic streaming. The first, Rayleigh streaming, is caused by relative oscillatory motion between the fluid and a boundary. The steady flow results from the rapid changes in the wave amplitude in the acoustic boundary layer. The effects of attenuation on the primary wave, though present, are usually considered to be negligible. The second, Eckart streaming or quartz wind, results from the attenuation of the wave in the bulk fluid. Any boundary effects are neglected. Here momentum transfer from the wave is converted into a steady flow moving away from the source. Eckart streaming is often seen with quartz transducer systems such as ultrasonic probes. The high amplitude tone generated by the cavity can induce acoustic streaming and thus be part of the Ranque-Hilsch effect as described by Kurosaka [*Kurosaka* 1982].

A schematic showing possible Ranque-Hilsch effect taking place in this study is shown in Figure A.2. But this doesn't explain why there is a necessity for a mesh in order for heat to be released. It was decided to postpone a detailed investigation of this phenomenon to a future study. Further detailed study is needed to provide a complete explanation for this phenomenon. But one could find many applications that could be based on this phenomenon.

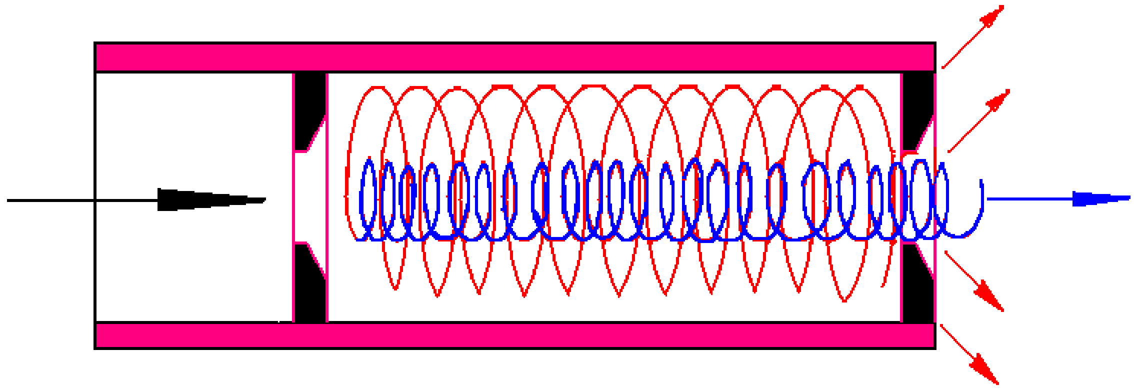

Figure A.2. Possible Ranque Hilsch effect in the current study

VITA

Abraham Joseph Meganathan was born in Tuticorin, INDIA on October 2, 1975. He completed his undergraduate studies in Mechanical Engineering at Karunya Institute of Technology (currently Karunya University), Coimbatore, INDIA in 1998. He entered the University of Tennessee Space Institute for his graduate studies in 1999. He received his Master of Science degree in Mechanical Engineering in December 2000 and the Doctor of Philosophy degree in May 2005.